*Sapienza Università di Roma*
*Dottorato di Ricerca in Scienze della Terra*

*XXXVI ciclo*

# *Structural and frictional properties of phyllosilicate-rich faults and implications for their seismogenic potential*

Ph.D. thesis

in

Solid Earth Geophysics (GEO/10)

Giuseppe Volpe

2023

**Ph.D. Supervisor:**

Prof. Cristiano Collettini, *Dipartimento di Scienze della Terra, Sapienza Università di Roma, Italy*

**Ph.D. Co-supervisor:**

Dott. Giacomo Pozzi, *Istituto Nazionale di Geofisica e Vulcanologia, Italy*

**External Revisors:**

Prof. Nicola de Paola, *Department of Earth Sciences, Durham University, Durham (United Kingdom)*

Prof. Telemaco Tesei, *Dipartimento di Geoscienze, Università degli Studi di Padova, Padova (Italy)*

# Sommario

*Abstract* ..... *4*

*Riassunto* ..... *6*

*1 Introduction* ..... *8*

**1.1 Frictional properties and earthquakes nucleation** ..... **8**

1.1.1 The nature of friction ..... 8

1.1.2 Fault reactivation criterion ..... 10

1.1.3 Rate and State Friction framework ..... 11

1.1.4 Fault restrengthening and healing rate ..... 12

1.1.5 The Spring slider model and the stability criterion ..... 13

**1.2 Influencing factors of frictional properties.** ..... **14**

1.2.1 Mineralogy ..... 15

1.2.2 Fluids ..... 16

1.2.3 Pressure ..... 17

1.2.4 Temperature ..... 18

**1.3 Fault fabric** ..... **19**

**1.4 Fault zone structures and fault slip behavior** ..... **21**

1.4.1 Slip behavior and seismicity along rheologically heterogeneous fault zones ..... 22

*2 Rationale of the thesis* ..... *24*

**2.1 The role of phyllosilicates in fault slip behavior** ..... **24**

**2.2 The objectives of the thesis and case-studies** ..... **26**

*3 Methods* ..... *27*

**3.1 Field work** ..... **27**

**3.2 Rock deformation experiments** ..... **27**

3.2.1 Experimental Apparatus ..... 27

3.2.2 Experimental assemblies ..... 28

3.2.3 Special methods ..... 30

3.2.4 Experimental rock samples ..... 30

**3.3 Microstructural analysis** ..... **31**

3.3.1 Natural Samples ..... 31

3.3.2 Experimentally deformed samples ..... 32

**3.4 Seismological analysis ..... 33**

***4 Results ..... 34***

**Chapter I ..... 34**

**Study of the frictional mechanisms of phyllosilicate-rich fault rocks at the microscale ..... 34**

Y-B-P-R or S-C-C'? Suggestion for the nomenclature of experimental brittle fault fabric in phyllosilicate-granular mixtures ..... 34

**Chapter II ..... 66**

***The role of Apennine basement in the seismic context of central Italy ..... 66***

Frictional controls on the seismogenic zone: insights from the Apenninic basement, Central Italy ..... 66

Rheological heterogeneities at the roots of the seismogenic zone ..... 85

**Chapter III ..... 94**

***The role of clay-rich sediments in the seismicity of shallow subduction zones ..... 94***

Frictional instabilities in clay illuminate the origin of slow earthquakes ..... 94

**Chapter IV ..... 104**

***Study of fluid-induced reactivation of granite-hosted fault in the Central Alps ..... 104***

Laboratory simulation of fault reactivation by fluid injection and implications for induced seismicity at the BedrettoLab, Swiss Alps. ..... 104

***5 Conclusions ..... 128***

***6 Open questions ..... 131***

***7 References ..... 134***

***8 Appendix ..... 157***

**Appendix of chapter I ..... 157**

***Study of the frictional mechanisms of phyllosilicate-rich fault rocks at the microscale. ..... 157***

Y-B-P-R or S-C-C'? Suggestion for the nomenclature of experimental brittle fault fabric in phyllosilicate-granular mixtures ..... 157

**Appendix of chapter II ..... 162**

***The role of Apennine basement in the seismic context of central Italy ..... 162***

Frictional controls on the seismogenic zone: insights from the Apenninic basement, Central Italy ..... 162

**Appendix of chapter III ..... 182**

***The role of clay-rich sediments in the seismicity of shallow subduction zones ..... 182***

Frictional instabilities in clay illuminate the origin of slow earthquakes .....182

**Appendix of chapter IV ..... 195**

***Study of fluid-induced reactivation of granite-hosted fault in the Central Alps ..... 195***

Laboratory simulation of fault reactivation by fluid injection and implications for induced seismicity at the BedrettoLab, Swiss Alps. .....195

# Abstract

Phyllosilicates minerals are a family of silicates characterized by a platy habitus derived from a layered structures where strong and weaker layers are alternated producing a marked strength anisotropy. Phyllosilicates such as micas, serpentines, talc, and clays, are abundant along fault zones belonging to all tectonic settings and can be found as primary product of the cataclastic deformation of phyllosilicate-rich rocks or as a secondary product of long-term fluid-rock interaction. The widespread occurrence of these minerals makes them a key controlling factor of the mechanics of faulting in the brittle crust. In the last 30 years an increasing attention has been given to the experimental characterization of the frictional properties of phyllosilicates. Experimental data show that phyllosilicate-rich fault rocks generally exhibit low friction, low healing, and rate-strengthening behavior over a large variety of boundary conditions. According to existing theory, these rocks due to their frictional properties cannot host earthquakes nucleation and thus deform aseismically. However, an increasing amount of geological, geophysical, and seismological data suggest that phyllosilicate-rich faults can be seismogenic or promote earthquakes nucleation elsewhere (e.g., on adjacent faults or asperities). Therefore, phyllosilicate-rich fault can represent an unexpected seismic hazard whose underlying mechanisms are still not well understood. To shed light on the seismogenic potential of phyllosilicate-rich fault rocks, I applied an interdisciplinary approach that integrates rock deformation experiments, structural and microstructural analysis with seismology. In the first chapter, I characterized the interplay between mineralogy, fabric, and frictional properties of phyllosilicates-granular mixtures, to understand how fault fabric influences frictional properties. The results show a strong influence of fault fabric on frictional properties highlighting how secondary fabric features, such as the shape of grains, the regularity of foliation, grain mantling, and the degree of localization, can be responsible for small but sensible changes in the frictional properties of rocks. In the second chapter, I investigated the role of the phyllitic basement of central Apennines in the Central Italy 2016-2017 seismic sequence. The results of the two works contained in this chapter show that the basement is rheologically heterogeneous and made of frictionally strong quartz-rich lenses enveloped by a frictionally weak phyllosilicate-rich matrix. The matrix controls the overall rheology of the basement favoring aseismic deformation that is compatible with the seismicity cutoff observed in correspondence of the basement. Furthermore, I found that the observed seismicity cutoff is not controlled by the canonical brittle-ductile transition, but it is rather controlled by the frictional properties of the basement rocks. Following the mainshock of the sequence, the basement shows a diffused microseismicity organized in clusters of co-located earthquakes. This behavior

can be explained as the seismic reactivation of small faults within the lenses loaded by accelerated but aseismic creep of the matrix caused by the post-mainshock loading-rate increase. The overall results of this chapters unveil the mechanisms behind the fault slip behavior of a rheologically heterogeneous phyllosilicate-rich shear zone. In the third chapter I shed light on the seismogenic potential of the clay-rich shallow subduction zones focusing on the nucleation of slow slip and tsunami earthquakes. The results of this chapters show that clay-rich faults can contemporaneously creep and nucleate slow slips in the form of slow ruptures driven by structural, frictional, and stress heterogeneities together with alternative frictional mechanisms which are imaged with an innovative technique that allows a direct observation of the fault surface during deformation. In the four and last chapter I assessed the potential of a phyllosilicate-rich fault selected for a limited fluid-induced reactivation that will take place within the activities of the Fault Activation and Earthquake Rupture (FEAR) project in the fully monitored environment provided by BedrettoLab (Swiss Alps). The results of this study highlight the strong influence of frictional, microstructural, and permeability properties on the fault slip behavior during fluid injection activity and therefore on its seismogenic potential. The overall findings presented in this PhD offer a new perspective on the seismogenic potential of phyllosilicate-rich faults with significant implication for earthquakes mechanisms and seismic hazard.

# Riassunto

I fillosilicati sono minerali caratterizzati da un abito cristallino lamellare derivante dalla loro struttura stratificata prodotta dall'alternanza di strati meccanicamente deboli e forti. Questa anisotropia è alla base del clivaggio basale che li caratterizza e che produce il loro tipico aspetto lamellare. Miche, serpentini, talco e argille sono tra i fillosilicati più abbondanti lungo le zone di faglia nei diversi contesti tettonici. I fillosilicati nelle zone di faglia possono essere il prodotto della cataclasi di rocce ricche in fillosilicati o possono anche essere il prodotto dell'alterazione chimica di altri minerali mediante processi di interazione fluido-roccia. La diffusa occorrenza di fillosilicati lungo le zone di faglia le rende un fattore fondamentale per meccanica dei terremoti. Infatti, negli ultimi 30 anni una sempre crescente attenzione è stata posta sulla caratterizzazione sperimentale delle proprietà di attrito di rocce ricche in fillosilicati. I fillosilicati risultano generalmente caratterizzati da un basso coefficiente di attrito, da un basso healing rate e da un comportamento rate-strengthening. Queste proprietà di attrito, secondo le teorie esistenti, non consentono la nucleazione di terremoti e consentono quindi solo uno scivolamento asismico. Contrariamente a ciò, un sempre crescente numero di evidenze scientifiche suggerisce che le faglie ricche in fillosilicati possano sia nucleare terremoti sia favorire la nucleazione di terremoti altrove (faglie limitrofe, asperità). Questa evidenza comporta che le faglie ricche in fillosilicati possono rappresentare un rischio sismico inaspettato i cui meccanismi sono ancora poco compresi. Per fare luce sul potenziale sismogenetico di faglie ricche in fillosilicati, ho applicato un approccio multidisciplinare che integra insieme esperimenti di laboratorio, analisi strutturale, microstrutturale e sismologica. Nel primo capitolo di questa tesi di dottorato ho caratterizzato la relazione tra proprietà di attrito, mineralogia e microstrutture di faglie sperimentali fatte di una mistura di minerali granulari e fillosilicati. I risultati di questo lavoro mostrano come le microstrutture influenzano fortemente le proprietà di attrito e mostrano anche come microstrutture di secondo ordine come la forma dei grani, la regolarità della foliazione e il grado di localizzazione siano responsabili di piccoli ma sensibili cambiamenti delle proprietà di attrito. Nel secondo capitolo ho analizzato il ruolo del basamento filladico dell'Appennino centrale durante la sequenza sismica dell'Italia centrale del 2016-2017. I risultati dei due lavori contenuti in questo capitolo mostrano come il basamento filladico sia caratterizzato da forti eterogeneità reologiche derivanti dalla presenza di una litologia ricca in fillosilicati e frizionalmente debole che ha il ruolo di matrice che circonda lenti di litologie ricche in quarzo e frizionalmente forti. La matrice controlla la reologia del basamento favorendo uno scivolamento asismico. Questo risultato è compatibile con la drastica diminuzione di sismicità in corrispondenza del basamento che risulta quindi essere controllata dalle proprietà

di attrito delle rocce di basamento piuttosto che dalla transizione fragile duttile controllata dalla temperatura A seguito dei terremoti principali della sequenza sismica, nel basamento si osserva un incremento di microsismicità organizzata in cluster di terremoti co-locati. Questa microsismicità può essere spiegata come la riattivazione di piccole faglie contenute nelle lenti provocata dal trasferimento di stress dalla matrice alle lenti a seguito di un aumento del loading rate a seguito del terremoto principale. I risultati di questo capitolo svelano i meccanismi che sottostanno al potenziale sismogenetico di faglie ricche in fillosilicati reologicamente eterogenee. Nel terzo capitolo, ho investigato il potenziale sismogenetico delle faglie ricche in argille tipiche delle zone di subduzione superficiali. In particolare, mi sono focalizzato sulla nucleazione di terremoti lenti e i cosiddetti "tsunami earthquakes". I risultati di questo capitolo mostrano come faglie ricche in argille possano contemporaneamente scivolare asismicamente e nucleare terremoti lenti grazie agli effetti di eterogeneità strutturali, frizionali e di carico insieme a meccanismi frizionali alternativi. Nel quarto e ultimo capitolo della mia tesi di dottorato ho caratterizzato il potenziale sismogenetico di una faglia ricca in fillosilicati selezionata per una riattivazione prodotta da attività di iniezione di fluidi all'interno del progetto FEAR presso il laboratorio sotterraneo del BedrettoLab (Alpi Svizzere). I risultati di questo ultimo capitolo mostrano come le proprietà di attrito, microstrutture e permeabilità possano fortemente influenzare il modo di scivolare di una faglia a seguito di attività antropiche di iniezione di fluidi. I risultati presentati in questa tesi di dottorato offrono una nuova prospettiva sul potenziale sismogenetico di faglie ricche in fillosilicati con implicazioni significative per la meccanica dei terremoti e il rischio sismico.

# 1 Introduction

## 1.1 Frictional properties and earthquakes nucleation

Faults are brittle discontinuities of the lithosphere, loci that accommodate the deformation induced by plate tectonics. Through geological time, the build-up of stress on faults can overcome their resistance to shear, resulting in the release of the accumulated potential (elastic) energy via a large spectrum of seismic phenomena. These can range from aseismic creep, slow-slip events, non-volcanic tremors, low frequency earthquakes, slow earthquakes, and fast regular earthquakes (Ide et al., 2007; Peng and Gomberg, 2010; Ide and Beroza, 2023). Aseismic creep and slow-slip events can be detected only by geodetic measurements, since their slow rupture process does not radiate seismic waves (Peng and Gomberg, 2010). Non-Volcanic tremors, low frequency earthquakes and slow earthquakes represent quasi-dynamic fault slip transients with slow rupture velocity, resulting in a diminished high-frequency seismic radiation (Peng and Gomberg, 2010; Scholz, 2019). Fast and regular earthquakes are instead the elasto-dynamic failure of faults, where the dynamic rupture velocity is responsible for the high frequency seismic radiation (Ide et al., 2007; Peng and Gomberg, 2010; Ide and Beroza, 2023). These differences in fault slip behavior are the result of a complex dynamic system of fault processes, and expecially the interplay between the mechanical properties of the surrounding rocks (i.e., the loading medium) and the frictional properties of the fault. The latter are strongly dependent not only on the material (mineralogy), but also on the boundary conditions (pressure, temperature, fluids) and the fault zone structure (Scholz, 2019).

In the following paragraphs I firstly present a review of the frictional properties of fault materials (paragraphs 1.1.1 to 1.1.5), then I discuss the most important influencing factors of the frictional properties (paragraphs 1.2 to 1.4.1).

### 1.1.1 The nature of friction

The nature of friction was systematically studied for the first time in the XV century by Leonardo da Vinci who discovered that friction is dependent on the load and on the roughness of the sliding surface. In the XVIII century, Amontons enunciated the two fundamental laws of friction: friction is independent of the size of the surface in contact, and friction is proportional to normal load. These assumptions were successively confirmed in the early XIX century by Coulomb

who understood that friction is mainly correlated to the roughness of the contact surface. Furthermore, Coulomb discovered that friction has two different natures, static and dynamic, the first is higher than the second. He also noticed that static friction grows with time of stationary contact, in fact he observed that the force necessary to move two wood blocks attached together is proportional to the time during which they were attached.

The modern concept of friction derives from the adhesion theory of friction postulated by Bowden and Tabor (1950). They proved that friction arises from the roughness of the sliding surface, which is always characterized by a roughness (fig. 1.1). They also assumed that, due to contact surface topography, the real contact area, *Ar,* is significantly lower than the nominal contact area, *An* (fig. 1.1 c).

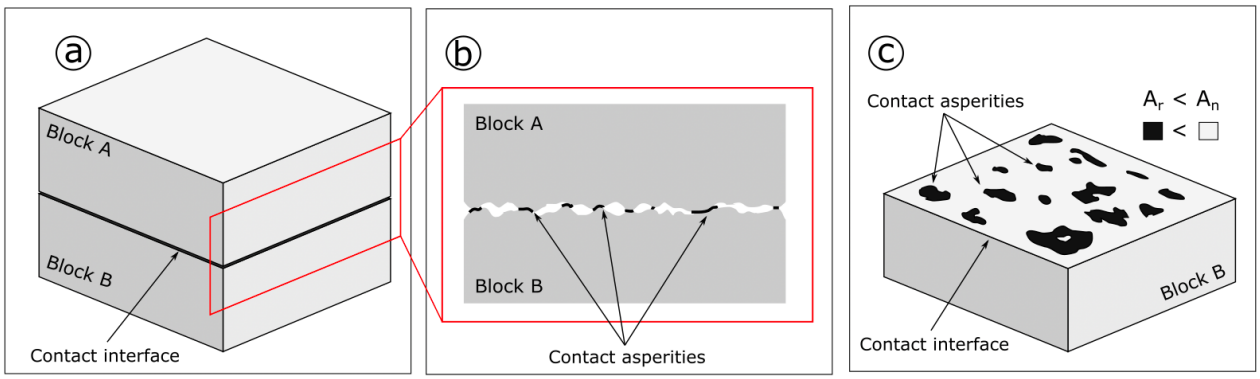


Figure 1.1: schematic drawing of the contacts (black colors) along an interface dividing two rigid blocks. a) Two blocks are put in contact along an interface (black surface). b) section view of the interface where the contact asperities between the two blocks are highlighted in black. c) Distribution of the contact asperities (black regions) on the contact interface.

This implies that all the normal stress, *N,* acting on the nominal contact area is sustained only by the few asperities or junctions contributing to the real contact area. The real contact area depends on the penetration strength (*p*) of the material of the asperities: the stronger is the material the lower is the real contact area (fig. 1.1 c).

$$N = p\,Ar \qquad eq.1$$

Stemming from these assumptions, Bowden and Tabor were able to define the frictional force (*F*) as the force necessary to overcome the sum of the junction resistance to shear (*s*).

$$F = s\,Ar \qquad eq.2$$

So, matching these two equations it is possible to define the friction coefficient $\mu$, as the ratio between *F* and *N*

$$\mu = \frac{F}{N} \qquad eq.3$$

It is also possible to derive that the friction coefficient is the ratio between the shear strength, *s*, and penetration strength, *p*, which is at first order independent from the material,

$$\mu = \frac{F}{N} = \frac{s\,Ar}{p\,Ar} = \frac{s}{p} \qquad eq.4$$

However, the friction coefficient can be sensibly increased by other frictional processes acting at the asperity scale such as ploughing, riding-up and interlocking (e.g., Scholz, 2019).

### 1.1.2 Fault reactivation criterion

Fault reactivation obeys the Coulomb shear failure law:

$$\tau = \mu\,\sigma n \qquad eq.5$$

Where τ is the stress needed to reactivate a fault (i.e., shear resistance), $\sigma_n$ is the normal stress acting perpendicularly to the fault surface and μ represents the constant of proportionality between normal and shear stress. In the presence of pressurized fluids along the fault, the Coulomb shear failure criterion is modified according to the Terzaghi principle, which states that the effective normal stress, $\sigma'_n$, is the difference between normal stress and pore fluid pressure, $P_f$:

$$\tau = \mu\,\sigma' n = \mu\,(\sigma n - Pf) \qquad eq.6$$

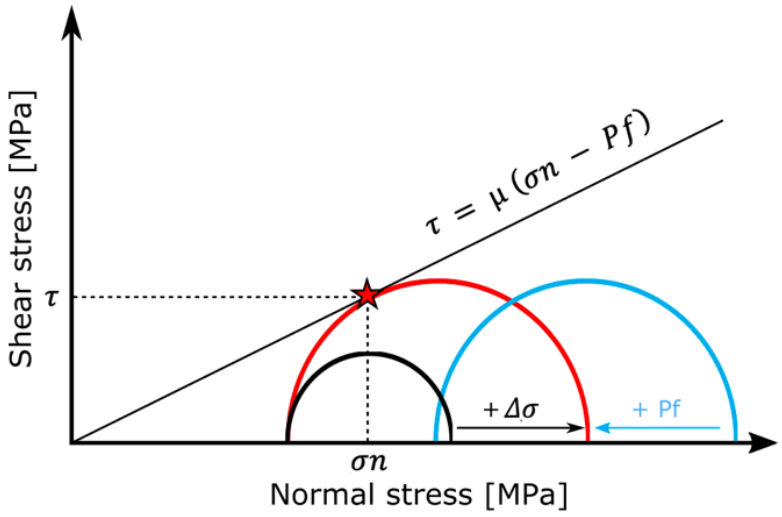


Figure 1.1.2. Mohr-Coulomb diagram showing the stress conditions for fault reactivation (red star). A fault can be reactivated by increasing its differential stress, Δσ, (from black to red circle) or by increasing the pore fluid pressure $Pf$ and therefore decreasing the effective normal stress (from blue to red circle).

Once a fault is reactivated, it can slide either in a stable or unstable way, in other words, with aseismic or seismic slip. The Coulomb criterion, however, does not contain information on the modality at which the fault will slip upon reactivation. In fact, friction (μ) is seldom a constant (Eq. 6) and is affected by the kinetic state of the sliding material and many other factors, listed in the following sections. In general, the main conditions necessary for unstable fault slip are the following: i) the frictional resistance of the fault must decrease with increasing sliding velocity, ii) the fault must regain strength (i.e., accumulating stress) during time of quiescence, and iii) the release of stress during slip (i.e., frictional weakening) must be faster than the elastic unloading of the loading medium (Dieterich, 1979; Ruina, 1983; Marone, 1998). These conditions were described in empirical constitutive laws integrated together in a theoretical framework known as the Rate and State Friction framework (RSF, Dieterich, 1979; Ruina, 1983; Marone, 1998, fig. 1.1.5).

### 1.1.3 Rate and State Friction framework

This theory collects the physical description of the evolution of friction as a function of slip velocity (rate) and an evolutionary effect (state), which describes a memory effect of the material. The fundamental law of the RSF is expressed as:

$$\mu = \mu 0 + aln\left(\frac{V}{V0}\right) + bln\left(\frac{V\theta}{Dc}\right) \qquad eq.7$$

where $\mu_0$ is the steady-state friction at a reference velocity *V0*. *a* and *b* are empirical constants describing the direct and evolution effect of friction during a change in velocity from $V_0$ to *V* over a characteristic distance, *Dc* which is the critical slip distance interpreted as the sliding distance needed to renew the population of frictional contacts (i.e., asperities, Dieterich, 1979; Ruina, 1983). The variable $\vartheta$ is the state variable, which is interpreted as the average lifetime of the asperities (Ruina, 1983) and determines the evolution effect. The state variable $\vartheta$ is not a constant and can be expressed with different choices of partial differential equations, that describe the evolution of $\vartheta$ with time (*t*). The most used are:

$$\frac{d\theta}{dt} = 1 - \frac{V\theta}{Dc} \qquad eq.8$$

$$\frac{d\theta}{dt} = -\frac{V0}{Dc} ln \ln\left(\frac{V\theta}{Dc}\right) \qquad eq.9$$

Eq. 8, the Aging law (Dieterich 1972), describes the evolution of $\vartheta$ during truly stationary contacts (*V* = 0), whereas Eq. 9, the Ruina law (Ruina 1983), describes the evolution of $\vartheta$ during quasi stationary contacts where a minimum slip distance *Dc* is required. RFS is an empirical law whose parameters (a, b, Dc) are assessed through velocity step tests in

laboratory experiments in which, for several selected initial velocities (V0), the fault is suddenly forced to slide at faster velocity (V) and the mechanical data are inverted to retrieve the constants of best fit. During the test, each near-instantaneous step in sliding velocity from $V_0$ to V produces an instantaneous change in friction that is proportional to $a\ln(V/V_0)$, which is known as direct effect. The subsequent evolution of friction leads to a new steady-state value that scales with the factor $b\ln(V/V_0)$, which known as evolution effect (Dieterich, 1979; Ruina, 1983). The velocity dependence of friction, described by the (*a-b)* parameter, is defined as:

$$a - b = \frac{\Delta\mu ss}{ln\left(\frac{V}{V0}\right)} \qquad eq.10$$

where $\Delta\mu_{ss}$ is the difference between the steady-state friction before and after the velocity step (Dieterich, 1979, Ruina, 1983). Positive values of (*a-b*) define velocity-strengthening behavior, indicating that aseismic creep is expected. Negative values of (*a-b*) define velocity-weakening behavior, which is a condition required but not sufficient to develop frictional instabilities (e.g., Marone 1998 and fig. 1.1.5 a).

To model the variation of frictional strength during sliding, Eqs. 7 and 10 must be coupled with a formula that accounts for the elastic medium that is transferring stress to the fault:

$$\frac{d\mu}{dt} = K(Vlp - V) \qquad eq.11$$

Where $d\mu$ is the variation of frictional strength in time ($dt$), $K$ is the elastic stiffness of the loading medium, and $V_{lp}$ is the measured loading point velocity (Gu et al., 1984; Marone, 1998). This equation describes the elastic coupling of the fault (Marone, 1998).

## 1.1.4 Fault restrengthening and healing rate

The other key factor that controls the fault slip behavior is the capacity of a fault to regain strength (i.e., frictional restrengthening) during time of quiescence called "interseismic time" (Dieterich and Kilgore, 1994). This process is quantified by the healing rate parameter, $\beta$, measured in the laboratory via slide-hold-slide tests (Marone, 1998; Marone and Saffer, 2015 and fig. 1.1.5 b). This test consists of the alternation of phases during which the fault is sheared at constant sliding velocity with phases during which the fault is stopped for increasing hold time, *Th*. The healing rate parameter, $\beta$, represents the slope of the linear relation (fig. 1.1.5 c) between fault frictional restrengthening, $\Delta\mu$, and the logarithm of hold time, *log(Th)*:

$$\beta = \frac{\Delta\mu}{log(Th)} \qquad eq.12$$

During slide-hold-slide tests, the amount of fault frictional restrengthening (Δμ) is calculated as the difference between the steady state friction measured before the hold and the peak friction coefficient achieved upon re-sliding (Marone, 1998 and fig. 1.1.5 b). The physical interpretation of this process is interpreted as the growth over time of the real contact area along the contact interface (Dieterich and Kilgore, 1994; Marone, 1998; Marone and Saffer, 2015). However, the same restrengthening effect can be produced by other physical-chemical processes as interlocking, adhesive-cohesive processes, and cementation (Dieterich and Kilgore, 1994; Marone and Saffer, 2015; Ikari et al., 2021).

### 1.1.5 The Spring slider model and the stability criterion

The last condition necessary to develop frictional instabilities is that the frictional weakening during slip is faster than the elastic unloading of the system (Dieterich, 1979; Ruina, 1983; Marone, 1998). The physics behind this concept can be illustrated by the spring-slider model. The spring slider is a mechanical system where a block of rock lays on a frictional interface and is pulled at constant velocity through a spring with known stiffness. While the spring elongates it accumulates elastic force. Once the pulling force is equivalent to the static frictional force of the frictional interface, the block unclamps and starts sliding (fig. 1.1.5 e). The mode of slip, stable or unstable, is controlled not only by the velocity dependence of friction (see 1.1.3), but also by the way elastic energy is dissipated during slip. This balance between driving force and opposing frictional force is expressed by the difference between the stiffness of the loading medium (the spring), *k*, and the critical frictional stiffness of the fault, *kc*, which is measured according to the following equation:

$$kc = \frac{(b-a)\ (s'n)}{Dc} \qquad eq.13$$

If critical stiffness of the fault is greater than the elastic stiffness of the loading medium (k/kc < 1) the system undergoes unstable slip (Gu et al., 1984; Marone, 1998). Otherwise, the fault will slide stably even if friction is velocity-weakening (fig. 1.1.5 e).

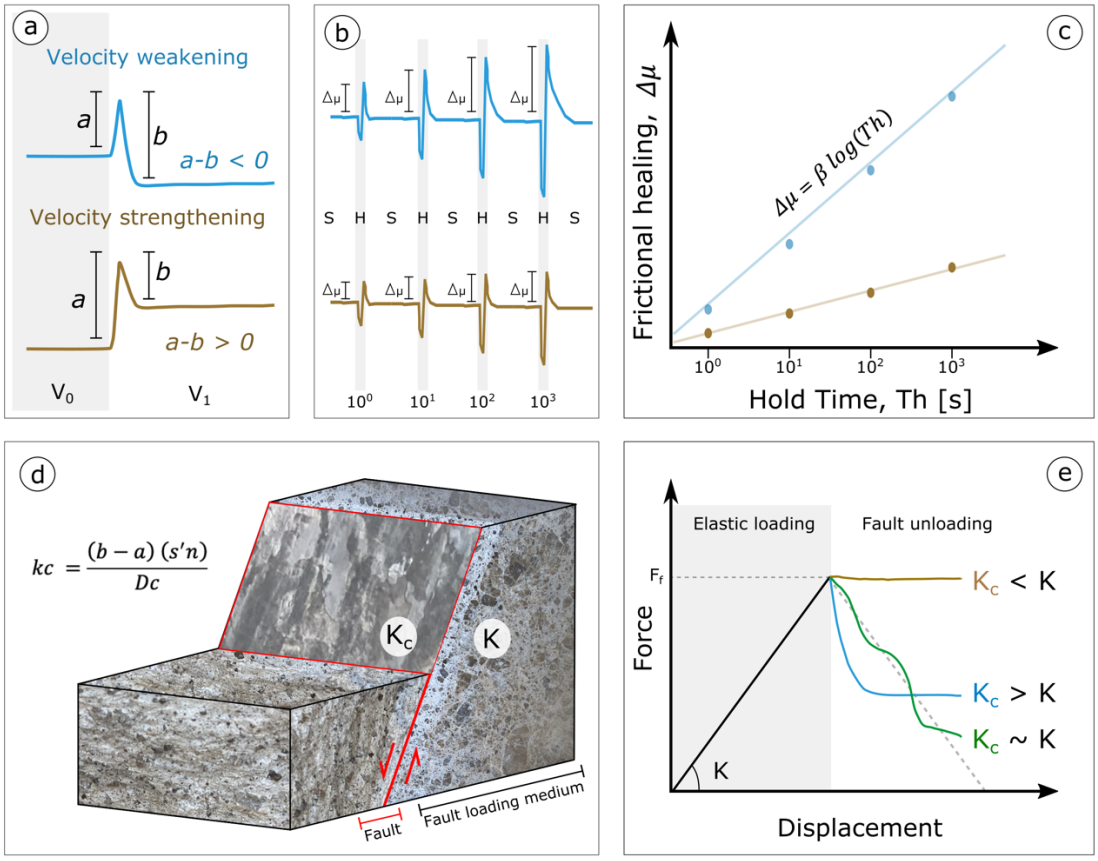


Figure 1.1.5. Schematic of the Rate and State frictional properties (R&S) and their impact on the fault slip behavior. a) evolution of friction during a velocity step from $V_0$ to $V_1$ ($V_0$<$V_1$) showing a velocity weakening behavior with $a$-$b$<0 (blue curve) and a velocity strengthening behavior with $a$-$b$>0 (brown curve). b) evolution of friction during slide-hold-slide sequence (SHS) for two materials showing a high and low (blue and brown respectively) value of frictional restrengthening, $\Delta\mu$. c) frictional restrengthening vs hold time for two materials showing higher and lower healing rates, $\beta$ (blue and brown respectively). d) Block diagram showing the elastic properties of a fault zone: K represents the stiffness of fault loading medium whereas $K_c$ the critical stiffness of the fault retrieved from R&S parameters (eq. 13). e) Force-displacement evolution according to the spring-slider model. Three different fault slip behaviors are expected: fast unstable slip if $K_c$>K (blue curve); slow unstable slip if $K_c$~K (green curve); stable slip if $K_c$<K (brown curve).

## 1.2 Influencing factors of frictional properties.

Frictional properties are influenced by several factors amongst which the most relevant are mineralogy, presence of fluids, pressure, temperature, fault structures. Knowing how these different factors influence singularly and collectively the frictional properties is of fundamental importance to understand and interpret the fault slip behavior both in the laboratory and in nature.

### 1.2.1 Mineralogy

Finely cataclased rocks compose the core of fault zones and control their sliding behavior. Since faults can either be entirely contained in the same formation or juxtapose completely different rocks, fault materials can range from being monomineralic to complex mixtures of different minerals, affecting the frictional properties. With his pioneering work, Byerlee (Byerlee, 1978) performed a large suite of laboratory experiments to test the friction of different rocks, showing that for most of them the steady-state friction coefficient ranges between 0.65 and 0.80 (Byerlee, 1978). However, this general rule does not apply to rocks that are rich in phyllosilicate minerals, which exhibit sensibly lower friction. Further studies strengthened the evidence that there is a clear separation between two classes of minerals: granular (e.g., carbonates, sulfates, quartz, feldspars, and mafic silicates) and platy (micas, clays, serpentines, talc), which are characterized, respectively, by high (> 0.6, Byerlee's range) and low (< 0.3) friction coefficients (Moore and Lockner, 2004; Collettini et al., 2019 and references therein and fig. 1.3). This dichotomy is bridged by a variety of rocks that are mixtures of these two classes. Successive studies revealed that the same dichotomy is not only reflected by a the first-order frictional properties but also by secondary mechanical characters of the rocks, such as the frictional healing (e.g., Carpenter et al., 2016) and the rate and state frictional properties (Tembe et al., 2010; Ikari et al., 2011; Collettini et al., 2019). Rocks rich in granular minerals have larger healing rates and tend to a velocity weakening behavior with low to negative value of $a$-$b$ (Ikari et al., 2011; Carpenter et al., 2016; Collettini et al., 2019 and fig. 1.3). Conversely, rocks rich in platy minerals have very low to null healing rates and a general velocity strengthening behavior with high $a$-$b$ values (Ikari et al., 2011; Carpenter et al., 2016; Collettini et al., 2019 and fig. 1.3). These experimental data suggest that rocks rich in granular minerals are frictionally strong and potentially seismogenic, whereas rocks rich in platy minerals are frictionally weak and have aseismic creep as the most likely fault slip behavior (Collettini et al., 2019 and fig. 1.3). This dichotomy has been explained as the results of the interplay between mineralogical properties (i.e., habit, cleavage, hardness) and the dominant deformation mechanism (i.e., grain-size reduction, fracturing, foliation sliding). Granular minerals deform predominantly by cataclastic processes (fracturing, grain-size reduction, and frictional sliding at the grain boundaries, e.g., Sibson, 1977) and dilatancy, resulting in high frictional strength (Sibson, 1977; Byerlee, 1978). Furthermore, the granular shape of such minerals, promote an increase of frictional contact area with time resulting in higher healing rates (Tembe et al., 2010; Ikari et al., 2011; Carpenter et al., 2016; Collettini et al., 2019; Volpe et al., 2022b). The tendence of to have low to negative $a$-$b$ values, has been generally explained as the results of strain localization (Ikari et al., 2011; Scuderi et al., 2013, 2017; Bedford and Faulkner, 2021; Volpe et al., 2022b). Rocks rich in

platy minerals deform mainly by frictional sliding along the mineral platelets (e.g., phyllosilicate foliae) resulting in low friction, particularly when the platelets are aligned producing a continuous and interconnected foliation (Collettini et al., 2009; Ikari et al., 2011; Giorgetti et al., 2015; Volpe et al., 2022b). Moreover, the platy shape of phyllosilicates, favors a faster saturation of the frictional contact area that results in very low healing rate and strongly positive *a*-*b* values due to low or negative *b* values (Ikari et al., 2011; Tesei et al., 2012; Giorgetti et al., 2015; Okamoto et al., 2019; Volpe et al., 2022b). Several experimental studies (Saffer and Marone, 2003; Niemeijer and Spiers, 2005; Tembe et al., 2010; Ikari et al., 2011; Giorgetti et al., 2015; Collettini et al., 2019; Ruggieri et al., 2021; Bedford et al., 2022; Volpe et al., 2022b) found that in phyllosilicate-granular rocks, 30% of phyllosilicates content is enough to shift the bulk frictional properties of the mixture towards those typical of phyllosilicate materials (i.e., low friction, low healing rate and velocity strengthening behavior). This stems from the fact that this threshold is enough to allow the development of an interconnected network of weak planes that isolate the granular fraction and preferentially accommodate the deformation (Saffer and Marone, 2003; Niemeijer and Spiers, 2005; Tembe et al., 2010; Ikari et al., 2011; Giorgetti et al., 2015; Collettini et al., 2019; Ruggieri et al., 2021; Bedford et al., 2022; Volpe et al., 2022b).

### 1.2.2 Fluids

Faults can be preferential pathway for fluid flow (e.g., Sibson, 1994; Caine et al., 1996; Wibberly, 2002; Faulkner et al., 2010), which in turn affects their frictional stability. Therefore, fluids represent an important, if not crucial, influencing factor for the seismogenesis (e.g., Sibson, 1994) and have become one of the most studied topics in the last 30 years. The simplest effect that fluid have on fault stability is related to their pressure. This is linked to the effect of the Terzaghi principle (Eq. 6), where an increase in fluid pressure reduces the effective normal stress, effectively diminishing the clamping force and favoring fault reactivation. In general, fluids and fluid pressure do not affect the intrinsic coefficient of friction of rocks (e.g., Frye and Marone, 2002; Scholz, 2019). However, for some phyllosilicate-rich rocks, water adsorption in the cation interlayer of phyllosilicates may promote a sensible decrease of the frictional strength (e.g., Moore and Lockner, 2007; Ikari et al., 2007; Behnsen and Faulkner, 2011; Beynon and Faulkner, 2020). Fluids and fluid pressure can have different effects on the fault healing behavior. Especially when rocks are rich in granular minerals (e.g., quartz, calcite, and halite), the healing rate can increase as the results of fluid-assisted processes such as pressure-solution, cementation, hydrolytic weakening. These physical-chemical processes have the effect of promoting the increase of frictional contact area with time as well as increasing of the quality of the contacts (e.g., Bos et al., 2000;

Frye and Marone, 2002; Niemeijer et al., 2008; Scuderi et al., 2014; Carpenter et al., 2016; Ruggieri et al., 2021). The kynetic of pressure-solution on can be enhanced by the presence of phyllosilicate minerals due to enhanced interphase boundary diffusivity (e.g., Rutter, 1983; Bos et al., 2000), but in turn may result in reduced healing rates depending on the quantity and distribution of platy minerals. In fact, if the phyllosilicates are abundant (>25%), the presence of fluid has small or no effect in reducing the already low healing rate of the rock (e.g., Ruggieri et al., 2021). Fluids have also a non-trivial role on the velocity dependence of friction (RSF) and related fault stability. In phyllosilicate-rich rocks, the presence of fluid has a stabilizing effect due to the increase of the $a$-$b$ value. Indeed, a marked velocity strengthening behavior is often observed during velocity step tests performed in fluid-saturated rocks (e.g., Ikari et al., 2007; Ruggieri et al., 2021), especially at higher fluid pressure (e.g., Ikari et al., 2009; Scuderi and Collettini, 2018). This behavior is generally associated with a decrease of the magnitude of the evolution effect, b, which can even achieve negative values (e.g., Ikari et al., 2009; Scuderi and Collettini, 2018; Beynon and Faulkner, 2020; Scuderi and Carpenter, 2022). Even though the mechanisms responsible of this effect are still unclear, a possible hypothesis is that, due to fast local dilation, the fluid pressure may transiently drop increasing the effective normal stress (Eq. 6) and thus the local frictional strength. This mechanism known as “dilation strengthening” (Segall et al., 2010) is especially efficient in phyllosilicate-rich rocks where the low permeability and hydraulic diffusivity hinders the fast re-equilibration of fluid pressure (Segall and Rice, 1995; Scuderi and Collettini, 2018; Beynon and Faulkner, 2020). Conversely, rocks rich in granular minerals, and in particular calcite, anhydrite, dolomite, and quartz, show a tendency to become more unstable in presence of water (e.g., Frye and Marone, 2002; Scuderi et al., 2013; Scuderi et al., 2014) or at high pore fluid pressure (e.g., calcite in Scuderi and Collettini, 2018). This is generally attributed to fluid-assisted healing processes (e.g., cementation, lithification, pressure-solution) together with strain localization (e.g., Scuderi et al., 2013; Carpenter et al., 2014; Ikari and Hupers, 2021; Pozzi et al., 2022).

### 1.2.3 Pressure

Even though the friction coefficient is, by definition, independent of normal stress (Eqs. 4, 5), this property of fault rocks can be sometimes restricted to a certain range of values. While the friction coefficient of granular-rich rocks seems not affected by the stress conditions applied in laboratory experiments, the friction coefficient of some phyllosilicates shows a slight increase with normal stress. This behavior has been interpreted as the results of the reduction of the thickness of the water interlayer (e.g., Moore and Lockner, 2007; Behnsen and Faulkner, 2012) or of an irregular arrangement of

the phyllosilicate foliae (Okamoto et al., 2019; Ruggieri et al. 2021; Volpe et al., 2022b). Normal stress has instead a stronger effect on the healing rate. In granular mineral phases the increase of normal stress promotes higher frictional restrengthening explained with the enhanced growth over time of contact area and indentation due to stress-sensitive processes (Dieterich and Kilgore, 1994) such as plastic mass transfer and dissolution-precipitation (Scholz, 2019). Contrarily, in phyllosilicate-rich gouges was observed (e.g., Tesei et al.,2014; Giorgetti et al., 2015) a slight decrease in healing rate with increasing normal stress. This is interpreted as the enhanced mobility of the phyllosilicate fraction to form a foliation and faster contact area saturation, resulting in the reduction of the healing rate (e.g, Saffer and Marone, 2015). The relation between the velocity dependence of friction (RSF) and normal stress is less clear (e.g, Mair and Marone, 1999). Some experimental works show that at low normal stress, velocity strengthening behavior is more common and results from the unconsolidated state of rocks that favors dilatancy-hardening mechanism promoting an increase in shear resistance with velocity (e.g., Marone and Scholz, 1988; Segall and Rice, 1995). This also finds agreement with the stability criterion (Eq. 13), where unstable slip is promoted at high stress due to a decrease of kc (e.g., Marone, 1998), fact observed in several experimental works (e.g., Leeman et al., 2018; Lyu et al., 2019). This condition implies a transition from stable to unstable slip with increasing normal stress, i.e., increasing depth (e.g., Saffer and Marone, 2015), that is consistent with the observed up-dip seismicity cutoff (e.g., Marone and Scholz, 1988).

### 1.2.4 Temperature

Temperature is an important influencing factor for rock friction. Temperature is the main controlling variable for the rheological brittle-ductile transition of rocks, which is the switch from frictional shearing at low temperature to viscous flow at higher temperatures (e.g., Scholz, 2019). The temperature at which this transition occurs is strongly controlled by rock mineralogy: quartz-rich rocks (i.e., granites) shows a transition from frictional to viscous shearing at temperature around 300-350 °C (Brace and Kohlstedt, 1980; Chen and Molnar, 1983); for calcite the transition occurs at temperatures around 500-550 °C (Verberne et al., 2015; Chen et al., 2020); conversely, phyllosilicate-rich rocks, shows a frictional behavior up to high temperatures (e.g., 700 °C; Mariani et al., 2006; Den Hartog et al., 2013; Okamoto et al., 2019) and a subsequent sensible increase of frictional strength linked to dehydration processes (e.g., Moore et al., 1996; Mariani et al., 2006; Moore and Lockner, 2008; Scholz, 2019). Within the brittle-frictional field, the role of temperature in influencing the frictional properties of rocks (i.e., RSF properties) is less clear (e.g., Byerlee, 1978; Scholz, 2019). Temperature favors the kinetics of physical-chemical processes such as pressure-solution that are responsible for a

reduction in the frictional strength of rocks characterized by a soluble mineral phase (e.g., calcite, quartz, halite) and by an insoluble mineral phase (e.g., phyllosilicates; Bos et al., 2000). It has also been observed that the healing rate of different rocks such as carbonates and quartz-rich rocks increases with increasing temperature (e.g., Scholz, 2019). This is also linked to processes such as pressure solution and cementation, whose kinetics is accelerated by temperature (Blanpied et al., 1995; Bos et al., 2000; Nakatani and Scholz, 2004; Yasuhara et al., 2005). Temperature has instead a clearer effect on fault stability. In fact, several experimental works show that most rocks, have a temperature window where they exhibit velocity weakening behavior: calcite is velocity-weakening (VW) between 100 and 550 °C (Verberne et al., 2015); phyllosilicates are VW between 200 and 500 °C (Den Hartog et al., 2013; Okamoto et al., 2019); granite is VW between 90 and 350 °C (Chester and Higgs, 1992; Blanpied et al., 1995); serpentines and other ultramafic rocks are VW generally below 600 °C (e.g., Moore et al., 1996; King and Marone, 2012; Mitchell et al., 2015). However, the physical meaning of this transition from velocity strengthening to velocity weakening behavior at a certain temperature is still not well understood (e.g., Scholz, 2019; Barbot, 2022).

## 1.3 Fault fabric

In the previous sections we explored how friction is influenced by the rock composition and the environmental (boundary) conditions, but this information is not sufficient to determine what are the effective frictional properties of fault materials. In fact, rocks with identical mineralogical composition and deformed using the same experimental protocol may show severely different sliding behavior depending on their inner fabric (e.g., Ruggieri et al., 2021; Bedford and Faulkner, 2021; Volpe et al., 2022b). Fabric cannot thus be considered separated from mineralogy in the control the fault slip behavior (e.g., Sibson, 1977; Logan, 1979; Wise et al., 1984; Marone and Scholz, 1988; Faulkner et al., 2010; Lockner et al., 2011; Smith et al., 2017; Collettini et al., 2019; Scholz, 2019; Kirkpatrick et al., 2021; Bedford and Faulkner, 2021). In natural and experimental faults, the spontaneous development of fabric is strongly linked to fault mineralogy. Characteristic brittle fault rock fabrics can be divided into two end members with specific nomenclature: YBPR and SCC'. YBPR fabric develops typically in granular-rich rocks (Logan, 1979; Logan et al., 1992; Mitchell and Faulkner 2009; Haines et al., 2013; Volpe et al., 2022b), whereas SCC', which was originally used to describe mylonitic fabric (Berthè et al., 1979; Platt and Vissers, 1980), is typical of phyllosilicate-rich fault rocks (Tullis et al., 1982; Chester et al., 1985; Rutter et al., 1986; Lin, 1999, 2001; Bos and Spiers, 2001; Haines et al., 2009). The principal difference between these two types of fabric is the degree of localization: YBPR fabric is characterized by narrow and discrete bands where deformation is

localized and accommodated by cataclastic processes (Sibson, 1977; Logan et al., 1992 and fig. 1.3). SCC' fabric is instead characterized by a more distributed deformation, highlighted by a pervasive foliation (results of the mechanical rearrangement of the phyllosilicate foliae as well as from pressure-solution processes). The main deformation mechanisms responsible of the development of YBPR fabric are cataclastic deformation, dilation, and strain localization. These are closely associated to frictionally strong and potentially seismogenic faults. SCC' textures, are mostly formed by distributed deformation, which is accommodated by frictional sliding along aligned phyllosilicate foliae (fig. 1.3). This fabric is typically associated to frictionally weak and aseismic faults (e.g., Collettini et al., 2019 and references therein). Again, we observe the dichotomy existing between granular-rich and phyllosilicate-rich in the YBPR and SCC' endmembers. At a smaller scale, other microstructural features may affect the slip behavior of the fault (e.g., Chapter 1), for example: grain-shape (Mair et al., 2002), foliation regularity (Okamoto et al., 2019), and grain mantling (Volpe et al., 2022b).

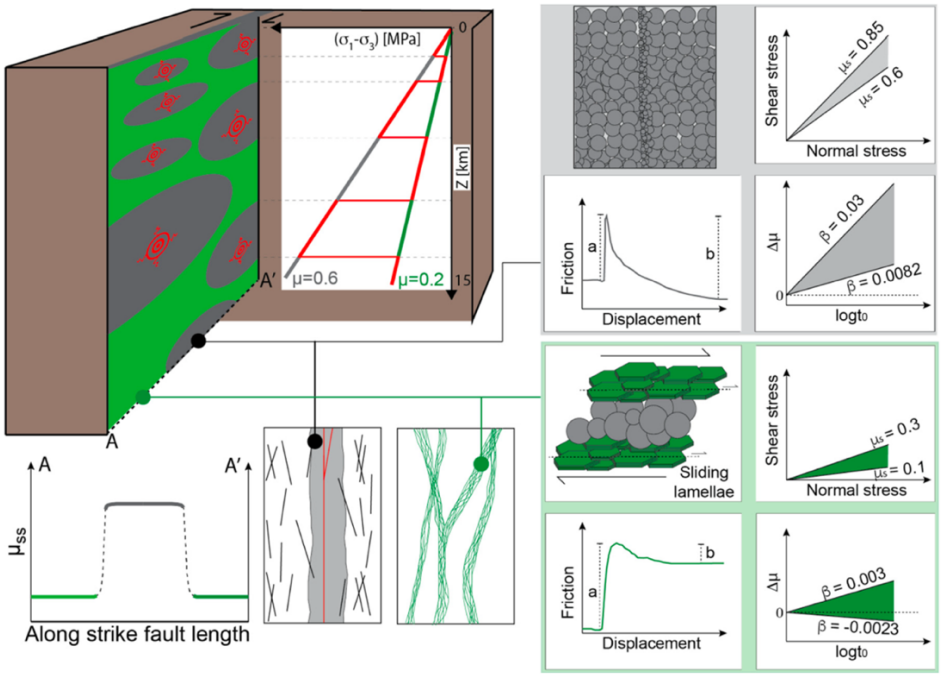


Figure 1.3: integration between fault zone structure, fabric, mineralogy, and frictional properties of an heterogenous fault zone characterized by strong (grey) and weak (green) fault rocks (image from Collettini et al., 2019). Left side shows the strength profile of a heterogeneous fault and the style of deformation: localized for the stronger rock whereas distributed for the weaker. On the right side are reported the deformation mechanisms and the frictional properties of the two fault rocks: cataclasis, high friction, high healing a velocity weakening behavior for strong fault rocks whereas frictional sliding along foliation, low friction, low healing rate and velocity strengthening behavior for weak fault rocks.

## 1.4 Fault zone structures and fault slip behavior

Fault zones, despite occupying small crustal volumes, exert a primary control on crustal deformation and mechanics (e.g., Faulkner et al., 2010). A typical model of a fault zone consists of a tabular volume composed by a thin fault core, which accommodates most of the shear deformation, and by a larger damage zone characterized by fractures and subsidiary small faults (Sibson, 1977; Chester and Logan, 1986; Caine et al., 1996; Faulkner et al., 2003, 2010; Perrin et al., 2016). This simple model, however, does not capture the degree of complexity and variety of natural faults. These can be made of single or multiple fault cores that, in some cases, are organized in an anastomosing network that separates domains of less deformed rock (Chester et al., 1993; Caine et al., 1996; Shipton and Cowie, 2001; Faulkner et al., 2003; Zoback et al., 2010; Fagereng and Sibson, 2010; Collettini et al., 2011; Rowe et al., 2013; Tesei et al., 2015; Fagereng and Beall, 2019). The slip behavior of a simple fault zone with a single core is mainly controlled by the frictional properties in its high-strain domain and the elastic properties of the surrounding rock (e.g., Scholz, 2019). Conversely, the mechanical behavior of heterogenous fault zones is far more complex and results from the nonlinear interaction between all its domains, which can show substantially different rheological attributes (e.g., Fagereng and Sibson, 2010; Collettini et al., 2011; Tesei et al., 2014; Fagereng and Beall, 2019).

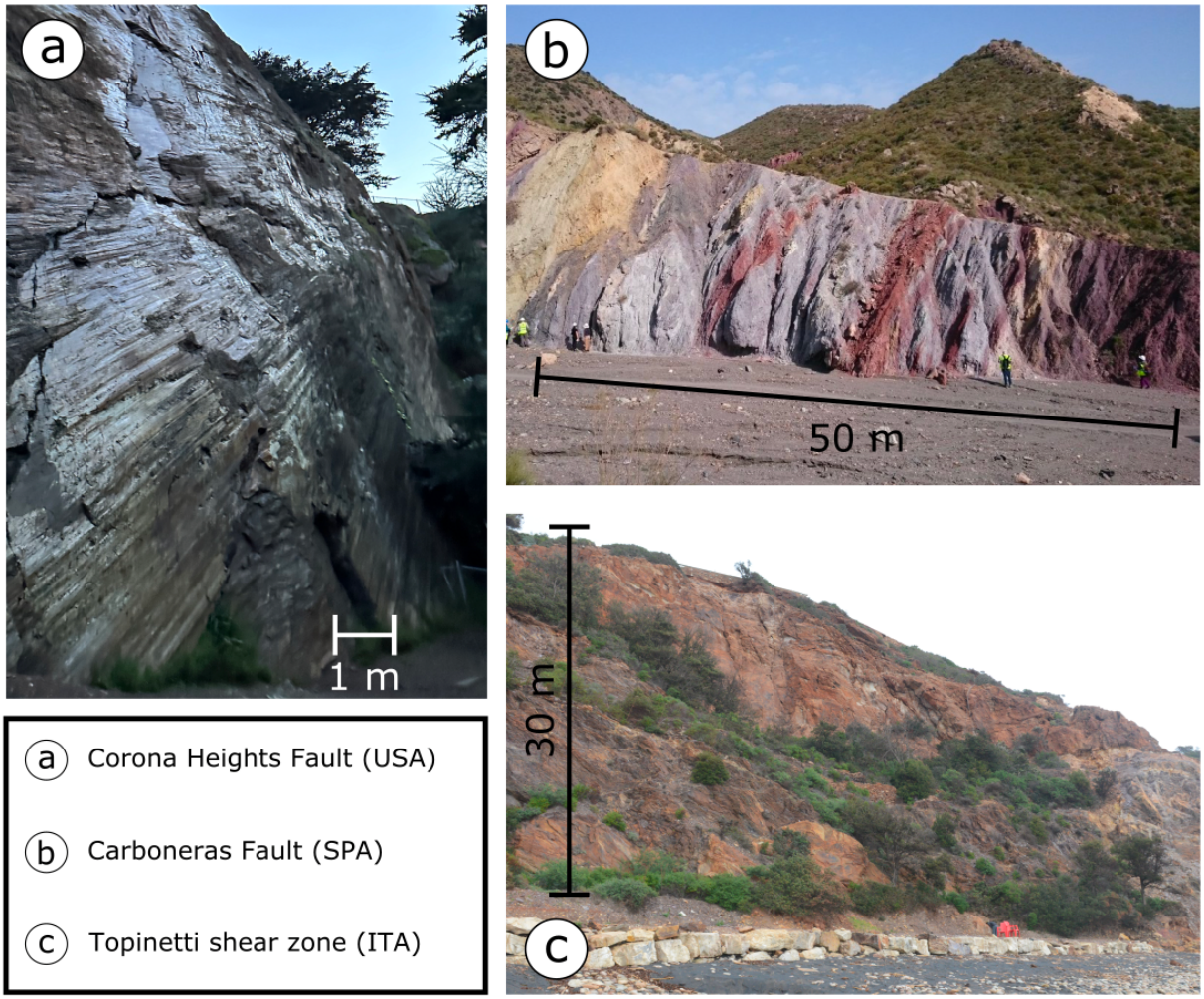


Figure 1.4: pictures of three faults with different fault zone structures. a) The Corona Heights Fault (California - USA) is characterized by a localized (< 1m thick) principal slip surface with well-developed slicken-lines and a mirror surface. b) The Carboneras Fault (Southern Spain) is characterized by a thick shear zone of distributed deformation occurring on different lithologies. c) The Topinetti Shear Zone (Elba island - Italy) is a rheologically heterogeneous deformation zone with strong lenses in a weak matrix.

### 1.4.1 Slip behavior and seismicity along rheologically heterogeneous fault zones

Rheological heterogeneities within fault zones commonly arise from the tectonic juxtaposition of different rocks with contrasting physical properties (e.g., Fagereng and Sibson, 2010; Wang and Bilek, 2011) or the development of an anastomotic entwining of low and high strain domains (Viti et al., 2018; Tarling et al., 2019). The rheological heterogeneities correspond to spatial variations of the deformation mechanisms and mechanical properties along the fault zone (e.g., Fagereng and Sibson, 2010; Collettini et al., 2011; Tesei et al., 2014; Tesei et al., 2018), which may result in a complex slip behavior (e.g., Fagereng and Sibson, 2010; Collettini et al., 2011; Tesei et al., 2014; Tesei et al., 2018;

Fagereng and Beall, 2019; Volpe et al., 2023). Indeed, rheological heterogeneities are often invoked to explain the coexistence of different fault slip behavior in the same area as well as their characteristic seismic signature (e.g., Lay et al., 2012; Uchida and Burgmann, 2019; Fagereng and Beall, 2021).

Earthquakes that occur along plate-boundary or large faults are argued to nucleate on locked asperities that represent frictionally strong and velocity weakening fault patches with different size (e.g., Lay et al., 2012; Burgmann, 2018). A similar explanation has been proposed for repeating earthquakes (i.e., small earthquakes with high waveform similarity, Uchida and Bürgmann, 2019). Repeating earthquakes are thereby interpreted as repeated ruptures of a persistent, velocity-weakening asperity (e.g., Uchida and Bürgmann, 2019 and reference therein), which is loaded by the aseismic creep of the weak surrounding regions characterized velocity strengthening behavior (Nadeau et al., 1994; Igarashi et al., 2003; Uchida and Bürgmann, 2019; Waldhauser et al., 2021). Tremor and slow slip events are peculiar seismic phenomena occurring along subduction zones (Scholz, 2019). Tremors are a low-amplitude seismic events with no clear impulsive phases (Ide et al., 2007; Peng and Gomberg, 2010) whereas slow slip events are events that propagate at intermediate rates between plate motion and dynamic slip velocity (i.e., generating seismic waves; Kanamori and Kikuchi, 1993; Ide et al., 2007; Peng and Gomberg, 2010; Scholz, 2019). These seismic phenomena have been interpreted as originating from brittle failures occurring within competent lenses enveloped by a viscously deforming creeping matrix (e.g., Burgmann, 2018; Beall et al., 2019; Fagereng and Beall, 2021). Similar interpretation was given to explain deep regular earthquakes occurring beneath the brittle-ductile transition (Sibson, 1980; Beall et al., 2019; Menegon and Fagereng, 2021; Fagereng and Beall, 2021). Despite the great importance given to rheological heterogeneities in influencing fault slip behavior and its seismic signature (Fagereng and Sibson, 2010; Uchida and Bürgmann, 2019; Fagereng and Beall, 2021), the mechanisms that control seismogenesis in these fault zones remain still partially unexplored.

# 2 Rationale of the thesis

## 2.1 The role of phyllosilicates in fault slip behavior

Phyllosilicates are a large family of minerals characterized by sheet-like structure, common components of several sedimentary, igneous, and metamorphic rocks. They are also commonly found in the cataclastic rocks of fault zones in several different tectonic settings (Collettini et al., 2019 and references therein). Significative examples of phyllosilicate-rich faults are the Carboneras fault in southern Spain (Faulkner et al., 2003); the Zuccale fault in central Italy (Collettini et al., 2011); the San Andreas fault in California (Holdsworth et al., 2011); the Livingstone fault (Tarling et al., 2018); the Chrystalls Beach Mélange (Fagereng and Sibson, 2010) and the Alpine fault (Barth et al., 2013) in New Zealand. Their presence in faults rocks can result from the deformation of phyllosilicate-rich lithologies as well as from production through metasomatic fluid-rock interaction (Vrolijk, 1990; Holdsworth, 2004; Faulkner et al., 2010; Collettini et al., 2019) enhanced by the brittle deformation processes. The most common phyllosilicate species found in fault zones include micas, serpentines, chlorite, talc, and clays (e.g., smectite, illite, and kaolinite; Vrolijk, 1990; von Huene and Scholl, 1991; Faulkner et al., 2003; Viti and Collettini, 2009; Tesei et al., 2012; Tarling et al., 2018; Collettini et al., 2019).

The peculiar morphology of phyllosilicate minerals is extremely relevant in the rheology of faults. Their crystal structure consists of the repetition of two fundamental layers: the T layer, composed by silica molecules in tetrahedral coordination, and the O layer, composed by cations (Al, Mg, etc.), oxygen, and hydroxyl group in octahedral coordination. Combined T-O-T-O, T-O-T, or T-O blocks can bond together and stack thanks to interlayers composed of cations (e.g., potassium in micas) or polar molecules (e.g., water in smectite), which present much weaker bonds and produce perfect (basal) cleavage. This property determines the marked crystallographic anisotropy of phyllosilicates that is also reflected by a directional mechanical weakness.

The widespread occurrence of phyllosilicates, combined with their intrinsic mechanical weakness, makes these minerals important protagonists of fault mechanics, and slip behavior. During deformation, the basal weakness results in the preferential splitting into small lamellae that impose peculiar frictional properties to their hosting rocks: low friction, low healing rates, and rate-strengthening behavior (e.g., Moore and Lockner, 2004; Collettini et al., 2009; Ikari et al., 2011; Collettini et al., 2019):. Theory and experimental data suggest that, because of these mechanical properties,

phyllosilicate-rich fault rocks cannot be sites of earthquake nucleation and thus they should deform aseismically under a large variety of boundary conditions (e.g., Collettini et al., 2019 and reference therein). However, increasing amount of geological, geophysical, and seismological data challenge this view pointing towards a more active role of these minerals in controlling the seismogenic behavior. For instance, phyllosilicate-rich fault rocks can be potential seismic sources of slow slip events and large tsunami earthquakes (Kanamori, 1972; Saffer and Wallace, 2015; Scholz, 2019; Wallace et al., 2020). Slow slip events along creeping segments of large faults have been detected before large mainshocks and interpreted as the potential mechanism of stress transfer to the mainshock's rupture patch ("pre-slip" and "progressive localization" models, e.g., Kato and Ben-Zion, 2021 and reference therein). Significant cases of this stress transfer process are the Iquique $M_w$ 8.1 earthquake (Kato and Nakagawa, 2014) and the Tohoku-Oki $M_w$ 9.0 earthquake (Kato et al., 2012). A similar interpretation has been given to repeating earthquakes, where the continuous aseismic creep of phyllosilicate-rich faults favors stress transfer to strong and locked fault patches more prone to fail seismically (Avouac, 2015; Uchida and Burgmann, 2019; Waldhauser et al., 2021). This mechanism has been also used to explain some cases of induced seismicity, like in Alberta, Canada (Eyre et al., 2019), where the hydraulic stimulation of strongly velocity-strengthening phyllosilicate-rich faults promoted accelerate creep (e.g., Scuderi and Collettini, 2018) that increased the shear stress at the edge of the creeping zone triggering earthquakes in unstable fault patches or even along neighboring seismogenic faults (e.g., Guglielmi et al., 2015; Cappa et al., 2019; Eyre et al., 2019). Furthermore, phyllosilicate-rich rocks can undergo dynamic weakening when deformed at high strain rates and thus accommodate seismic slip (Niemeijer and Spiers, 2007; Aretusini et al., 2017). Emblematic is the case of Tohoku-Oki $M_w$ 9.0 earthquake, where the largest seismic slip (~ 50 m) occurred in a creeping segment dominated by clay-rich rocks (Noda and Lapusta, 2013).

Despite the vast amount of evidence that supports the active role of phyllosilicate-rich rocks in the entire seismic cycle, the community is yet far from reconciling it with the theoretically aseismic attributes of phyllosilicate rheology. The underlying processes are thus still unclear and further research is needed to improve our understanding. To find the conditions at which phyllosilicate-rich faults can become unstable is crucial for a better assessment of their seismogenic potential, which is obviously of paramount importance for society.

## 2.2 The objectives of the thesis and case-studies

The research objective of this PhD thesis is to improve our understanding of the seismogenic potential of phyllosilicate-rich fault rocks by characterizing their structural and frictional properties. For a complete study, I selected four different research topics, which include multidisciplinary approach, different scales of observation, and different geological settings:

1. ***Study of the frictional mechanisms of phyllosilicate-rich fault rocks at the microscale***. Here I used experimental and analytical techniques to characterize the relation between mineralogy, fabric and frictional properties of natural fault gouges deformed at different normal stresses and fluid conditions. With this dataset I provide a systematic interpretation of the mechanical behavior granular-phyllosilicate mixtures, assessed through the interpretation of their characteristic microstructures. This study provides a benchmark for the interpretation of the experimental mechanical results and microstructures.
2. ***The phyllitic basement of central Apennines***. Here I integrated field with experimental studies to investigate the role of phyllosilicate-rich rocks in the seismo-tectonic context of the acoustic basement of the central Apennines. To test my results, I have also integrated a detailed seismological analysis of the basement seismicity. This case study unveils the seismogenic potential of structural and frictional heterogeneities at the large scale.
3. ***The role of clay-rich sediments in the seismicity of shallow subduction zones.*** With a suite of experiments and a novel investigation technique, I studied the complex mechanical behavior of clay-rich fault rocks at conditions comparable to those of shallow subduction zones. The results of this case study shed light on the enigmatic origin of shallow slow slip and tsunami earthquakes.
4. ***Study of fluid-induced reactivation of granite-hosted fault in the Central Alps***. This study is a cross-disciplinary characterization of a candidate phyllosilicate-rich fault for in-situ injection experiments, funded by the ERC Synergy project FEAR (grant number 856559). My investigation included field studies on outcrop structures, mineralogical analysis of the fault gouge, experiments to test the frictional behavior, the analysis of experimental and natural microstructures, and the simulation in the laboratory of reactivation by fluid injection. With these results I could assess the seismogenic potential of the candidate fault with implications for induced seismicity.

# 3 Methods

The interdisciplinary approach that I applied to the four case studies integrates: field work with structural analysis of selected outcrops, rock deformation experiments, microstructural analysis on both natural and experimentally deformed samples, and seismological analysis of high-resolution seismic catalogues. This integrated approach allows an all-around vision of tectonic faulting and seismogenic processes. Additional technical information can be found from Chapter I to Chapter IV and in the Appendixes.

## 3.1 Field work

Field work is a fundamental investigation activity for the aim of this PhD thesis, which mainly consisted of structural analysis of exhumed fault zones at the meso-scale (< km). Particular care was dedicated to the characterization of the fault architecture, which includes important information such as: the relative distribution of competent vs incompetent lithologies, the distribution of gouge vs bare-surface patches, and the distribution of different deformation styles along the fault zone. These details are extremely relevant to understand the mechanical behavior at the mesoscale, which cannot be assessed in the laboratory. Rock samples were carefully selected and collected for rock deformation experiments and microstructural analysis.

## 3.2 Rock deformation experiments

I performed rock deformation experiments to characterize the frictional properties that control the seismogenic potential of the natural fault rocks from each case study. My experimental activity was hosted at the High Pressure – High Temperature laboratory of the Istituto Nazionale di Geofisica e Vulcanologia (INGV) of Rome.

### 3.2.1 Experimental Apparatus

All friction experiments were conducted using BRAVA (Brittle Rock deformAtion Versatile Apparatus), a high-precision, servo-controlled biaxial testing apparatus (Collettini et al., 2014 and fig. 3.2.1). In this apparatus experimental faults are

deformed by applying shear and normal stress via two high-precision fast-acting hydraulic servo-controlled rams (Collettini et al., 2014), able to simulate tectonic stresses comparable to those at seismogenic depths (>100 MPa, ~4km of depth). The large vessel of BRAVA, which contains the samples, can also be pressurized with oil up to 70 MPa to simulate confining lithostatic pressure. When samples are mounted with non-zero confining pressure, they can also be saturated with pore fluids, whose flow and pressure are controlled by two hydraulic servo-controlled intensifiers (Collettini et al., 2014). All the mechanical data are recorded continuously at frequencies of 1 Hz to 1 kHz using a 16 channel 24-bit analog to digital acquisition system (Collettini et al., 2014).

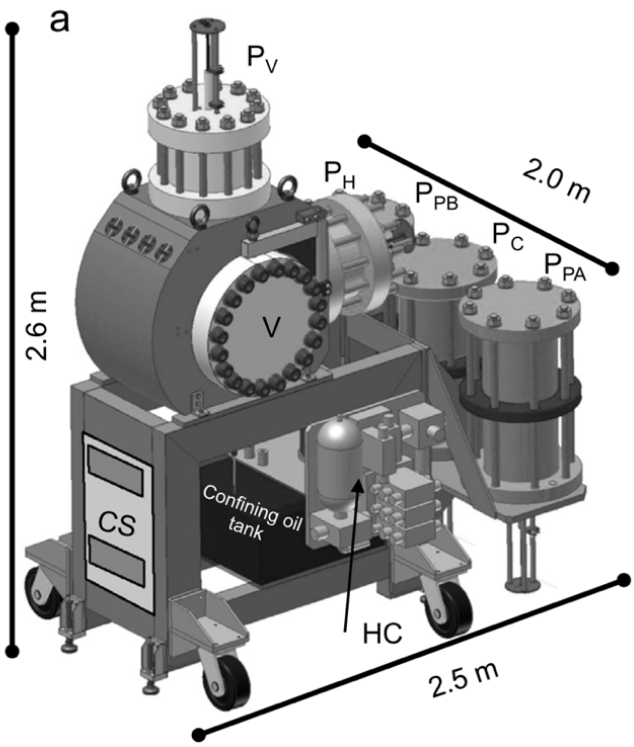


Figure 3.2.1: schematic drawing of the BRAVA apparatus. Pv is the vertical piston applying shear deformation. Ph is the horizontal piston that apply normal stress. Ppb and Ppa are the pore fluid intensifiers applying up-stream and down-stream flow respectively. Pc is the intensifier applying confining pressure. V is the vessel and HC is the hydraulic control system (image from Collettini et al., 2014).

## 3.2.2 Experimental assemblies

All the experiments collected in this thesis were performed using the Double Direct Shear configuration (DDS), which consists of three steel forcing blocks, two laterals and one central (fig. 3.2.2). Two identical samples, either pulverized

rocks (gouge) or intact sections (wafers), are positioned between the central block and each lateral forcing block. Lateral extrusion and misalignment of the central block is prevented by four steel guide plates fixed on each side of the lateral forcing blocks (Collettini et al., 2014). The two lateral blocks are used to apply normal stress to the analogue fault (sample) whereas the central forcing block applies the shear stress. The presence of grooves on the faces of the forcing blocks that are in contact with the sample ensure the localization of deformation within the sample and not at the steel-rock interface (Collettini et al., 2014). This DDS assembly is mostly used for experiments performed at room pressure (fig. 3.2.2 a). To perform experiments with confining pressure and pore fluid pressure, I used a similar DDS assembly whose forcing blocks contain channels to allow fluid to flow perpendicularly to the layers of gouge (fig. 3.2.2 b). These forcing blocks are connected to the fluid pressure intensifiers using steel pipes mounted on feed-through connections on the side of BRAVA. Grooved porous frits (with a permeability of $10^{-14}$ $m^2$) are mounted on the blocks prevent the intrusion of samples in the pipes. This assemblage also ensures a homogenous fluid distribution on the entire sample surface. The ensembled DDS assembly is covered by a rubber jacket to separate the sample and fluid lines from the confining oil (e.g., Collettini et al. 2014; Scuderi and Collettini, 2016, 2018).

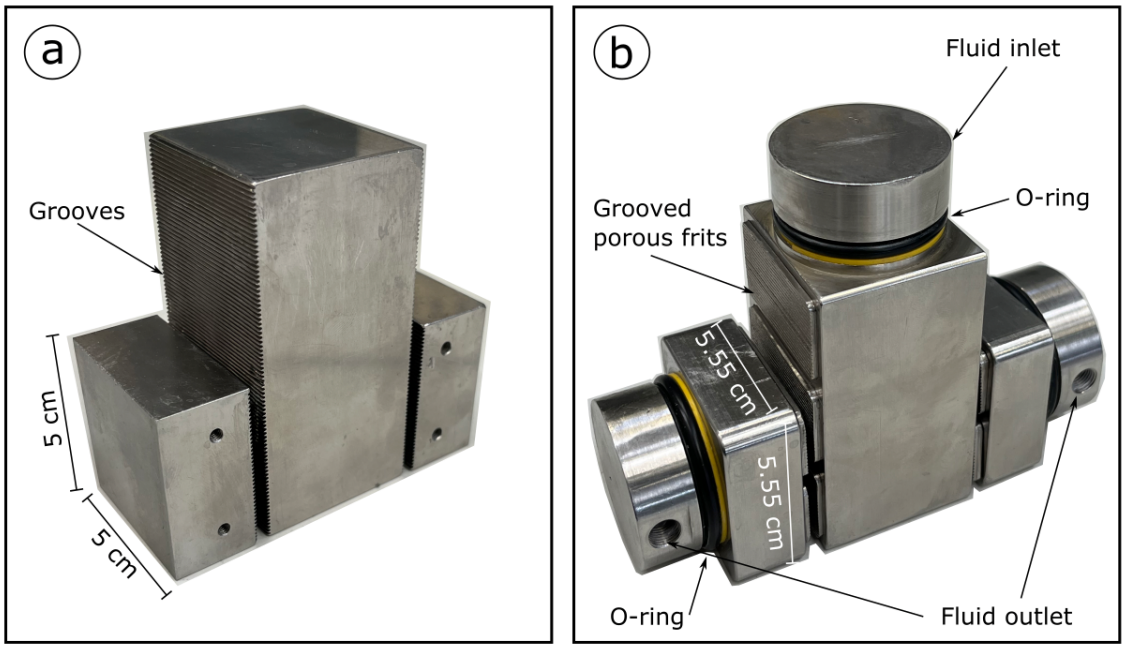


Figure 3.2.2: Double Direct Shear (DDS) assemblies. a) DDS for experiments without fluid pressure and b) DDS for experiment with confining and fluid pressure.

### 3.2.3 Special methods

A new technique was developed to allow the direct optical documentation of the deformation processes occurring on the fault surface during deformation experiments. This technique consists in the use of a DDS assembly formed by an acrylic transparent central forcing block (the one applying shear stress) and two synthetic sandstone lateral blocks instead of the conventional metal ones. Both the central and lateral blocks had a nominally flat surface in contact with the sample. To perform video documentation of the active deformation occurring at the fault-block interface, a high-speed camera was positioned with a line of sight tilted by 45° from the fault surface and perpendicular to the sliding direction. At the other side of the acrylic block was positioned a diffused source of white light to provide a uniform illumination on the block-sample interface. The video footage recorded with the camera tracked the changes in the sample-bloc interface reflectivity, which correspond to different coupling of the fault surface due to the changes in the local state of stress (e.g., changes of local porosity resulting in changes area of contact). Image processing has been carried out on the footage using MATLAB custom scripts. Two procedures of background removal were used to enhance and quantify the changes of reflectivity: i) static and ii) rolling. In the first procedure, the background image was calculated as the pixel-wise average of a number of frames immediately preceding the portion of interest of the video. This background image produced this way is representative of the state of stress on the fault surface at the beginning of the video clip. The background image was then subtracted from each of the subsequent frames, obtaining the local value of reflectivity change (change of stress). The rolling background removal consists instead in the subtraction of the subtraction from each frame of the $n^{th}$ preceding frame. The rolling background restitutes a semiquantitative measure of the reflectivity change rate, which roughly corresponds to the local stressing rate. In both procedures, the number or positioning of the frames used as background is selected by trial and error to optimize the output for subsequent analysis.

### 3.2.4 Experimental rock samples

Two types of rock samples were tested during frictional experiments: gouge and wafers (fig. 3.2.4). Gouge was obtained by crushing, milling, and sieving ($\phi < 125$ μm) the sampled rocks or by directly collecting the natural fault gouge (fig. 3.2.4 a). Wafers (i.e., intact foliated rock samples) were instead produced only for foliated and cohesive fault rocks by cutting the rock sample, according with their in-situ orientation, in parallelepipeds of 5 x 5 $cm^2$ of area and 1 cm of thickness (fig. 3.2.4.b). Wafers were then sheared according to the in-situ shear direction, therefore reactivating their

natural foliation (e.g., Collettini et al., 2009). Using these two types of samples allows a direct comparison between the frictional properties of intact foliated fault rocks (wafers) and their powdered equivalents (gouge). Furthermore, because gouge and wafers samples of the same rock have the same mineralogical composition, comparing their mechanical results allows to directly discriminate the contribution of the fault fabric on frictional properties (e.g., Collettini et al., 2009).

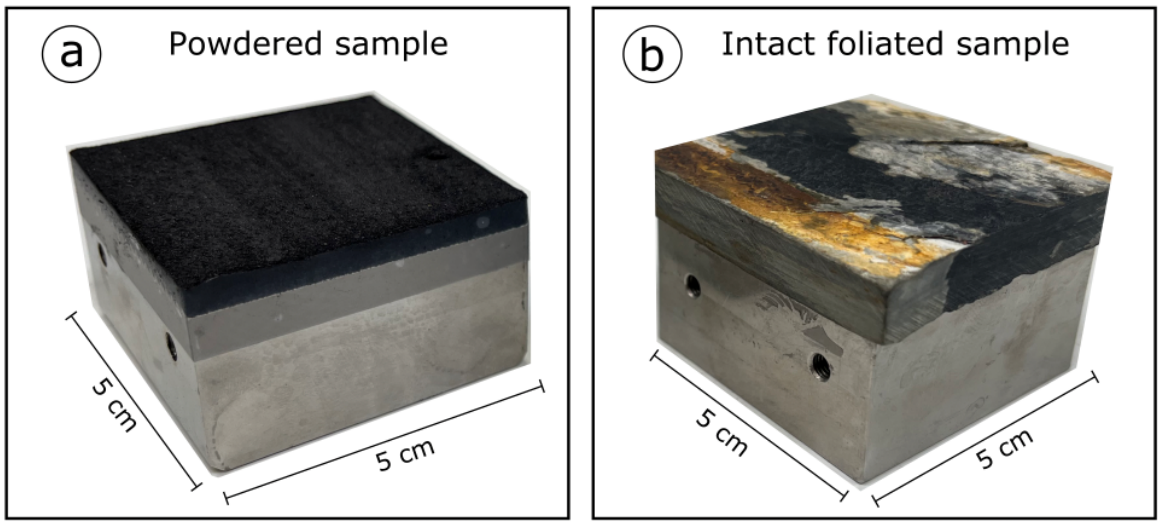


Figure 3.2.4: tested experimental samples. a) powdered rock sample (gouge) and b) intact foliated rock sample (wafers).

# 3.3 Microstructural analysis

## 3.3.1 Natural Samples

Samples of natural fault rocks were collected during field work to study their fabric (i.e., fault micro-architecture, secondary fabric features, mineral phases distributions). The natural fabric can be used to infer the frictional properties of the natural fault rock through comparative analysis with the experimentally deformed samples. During field sampling, especially in case of non-cohesive fault rocks, samples were carefully collected and handled to avoid fracturing and/or loss of material. The rock samples were then embedded in epoxy resin and cut to expose a kinematic section, which is perpendicular to the shear plane and parallel to the shear direction (e.g., Passchier, 1990). Petrographic thin section was then prepared from the rock sample by reducing its thickness to 30 µm. Thin sections were analyzed at the petrographic optical microscope.

### 3.3.2 Experimentally deformed samples

Microstructural analysis on experimentally deformed samples has been conducted to better characterize the deformation processes responsible for the recorded mechanical behavior. The deformed samples were carefully extracted from the assembly after each experiment and were then carefully embedded in epoxy resin. Once hardened, the samples were cut to expose a kinematic section, which was then polished for microstructural analysis. Samples prepared for electron microscopy were also previously coated with a thin layer of graphite (< 50 nm). The collection of microstructural imagery was conducted using a Field-Emission Scanning-Electron-Microscope (SEM) hosted at the Istituto Nazionale di Geofisica e Vulcanologia of Rome. Imagery was collected in back-scattered mode (BSE). This technique allows to image the inner morphology of fault structure (fabric) down to the sub-micron scale. The grayscale image produced with this technique pictures the local averaged (depending on the SEM spot size) weight of the investigated materials, which is determined by, e.g., different composition, porosity, or crystalline mismatch (e.g., grain boundaries). For each microstructure were collected several high-resolution images, either with focus on a single area or contiguous, allowing to be merged into a panoramic view of the whole sample. The panoramic view is used to capture the overall fault architecture (i.e., fabric), which is important to assess the bulk deformation process. Furthermore, chemical maps of the samples were collected to characterize the spatial distribution of mineral phases (e.g., granular vs phyllosilicates) and their spatial relation with fault fabric. Deformation processes at the asperity scale were investigated using high resolution close-ups of grain-scale features. Comparison between natural and experimental samples supports the applicability of laboratory results to nature.

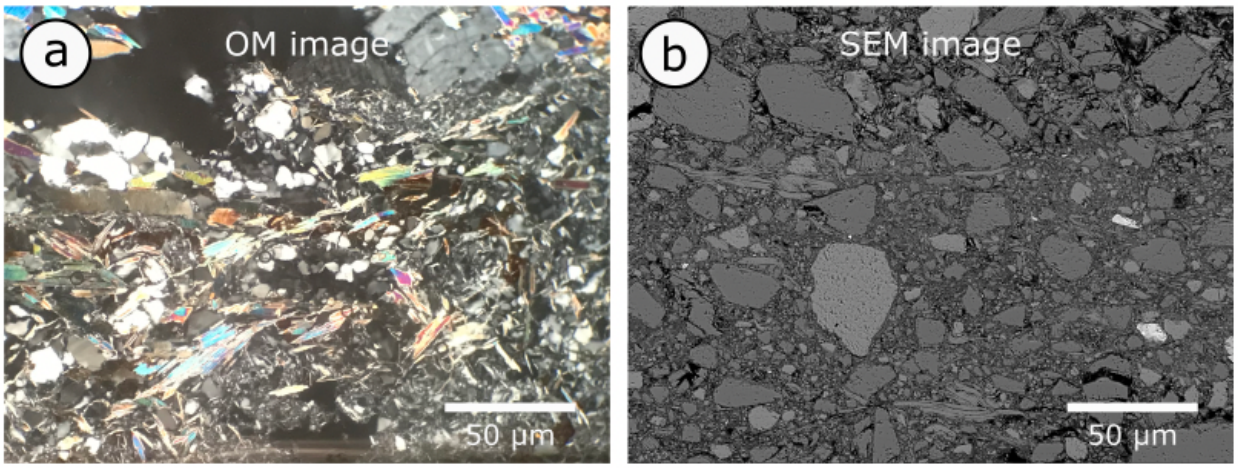


Figure 3.3.2: Comparison between a natural (a) and experimental (b) fault microstructures of the same fault (Volpe et al., 2022b).

## 3.4 Seismological analysis

The seismological analysis on high resolution seismic catalogues can provide unique insights into the geometries and the deformation processes within a study area. Geometries of the active structures can be reconstructed by the comparison of existing geological data (e.g., seismic reflection profiles, geological cross-sections, deep boreholes) with vertical seismicity cross-sections built by projecting on a selected vertical plane all the events within an arbitrary normal distance from the trace of the section (e.g., Barchi et al., 2021; Collettini et al., 2022). Furthermore, smaller geological structures such as lesser faults or seismic clusters can be also found by applying a spatial-temporal seismic clustering on selected crustal volumes (Waldhauser et al., 2021; Collettini et al., 2022). Insights on the deformation processes occurring at seismogenic depths can be provided by the analysis of the temporal evolution during the sequence of the seismic parameters such as seismic rate and magnitude. The temporal evolution of the seismic rate and magnitude of the earthquakes in a sequence can follow three different classes of sequences: Mainshock-Aftershocks, Foreshocks-Mainshocks-Aftershocks, and Swarms sequences (Vidale and Shearer, 2006; Scholz, 2019). The first two classes result from the stress redistribution (i.e., Coulomb stress change, Toda et al., 2011) caused by the mainshock (e.g., Toda et al., 2002), whereas swarms are generally associated to transient stress perturbation produced by external processes such as an increase of tectonic loading rates, a transient fluid overpressure, or an accelerated aseismic slip (e.g., Toda et al., 2002; Vidale and Shearer, 2006; Shelley et al., 2016; Essing and Poli, 2022). Further details on the origin of seismicity can be retrieved from the cross-correlation analysis performed on the waveforms of the earthquakes in a single geological structure (e.g., Igarashi et al., 2003; Schaff and Waldhauser, 2005). Earthquakes that are co-located (i.e., with partial overlapping source regions) and show cross-correlation coefficient values greater than 0.8 (i.e., with high waveform similarity), are defined repeating earthquakes and therefore interpreted as originated from repeated ruptures of the same fault patch (Uchida and Burgmann, 2019).

# 4 Results

## Chapter I

## Study of the frictional mechanisms of phyllosilicate-rich fault rocks at the microscale

### Y-B-P-R or S-C-C'? Suggestion for the nomenclature of experimental brittle fault fabric in phyllosilicate-granular mixtures

G. Volpe[a], G. Pozzi[b], C. Collettini[a,b]

a: Università degli Studi di Roma, La Sapienza, Italy

b: Istituto Nazionale di Geofisica e Vulcanologia, Italy

*Published in Journal of Structural Geology*

https://doi.org/10.1016/j.jsg.2022.104743

**Abstract**

Mineralogy, fabric, and frictional properties are fundamental aspects of faults. Despite the extensive effort spent in the characterization of such fault properties, the description of fabric elements is not always univocal and nomenclatures such as the Y-B-P-R and the S-C-C' are at times used interchangeably. This work presents a systematic mineralogical, microstructural, and frictional characterization of natural gouges designed to constrain a criterion for the distinction between the Y-B-P-R and S-C-C' fabric. For this purpose, we tested four representative natural mixtures of granular minerals (quartz) with increasing amount of phyllosilicates (muscovite). 24 frictional experiments were performed at

constant normal stresses of 25, 50, 75 and 100 MPa, at both room dry and water saturated condition. We document that Y-B-P-R fabric typically develops in frictionally strong, granular-rich experimental faults. This fabric is associated to strain localization in narrow shear zones characterized by intense grain size reduction and dominant cataclastic processes. Conversely, S-C-C' fabric is observed in phyllosilicate-rich experimental faults, which are characterized by distributed deformation and pervasive foliation. Deformation is mainly accommodated by frictional sliding along the well-oriented phyllosilicate foliae. The transition from Y-B-P-R to S-C-C' is observed for phyllosilicates content > 30% and is facilitated by secondary mechanical processes as networking of phyllosilicates and grain mantling. The evolution from Y-B-P-R to S-C-C' fabric is also associated with a marked reduction in friction, in healing rate and changes in the rate and state friction parameters. Despite their geometrical similarities, we show that Y-B-P-R and S-C-C' represent distinct fabrics reflecting the dichotomy that exists between frictionally strong, granular-rich, and frictionally weak, phyllosilicate-rich faults.

## 1 Introduction

Mineralogy, fabric, and frictional properties are considered fundamental ingredients to characterize the mechanical behaviour of faults. These three components cannot be considered separated because they concur in controlling the fault strength and the fault slip behaviour (e.g., Sibson, 1977; Logan, 1979; Wise et al., 1984; Marone and Scholz, 1988; Faulkner et al., 2010; Lockner, 2011; Smith et al.,2017; Collettini et al., 2019; Scholz, 2019; Kirkpatrick et al., 2021; Bedford and Faulkner, 2021). Faults rich in granular minerals (i.e., quartz, feldspars, pyroxenes, calcite, etc.) are considered frictionally strong because they deform predominantly by cataclastic processes (fracturing, grain-size reduction, and frictional sliding at the grain boundaries, e.g., Sibson, 1977) and dilatancy, resulting in high frictional coefficients ($\mu > 0.6$, Byerlee, 1978). Faults rich in phyllosilicate minerals (clays, serpentines, micas) are considered frictionally weak because deformation is mainly accommodated by frictional sliding along the phyllosilicate foliae, which promotes low friction ($\mu < 0.3$), particularly when the phyllosilicate networks are continuous and/or the phyllosilicates are abundant (Collettini et al., 2009; 2019; Ikari, 2011; Niemeijer et al., 2010; Tembe et al., 2010; Niemeijer et al., 2010; Ikari et al., 2011; Giorgetti et al., 2015; Smith et al.,2017; Tesei et al., 2018; Bedford et al., 2022). Granular-rich faults are characterized by a high degree of shear localization, which means that deformation is confined within discrete, narrow shear bands that bound almost undeformed domains (i.e., Logan, 1979; Marone and Scholz, 1988, 1989; Biegel et al., 1989; Logan et al., 1992; Mair et al., 2002; Anthony and Marone, 2003; Tembe et al. 2010; Scuderi et al., 2013; Tesei et al., 2014; Giorgetti et al., 2015; Bedford and Faulkner, 2021; Ruggieri et al., 2021). On the contrary phyllosilicate-

rich faults are generally affected by distributed deformation across the whole sample (i.e., Niemeijer and Spiers, 2005; 2006; Haines et al., 2009; 2013; Tembe et al., 2010; Giorgetti et al., 2015; Niemeijer et al., 2018; Okamoto et al., 2019; Ruggieri et al., 2021). This distributed deformation is often associated to the presence of a foliation represented by the preferential alignment of the phyllosilicates foliae that coat, envelope and isolate the granular mineral fraction (e.g., Niemeijer and Spiers, 2005; Tembe et al., 2010; Giorgetti et al., 2015; Smith et al.,2017; Niemeijer, 2018; Scuderi and Collettini, 2018; Orellana et al., 2018; Ruggieri et al., 2021; Bedford et al., 2022). Foliation can also be enhanced by chemical processes such as pressure solution, which concentrates phyllosilicates along interconnected networks (i.e., Janecke and Evans, 1988; Calamita, 1991; Wintsch et al., 1995; Imber et al., 2001; Collettini and Holdsworth, 2004; Bos and Spiers, 2001; Niemeijer and Spiers, 2005; 2006; Tesei et al. 2014; Smith et al.,2017; Collettini et al., 2019). To describe the fabric of brittle experimental faults, two main nomenclatures are commonly used: Y-B-P-R and S-C-C'. The Y-B-P-R nomenclature (Logan, 1979) is mainly adopted for granular faults, which experienced localized deformation. When fault rocks are enriched in phyllosilicates, several authors recognized a striking similarity with the fabric of ductilely deformed rocks such as mylonites (e.g., Tullis et al., 1982; Rutter et al., 1986; Chester and Logan, 1987; Lin, 1999, 2001; Bos & Spiers, 2001) and often this fabric is described using the S-C or S-C-C' nomenclature (Berthè et al., 1979; Platt and Vissers, 1980; White et al., 1980). In phyllosilicate-granular mixtures, both Y-B-P-R and S-C-C' nomenclatures have been used interchangeably. This likely occurs because the Y (B), R and P shear bands relate geometrically and kinematically to the C, C' and S planes of Berthè et al. (1979), respectively (e.g., Fig. 1). Examples of Y-B-P-R fabric described in phyllosilicate-rich experimental rocks are presented in Haines et al. (2009, 2013), Collettini et al., (2011), Giorgetti et al. (2015), Orellana et al. (2018), Okamoto et al. (2019), Ruggieri et al. (2021), whereas the use of S-C-C' fabric for similar phyllosilicate-rich materials is used in the work of Bos and Spiers (2001), Niemeijer and Spiers (2005; 2006), Tesei et al. (2012, 2014). In this work we start with a review of the key elements for the description of the Y-B-P-R vs S-C-C' fabric. Then we present a systematic characterization of fault fabric for experimental fault rocks with increasing amount of phyllosilicates. Our results indicate that it is possible to discriminate a transition between Y-B-P-R to S-C-C' fabric. This transition is function of the amount of phyllosilicates, their degree of interconnectivity and the overall geometrical arrangement of the minerals.

## 2 Fabric elements of brittle fault rocks

One of the first systematic works on the characterization of fault rock fabric and its evolution with strain was conducted by Logan (1979) in friction experiments with a saw-cut geometry using simulated quartz fault gouge. Logan (1979) gave

a geometrical characterization of the fabric elements by individuating a common and repeatable fabric made of planar shear bands associated with purely brittle processes (e.g., fracturing and cataclasis, and linear dependence between shear and normal stress, Logan et al., 1992). This fabric characterization is described as the Y-B-P-R fabric (Fig. 1a):

- Y shear bands are parallel to the experimental fault boundaries. They can be discontinuous but are located entirely within the deforming gouge.

- B (Boundary) shear bands are similar to the Y-shears, but they are continuous, wider and are located close to the boundary of the fault, in proximity of the forcing blocks (or the country rock).

- P shear bands form a "negative" angle (dipping backward) with the shear direction and have a compressive kinematic (P-thrust according to Tchalenko, 1968).

- R and R' shear (collectively, R, Riedel) bands represent conjugate planes oriented with "positive" angle with the direction of shear and act as extensional faults (Riedel, 1929).

The fabric elements introduced by Logan were also recognized earlier in experiments on clay cakes (Riedel, 1929; Tchalenko, 1968), in shear-box experiments on sand and other granular materials (Mandl et al., 1977), and experiments of deformation of intact rock layers (Bartlett et al., 1981). The Y-B-P-R fabric seems to form under a wide range of experimental conditions suggesting that there is a generic relationship with shear strain accommodated by brittle processes (Logan et al., 1992). Structural studies have documented the same fabric also in natural faults at different scales (Tchalenko, 1968; Rutter et al., 1986; Chester and Logan, 1987; Cladouhos, 1999; Mitchell & Faulkner, 2009). In phyllosilicates-rich faults, the rock fabric is similar to that of ductilely deformed mylonites (Tullis et al., 1982; Chester et al., 1985; Rutter et al., 1986; Calamita, 1991; Lin, 1999, 2001; Bos & Spiers, 2001; Haines et al., 2009; Pace et al., 2022). This similarity originates from the presence of a pervasive foliation produced by the shape preferred orientation of the anisotropic phyllosilicates that form an S-C fabric like that observed in mylonites (Berthè et al. 1979; Lister and Snoke, 1984). The S and C planes are distinguished depending on their orientation (Fig. 1b):

- C planes accommodate shear deformation parallelly to the fault boundaries (from the French word for cut, *Cisaillement*)

- S foliation is oblique to the C-planes and formed by passive rotation and reorientation (and dynamic recrystallisation in mylonites) of anisotropic grains along the local strain ellipsoid (from the French word for schistosity, *Schistosité*).

Later were added the C' planes that represent conjugate shear planes oriented similarly to the R shear bands or to extensional crenulation cleavage (Platt and Vissers, 1980; White et al., 1980).

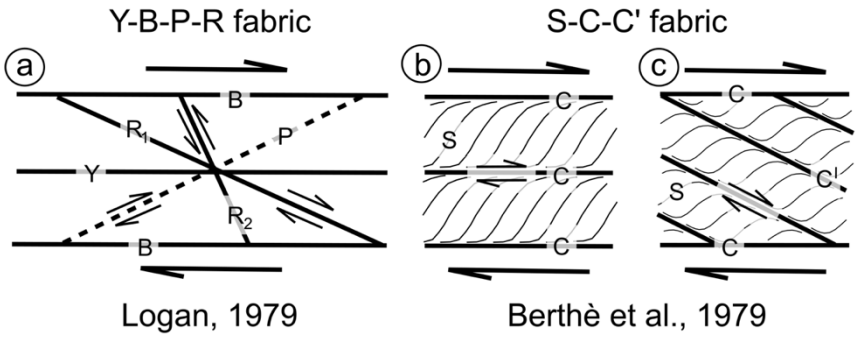


Fig. 1: Nomenclature and geometrical arrangement of shear fabric elements for granular-rich faults (left) and for phyllosilicate-rich faults (right): a) the Y-B-P-R fabric proposed by Logan (1979). b) S-C and c) the S-C-C' fabric proposed by Berthé (1979).

Building on previous studies aimed at fabric characterization, in this work we use the following criterion of distinction between the two nomenclatures:

- Y-B-P-R fabric elements are discrete, localized volumes of gouge characterized by intense grain size reduction, which indicate cataclastic processes as the principal deformation mechanism. The scale of Y-B-P-R shear bands largely exceeds the local dimension of grains. Y-B-P-R shear zones are representative of processes that promote shear localisation.

- S-C-C' fabric is the penetrative foliation produced by mechanical alignment and an iso-orientation of anisotropic grains like phyllosilicates (shape preferred orientation). This last feature favours frictional sliding along foliation as the main deformation mechanism. S-C-C' foliation can be easily traced to the scale of the average dimension of the grains. S-C-C' foliation is representative of processes that promote distributed strain.

## 3 Methods

### 3.1 Selection of rocks

For the study of brittle fault fabrics, we selected four rocks from shear zones of the Apenninic basement (Volpe et al., 2022a). The samples represent natural mixtures of granular minerals (mainly quartz) and phyllosilicates (mainly muscovite) that are common components of crustal fault rocks (Chester et al., 1993; Faulkner et al., 2010; Collettini et al., 2019, Scholz, 2019). The range of variability between granular and phyllosilicate content (Table 1) makes them ideal to explore how the heterogeneities in mineralogy and in grain size of the starting material can influence the resulting deformation fabric and bulk frictional properties (e.g., Haines et al., 2013). The starting materials were prepared by crushing the sampled rocks and sieving the powders between 63 and 125 μm, obtaining an analogue fault gouge. A controlled range of grain sizes allows for a better characterization of the cataclastic and localization processes by eliminating the initial fine-grained fraction. The mineralogical composition of the powders obtained in this way was determined by XRD analysis using a Bruker D8 Advance X-ray system equipped with Lynxeye XE-T silicon-strip detector at the Department of Earth Sciences, Sapienza University of Rome. XRD analysis provided semi-quantitative mineralogical analysis (e.g., Moore, and Reynolds, 1997) of the rocks (Table 1, details in Volpe et al., 2022a). The experimental gouges consist of quartz and phyllosilicates (muscovite, pyrophyllite and chlorite) mixtures and for ease of reading, rocks will be referred to with the label "Phy" and their relative amount of phyllosilicates in weight percent, from 24% to 58%. The mineral content of the four gouges can be divided in two types: I) phyllosilicate-rich gouges represented by Phy58 and Phy46 characterized by 46% and 58% of phyllosilicates respectively; and II) granular-rich gouges represented by Phy35 and Phy24 respectively with 65% and 76% of granular minerals. See supplementary materials section SM1 for details.

| Label | Mineralogy | | | | |
|---|---|---|---|---|---|
| | **Phyllosilicates** | | **Granular minerals** | | Mixtures |
| **Phy58** | **58%** | Muscovite<br>Paragonite<br>Clinochlore | **42%** | Quartz Rutile | **Phyllosilicates-rich** |
| **Phy46** | **46%** | Muscovite<br>Clinochlore | **54%** | Quartz<br>Hematite<br>Rutile | |
| **Phy33** | **33%** | Muscovite<br>Paragonite<br>Clinochlore | **67%** | Quartz Rutile | **Granular-rich** |
| **Phy24** | **24%** | Muscovite<br>Pyrophyllite<br>Clinochlore | **76%** | Quartz<br>Carbonates<br>Hematite | |

Table 1: mineral composition of the tested gouges.

## 3.2 Experimental procedure

Friction experiments were conducted using BRAVA (Brittle Rock deformAtion Versatile Apparatus), a servo-controlled biaxial testing apparatus (Collettini et al., 2014) hosted at the Istituto Nazionale di Geofisica e Vulcanologia of Rome. Experiments were performed simulating a thin (5 mm thick) fault core in Double Direct Shear configuration (DDS), which consists of three steel grooved blocks sandwiching two identical layers of gouge (Fig. 2a and Fig. 3a). Normal and shear stress are applied on the gouge layers by fast-acting hydraulic servo-controlled rams and are measured by strain-gauged load-cells with an accuracy of ± 0.03 kN in a range from 0.2 kN to 1.5 MN. Stresses are obtained by dividing the applied load by the contact area of the sample of 5 by 5 $cm^2$. The vertical and horizontal load point displacement are measured by LVDT (linear variable displacement transformers) with an accuracy of ± 0.1 µm. The on-fault displacements of the vertical and horizontal frames were corrected for the elastic stretch of each loading frame, considering that the machine stiffness is 1283 kN/mm on the horizontal axis and 928.5 kN/mm on the vertical axis. The elastic response of the rams is linear in the range of stresses used for these experiments. Data were sampled at frequencies of 1 to 1000 Hz and recorded continuously with a 16 channel 24-bit analog to digital acquisition system (Collettini et al., 2014). The experiments were performed at room temperature at four selected normal stresses of 25, 50, 75 and 100 MPa. All rocks were tested in water saturated conditions (thereinafter wet experiments) by placing the experimental assembly within a plastic membrane and submerging it with water. Only for the two lithologies with the highest and lowest content of phyllosilicates (Phy58 and Phy24, respectively) additional experiments were conducted at room humidity conditions (thereinafter dry experiments). In total we performed 24 experiments: 16 wet and 8 dry (see details in the Supplementary Materials section SM2). For each experiment, the sample was initially sheared for 10 mm at a displacement rate of 10 µm/s. This phase is called “run-in” and allows the fault enough displacement to reach a steady-state shear strength (Fig. 2a). After the run-in, we performed slide-hold-slide (SHS) tests consisting of hold periods ranging from 1 to 3000 s, each followed by a shear phase at 10 µm/s for 500 µm of displacement (Fig. 2b). Finally, we performed velocity steps by shearing the sample at increasing velocity, from 0.1 to 300 µm/s, for a total of 750 µm of displacement for each velocity (Fig. 2c). Our friction measurements yield: I) a steady-state sliding friction, II) frictional healing rates (e.g., Marone, 1998) during slide-hold-slide tests (Fig. 2b), III) rate and state friction parameters (Fig. 2c) $a$ (direct effect), $b$ (evolution effect) and $Dc$ (critical slip distance). The rate and state friction theory, RSF, (Dieterich, 1979; Ruina, 1983; Dieterich and Kilgore, 1994; Marone, 1998; Blanpied et al., 1998; Marone and Saffer, 2003) is used as framework for this analysis (for analytical procedures see details in Supplementary Materials section SM2).

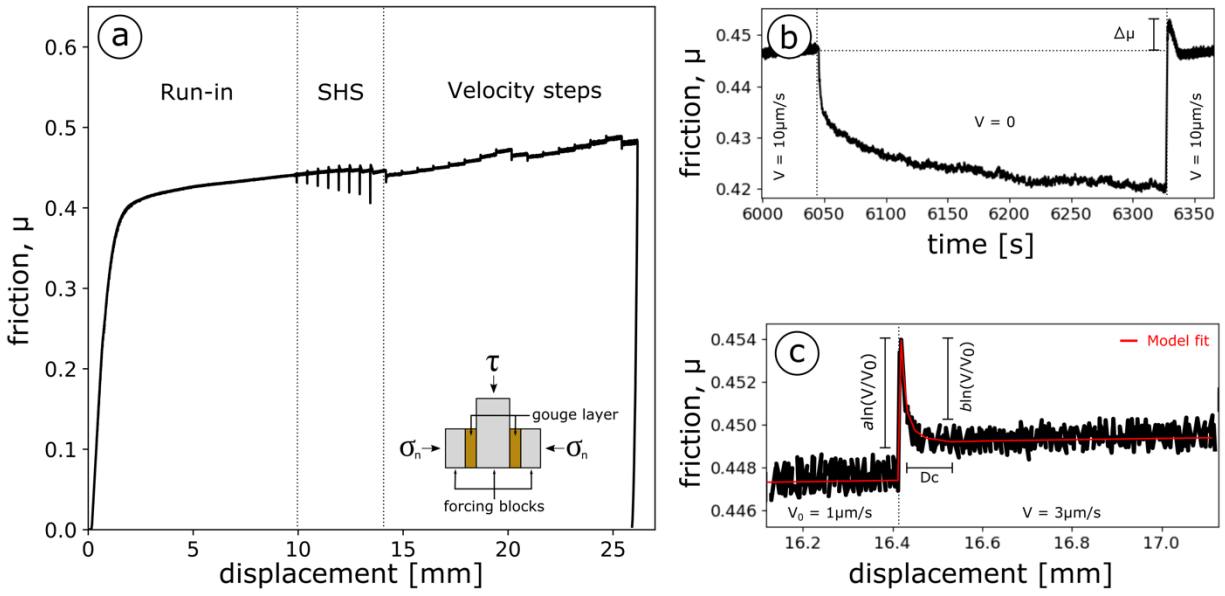


Fig. 2: a) friction vs shear displacement for one complete experiment conducted on Phy35. The inset shows the experimental double-direct shear configuration. Our procedure consisted of a run-in phase followed by slide-hold-slide tests (SHS) and velocity step tests. b) Detail of a 300-s slide-hold-slide test showing evolution of friction with hold time and re-shear. Δμ is the difference between the peak friction measured upon re-shear after each hold and the pre-hold steady state friction. c) Detail of a velocity step test from 1 to 3 μm/s (black line) and a best-fit (red line) using RSF model (Dieterich, 1979; Ruina, 1983). See supplementary materials for details (section SM2).

## 3.3 Microstructure collection, preparation, and analysis

At the end of each experiment the deformed samples were carefully extracted from the assembly (Fig. 3a). The collection of each microstructure was conducted with the aim of preserving the full thickness of the gouge layer sandwiched between the indenters of the forcing blocks (Fig. 3b and c) and reducing the accidental reworking of fault textures. Once extracted, the rock chips were carefully embedded in epoxy (Fig. 3d) at room pressure. Vacuum impregnation was excluded to avoid sample damage induced by forced intrusion of resin due to the low permeability of phyllosilicate-rich samples. Once hardened, the embedded samples were cut to expose a characteristic kinematic section of the rock chips, which is perpendicular to the shear plane and parallel to the shear direction (Fig. 3e, e.g., Passchier, 1990). The exposed surfaces were then prepared by abrasion with increasingly finer sandpaper (grit of 600 to 2000) and then by lapping using increasingly finer diamond paste (6 to 1 μm). All lapping steps were performed using an oil-based lubricant instead of water, which would render impossible the preparation due to softening and enhanced erosion of the samples. Polished surfaces were then prepared for SEM analysis by applying graphite coating.

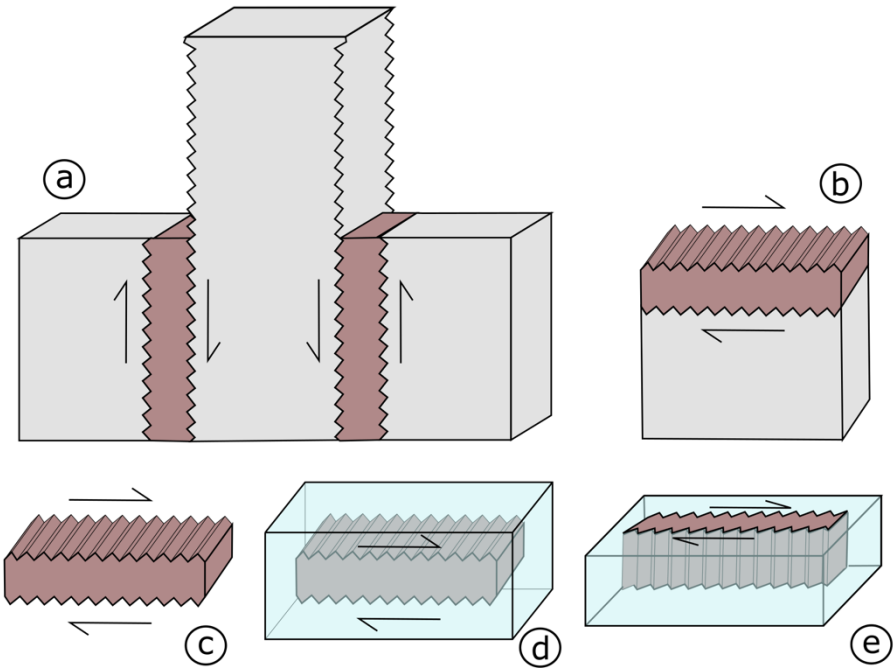


Fig. 3: Schematic drawings showing the steps used to prepare samples for microstructural investigation. a) At the end of the experiment, the double-direct shear configuration is removed; representative sample chips are recovered by first removing the central block (b) and then by detaching them from the lateral forcing block (c); sample chips are then embedded in epoxy (d) and, after hardening, cut to expose a kinematic section (e). The surface obtained this way is then polished and lapped with diamond paste down to ¼ µm. The arrows indicate the shear sense.

The collection of microstructural documentation was conducted using a Field-Emission Scanning-Electron-Microscope (SEM) hosted at the Istituto Nazionale di Geofisica e Vulcanologia of Rome. Imagery was collected in back-scattered mode.

## 4 Microstructures

For each gouge we firstly present an image of the starting material (Fig. 4) for comparison with the sheared material. Then for each microstructure we present a panorama generated by merging several high-resolution images collected in back-scattered mode. Panoramas of Fig. 5 to Fig. 10 present fabric evolution as a function of phyllosilicate content normal stress, and dry vs wet conditions. Fabric elements are better documented in selected close-ups in Fig. 11. The nomenclature used for the description of fabric elements is that described in chapter 2.

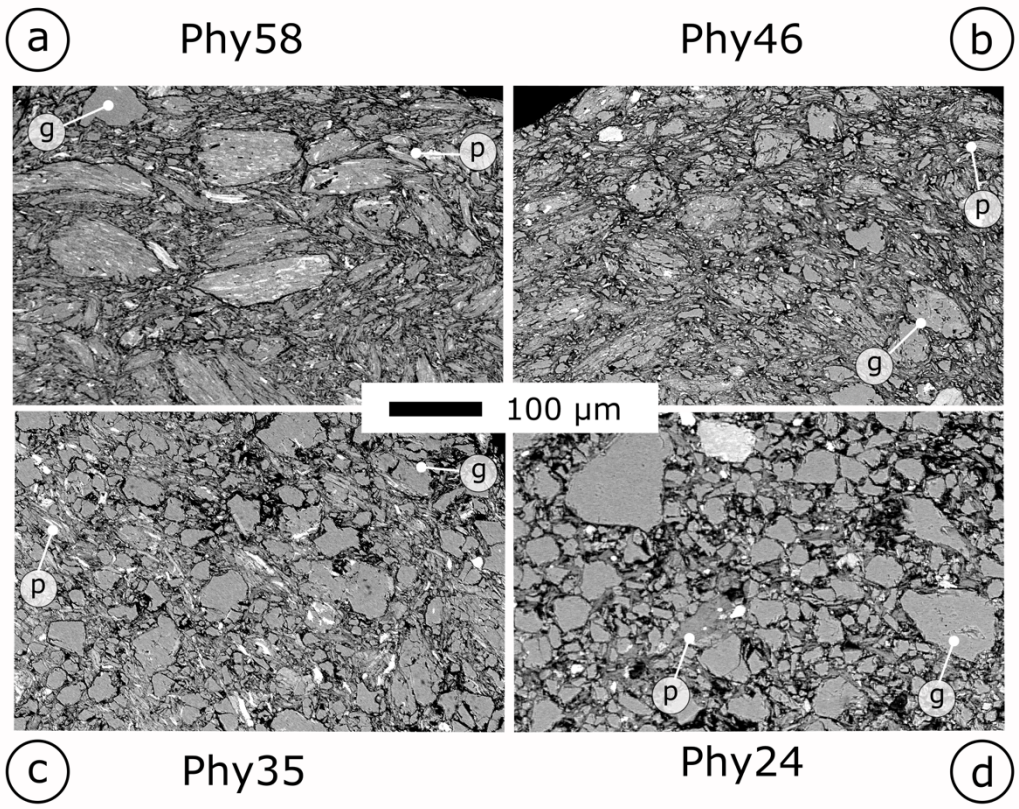


Fig. 4: SEM-BSE images of the starting material of the four tested gouges. Mineralogy is highlighted in circles: *g* for granular minerals, *p* for phyllosilicates. See table 1 for detailed mineralogy of granular and phyllosilicates minerals.

## 4.1 Phyllosilicate rich gouges

Phy58 gouge deformed in water-saturated conditions (Phy58-w) shows distributed deformation characterized by widespread comminution, which becomes more intense with increasing normal stress (compare Fig. 5 to Fig. 6). Some dispersed grains with dimension comparable to the initial grain size are preserved only at the lowest normal stress (25 MPa, Fig. 5a and Fig. 6a). The overall texture is a penetrative S-C-C' fabric, which persists down to the grain scale (e.g., Fig. 11a). C' planes are extremely continuous and extend in straight lines across the entire thickness of the samples. The spacing of C' planes decreases from ~100 to 50 µm with increasing normal stresses and comminution (Fig. 11i and o). S foliation is also well developed, and it densely decorates the domains bounded by C' planes (Fig. 11i and o). C planes are mostly observed at both sample boundaries, decorating a small layer (< 40 µm) in proximity of the block indenter (Fig. 11a and e). These planes tend to be discontinuous and rather undulous (Fig. 5d). With increasing stress conditions, the inclination of the S and C' planes decreases (Fig. 5). At higher magnification, the granular materials appear completely wrapped by phyllosilicates foliae and bounded by the S foliation (Fig. 11a, i, and o). Elongated grains are often boudinated parallelly to the S foliation (Fig. 11o). Phy58 deformed at room dry condition (Phy58-d) also shows

distributed deformation (Fig. 6), with the exception of the lowest normal stress (25 MPa, Fig. 6a), where important volumes of low strain domains are characterized by limited grain size reduction, imbricated clasts, and kinked phyllosilicate foliae. At higher normal stress only a few large clasts (< 100 μm) remain dispersed in the foliated gouge (Fig. 6c and d). The textures observed are not different from those formed in saturated conditions, with prominent C' planes and dense S foliation (Fig. 6). C planes are again found close to the indenter in a narrow zone (< 40 μm of thickness) and the inclination of the S and C' planes decreases at increasing normal stress (Fig. 6). Phy46 samples deformed in water saturated conditions are characterized by distributed deformation, extremely homogeneous texture, and very fine grain sizes even at low normal stress (Fig. 7). The fault is composed of homogeneously distributed angular quartz grains embedded in the phyllosilicate matrix (Fig. 7, Fig. 11 b, l, and p). The size of the quartz grains is consistent across the experiments (~ 80 μm, Phy46 in Fig. 11) while the phyllosilicates become finer at higher normal stress (from 10 μm to <1 μm, at 25 and 100 MPa, respectively). The fabric is dominated by a faint S-C-C' foliation, which is of difficult individuation at the panorama scale due to the lack of prominent fabric elements or preferential splitting (Fig. 7). The foliation becomes less intense with increasing normal stress (Fig. 7 and Fig. 11b vs f). The S foliation is also rather irregular and largely influenced by the shape of the hosted granular materials (Fig. 11b). At low normal stress (25 MPa), the phyllosilicates form a better organized S-C-C' foliation while at high normal stress they form more convoluted texture characterized by kinking and crenulation (Fig. 11l, Fig. 13, and Okamoto et al., 2019). Some material is preserved in unsheared state within the block indenters and shows that the initial grains are formed by aggregates of fine-grained material comparable with that observed in the deformed volume (Fig. 4b). In summary, phyllosilicate-rich gouges, Phy58 and Phy46, are characterized by deformation distributed across the entire sample layer and widespread grain size reduction (Fig. 5 to Fig. 7). Grain size is dramatically reduced at normal stresses of 50 MPa and higher, especially in water saturated conditions, where isolated aggregates of the original material are no more evident within the experimental fault (Fig. 5 and Fig. 7). The overall texture is dominated by S-C-C' fabric (line drawings from Fig. 5 to Fig. 7 and Phy58 and Phy46 in Fig. 11) formed by preferential alignment of phyllosilicate foliae. The intensity of foliation is strongly influenced by the grain size of the phyllosilicate matrix. Finer clasts hinder the formation of a regular foliation and produce convoluted textures at the micron scale (e.g., Fig. 11o vs p). Strong S-C-C' fabric is observed when phyllosilicate foliae are wider (>> 40 μm) and becomes more regular with increasing normal stress (e.g., Phy58 vs Phy46 in Fig. 11). C' planes are extremely continuous and connect the two boundaries of the experimental faults (Fig. 5 to Fig. 7). C' and S foliations become less inclined with increasing stress conditions. Deformation occurs mainly by frictional sliding along the phyllosilicate foliae and subordinated cataclastic deformation (Fig. 14).

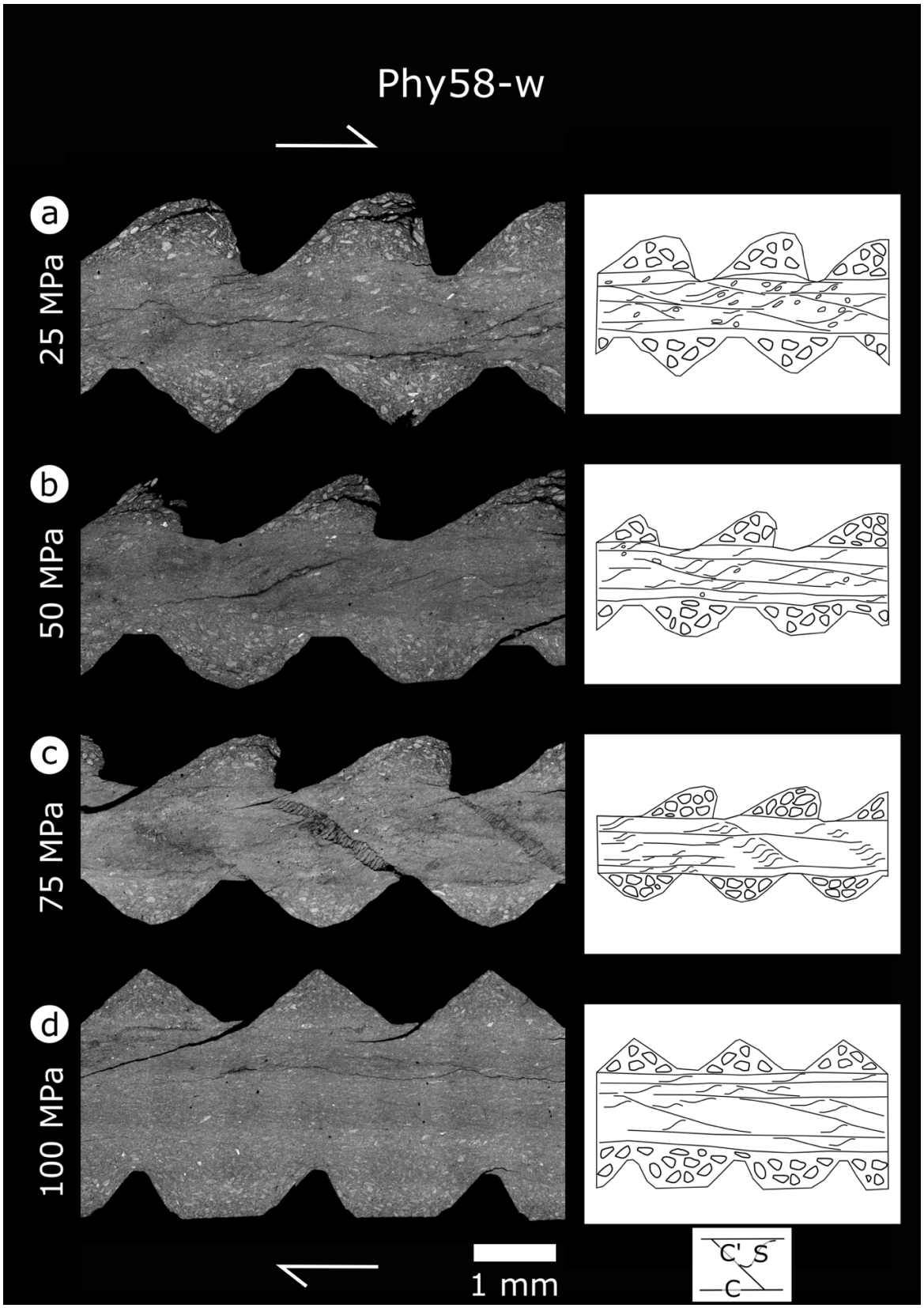


Fig. 5: Microstructures of Phy58 in wet conditions (Phy58-w). In the left column are reported the SEM-BSE image for each experiment whereas in the right column the line-drawing of the main fabric features for each image. The normal stress for each experiment is shown at the left of each figure.

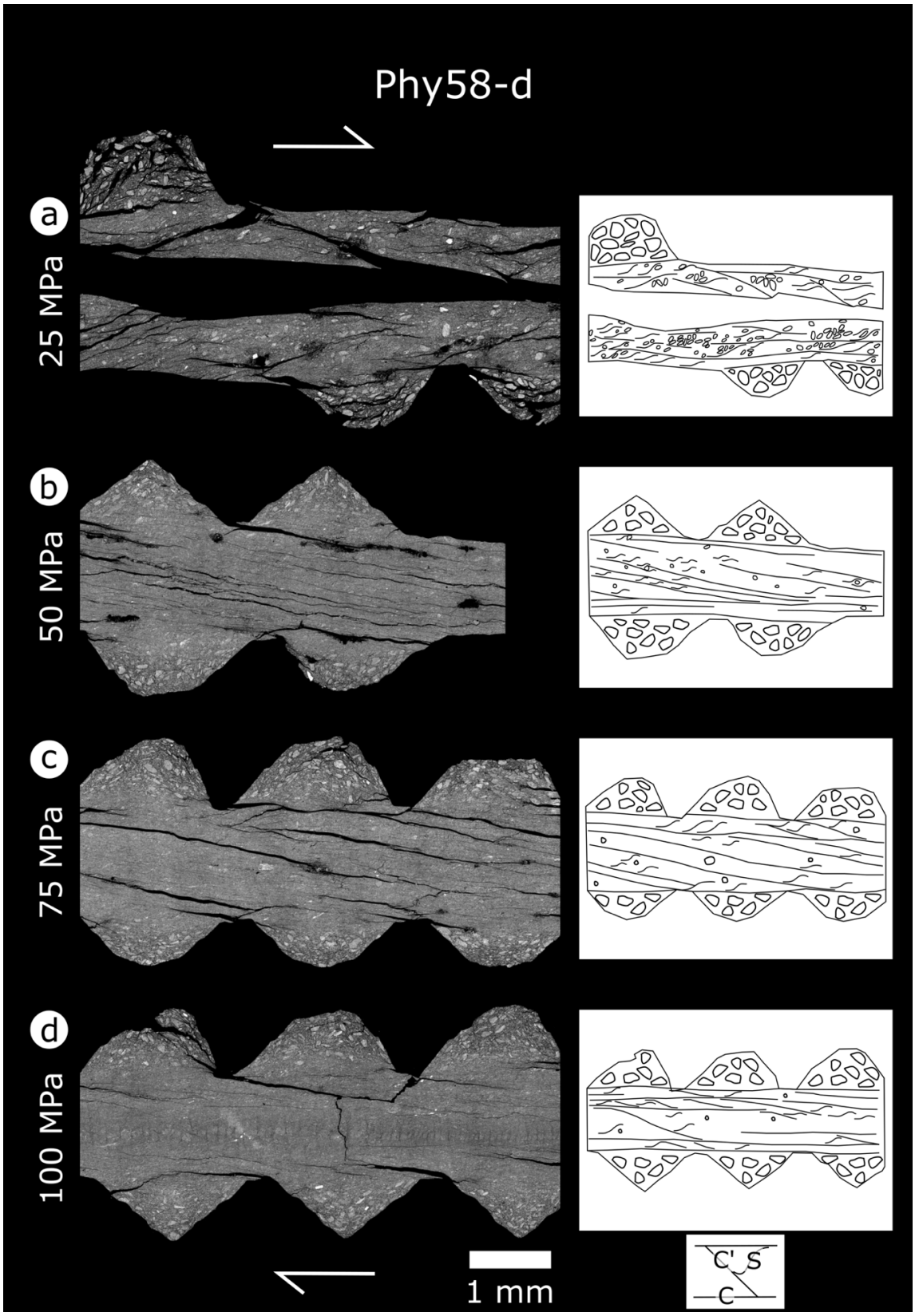


Fig. 6: Microstructures of Phy58 in dry conditions (Phy58-d). In the left column are reported the SEM-BSE image for each experiment whereas in the right column the line-drawing of the main fabric features for each image. The normal stress for each experiment is shown at the left of each figure.

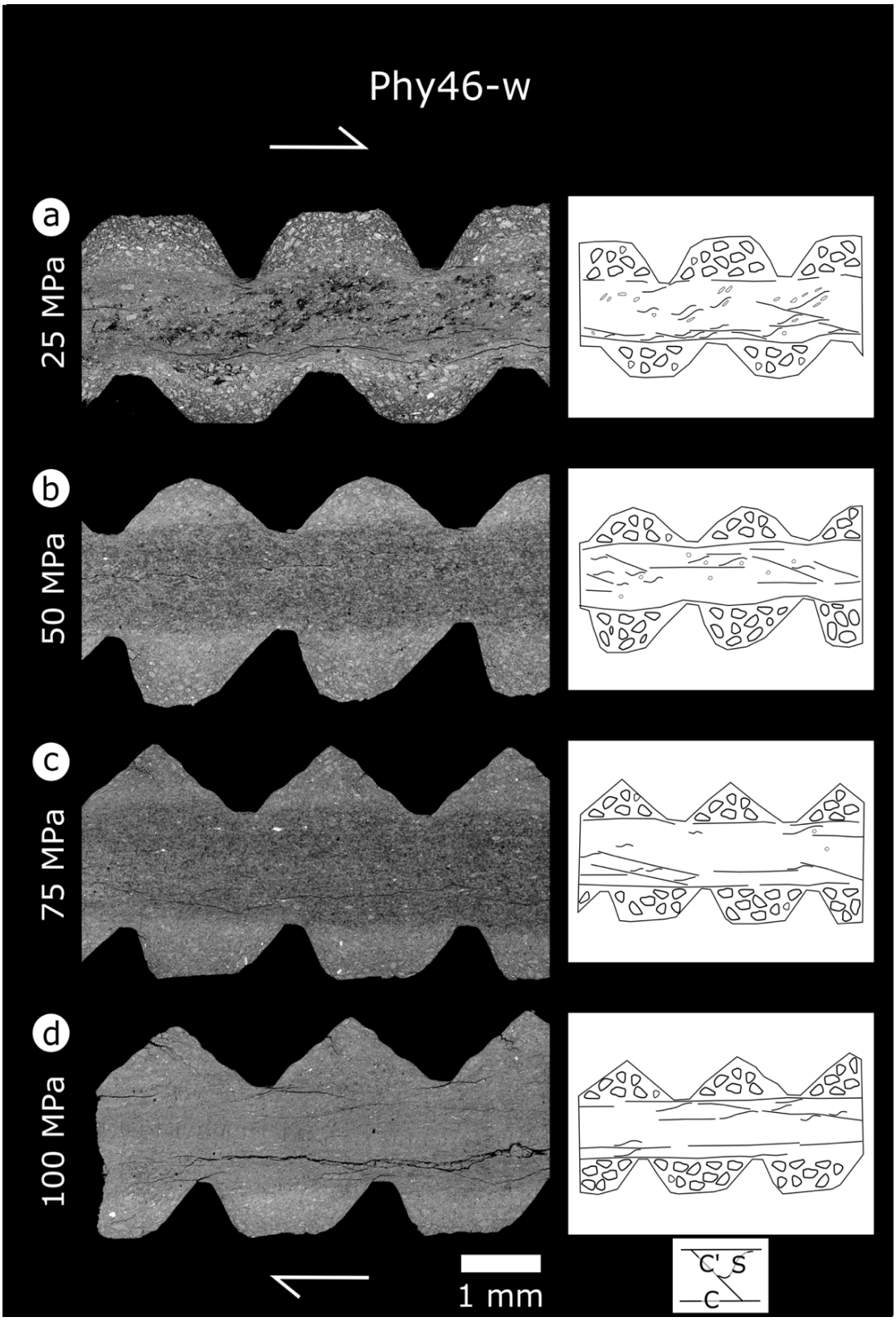


Fig. 7: Microstructures of Phy46 in wet conditions (Phy46-w). In the left column are reported the SEM-BSE image for each experiment whereas in the right column the line-drawing of the main fabric features for each image. The normal stress for each experiment is shown at the left of each figure.

## 4.2 Granular-rich gouges

Phy35 deformed samples are characterized by widespread grain size reduction (Fig. 8) associated with localized shear zones of intense cataclastic comminution. Boundary shear bands, B, form at all the normal stresses investigated, while oblique shear bands (R and P) emerge gradually with increasing normal stress (Fig. 8b, c, and d). The fault architecture is therefore dominated by Y-B-P-R fabric (Fig. 8). By increasing normal stress, the shear bands become more localized, display more intense grain size reduction (Fig. 8c, d, and Fig. 11c and g). Even though it is possible to clearly individuate low strain domains bounded by the main shear zones, distributed deformation across the entire fault layer is highlighted by passive tilting and imbrication of anisotropic clasts, especially phyllosilicates, as well as elongated trails of cataclastic materials (Fig. 8 and Fig. 11g, q). These elements produce a bulk texture - sometimes referred to a textural "layering" (Chester et al., 1985) - similar to the S foliation observed in the phyllosilicate-rich gouges, which appears more evident at high normal stresses (Fig. 11g and q). Isolated P shear zones are highlighted by long trails of fragmented materials, especially visible by drag of oxides (white material), and minor aligned phyllosilicates (Fig. 8c, d and Fig. 11g and q). P shears are cut and deflected by B and R shear zones (Fig. 8c, d). The microstructures of water-saturated Phy24 (Phy24-w) are characterized by localized deformation along Y-B-P-R shear zones composed by fine-grained cataclastic products. Comminution and grain size reduction are more intense at high normal stresses (Fig. 9 and Fig. 11d and h). Differently from Phy35, the low strain domains are coarse-grained and only at $\sigma_N$ = 75 and 100 MPa they present some S-like oblique texture at their boundaries (Fig. 9c, d, Fig. 11h and r). This S-like texture is predominantly formed by elongated cataclastic trails (Fig. 9c, d, and Fig. 11h and r). The grain size reduction within the boundary shear zone enhances the rounding of granular materials and favors the interconnection of a phyllosilicate-rich matrix (Fig. 9 and Fig. 11d vs h). With increasing normal load, both B and R shear zones widen while their boundaries become transitional with the low strain domains (Fig. 9d and Fig. 11r). Phy24 samples deformed at room dry conditions (Phy24-d) show Y-B-P-R fabric with shear bands much more localized than those at water-saturated conditions (Fig. 10 vs Fig. 9). Grain-size reduction is more intense at higher normal stress (e.g., Fig. 10d). The samples show (>25 MPa) R-shears that are more closely spaced than those formed at water-saturated conditions (Fig. 10 vs Fig. 9). Low-strain domains are characterized by a much more intense grain-size reduction than those observed in wet condition. No oblique texture is observed (Fig. 10). These shear zones are often highlighted by opened fractures (Fig. 10). An evolution with normal stress of the fabric can be observed: at low normal stress the main fabric elements are represented mainly by R shear (Fig. 10a and b) whereas at higher normal stress the gouges display sharp, and well-developed Y-B-R shear planes and P shear highlighted by

trails of fragmented carbonates (e.g., Fig. 10c and d). At higher magnification the shear zones are characterized by fractured grains with heterogeneous size and shape. This feature results in the development of a grain load bearing framework (Fig. 10, Fig. 13e, g, and Fig. 14). The overall fabric of granular-rich gouge, Phy35 and Phy24, is Y-B-P-R type and is highlighted by localized deformation in discrete shear zones (Fig. 8 to Fig. 10 and, Phy35 and Phy24 in Fig. 11). Most of the strain is accommodated along a B-shear zone that frequently nucleates at one side of the experimental fault. An accessory, less evolved B-shear zone, is commonly observed at $\sigma_N$ > 50 MPa close to the opposite side of the experimental fault. With increasing normal stress, grain size is dramatically reduced in the main shear zones, that are associated with rounding of the granular materials and enhanced interconnection of the phyllosilicate fraction in wet condition (Fig. 8, Fig. 9, and Fig. 11d vs h). The shear bands bound areas of less deformed gouge (low-strain domains), where S-like texture - or layering - may develop at high normal stress by trailing of cataclastic products, especially in presence of high phyllosilicate content (Fig. 11g, h, q, and r). The overall deformation style is dominated by cataclastic processes within the principal shear zones and indicating a granular load bearing framework (Fig. 8 to Fig. 10 and Fig. 14).

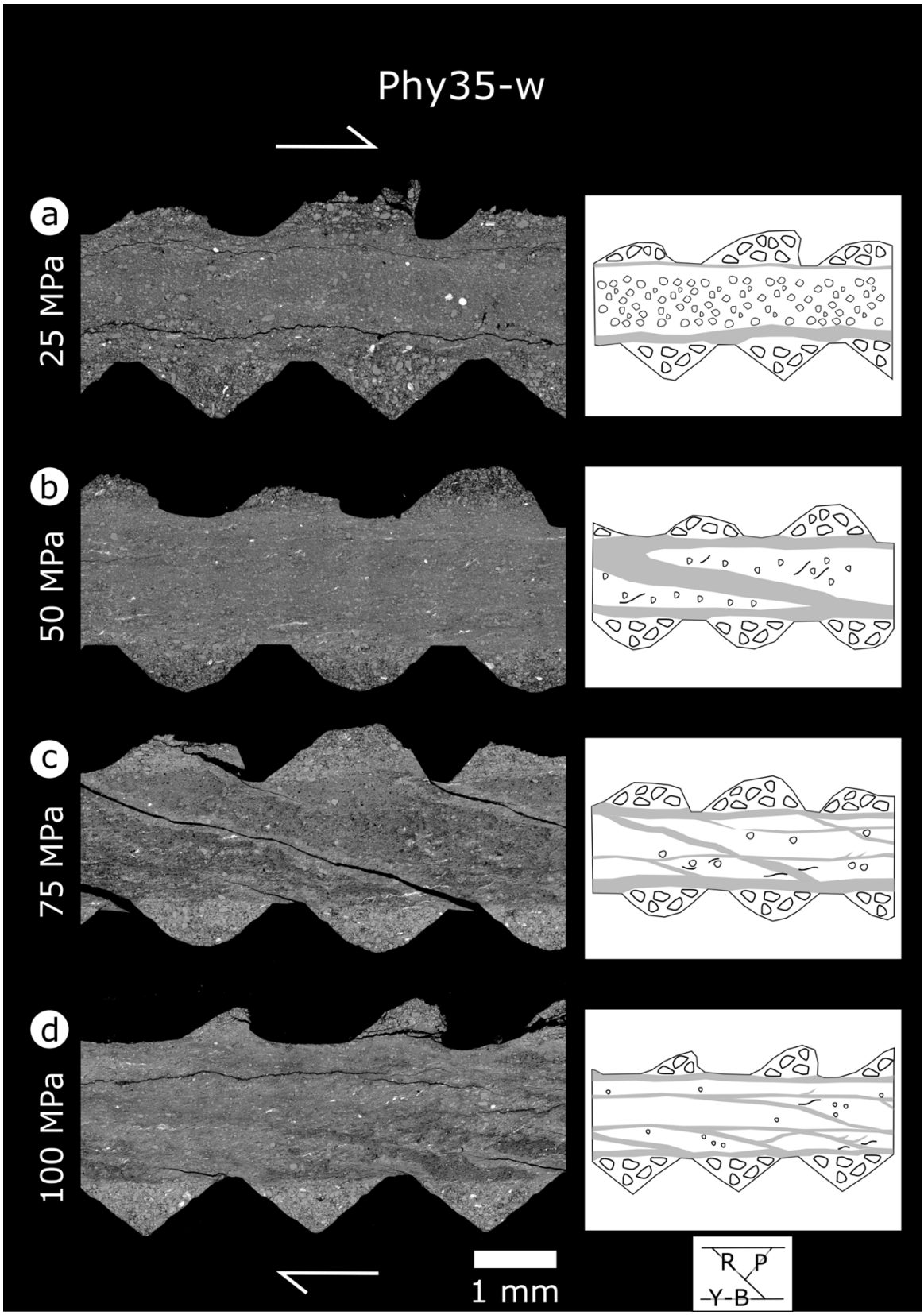


Fig. 8: Microstructures of Phy35 in wet conditions (Phy35-w). In the left column are reported the SEM-BSE image for each experiment. In the right column are reported schematic representations of the main fabric features observed. Grey shaded areas represent the shear bands. The normal stress for each experiment is shown at the left of each figure.

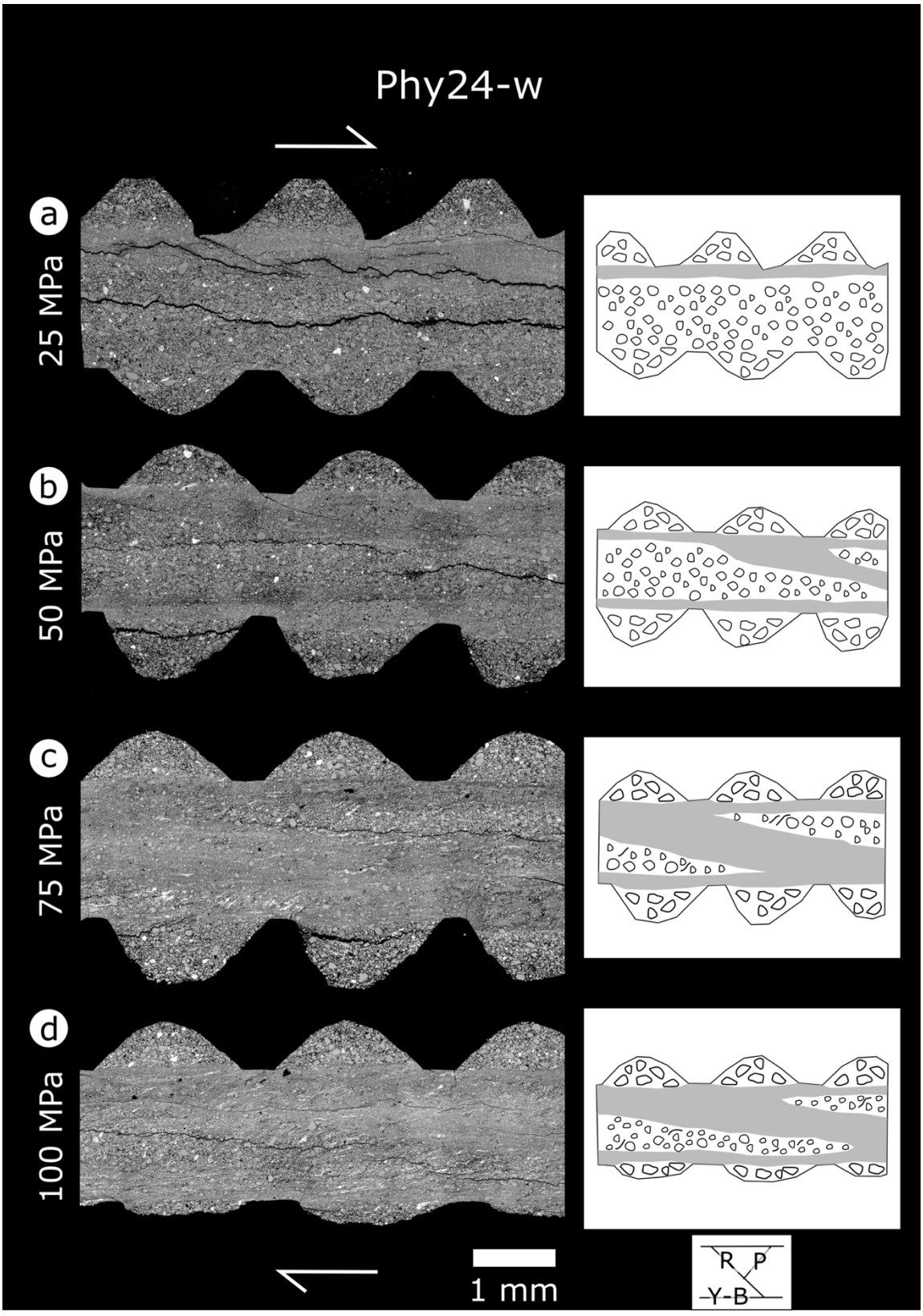


Fig. 9: Microstructures of Phy24 in wet conditions (Phy24-w). In the left column are reported the SEM-BSE image for each experiment. In the right column are reported schematic representations of the main fabric features observed. Grey shaded areas represent the shear bands. The normal stress for each experiment is shown at the left of each figure.

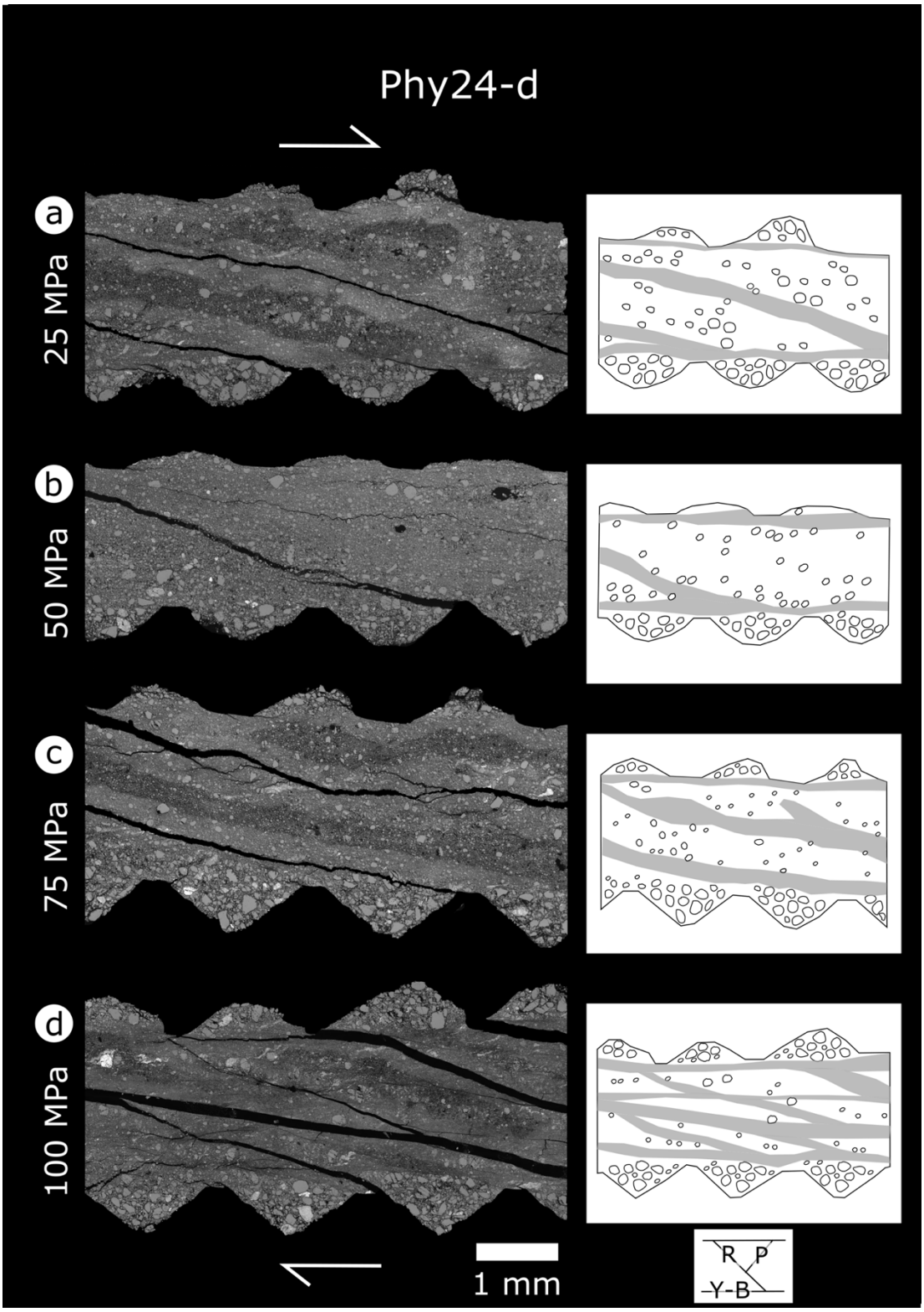


Fig. 10: Microstructures of Phy24 in dry conditions (Phy24-d). In the left column are reported the SEM-BSE image for each experiment. In the right column are reported schematic representations of the main fabric features observed. Grey shaded areas represent the shear bands. The normal stress for each experiment is shown at the left of each figure.

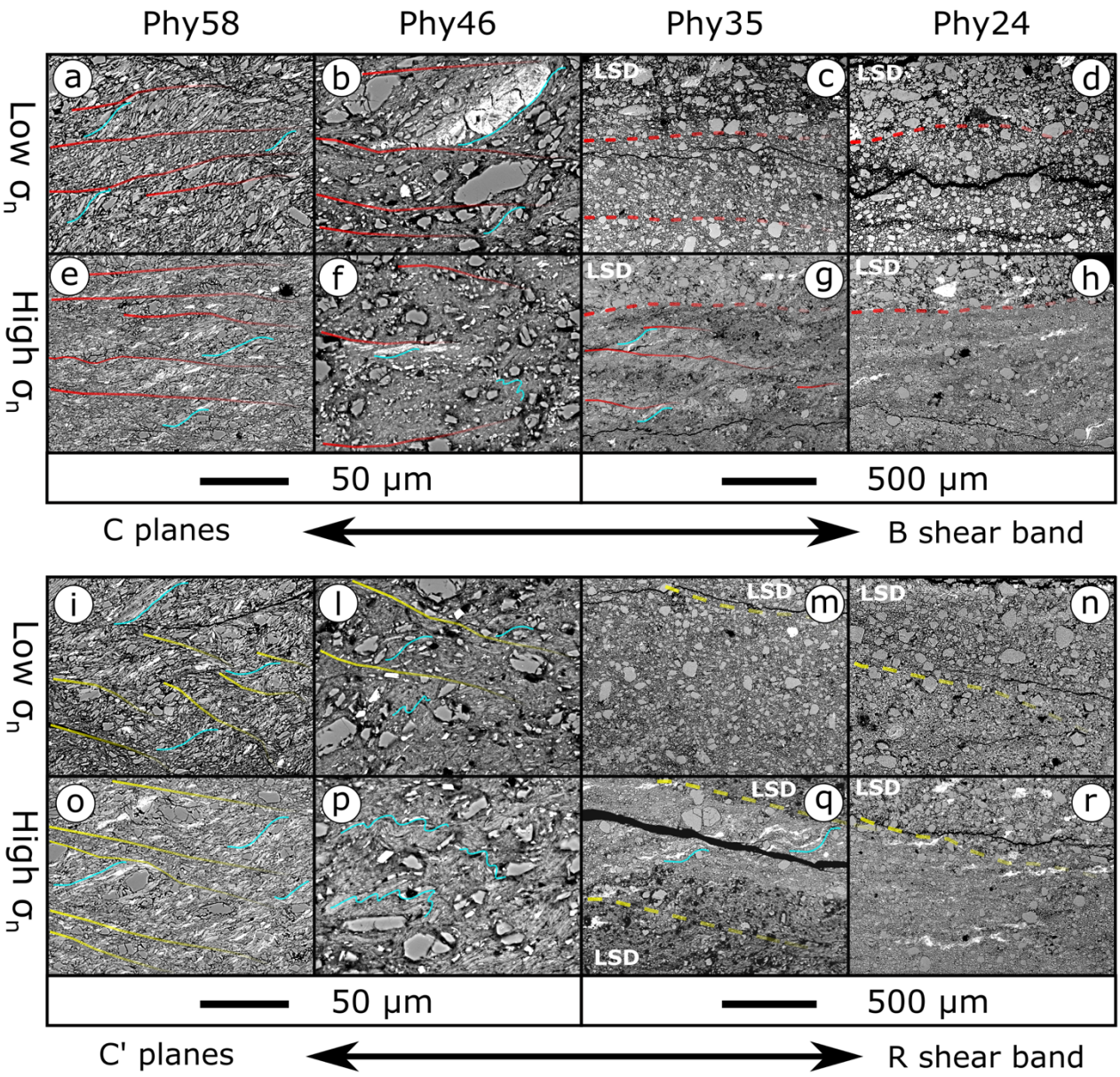


Fig. 11: Schematic summary (SEM-BSE images) of the effects of normal stress and phyllosilicates content on the main fabric elements of water-saturated samples: Phy58-w; Phy46; Phy35; Phy24-w. Upper panel shows the transition from C planes to (Y) B shear bands, both highlighted in red. The dashed red lines mark the transition to low strain domains (LSD). Lower panel shows the transition from C′ planes to R shear bands, both highlighted yellow. Dotted yellow lines represent boundaries of LSD. Foliation is highlighted in cyan. The arrow represents the transition from the two fabric elements.

## 5 Mechanical results

For each gouge we characterized frictional strength (μ), healing rate ($b$), and the rate and state friction parameters: $a$, $b$, and $a$-$b$ (details in Table 2 and in supplementary materials). In a normal stress – shear stress plot, the steady-state

shear stress values of each gouge plot along a straight line in agreement with Coulomb failure criterion and therefore diagnostic of brittle deformation processes (Fig. 12a). The envelopes for each gouge show negligible cohesion (Fig. 12a) indicating the absence of pressure solution and diffusion creep with cementation. The steady state friction for the tested gouges ranges between 0.28 to 0.56 and is affected by gouge mineralogy (phyllosilicates content) and experimental conditions (i.e., wet vs dry). In water-saturated conditions Phy24 (Phy24-w) and Phy35 show high friction coefficient, 0.50 and 0.47 respectively and 0.56 for Phy24 in room-dry conditions (Phy24-d, Fig. 12a). In water-saturated conditions Phy58 (Phy58-w) and Phy46 display lower friction coefficient, 0.32 and 0.28 respectively and 0.41 for Phy58 at room dry conditions (Phy58-d, Fig. 12a).

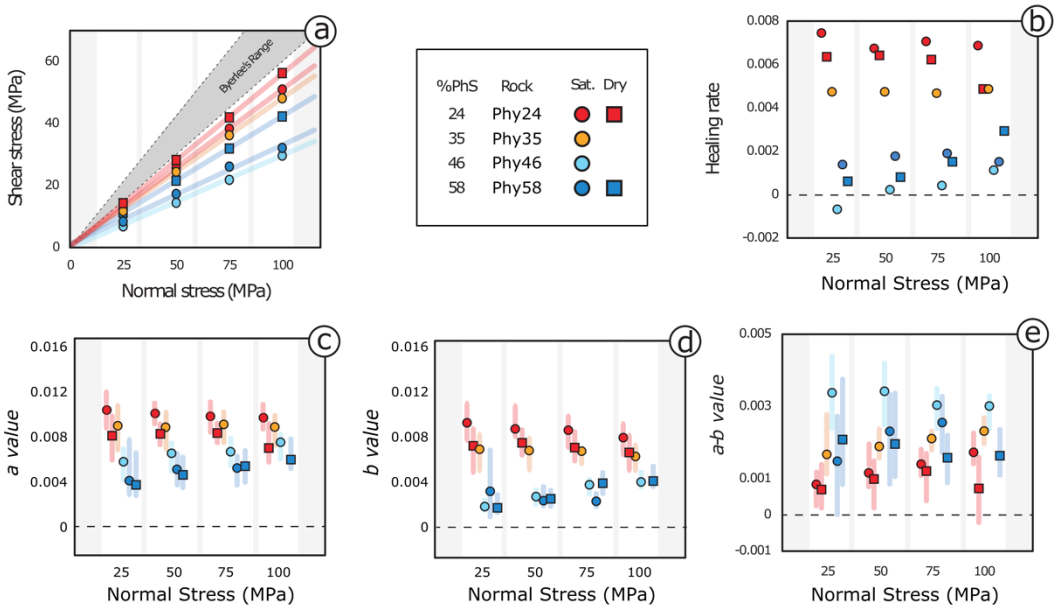


Fig. 12: summary of the mechanical results. a) shear stress vs normal stress plot highlighting a linear relationship diagnostic of the Coulomb criterium. b) healing rate vs normal stress for each gouge. c) direct effect, *a*, as a function of normal stress. d) evolution effect, *b*, as a function of normal stress. e) velocity dependence of friction, *a-b*, as a function of normal stress. Shaded bars in c, d, and e, represent the range of values obtained at different sliding velocities (see methods), whereas the filled symbol represents the mean value. A clear separation between the granular-rich gouges (blues) and phyllosilicate-rich gouges (reds) is visible in each plot.

Frictional healing changes as a function of gouge composition, normal stress, and water content conditions (Fig. 12b). Phy46 and Phy58 gouges (Fig. 12b) show small and even negative values of healing rate, $\beta$, that slightly increase with normal stress from -0.0006 to >0.002. The same trend is observed in Phy58 at room dry conditions. Phy35 and Phy24 (Fig. 12b) are characterized by higher $\beta$ values, ranging between 0.0047 to 0.0074. $\beta$ slightly decreases with increasing normal stress (Fig. 12b). Again, no significant difference is observed for different water saturation. For characterization

of rate and state mechanical data (i.e., *a*, *b*, *a-b*), we decided to use the average value calculated using all the velocity steps. The spread of rate and state parameters is represented for each normal stress with faded bars in Fig. 12c, d and e. The direct effect of friction, *a*, and the evolution effect, *b*, have a similar behavior with normal stress: Phy58 and Phy46 display an increase of the mean value of both parameters with increasing normal stress, whereas Phy35 and Phy46 show a slight decrease of these values at higher normal stress (Fig. 12c and d). The velocity dependence of friction, expressed by the *a-b* parameter (Fig. 12e), is quite variable. All gouges display rate strengthening behavior (*a-b* positive) with values between ~ 0 and 0.0043. Phy46 displays the highest *a-b* values (> 0.003), Phy24 the lowest (< 0.002). *a-b* values tend to slightly increase with increasing normal stress with the exception of Phy46 and Phy58 at dry conditions, whose values, in turn, decrease slightly (Fig. 12e).

Gouges, experimental conditions, and summary of frictional results for the tested gouges. See Fig. SM3 in supplementary materials for experiment identifying number.

| rock | Phyllosilicate content [%] | Normal stress [MPa] | Friction | | Healing rate, β | | direct effect, *a* | | evolution effect, *b* | | velocity dependence, *a-b* | | Bulk shear strain | | |
|---|---|---|---|---|---|---|---|---|---|---|---|---|---|---|---|
| | | | wet | dry | wet | dry | wet | dry | wet | dry | wet | dry | wet | dry | |
| **Phy58** | 58 | 25 | 0.32 | 0.41 | 0.00142 | 0.00061 | 0.0045 | 0.0038 | 0.0038 | 0.0017 | 0.0007 | 0.0011 | 13.4 | 13.4 | **Phyllosilicate-rich** |
| | | 50 | | | 0.00176 | 0.00081 | 0.0049 | 0.0044 | 0.0026 | 0.0024 | 0.0022 | 0.0019 | 14.1 | 14.4 | |
| | | 75 | | | 0.00193 | 0.00155 | 0.0049 | 0.0053 | 0.0023 | 0.0037 | 0.0025 | 0.0019 | 16.8 | 15.1 | |
| | | 100 | | | 0.00154 | 0.00295 | | 0.0059 | | 0.0043 | | 0.0016 | 4.6 | 15.2 | |
| **Phy46** | 46 | 25 | 0.28 | | −0.0006 | | 0.0055 | | 0.0021 | | 0.0034 | | 25.6 | | |
| | | 50 | | | 0.00023 | | 0.0063 | | 0.0028 | | 0.0035 | | 28.8 | | |
| | | 75 | | | 0.00044 | | 0.0067 | | 0.0036 | | 0.0031 | | 15.6 | | |
| | | 100 | | | 0.00112 | | 0.0071 | | 0.0041 | | 0.003 | | 25.6 | | |
| **Phy35** | 35 | 25 | 0.47 | | 0.00474 | | 0.0089 | | 0.0067 | | 0.0022 | | 11.5 | | **Granular-rich** |
| | | 50 | | | 0.00471 | | 0.0085 | | 0.0066 | | 0.0019 | | 10.8 | | |
| | | 75 | | | 0.00468 | | 0.0087 | | 0.0066 | | 0.0021 | | 11.6 | | |
| | | 100 | | | 0.00485 | | 0.0086 | | 0.0063 | | 0.0023 | | 12.3 | | |
| **Phy24** | 24 | 25 | 0.5 | 0.56 | 0.00742 | 0.00631 | 0.0103 | 0.0076 | 0.0095 | 0.0069 | 0.0008 | 0.0007 | 14.6 | 15.5 | |
| | | 50 | | | 0.00674 | 0.00642 | 0.0104 | 0.0083 | 0.0092 | 0.0073 | 0.0011 | 0.0009 | 13.2 | 15.9 | |
| | | 75 | | | 0.00707 | 0.00621 | 0.0097 | 0.0081 | 0.0082 | 0.0069 | 0.0014 | 0.0012 | 19.5 | 14.6 | |
| | | 100 | | | 0.00682 | 0.00484 | 0.0095 | 0.0073 | 0.0078 | 0.0065 | 0.0017 | 0.0007 | 24.9 | 15.9 | |

Tab.2: gouges, experimental conditions, and summary of frictional results for the tested gouges. See Fig. SM3 in supplementary materials for experiment identifying number.

## 6 Discussions

### 6.1 Mineralogy, fabric, and deformation mechanisms

The phyllosilicates-rich experimental faults are characterized by distributed deformation and a S-C-C' fabric (Phy58 and Phy46 in Fig. 11 and Fig. 13a, b, c, and d). The fabric is defined by the preferential orientation of phyllosilicates across the entire experimental fault zone (Phy58 and Phy46 in Fig. 11 and Fig. 13a, b, c, and d). This fabric has been described in phyllosilicate-rich gouges sheared at similar experimental conditions, normal stress and sliding velocities (e.g., Rutter, 1986; Chester and Logan, 1987; Niemeijer and Spiers, 2005, 2006; Behnsen and Faulkner, 2012; Haines et al., 2013; Giorgetti et al., 2015; Orellana et al., 2018; Ruggieri et al., 2021) and even at higher, up to seismic, sliding velocities (Aretusini et al., 2017; Okamoto et al., 2019) and high temperature (Moore and Lockner, 2010; Den Hartog et al., 2013).

The dominant deformation mechanism is frictional sliding along oriented phyllosilicate foliae (Fig. 14; e.g., Moore and Lockner, 2004; Niemeijer and Spiers, 2007; Collettini et al., 2009; Smith et al.,2017). Cataclastic processes are still present and are evidenced by the widespread grain size reduction of the granular fraction (e.g., Fig. 11b, o and p). Quartz grains wrapped by the S foliation are fractured and boudinaged (Fig. 11b, o, and n). Similar observations were made in different mineral mixtures, such as calcite and phyllosilicates (Giorgetti et al., 2015; Orellana et al., 2018; Ruggieri et al., 2021). Grain size reduction also occurs by disaggregation of polymineralic aggregates, which retained the original contacts between phases with grain sizes much smaller than the sieve mesh (compare Fig. 4a with Phy58 in Fig. 11 and Fig. SM4 in supplementary materials). This mechanism is not well documented in literature since analogous mixtures are often preferred to natural ones (i.e., Haines et al., 2013). Nonetheless, this mechanism might be relevant in nature since different frictional behavior exists between analogous and natural starting materials (Haines et al., 2013). Higher normal stress and the presence of fluids favor the separation of grains and the splitting of cleavage along phyllosilicate foliae (Fig. 4a, b and Fig. SM4 in supplementary materials), thus resulting in a finer grain-size, and a more distributed deformation in comparison to dry conditions and low normal stresses (Fig. 5 vs Fig. 6 and Fig. 11f and p), which suggest strain hardening and delocalization processes (e.g., Niemejier and Spiers 2005, 2007; Behnsen and Faulkner, 2012; Haines et al., 2013; Giorgetti et al., 2015; Orellana et al., 2018 and Okamoto et al., 2019). Phy46 shows more homogeneous deformation and finer grain sizes of the phyllosilicates fraction than Phy58, even at lower normal stress (Fig. 11a vs b and Fig. 11i vs l). This can be explained by the fact that the original rock of Phy46 has a finer natural grain size (smaller than the initial grain size of the prepared powder, Fig. 4a vs b). Notably, the smaller dimension of the phyllosilicate foliae prevents the formation of well-organized S-C-C' fabric, which shows a high degree of asymmetric folding at the micron scale (Fig. 11f, l and p). The granular-rich experimental faults show localized deformation along discrete shear zones that bound volumes of little to non-deformed starting materials (i.e., low-strain domains, LSD in Fig. 11). This fabric has been observed for gouges with similar (i.e., quartz gouges, Marone and Scholz, 1989; Anthony and Marone, 2005; Mair et al., 2002; Scuderi et al., 2020; Bedford and Faulkner, 2021) and different mineralogical composition (i.e., carbonates in Tesei et al., 2014; Giorgetti et al., 2015; Pozzi et al., 2018; Ruggieri et al., 2021; anhydrites/dolostone mixtures in Scuderi et al., 2013, 2020, and phyllosilicates/mafic materials Collettini et al., 2011). These microstructures correspond to Y-B-P-R fabric (Fig. 8 to Fig. 10 and closeups of Phy35 and Phy24 in Fig. 11; e.g., Logan, 1979). Y, B, P and R shear bands are characterized by remarkable decrease in the grain-size (i.e., compare Phy35 and Phy24 in Fig. 11 with Fig. 4c and d, presenting the grain-size of the starting material). As it is pointed out in several works (e.g., Collettini et al., 2019 for a review) the dominant deformation mechanisms in granular load bearing

frameworks is cataclasis, characterized by fracturing and comminution (i.e., Sibson, 1977). Minor frictional sliding along phyllosilicates foliae is observed within P and R shear zones in Phy35, which has a higher amount of phyllosilicates, high enough to promote the development of a proto-foliation with increasing normal stress (e.g., Fig. 11g and q and Giorgetti et al., 2015). Phyllosilicate content higher than 30% is documented to be enough to affect the bulk frictional properties (frictional strength, healing rate, and *a-b*) of a granular-phyllosilicates gouge mixture (e.g., Crawford et al., 2008; Tembe et al., 2010; Ikari et al., 2011; Tesei et al., 2012; Giorgetti et al., 2015). This is also suggested by the formation of a cataclastic S-like layering and by the overall fault architecture, where a Y-B-P-R fabric closely resembles a S-C-C' type.

## 6.2 The effect of normal stress on microstructures

The normal stress plays a key role in fault rock fabric. A first, trivial effect is the reduction of the grain-size with increasing values of normal stress (e.g., Fig. 5 to Fig. 10). The normal stress favors cataclastic processes such as fracturing and disaggregation along grain boundaries (Fig. SM4 in supplementary materials) as an effect of the major work necessary to dilate (e.g., Logan, 1979; Mair and Abe, 2008; Bedford and Faulkner, 2021). The increase of normal stress accompanied with a reduction in grain-size results in a more distributed deformation which is represented by the widening of the Y-B-P-R shear bands in granular materials, and a more pervasive foliation and homogeneous grain size distribution in phyllosilicate-rich rocks (Haines et al., 2013; Ruggieri et al., 2021). This does not seem the case for extremely fine-grained phyllosilicates rich samples like in Phy46, where the fabric becomes less regular with the increase of normal stress (Fig. 11f and p). High normal stresses also favor networking of phyllosilicates within the shear bands of granular-rich gouges mimicking the fabric elements displayed by phyllosilicate-rich gouges (e.g., Fig. 8, Fig. 11g and q and upper row in Fig. 14). In general, the difference of toughness between granular (fracturing) and phyllosilicate (cleavage and frictional sliding) materials affects the modal distribution of grain sizes (e.g., the bi-trimodal grain-size curve observed by Haines et al., 2009, 2013) and explains the interconnectivity of the fine-grained weak matrix in the principal shear zones (Fig. 14). This mechanism leads to foliated shear zones in dominantly Y-B-P-R fabrics (e.g., Den Hartog et al., 2013; Giorgetti et al., 2015; Orellana et al., 2018), with the evolution with strain towards S-C-C' fabric (e.g., Fig. 11m vs q, and Bos and Spiers, 2001; Haines et al., 2013; Collettini et al., 2019). Finally, higher normal stresses have been observed to flatten the main fabric elements (of wet gouges) producing lower angle R-P shear bands and S-C' foliation in granular-rich and phyllosilicate-rich samples (i.e., foliation flattening in Fig. 14), respectively (Fig. 5 to Fig. 10 and Fig. 13).

## 6.3 Effect of water saturation on microstructures

Water saturation has different effects in the two groups of analyzed starting mixtures. In phyllosilicate-rich gouges (Fig. 5, vs Fig. 6), the presence of water favors a more distributed deformation and a more comminuted grain size with respect to dry conditions. This results in homogeneous textures across the entire experimental fault associated with higher spatial density of the foliation (e.g., a decreased spacing of C' planes, Fig. 13a and b). Similar observations were made in the work of Haines et al. (2009, 2013). The presence of water has a primary effect on the disaggregating and delaminating grain aggregates (Fig. SM4 in supplementary materials) by chemical corrosion at the crack tip and decreased toughness of intragranular bonds (i.e., *stress fatigue*, Scholz, 2019), especially in the case of phyllosilicates (e.g., decrease of friction between dry and wet Phy58 and Phy24 in Fig. 12a). The development of water overpressure at grain boundaries has also been used to explain frictional weakness in phyllosilicates gouges (Ikari et al., 2007; Haines et al., 2013; Faulkner et al., 2018). The water-saturated granular-rich gouges display less efficient comminution and a widening of the Y-B-P-R shear zones (Fig. 9 vs Fig. 10 and Fig. 13e vs f). This results in the segregation of low strain domains with remnants of the initial material (Fig. 8, Fig. 9, and Fig. 13h). The presence of water in granular-rich gouges seems to hinder the efficiency of brittle processes, such as the grain-size reduction by cataclasis and strain localization (Fig. 13g, h and Fig. 14) within the granular fraction. On the other hand, the presence of water seems to favor the comminution of the phyllosilicates fraction thus promoting the development of a phyllosilicate-enriched matrix. We propose that the phyllosilicate-enriched matrix is weaker at water-saturated conditions (see above) thus favoring its mobilization and networking (Fig. 11g and q and Fig. 14). This has the prime effect of mantling the granular fraction and hindering direct grain-grain contact and indentation, producing a damping effect (Cladouhos, 1999; Ben Zion and Sammis, 2013 and ''grain mantling'' in Fig. 14). A second effect is found in the developing of wider shear zones thickness due to increased mobility of the gouge (upper row in Fig. 14). In dry conditions the granular-rich samples experience enhanced grain size reduction, both in the low strain domains and, especially, within the bounding shear bands (Fig. 10 vs Fig. 9). These latter appear narrower and more closely spaced, (Fig. 9 vs Fig. 10 and Fig. 14g and h). Similar observations were made in the work of Scuderi et al. (2013) and Ruggieri et al. (2021).

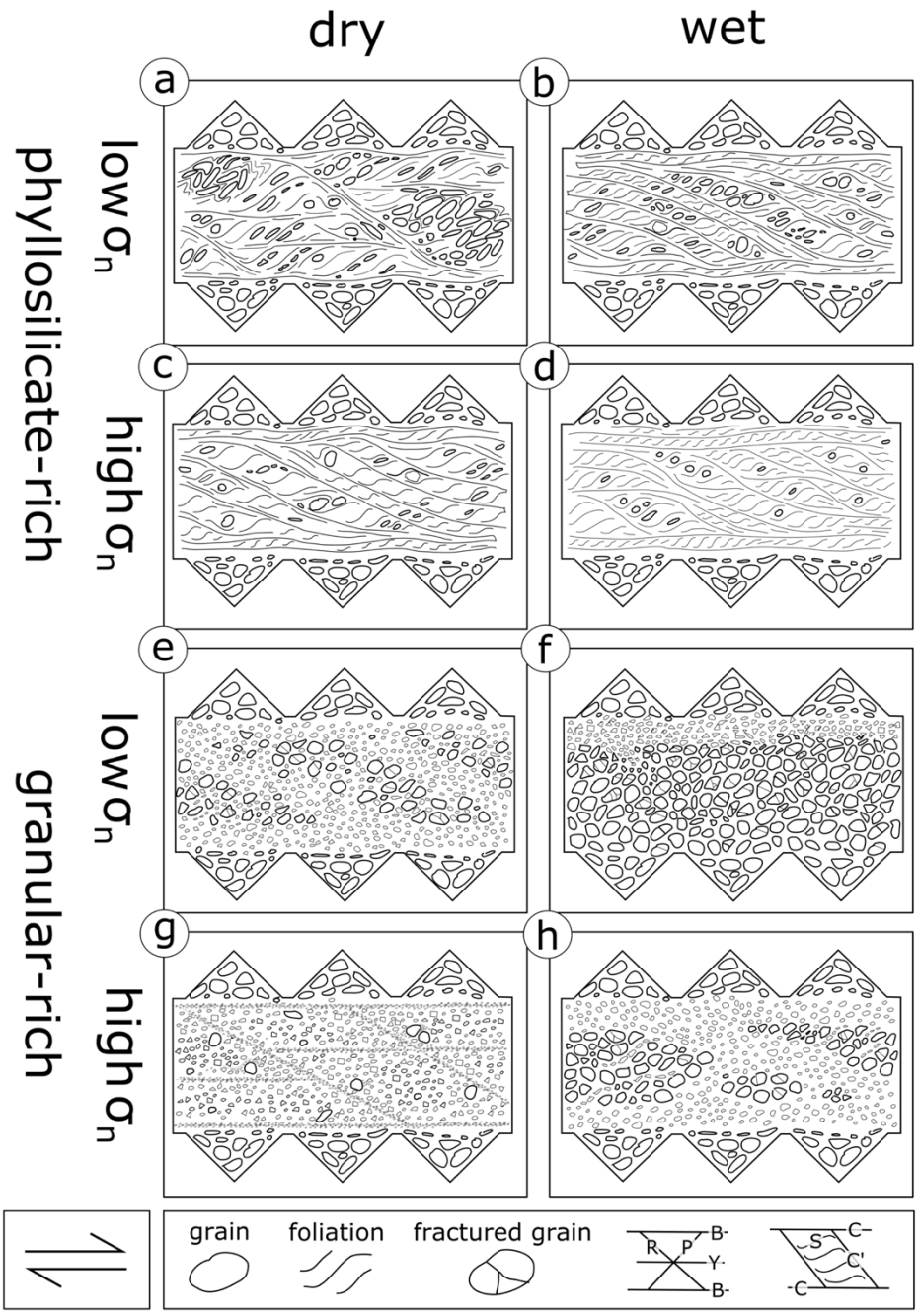


Fig. 13: schematic summary of the microstructural analysis highlighting the evolution of the fabric with normal stress, humidity, and mineralogy (phyllosilicates content). The mineralogical endmembers (i.e., Phy58 and Phy24) are taken as significant examples.

## 6.4 Mineralogy, fabric, and frictional properties

### 6.4.1 Phyllosilicate-rich gouges

The measured shear stress values of Phy46 and Phy58 plot along a straight line in a normal stress-shear stress plot according to a Coulomb criterion, thus diagnostic of deformation in a brittle frictional regime (Fig. 12a). These materials

are characterized by low values of friction ($0.30 < \mu < 0.41$) at both room dry and water-saturated conditions, as expected by their high percentage of phyllosilicates (e.g., Saffer and Marone, 2003; Tembe et al., 2010; Ikari et al., 2011; Giorgetti et al., 2015; Collettini et al., 2019). Their frictional weakness is due to preferential frictional sliding along the phyllosilicate foliae (Fig. 14), which are organized in favorably oriented planes such as those forming the C foliation (e.g., Haines et al., 2009, 2013). This mechanism also diminishes the dilatancy and the activity of cataclastic processes as evidenced by the angularity of quartz clasts (i.e., Fig. 11b, f, and l). Conversely, microstructures characterized by an irregular foliation accompanied with folding, kinking, and crenulation (Fig. 11f, I and p, and Fig. 14), can slightly increase the apparent frictional strength of the gouge (e.g., Okamoto et al., 2019). This feature explains the marked strain hardening behavior observed in the case of Phy46 (Fig. SM4 in supplementary materials). Phy46 displays a lower friction coefficient than Phy58 (Fig. 12a), which seems counterintuitive considering the inverse correlation with the content of phyllosilicates (e.g., Tembe et al., 2010; Ikari et al., 2011). An explanation can be found in the finer grain sizes of the phyllosilicates in Phy46 than in Phy58 (Fig. 4a, b), that facilitates both phyllosilicate networking and grain mantling (Fig. 11o, p and Fig. 14) favoring a reduction in frictional strength. Phyllosilicate networking and grain mantling may also hinder the contact among the granular fraction (Fig. 14), with the consequence of reducing the bulk friction (i.e., Phy58 and Phy46). The decrease of frictional strength of phyllosilicate-rich gouges in saturated conditions (Fig. 12a) stems from the lubricant role of water within the phyllosilicate foliae (Saffer and Marone, 2003; Moore and Lockner, 2004; Ikari et al., 2007; Behnsen and Faulkner, 2012). An interconnected and well-developed foliation may also decrease the permeability favoring transient local fluid pressurization, which results in fault weakening (Ikari et al., 2007; Haines et al., 2013; Faulkner et al., 2018). The healing rate, $\beta$, of the phyllosilicate-rich gouges is very low or negative and increases slightly with normal stress (Fig. 12b). The low values can be explained by the role of phyllosilicates in damping the interaction between granular materials (e.g., mantling, Fig. 14) and in promoting contact area saturation due to their platy habit (e.g., Saffer and Marone, 2003; Ikari et al., 2009; Carpenter et al., 2011, 2016; Collettini et al., 2011; Tesei et al., 2012). In the case of wet Phy58 the frictional healing is not influenced by normal stress possibly due to more regular foliation and an enhanced interconnectivity of the phyllosilicate network (i.e., Fig. 14) that promotes contact area saturation and facilitates slip upon reactivation (e.g., Saffer and Marone, 2003). Conversely, in dry Phy58 and wet Phy46, the healing rate slightly increases with normal stress (Fig. 12b). This can be attributed to a less regular foliation (e.g., Fig. 14) that either hinders a fast contact area saturation and/or promotes a stronger interaction within the granular fraction (grain mantling in Fig. 14). Phy58 and Phy46 show a strong velocity strengthening behavior with $a$-$b$ values ranging between 0.0011 and 0.0035 (Fig. 12e and Tab. 2). The velocity strengthening behavior of this gouges is well

explained by the role of phyllosilicates. They promote contact area saturation resulting in very low to negative value of the evolution effect, *b* (Fig. 12d), thus resulting in strongly positive values of *a-b* (e.g., Saffer and Marone, 2003; Ikari et al., 2009; Ruggieri et al., 2021). In the case of wet Phy58 we observe an increase of *a-b* with normal stress (Fig. 12e). This feature can be attributed to the more regular and interconnected foliation displayed by wet Phy58 (Fig. 5c and d) that enhances contact area saturation promoting low *b* values (Fig. 12d). The slight decrease of the *a-b* parameter in dry Phy58 and wet Phy46 can be related to an increase with normal stress of the evolution effect, *b*, that almost reaches the values of the granular-rich gouges at the same normal stresses (Fig. 12d). This suggests a stronger interaction between the granular fraction caused by a less regular foliation and grain mantling (Fig. 6, Fig. 11p, f and Fig. 14).

6.4.2 Granular-rich gouges

Granular-rich gouges, Phy35 and Phy24, display friction values between 0.47 and 0.56. The measured shear stresses are aligned along a straight line in a normal stress-shear stress plot, in agreement with brittle behavior (Fig. 12a). The friction higher than that of phyllosilicate-rich gouges is explained by deformation accommodated dominantly by the strong granular fraction (quartz). At these conditions is favored the development of a grain load bearing framework that deforms mainly by cataclastic processes and is subject to dilatancy-related hardening (Fig. 14, Marone and Scholz, 1989; Anthony and Marone, 2005; Mair et al., 2002; Knuth and Marone, 2007; Collettini et al., 2019; Scuderi et al., 2020). Indeed, in granular-rich samples, the main deformation mechanisms observed are fracturing and grain size reduction within localized shear bands (Fig. 8 to Fig. 10 and Fig. 14). The lower friction coefficient of Phy35 ($\mu = 0.47$) is explained by the higher amount of phyllosilicates, which form a foliated, interconnected phyllosilicate matrix within the main shear zones (e.g., R and P, Fig. 8, Fig. 11g, q, and Fig. 14). The organized phyllosilicate network favors shear along oriented weak surfaces and limits grain-to-grain contact, with the consequence of reducing the bulk friction (Fig. 11q and Fig. 14, e.g., Collettini et al., 2009; Niemeijer et al., 2010; Giorgetti et al., 2015, Tesei et al., 2018). Interconnectivity of the phyllosilicate matrix is also enhanced at increasing normal stress in both Phy24 (wet) and Phy35. The microstructures of the localized shear zones (i.e., B and R surfaces) highlight a reduction in grain size that favors the mobility and networking of the weak matrix while isolating the granular clasts (i.e., Fig. 11g and q). The result is the development of a grain mantling by the foliation (i.e., Cladouhos, 1999 and Fig. 14). At high normal stresses, the roundness of grains also contributes to reduce the friction (e.g., Biegel et al., 1989; Marone and Scholz, 1989; Mair et al., 2002; Anthony and Marone, 2005; Fig. 14). The decrease in friction of Phy24 gouges from $\mu = 0.56$ at dry conditions to $\mu = 0.51$ at water-saturated conditions (Fig. 12a) is mostly related to the lubricating effect of water on phyllosilicate

foliae. In fact, friction of pure granular materials is in general not very sensitive to the content of pore water (e.g., Frye and Marone, 2002). At room-dry conditions, the higher friction values of Phy24 relate to the less organized network of phyllosilicate matrix as well as the higher angularity of clasts (e.g., Mair et al., 2002; Anthony and Marone, 2005, Fig. 14). Granular-rich gouges (Phy35 and Phy24) display high healing rate values ranging between 0.0046 and 0.0074 (Fig. 12b). These values are concordant to the healing rate observed in gouge of similar composition (e.g., Carpenter et al., 2016) and are consistent with the increase with hold time of the contact area at the asperities (e.g., Dieterich and Kilgore, 1994; Marone, 1998). The difference in healing rate between Phy24 and Phy35 at water-saturated conditions, 0.0074 and 0.0047 respectively, is explained by the higher phyllosilicate content in Phy35, that promotes the formation of continuous foliated horizons (Fig. 11q, r and Fig. 14) facilitating slip upon reactivation. In these gouges, normal stress and water saturation seem to not affect the healing rate (Fig. 12b). Phy35 and Phy24 display a slight velocity strengthening behavior with *a-b* values around 0.0013 (Fig. 12e) concordant with gouges of similar composition (i.e., Ikari et al., 2011). The velocity strengthening behavior can be well explained by the interplay of cataclastic processes and dilation (e.g., Marone and Scholz, 1988; Scholz, 1998). Phy35 shows higher values of *a-b* than Phy24 (0.002 and 0.001 respectively). This difference can be explained by larger amount of phyllosilicates in Phy35 that are concentrated along the shear zones (Fig. 11q, r and Fig. 14). This feature favors contact area saturation resulting in a more pronounced velocity strengthening behavior (Saffer and Marone, 2003; Ikari et al., 2009; Carpenter et al., 2011, 2015; Collettini et al., 2011; Tesei et al., 2012). The opposite trend of the *a-b* values with normal stress (i.e., by increasing normal stress, dry Phy24 is more weakening whereas wet Phy24 is more strengthening, Fig. 12e) can be explained by the difference in strain localization and grain-size reduction. At higher normal stress, dry Phy24 displays a strong localization along narrow shear zones, whereas wet Phy24 shows a more distributed deformation (Fig. 9 vs Fig. 10). At lower normal stress the behavior is opposite. This microstructural evidence supports the role of strain localization in favoring the transition from rate strengthening and rate weakening behavior (Marone, 1998; Ikari et al., 2011; Scuderi et al., 2013, 2017; Bedford and Faulkner, 2021).

### 6.4.3 The influence of microstructures on frictional properties

From the previous discussions, it clearly emerges that mineralogy (phyllosilicates content) and the overall fabric architecture can explain both the first and second order frictional behavior of simulated gouges. We here provide a synoptic description of the control that texture elements exert on fault friction (Fig. 14). The foremost effect on bulk friction is exerted by the Y-B-P-R and S-C-C' fabrics, which are function of the amount of phyllosilicates (Fig. 14). Y-B-P-

R indicates cataclastic processes as principal deformation mechanism, driven by deformation accommodated mostly by the granular fraction. S-C-C' fabric is instead symptomatic of deformation accommodated principally by a phyllosilicate matrix, which means that interaction within the granular fraction is hindered. This is indeed evident by the organization of the phyllosilicates into a regular foliation (Fig. 14). Nonetheless, this dichotomy between two end-member fabrics cannot alone capture the broad spectrum of frictional behaviors of mixed phyllosilicate-granular materials as seen above. For instance, if the phyllosilicate content is relevant, S-C-C' fabric can develop within localized shear bands in Y-B-P-R fabric (e.g., Fig. 11g, q). Segregation of phyllosilicates in localized shear zones is indeed commonly reported in literature (e.g., Giorgetti et al., 2015; Ruggieri et al., 2021, and Fig. 11b, o, and q) and results in frictional weakening. Several second order effects on the frictional properties of laboratory faults are indeed associated to specific fabric elements, which are summarized in Fig. 14. An important role is played by the shape of grains (Fig. 14), where the granular fraction is the actively deforming medium. Rounder grain shape corresponds to lower frictional strength (i.e., Phy24 in Fig. 11 and Fig. 12a), which is also observed in the works of Mair and Marone (2002) and Anthony and Marone (2005). The roundness of grains is enhanced at increasing normal stress, resulting in a slight decrease of the bulk shear resistance of granular-rich gouges (e.g., Fig. SM4). The shape of grains does not seem to affect the rate and state parameters (Fig. 12). When the phyllosilicate content is high enough to produce a continuous network (e.g., Phy35 in fig. 14), we observe a moderate decrease in friction, in frictional healing rate, as well as an increase in $a$-$b$ values (Fig. 12a, b, e). Together with increasing phyllosilicate amount, networking is also promoted by increasing normal stress (enhanced grain size reduction) and water content (lubrication effects). At higher phyllosilicate content, mantling (fig. 14) of the granular fraction by oriented foliae limits the interaction of the granular fraction, contributing to the frictional weakening effect (e.g., Phy35 and Phy46 in Fig. 11 and Fig. 14). The arrangement of foliation is important: while a regular and flattened foliation (favorably oriented to the shear direction, Fig. 14) can promote a further frictional weakening (see also Haines et al., 2009, 2013; Okamoto et al., 2019), a more convoluted texture characterized by kinking and crenulation can slightly increase the fault frictional strength (Fig. 14 and Okamoto et al., 2019).

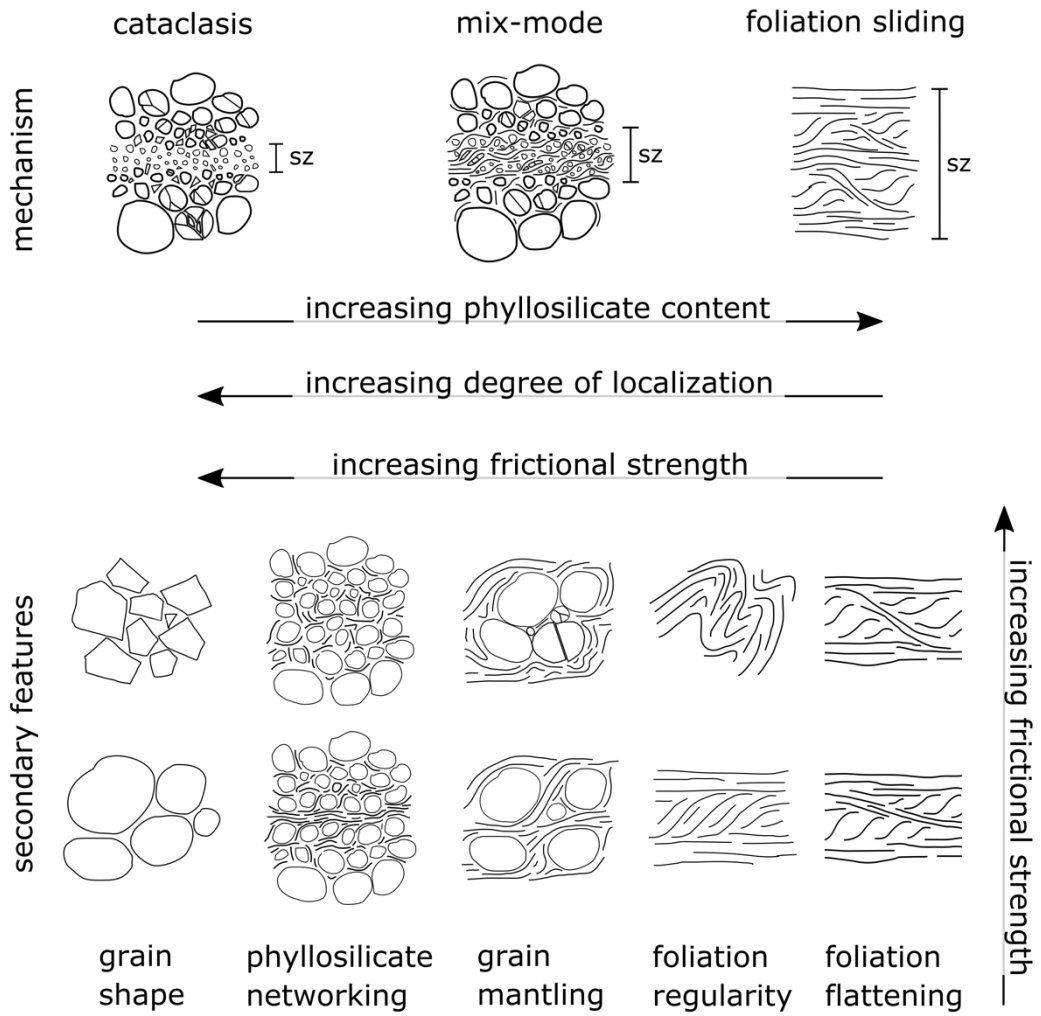


Fig. 14: schematic summary of the fabric features that link to phyllosilicates content with the frictional strength. SZ in the upper row is for shear zone thickness.

## 7 Conclusions

The integration of microstructural, mineralogical, and frictional data shows an intimate correlation between mechanical behavior and fabric for fault gouges made of phyllosilicate-granular mixtures. We recognized two distinct groups of fault architectures in our microstructures: one dominated by Y-B-P-R fabric and one by S-C-C' fabric. The Y-B-P-R fabric is associated to strong faults, where shear deformation is accommodated by cataclastic processes (i.e., fracturing, grain size reduction and frictional sliding) and strain localization, as a result of deformation controlled by the interaction of granular minerals forming a rigid load-bearing framework. This fabric is generally observed when the phyllosilicate fraction is relatively low (< 30% wt). The increase of normal stress favors lower angle P-R shear bands and enhances the distribution of deformation in the gouge layer. The presence of water decreases the effect of grain-size reduction and

promotes a widening of the shear zones. The S-C-C' fabric is instead associated to weak faults, which are characterized by frictional sliding along phyllosilicate foliae as main deformation mechanism. These faults are characterized by a pervasive foliation caused by the mechanical reorientation of the phyllosilicates foliae, which are passively flattened in favor of the shear direction. Higher normal stresses and water saturation promote similar features such as grain-size reduction, more distributed deformation, and a more regular and pervasive foliation. The Y-B-P-R and S-C-C' fabrics represent therefore two endmembers closely associated to frictionally strong and weak faults, respectively. The transition from one fabric to another is rather sharp and is mainly controlled by the critical amount of phyllosilicates and by other processes that promote the development of a network of well-oriented weak planes. We conclude that fault fabric plays a crucial role in fault rheology since it is at the base of the bulk mechanical properties. A detailed and systematic microstructural analysis can then support and strengthen the interpretation of the mechanical results in the laboratory and provide a better link with natural faults.

## 8 Acknowledgement

We thank dr. P. Scarlato for support at the INGV HP-HT laboratory, prof. M. M. Scuderi for his help in frictional analysis, prof. L. Aldega for providing the XRD analysis, dr. D. Mannetta for his help with sample preparation and dr. M. Nazzari for the support at the SEM-INGV labo- ratory. We also thank to reviewers Dr. J. Bedford and Dr. E. Tavarnelli and editor Prof. T. Takeshita for their help in improving the quality of the manuscript. This research was supported by ERC grant Nr. 259256 GLASS and Ateneo 2018 to C. Collettini.

# Chapter II

## *The role of Apennine basement in the seismic context of central Italy*

---

### Frictional controls on the seismogenic zone: insights from the Apenninic basement, Central Italy

G. Volpe [a], G. Pozzi [b], E. Carminati [a], M.R. Barchi [c], M.M. Scuderi [a], E. Tinti [a], L. Aldega [a], C. Marone [a,d], C. Collettini [a]

a: Università degli Studi di Roma, La Sapienza, Italy

b: Istituto Nazionale di Geofisica e Vulcanologia, Italy

c: Dipartimento di Fisica e Geologia, Università degli Studi di Perugia, Italy

d: Department of Geoscience, The Pennsylvania State University, USA

*Published in Earth and Planetary Science Letters*

https://doi.org/10.1016/j.epsl.2022.117444

## Abstract

Crustal seismicity is in general confined within the seismogenic layer, which is bounded at depth by processes related to the brittle-ductile transition (BDT) and in the shallow region by fault zone consolidation state and mineralogy. In the past 10-15 years, high resolution seismological and geodetic data have shown that faulting within and around the traditional seismogenic zone occurs in a large variety of slip modes. Frictional and structural heterogeneities have been invoked to explain such differences in fault slip mode and behaviour. However, an integrated and comprehensive picture remains extremely challenging because of difficulties to properly characterize fault rocks at seismogenic depths. Thus, the central-northern Apennines provide a unique opportunity because of the integration of deep-borehole stratigraphy and seismic reflection profiles with high resolution seismological data and outcrop studies. These works show that seismic sequences are limited within the sedimentary cover (depth < 9-10 km), suggesting that the underlaying basement plays a key-role in dictating the lower boundary of the seismogenic zone. Here we integrate structural data on exhumed outcrops of basement rocks with laboratory friction data to shed light on the mechanics of the Apenninic

basement. Structural data highlight heterogeneous and pervasive deformation where foliated and phyllosilicate-rich rocks surround more competent quartz-rich lenses up to hundreds of meters in thickness. Phyllosilicate horizons deform predominantly by folding and foliation-parallel frictional sliding whereas quartz-rich lenses are characterized by brittle signatures represented by extensive fracturing and minor faulting. Laboratory experiments revealed that quartz-rich lithologies have relatively high friction, $\mu \approx 0.51$, velocity-strengthening to neutral behaviour, and elevated healing rates. On the contrary, phyllosilicate-rich (muscovite and chlorite) lithologies show low friction, $0.23 < \mu < 0.31$, a marked velocity strengthening behaviour that increases with increasing sliding velocity and negligible rates of frictional healing. Our integrated approach suggests that in the Apenninic basement deformation occurs along shear zones distributed on thickness up-to several kilometers, where the frictionally stable, foliated, and phyllosilicate-rich horizons favour aseismic deformation and therefore confine the depth of major earthquake ruptures and the seismogenic zone.

## 1 Introduction

The seismogenic regime is defined by the distribution of background microearthquake activity within the upper 10-15 km of the continental crust (Sibson, 1989). The base of the seismogenic regime, or the brittle-ductile transition (hereinafter, BDT) represents a transition zone from elasto-frictional faulting along localised brittle structures to viscous shearing in thick mylonites (e.g., Sibson, 1977; Scholz 2019). In this canonical view, the base of the BDT is mainly constrained by the extrapolation of quartzite flow laws that place the transition at about 300-350 °C (Brace & Kohlstedt, 1980; Chen and Molnar 1983). Frictional arguments, building on rate and state friction, have proposed that within the seismogenic layer, earthquake nucleation is promoted by the rate-weakening behaviour induced by localization along brittle faults (Dietrich, 1979; Marone and Scholz, 1988; Beeler et al., 1996; Scholz 1998). In this framework, the seismogenic layer is confined at depth by the viscously deforming mylonites, and at shallow (1-2 km) levels by cataclastic flow at low confining pressure involving velocity strengthening and dilatancy-hardening (Scholz, 1998). However, in the last 10-15 years high-resolution seismological and geodetic data have documented a large gamut of fault slip behaviour along structures belonging to the elasto-frictional regime. For example, aseismic creep and repeating earthquakes have been documented along some segments of the San Andreas fault (Waldhauser et al., 2004) or along extensional detachments (Chiaraluce et al., 2007). Aseismic slip is sometimes prevalent over the entire depth range of the seismogenic portions of subduction megathrusts (Perfettini et al., 2010; Avouac, 2015), calling into question the simple concepts and methods used to define the seismogenic zone. Moreover, slow slip events appear to be ubiquitous on seismic faults (e.g., Jolivet and Frank, 2020) where they play an important role throughout the earthquake cycle

(Bürgmann, 2018 and references therein). Finally, accelerated creep has been recorded during hydraulic stimulations of faults (Eyre et al., 2019; Cappa et al., 2019). Several arguments have been proposed to explain the observed spectrum of fault slip behaviour. Friction laboratory experiments indicate that slow slip events arise near the threshold between stable and unstable failure and are controlled by fault frictional properties, the effective normal stress and the stiffness of the fault loading medium (e.g., Baumberger et al., 1994; Gu and Wong, 1994; Leeman et al., 2016; Scuderi et al., 2017; Mclaskey and Yamashita, 2017; Marone, 2019; Passelègue et al., 2019; Bedford and Faulkner, 2021). Works building on the integration of rheological and mechanical data indicate that structural and frictional heterogeneities are relevant for complex fault slip behavior (e.g., Tesei et al., 2014; Collettini et al., 2019; Fagereng and Beall., 2021). Although recent works have significantly improved our understanding of the beauty and complexity of fault slip behaviour, an integrated and comprehensive picture that incorporates structural and frictional aspects of the seismogenic zone remains unresolved. Here, we integrate subsurface geology and seismological data from the Apennines with structural observations and friction experiments on rocks that represent exhumed analogues of those present at seismogenic depths to propose a model in which the seismogenic zone, and confinement at depth of the major seismic sequences of the Apennines, is dictated by the frictional, rate-strengthening properties of basement rocks.

## 2. Seismicity distribution and the Apenninic basement

From the Oligocene to the present day, the central-northern Apennines have experienced two phases of eastward migrating deformation: an early compression with eastward directed thrusting and a later phase of extension (e.g., Carminati et al., 2012). Compressional tectonics is now active in the Adriatic coast and Po Plain (Carminati et al., 2012; Govoni et al., 2014; Montone and Mariucci, 2016) whereas active extension (Fig. 1a) is located along the axial zone of the Apennines (e.g., Montone and Mariucci, 2016). This seismo-tectonic setting makes the Apenninic chain one of the most seismically active area in Europe, as confirmed by four catastrophic seismic sequences since 1997: Colfiorito 1997-98, L'Aquila 2009, Emilia 2012, and Amatrice-Norcia 2016-17. In this region, 150 years of work on surface geology and stratigraphy (Centamore et al., 1986; Cresta et al., 1989), the availability of an extensive dataset of seismic reflection profiles (Bally et al., 1986; Pialli et al., 1998) and high-resolution seismic data (Chiaraluce et al., 2003; Chiaraluce et al., 2017; Improta et al., 2019; Chiarabba et al., 2009; Chiarabba et al., 2014; Waldhauser et al., 2021) allow for a unique comparison between geological and seismological data. From this comparison several common aspects have been noted: a) the mainshocks (M > 5) of all the seismic sequences nucleate within the Triassic evaporites (Mirabella et al.,

2008; Govoni et al., 2014; Baccheschi et al., 2020; Barchi et al., 2021; Buttinelli et al., 2021); b) Seismicity occurs within the sedimentary cover (Mirabella et al., 2008; Govoni et al., 2014; Barchi & Collettini, 2019; Baccheschi et al., 2020; Barchi et al., 2021), with aftershock distributions mainly confined between 1 and 10 km of depth (Chiaraluce et al., 2003; Chiaraluce et al., 2017; Chiarabba et al., 2009; Chiarabba et al., 2014); c) the base of the sedimentary cover and its contact with the basement marks the transition from seismic to aseismic deformation (Barchi et al., 2021). In the area of active Apenninic extension, the basement is present only at seismogenic depths. It has been drilled by few deep boreholes: San Donato, Pieve Santo Stefano, and Perugia wells (Bally et al., 1986; Anelli et al., 1994; Barchi et al. 1998, and Fig. 1a). In some of these boreholes, the tectonic superposition of basement slices above the Triassic Evaporites indicates that some major thrust faults are rooted at least within the shallower portion of the basement (Barchi et al., 1998; Scrocca et al., 2005). In seismic reflection profiles the basement is characterized by a set of oblique, medium to high amplitude, low-continuity reflections, contrasting with the overlying transparent facies of the Evaporites (Fig. 1c). These peculiar seismic facies have been defined as the "acoustic basement" (Bally et al., 1986; Barchi et al., 1998; Mirabella et al., 2008). The boundary between the evaporites and the basement also corresponds to an important inversion in seismic velocity, with Triassic evaporites, characterised by Vp = 6.0 - 6.3 km/s (Bally et al., 1986; Trippetta et al., 2013) and the acoustic basement with Vp at about 5.0 km/s (Bally et al., 1986; Ponziani et al., 1995; Montone & Mariucci, 2020). Some interpretations of seismic profiles suggest a basement with a thickness up to 7.5 km (Patacca et al., 2008). Since extensional tectonic migrated eastwardly with time from the Tyrrhenian Sea to Apenninic chain, extension in the Tyrrhenian islands and Tuscany has been active for enough time to change the geological and geophysical character of the area and to allow exhumation of basement rocks (Fig. 1a). Here we have studied the basement rocks corresponding to the "acoustic basement" in boreholes and seismic reflection profiles. This basement is represented by Triassic clastic deposits (Verrucano formation) that overlies low grade meta-sediments belonging to the foredeep-foreland system of the Hercinic chain, upper Palaeozoic basement (Bally et al., 1986; Lazzarotto et al., 2003; Carminati & Doglioni, 2012; and Fig. 1b). The Verrucano formation consists of two main lithologies: phyllites (Scisti Viola) and meta-conglomerates (Anageniti, Aldinucci et al., 2008; Cassinis et al., 2018). The upper Palaeozoic basement is represented by Carboniferous phyllites and quartzites of low metamorphic grade (Moretti et al., 1990; Verrucchi et al., 1994; Pandeli et al., 1994).

## 3 Materials and methods

### 3.1 Structural geology and rock sampling

We studied the Verrucano formation and the upper Palaeozoic basement in selected outcrops in the Tuscany region (Fig. 1a and Table 1). We focused on characterizing the lithological and structural heterogeneities of exhumed shear zones of the basement at the meso-scale (< km) together with the distribution of competent vs. incompetent lithologies. Representative endmember lithologies from each locality were chosen and analysed with the optical microscope (details in paragraph 4.2). From the Verrucano formation we sampled quartz-meta-conglomerates, Anageniti, and phyllites, Scisti Viola (Tongiorgi et al., 1977, Aldinucci et al., 2008) while for the upper Palaeozoic basement, quartzite and phyllites (Moretti et al., 1990).

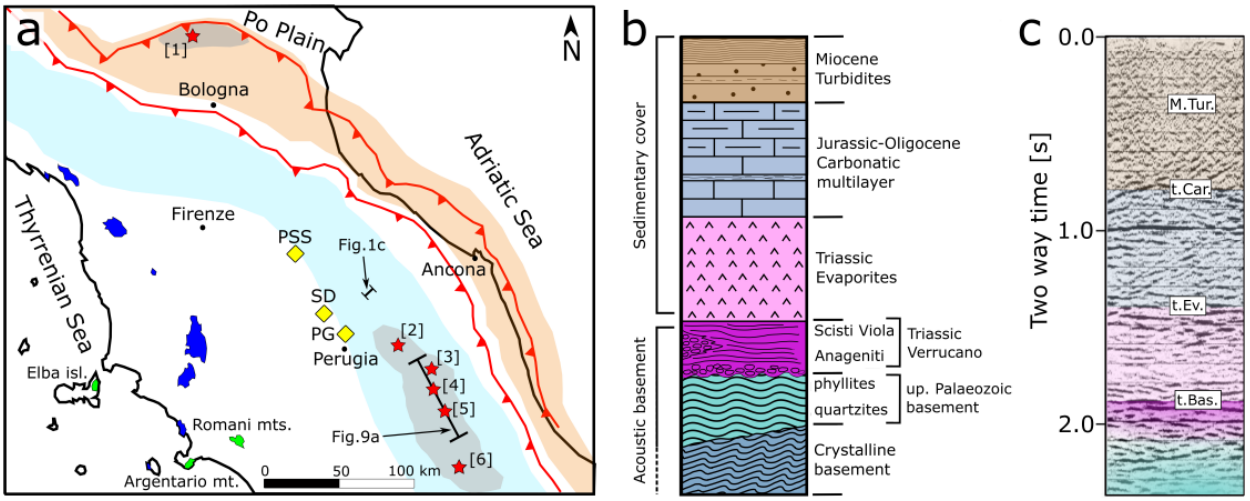


Fig. 1: a) Location map of the study area. Mainshocks (red stars: [1], Emilia 2012; [2] Colfiorito 1997; [3] Visso 2017; [4] Norcia 2017; [5] Amatrice 2017; [6] L'Aquila 2009) and aftershocks (shaded grey area) of the major seismic sequences since 1997. Yellow diamonds mark locations of deep-boreholes where acoustic basement was encountered: PSS-Pieve Santo Stefano, SD-San Donato, PG-Perugia 1. Blue and green to the west show basement outcrop locations; studied and sampled outcrops are represented in green. Black arrows indicate sections reported in Fig.1c and Fig.9a. Red lines represent major thrust faults. Active compressional (red shaded area) and active extensional (blue shaded area) areas constrained by GPS (Anderlini et al., 2016) and stress measurements (Montone and Mariucci, 2016). b) Stratigraphic column of the Umbria-Marche region consisting of Miocene turbidites, Jurassic-Oligocene carbonates and Triassic Evaporites laying above the "acoustic basement": Verrucano formation (Triassic) and upper Palaeozoic basement. c) Time-migrated seismic profile (location in panel a) approximatively corresponding to a 7.5 km thick stratigraphic column: M.Tur., Miocene turbidites; t.Car., top Jurassic-Oligocene carbonatic multilayer; t.Ev., top Triassic Evaporites; t.Bas., top acoustic basement (modified from Collettini & Barchi, 2002).

## 3.2 X-ray diffraction (XRD) analysis

The mineralogical composition of the sampled rocks was determined by XRD analysis on the same powders used for the friction experiments (grain size, $\phi < 125$ μm). The analysis was conducted using a Bruker D8 Advance X-ray system equipped with Lynxeye XE-T silicon-strip detector at the Department of Earth Sciences, Sapienza University of Rome. The instrument was operated at 40 kV and 30 mA using CuKα radiation (λ=1.5406 Å). Samples were run between 2–70° 2θ with step sizes of 0.02° 2θ while spinning the sample. Data were collected with variable slit mode to keep the irradiated area on the sample surface constant and converted to fixed slit mode for semiquantitative analysis. Semiquantitative estimation of mineral phases was performed by calculating peak areas and using mineral intensity factors as calibration constants (Moore & Reynolds, 1997).

### 3.3 Friction experiments

Friction experiments were conducted using BRAVA (Brittle Rock deformAtion Versatile Apparatus), a servo-controlled biaxial testing apparatus (Collettini et al., 2014). Experiments were performed in the Double Direct Shear configuration (DDS) consisting of three steel grooved blocks which sandwich two identical layers of gouge or intact rock wafers. Normal and shear stress are applied by fast-acting hydraulic servo-controlled rams and measured by strain gauged load-cells with an accuracy of ± 0.03 kN in a range from 0.2 kN to 1.5 MN. Stresses are obtained using the contact sample area (5 x 5 $cm^2$). The vertical and horizontal load point displacement are measured by LVDT (linear variable displacement transformers) with an accuracy of ± 0.1 μm (Collettini et al., 2014). The displacement time series were corrected for the elastic stretch of the load frame, considering that the machine stiffness is 329.50 kN/mm on the horizontal direction and 386.12 kN/mm on the vertical direction. Data were sampled at frequencies of 1 Hz to 1 kHz and recorded continuously with a 16 channel 24-bit analog to digital acquisition system (Collettini et al., 2014). Two types of experimental samples were tested: one using gouge formed from for all the sampled lithologies and another using intact wafers only for foliated lithologies (phyllites and quartzites of upper Palaeozoic basement). The gouge was produced by crushing, milling, and sieving ($\phi < 125$ μm) the sampled rocks whereas the intact wafers were obtained by cutting the sampled rocks, according with their in-situ orientation, in parallelepipeds of 5 x 5 $cm^2$ of area and 1.0 cm of thickness. The experiments were performed at room temperature and at normal stress of 25, 50, 75 and 100 MPa for gouges and 10, 25, 35 and 50 MPa for intact wafers. We report on a total of 24 experiments (details in Table 2) with several other tests done to check consistency and perform calibrations. All experiments were performed under water saturated conditions by placing the experimental assembly within a plastic membrane and submerging it with $CaCO_3$-rich water. To ensure water percolation and full sample saturation, the samples were left under a low normal load of 1 kN for 30

minutes. After sample saturation, we increased the normal stress at steps of 0.4 MPa until the target normal stress was reached. Once the sample compacted to a constant layer thickness, during the run-in, the sample was sheared for 10 mm by imposing a displacement rate of 10 μm/s. During this phase, the fault reaches a steady state shear strength (Fig. 2a). After the run-in, we performed slide-hold-slide tests consisting of a shearing phase at 10 μm/s for 500 μm of displacement, alternated with hold periods ranging from 1 to 3000 s (Fig. 2b). Finally, we performed velocity steps by shearing the sample at increasing velocity, from 0.1 to 300 μm/s (Fig. 2c). Our friction measurements include steady-state sliding friction, healing behaviour during slide-hold-slide tests, and velocity/state dependence of friction. The Rate and State friction theory (Dieterich, 1979; Ruina, 1983) is used as framework for this analysis (Fig. 2). The steady state friction coefficient (μ) was calculated as the shear stress normal stress ratio, and assuming negligible cohesion.

$$\mu_{ss} = \tau_{ss} / \sigma n \quad (1)$$

During slide-hold-slide tests, the amount of frictional healing (Δμ) was calculated as the difference between the peak friction measured upon re-shear after each hold and the pre-hold steady state friction (Marone, 1998). Frictional healing rate (β) was calculated by diving the frictional healing (Δμ) by the logarithm of the hold time, $\log_{10}(\Delta t)$.

$$\beta = \Delta\mu / \log_{10}(\Delta t). \quad (2)$$

During velocity steps test, the near-instantaneous step in sliding velocity from $V_0$ to V corresponds to an instantaneous change in friction that scales as the friction parameter $a\ln(V/V_0)$, where *a* is an empirical constant defined as the direct effect. The subsequent evolution to a new steady-state value of friction scales as the friction parameter $b\ln(V/V_0)$, where *b* is an empirical constant defined as the evolution effect (Dieterich, 1979; Ruina, 1983). The velocity dependence of friction, described by the *a*-*b* parameter, is defined as:

$$(a-b) = \Delta\mu_{ss} / \ln(V/V_0) \quad (3)$$

where $\Delta\mu_{ss}$ is the difference between the dynamic steady-state friction after and before a change in sliding velocity from $V_0$ to V (Dieterich, 1979, Ruina, 1983). Positive values of (*a*-*b*) define velocity-strengthening behaviour, indicating that aseismic creep is expected. Negative values of (*a*-*b*) define velocity-weakening behaviour, which is a condition required to develop a frictional instability (Dieterich and Kilgore, 1994; Marone 1998). The velocity steps were modelled (Fig. 2c) using the Dieterich time-dependent evolution law coupled with the RSF equation (Dieterich, 1979):

$$\mu = \mu_0 + a \ln(V/V_0) + b \ln(V\theta / Dc) \quad (4)$$

$$\delta\theta/\delta t = 1 - \theta V/Dc \quad (5)$$

Where $\mu_0$ is friction for steady-state slip at velocity $V_0$, V is the frictional slip rate and Dc is the critical slip distance needed to renew the asperities. Parameter θ, also calculated as Dc/V at steady state, represents the state variable that

describes the average lifetime of the asperities (Ruina, 1983). For modelling, these two equations are coupled with an equation that describes the elastic coupling between the frictional surface and the loading surrounding:

$$d\mu/dt = K(V_{lp}-V) \quad (6)$$

Where $V_{lp}$ is the measured loading point velocity and K is the stiffness of the loading apparatus and the assembly, normalized by the normal stress, in units of coefficient of friction per displacement (Saffer and Marone, 2003). These last three equations (eq. 4, 5 and 6) are simultaneously solved by using a fifth order Runge-Kutta numerical integration. The constitutive parameters *a*, *b*, and Dc for each velocity step, were obtained as best fit parameter values using an iterative, least squares method to solve the nonlinear inverse problem (Blanpied et al., 1998; Saffer and Marone, 2003).

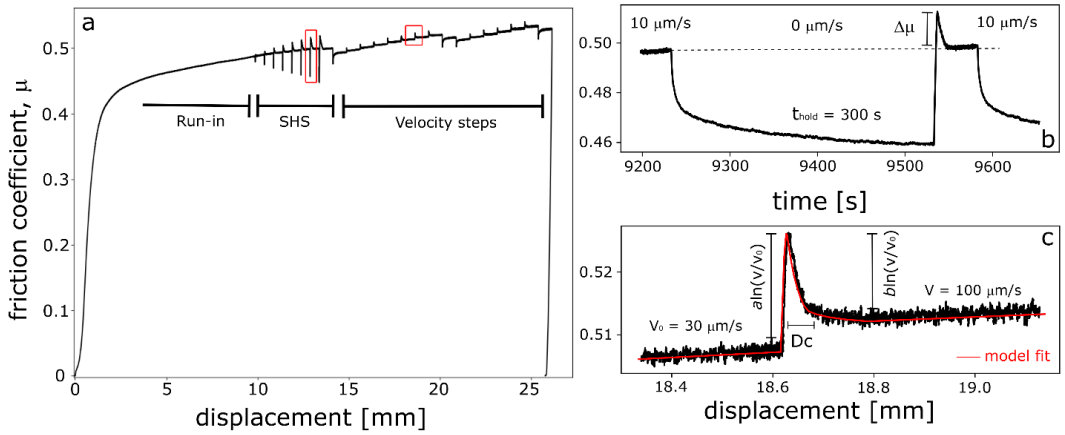


Fig. 2: a) Evolution of friction as a function of shear displacement for one complete experiment (b989). Our procedure consisted of a run-in phase followed by slide-hold-slide tests (SHS) and velocity step tests. b) Detail of a 300-s slide-hold-slide test showing evolution of friction with hold time and re-shear. c) Detail of a velocity step test from 30 to 100 s (black line) and a best-fit model using RSF (red line) (see text for details).

## 4 Results

### 4.1 Field work

One of the best exposures of the Verrucano formation, 500 m long and 250 m high, is located in Monte Argentario (Fig.1 and Fig.3). The outcrop consists of anastomosed and foliated phyllosilicate-rich rocks (Scisti Viola, Fig. 3a-c) that surround more competent quartz-rich sandstone and conglomerate lenses (Anageniti, Fig. 3b-d). The Scisti Viola are highly deformed domains characterized by phyllosilicate-rich pervasive foliation (details in paragraph 4.2) that obliterates the primary sedimentary features. In contrast to the Scisti Viola, the Anageniti are domains of lesser deformation that include places where the original sedimentary structures (e.g., stratification and pebbles imbrication)

are preserved. Within the Anageniti we observed brittle features represented by different sets of quartz veins with a maximum thickness of 10 cm, veins of Fe and Mn oxides and minor faults with displacement lower than a few meters (Fig. 3d). Similar features have been observed in the Verrucano formation in eastern Elba, but here the geometries of the structures are not very well preserved. These features are obliterated by deformation that includes distributed Fe-rich mineralization and post-orogenic magmatism (Bortolotti et al., 2001; Smith et al., 2011).

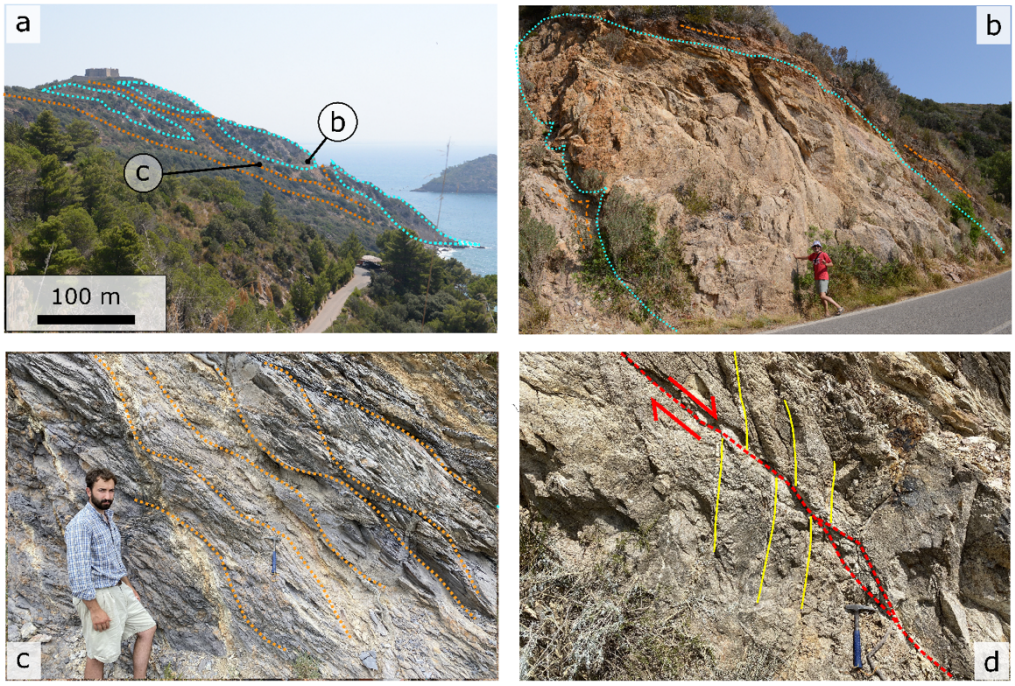


Fig. 3: Verrucano outcrops in Monte Argentario (see location in Fig. 1). a) panoramic view of the area, blue dotted lines highlight Anageniti lenses contained within the Scisti Viola matrix (foliation in brown dotted lines). b) decametric lens of Anageniti embedded with foliated Scisti Viola (brown dotted lines). c) Distributed deformation within the foliated (brown dotted line) Scisti Viola. d) Brittle fault within an Anageniti lens, yellow lines highlight subvertical quartz veins cut and displaced by the fault.

We studied the upper Palaeozoic basement primarily in the Monti Romani area (Fig. 1 and details in Moretti et al. 1990). Here, phyllites alternate with fine grained quartzites (Fig. 4a) and, in some areas quartz-rich lenses are contained within an interconnected phyllosilicate-rich foliation (Fig. 4c-d and details in paragraph 4.2). In these outcrops the quartz-rich lenses range in size from centimetres to several meters. In some cases, brittle normal faults cut and displace the foliation, in others, normal faults mark the boundaries between the foliated matrix and the competent lenses (Fig. 4a).

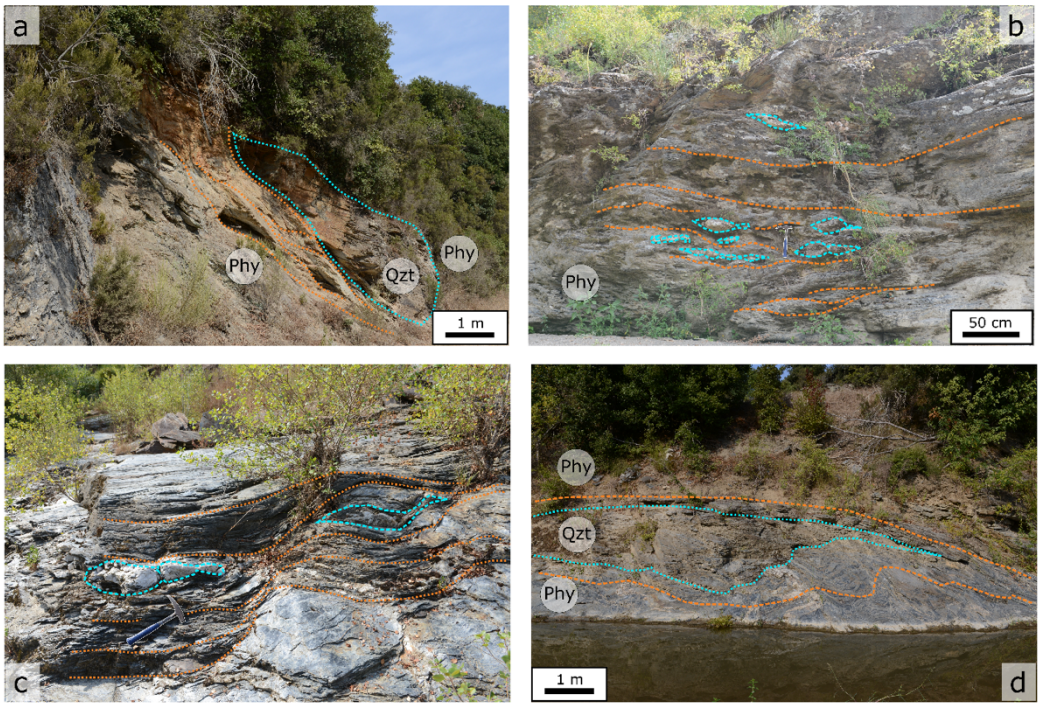


Fig. 4: Interpretation of outcrops of upper Palaeozoic basement in Monti Romani (see location in Fig. 1). a) Quartzite lens within foliated phyllite matrix. The boundary between the phyllites and the quartzites lens is marked by a distributed shear zone. b) Outcrop with the presence of strong quartz lenses surrounded by foliated phyllite matrix. c) Boudinated quartz lenses within a foliated phyllite matrix. d) Quartzite lens within phyllites foliated matrix. In circles: Phy is for phyllites, Qzt is for quartzites. Brown dashed lines marks foliation in phyllite matrix; light blue dashed lines encompass stronger quarts-rich lenses.

## 4.2 Mineralogy and microstructures

XRD analysis provides semi-quantitative mineralogical analysis of the sampled basement rocks (Tab.1). The composition is similar among the samples, which are mainly composed of quartz and phyllosilicates (muscovite and chlorite, with minor paragonite in upper Palaeozoic basement, and pyrophyllite in Anageniti). Minor mineral phases are oxides (rutile and hematite) and carbonates (calcite and dolomite).

Microstructural analysis was made on petrographic thin sections (30 µm thick) prepared by cutting the sampled rocks perpendicularly to foliation and parallel to the sense of shear. Images acquired using a petrographic microscope are reported in supplementary materials (Fig. S2). The sampled basement rocks show different microstructures that span between highly anisotropic (foliated) to isotropic (massive) textures. The Scisti Viola and upper Palaeozoic phyllites are characterized by a highly anisotropic texture due to pervasive plane-parallel foliation made of an alignment of phyllosilicate crystals that bound minor quartz microlithons (Fig. S2). Upper Palaeozoic quartzites show a schist-to-

gneissic texture made of aligned phyllosilicate seams that envelop quartz-rich lenses. Anageniti is characterized by an isotropic, grain-supported texture made of sub-rounded quartz grains (up to several centimetres in diameter) with an interstitial non-foliated phyllosilicate matrix.

| Formation | Rock | Lithology | Mineralogy | Outcrop |
|---|---|---|---|---|
| Verrucano formation | Scisti Viola | phyllites | Quartz = 37%<br>Phyllosilicates = 46%<br>Oxides = 17% | Eastern Elba Island |
| | Anageniti | meta-conglomerates | Quartz = 66%<br>Phyllosilicates = 24%<br>Carbonates = 8%<br>Oxides = 2% | Monte Argentario |
| Upper Palaeozoic basement | phyllites | phyllites | Quartz = 36%<br>Phyllosilicates = 58%<br>Oxides = 6% | Monti Romani |
| | quartzites | meta-quartzarenites | Quartz = 65%<br>Phyllosilicates = 33%<br>Oxides = 2% | Monti Romani |

Table 1: summary of lithology and mineral content of the sampled basement rocks. See Fig.1 for the location of the outcrops.

## 4.2 Mechanical results

For each lithology we have characterized frictional strength, healing rate and velocity dependence of friction (details in Table 2).

| Formation | Rock | Type | $\sigma$n | Experiment | $\mu$ss | Healing rate | *a-b* |
|---|---|---|---|---|---|---|---|
| Verrucano | Scisti Viola | gouge | 25 | b996 | 0.28 | −0.00064 | 0.0034 |
| | | | 50 | b997 | 0.28 | 0.00023 | 0.0035 |
| | | | 75 | b998 | 0.29 | 0.00044 | 0.0031 |
| | | | 100 | b999 | 0.29 | 0.00112 | 0.003 |
| | Anageniti | gouge | 25 | b1003 | 0.52 | 0.00742 | 0.0008 |
| | | | 50 | b1006 | 0.51 | 0.00674 | 0.0011 |
| | | | 75 | b1008 | 0.51 | 0.00707 | 0.0014 |
| | | | 100 | b1007 | 0.51 | 0.00682 | 0.0017 |
| Upper Palaeozoic basement | phyllites | gouge | 25 | b955 | 0.33 | 0.00142 | 0.0007 |
| | | | 50 | b973 | 0.34 | 0.00176 | 0.0022 |
| | | | 75 | b974 | 0.34 | 0.00193 | 0.0025 |
| | | | 100 | b975 | 0.32 | 0.00154 | / |
| | | wafer | 10 | b1009 | 0.27 | 0.00046 | 0.0034 |
| | | | 25 | b981 | 0.19 | 0.00091 | 0.0031 |
| | | | 35 | b1011 | 0.35 | / | / |
| | | | 50 | b985 | 0.20 | 0.00036 | 0.0026 |
| | quartzites | gouge | 25 | b987 | 0.49 | 0.00474 | 0.0022 |
| | | | 50 | b988 | 0.49 | 0.00471 | 0.0019 |
| | | | 75 | b989 | 0.48 | 0.00468 | 0.0021 |
| | | | 100 | b990 | 0.48 | 0.00485 | 0.0023 |
| | | wafer | 10 | b1004 | 0.32 | / | / |
| | | | 25 | b995 | 0.24 | 0.00149 | 0.0024 |
| | | | 35 | b1002 | 0.25 | 0.00138 | 0.0026 |
| | | | 50 | b991 | 0.27 | 0.00129 | 0.0025 |

Table 2: experimental results for the tested lithologies. ‘’/’’ symbol indicated missing data related to premature end of experiments.

### 4.2.1 Frictional strength

During the run-in phase, the powdered material (blue curves in Fig. 5) reaches steady state friction with minor strain hardening trends, mostly appreciable in the Scisti Viola at high normal stresses (Fig. 5a). For wafers (red curves in Fig. 5c-d) we observe an initial, modest strain-weakening following the peak friction. The friction displacement curves for wafers are characterized by small oscillations while the curves for gouges are relatively smooth and steady.

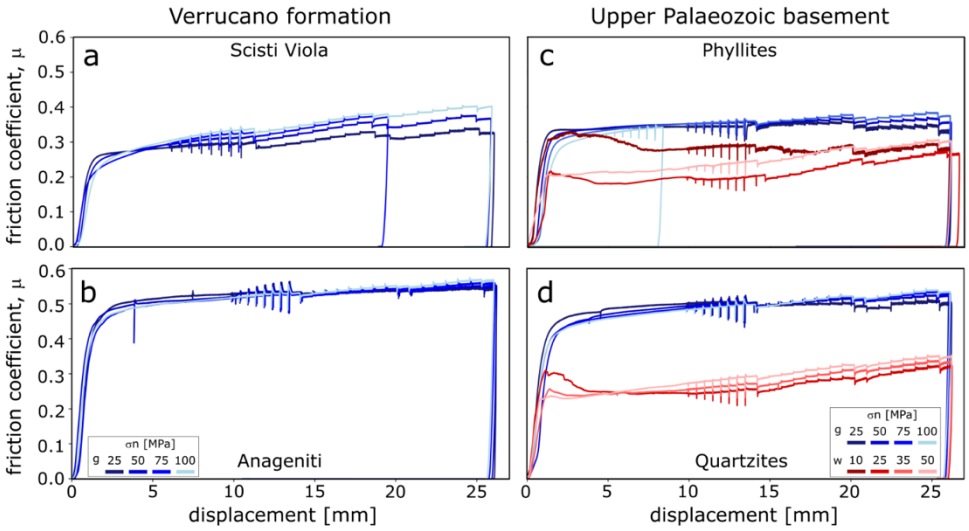


Fig. 5: friction vs displacement curves for 22 experiments: gouge (p) results are shown in blue, wafers (w) results in red. Note that strain hardening occurs initially, after which, friction reaches a steady-state value for most of the experiments. See Table 2 for experiment details.

The steady-state shear stress values for each lithology define a linear relation (Fig. 6) in agreement with Coulomb failure and cataclastic dominated processes and/or frictional sliding along phyllosilicate foliae. The steady state friction of the tested lithologies ranges between 0.19 and 0.52 (table 2). Verrucano formation shows a large range in friction between the end member lithologies: for Scisti Viola μ = 0.30 and for Anageniti μ = 0.51. Concerning the upper Palaeozoic basement, powdered samples display μ = 0.31 in phyllites and μ = 0.47 in quartzites, whereas wafers samples show lower but similar fiction values in both lithologies: 0.23 for phyllites and 0.25 for quartzites.

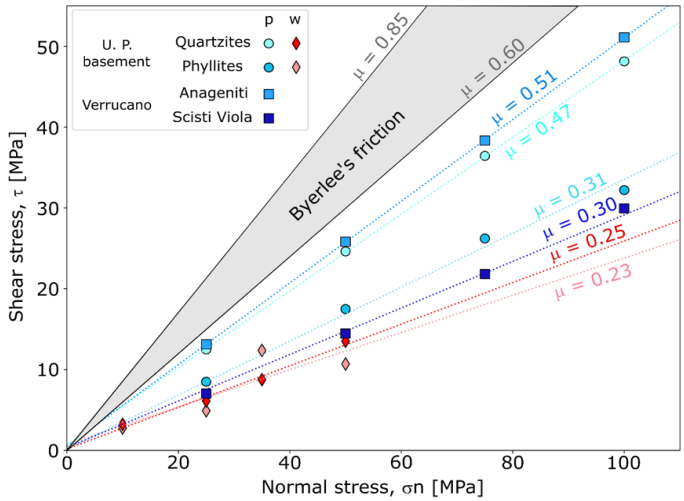


Fig. 6: Normal stress vs shear stress diagram of the tested lithologies: gouge (blues) and wafers (red diamonds). In grey the Byerlee range of friction (Byerlee, 1978). Data for both powdered and wafers plot along a linear trend in agreement with Coulomb failure and cataclastic dominated processes and/or frictional sliding along phyllosilicate foliae.

### 4.2.2 Healing properties

Frictional restrengthening (Δμ) shows different behaviour depending on the lithologies as well as the sample type (gouge and wafer). Within the Verrucano formation, Scisti Viola samples are characterized by small Δμ values that slightly increase with increasing hold time and normal stress (Fig. 7a). All the experiments conducted on Anageniti display a high healing rate that slightly decreases with normal stress (β = 0.0074 at 25 MPa and β = 0.0068 at 100 MPa, Fig. 7b). Within the upper Palaeozoic basement quartzite gouges have the highest values of Δμ which increase with hold time and slightly decrease with applied normal stress, maintaining an almost constant healing rate (β = 0.0047, Fig. 7d). The wafers of this lithology show lower values of frictional restrengthening resulting in lower healing rates (β = 0.0014, Fig. 7d). The phyllites of the upper Palaeozoic basement are characterized by low healing rates: β = 0.0015 and β = 0.0005 for gouges and wafers, respectively (Fig. 7c).

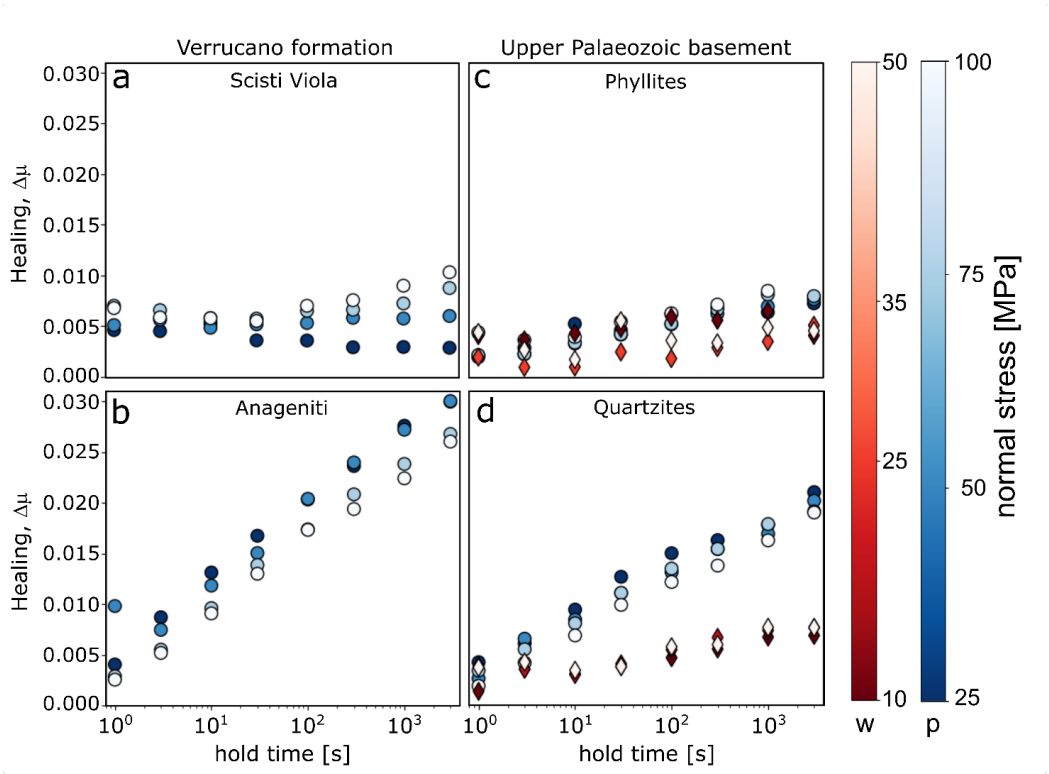


Fig. 7: Frictional healing, Δμ, as function of hold time and applied normal stress: Triassic Verrucano left column, upper Palaeozoic basement right column. Circles for gouge (p) and diamonds for wafers (w). Note that the quartz dominated lithologies (Anageniti and Quartzites gouge) have the higher slopes, i.e., higher healing rates (details are reported in table 2).

### 4.2.3 Velocity dependence of friction

The velocity dependence of friction for the Verrucano formation is strongly controlled by lithology. Scisti Viola gouges have the strongest velocity strengthening behaviour with *a-b* values that increase with increasing sliding velocities, i.e.,

*a-b* evolves from 0.002 to 0.004 (Fig. 8a). The Anageniti gouges show the lowest value of *a-b* around 0.0002, with a reduction in *a-b* values with decreasing normal stress (Fig. 8b). Gouges and wafers of the upper Palaeozoic phyllites and quartzites (Fig. 8c-d) are characterized by a velocity strengthening behaviour that increases with increasing sliding velocities. A few slightly negative *a-b* values were documented for phyllite gouges at 25 MPa of normal stress and shearing velocities in the range of 10-100 µm/s (Fig. 8c).

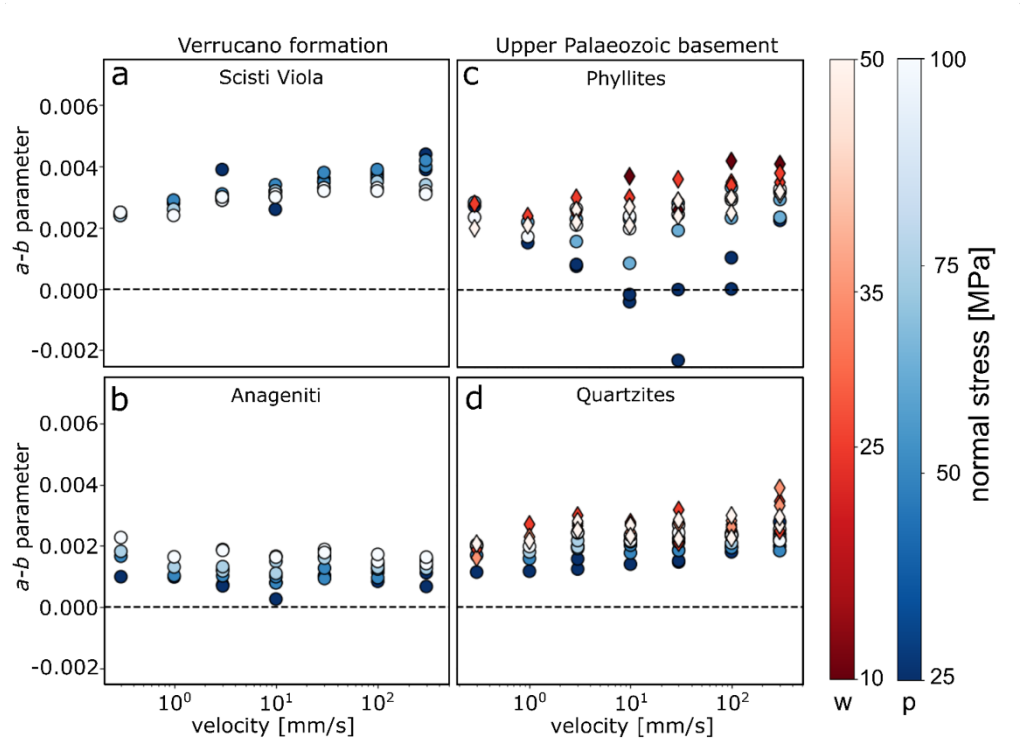


Fig. 8: velocity dependence of friction, *a-b*, for the tested rocks: Triassic Verrucano left column, upper Palaeozoic basement right column. Circles for gouges (p) and diamonds for wafers (w). All the materials are characterized by a velocity strengthening behaviour (positive *a-b*). Wafers samples show the largest velocity strengthening behaviour that increases with increasing sliding velocity. Velocity strengthening decreases for Anageniti at lower normal stresses.

## 5 Discussion

### 5.1 Mineralogy, fabric, and mechanical data

The integration of mineralogical and mechanical data highlights key aspects of two main rock types with different mechanical behaviour within the Apenninic basement: I) phyllosilicate-rich rocks represented by Scisti Viola and upper Palaeozoic phyllites characterized by 46% and 58% of muscovite and chlorite respectively; and II) quartz-rich rocks with about 65% of quartz, and minor phyllosilicates (i.e., Anageniti and quartzites, details in Table 1). The phyllosilicate-rich lithologies are characterized by low friction, $\mu \approx 0.3$ (Fig. 6), very low healing rates ($-0.0006 < \beta < 0.0017$, Fig.7) and a

marked velocity strengthening behaviour that increases with increasing sliding velocity (Fig. 8a-c). This behaviour is well-explained by the large amount of phyllosilicates contained within the phyllites and Scisti Viola that, during deformation, promotes the development of an interconnected networks of phyllosilicates (Fig. 3c and Ruggieri et al. 2021) Frictional sliding along the phyllosilicate foliae favours low friction (e.g., Saffer and Marone, 2003; Moore & Lockner, 2004; Tembe et al., 2010; Ikari et al., 2011; Collettini et al., 2019), while the platy habit of the phyllosilicate affects the low healing and the marked velocity strengthening behaviour. This has been interpreted as a saturation of contact area for weak phyllosilicates at normal stresses above ~ 25 MPa and for longer hold periods and lower slip velocity (Saffer and Marone, 2003; Ikari et al., 2009; Carpenter et al., 2011; Collettini et al., 2011; Tesei et al., 2012). We suggest that this observation is the result of a transition from phyllosilicate-dominated behaviour at low normal stress to a more pronounced quartz grains contact interaction, with some growth in contact area of quartz grains promoting the observed increase of $\beta$.

The quartz-dominated rocks of the Verrucano, and upper Palaeozoic basement show a relatively high friction coefficient $\mu \approx 0.5$ (Fig. 6), high healing rates ($0.0047 < \beta < 0.0076$, Fig. 7b-d) and a velocity strengthening behaviour that, for Anageniti evolves into a velocity neutral behaviour with decreasing normal stress (Fig. 8b). Here the mechanical data are mainly controlled by the large amount of quartz contained within these rocks. Cataclastic deformation with grain-size reduction and dilation well explains the high friction and the velocity strengthening behaviour (e.g., Marone and Scholz, 1988; Scholz, 1998), whereas the high healing rates is consistent with the increase of grain contact junctions with hold time (e.g., Dieterich and Kilgore, 1994; Marone, 1998). With increasing normal stress, we observe a reduction in frictional healing (Fig. 7b) and a more pronounced velocity strengthening behaviour (Fig. 8b). We interpret this as an increase in contact area saturation, either promoted by a quick saturation of quartz grain contacts at higher normal stresses (e.g., Ruggieri et al., 2021) and/or phyllosilicate enrichment within the shear zones.

Mechanical tests on wafers have been conducted only for foliated rock of the upper Palaeozoic basement. Despite the significant differences in phyllosilicates content, (i.e., 58% for phyllites and 33% for quartzites), their mechanical behaviour is very similar, and it is also similar to phyllosilicate-rich powdered samples (e.g., Fig. 6). In particular, friction is low, $0.23 < \mu < 0.25$, healing rate is close to zero ($0.0003 < \beta < 0.0014$), and a marked rate-strengthening behaviour is observed (Fig. 8c-d). In addition, the comparison of powdered vs. foliated quartzites shows completely different frictional properties, although mineralogical composition is the same. This result agrees with previous works showing that weakness of the foliated fault rocks is due to the reactivation of pre-existing phyllosilicate-rich surfaces that are absent in the powders (e.g., Collettini et al., 2009; Niemeijer et al., 2010). This observation emphasizes the role of fabric in frictional properties of phyllosilicate-rich rocks.

## 5.2 Structural and frictional properties of the basement and seismicity cut-off

Although the role of basement in the seismicity cut-off has been observed for the Colfiorito 1997 (Mirabella et al., 2008), L'Aquila 2009 (Baccheschi et al., 2020) and Emilia 2012 (Govoni et al., 2014) seismic sequences, the 2016-2017 Central Italy sequence is the best example to capture insights on fault rheology via the comparison between seismological, geological, and experimental mechanical data. For this seismic sequence, comprehensive seismological catalogues, based on machine learning techniques are available (e.g., Tan et al., 2021) and subsurface geology is constrained by seismic profiles and borehole data (Porreca et al., 2018; Barchi et al., 2021; Buttinelli et al., 2021). The sequence is characterized by three major earthquakes, the Mw 6.0 Amatrice event on 24$^{th}$ August 2016, the Mw 5.9 Visso event on 26$^{th}$ October and the Mw 6.5 Norcia event on 30$^{th}$ October. These events occurred on SW-dipping normal faults and details on fault geometry and kinematics can be found in the literature (Chiaraluce et al., 2017; Improta et al., 2019; Michele et al., 2020; Tan et al.,2021; Waldhauser et al., 2021). Along a crustal section that is parallel to the strike (147°, see trace in Fig.1a) of the Norcia, Mw 6.5, mainshock (Chiaraluce et al., 2017), the aftershock distribution is mainly confined at depth < 9-10 km (Fig. 9). In addition, co-seismic fault slip distribution (Chiaraluce et al., 2017; Scognamiglio et al., 2018), shows that all the slip along the faults hosting the mainshocks is confined within the first 10 km of depth. At depth greater than 6 km, i.e., below the mainshock nucleation, the seismicity is concentrated on 2-4 km thick, sub-horizontal and imbricated bands (Fig. 9a). Different interpretations have been proposed for this basal seismicity. On the grounds of aftershock geometry and extensional focal mechanisms, Chiaraluce et al., (2017) interpret this seismicity as a basal extensional shear zone that in some places is fragmented (Waldhauser et al., 2021). From the imbrication of the basal seismicity bands, Improta et al., (2019) suggested a reactivation of previously developed compressional structures that root into the basement. Here, building on the observation that the bottom of the basal seismicity coincides with the top of the basement (Fig. 9), we propose that this seismicity cut-off is mainly controlled by the basement rheology. Significant insights into the rheology of the basement can be obtained from the geological and mechanical investigations reported in this paper. The studied outcrops of the Verrucano formation and upper Palaeozoic basement rock schematically consist of interconnected networks of foliated and phyllosilicate-rich horizons (the Scisti Viola in the Verrucano and the phyllites in the upper Palaeozoic basement) that surround more competent quartz-rich lithologies (Anageniti in Verrucano and quartzites in the upper Palaeozoic basement). Due to their interconnectivity (Fig. 9c), the phyllosilicate-rich horizons control the rheology of the basement. These rocks are characterized by low friction, very low or null healing rates, and a marked rate strengthening behaviour (Fig. 9e). These data define the basement as a

several kilometres thick, weak layer, which accommodates deformation predominantly by aseismic creep. In other words, the basement is a good horizon for a frictionally controlled seismicity cut-off. The seismicity, above the phyllitic basement is well explained, on the other hand, by the frictional properties of the carbonates-anhydrites rich faults hosted within the sedimentary cover (high-friction, velocity neutral-weakening behaviour and high healing rates; Scuderi et al., 2013; Carpenter et al., 2014; Scuderi et al., 2020). Our results suggest that the documented seismicity cut-off is frictionally controlled and does not correspond to the canonical brittle-ductile transition, BDT, i.e., a transition zone where the deformation switches from frictional faulting along brittle structures to viscous shearing in thick mylonites once achieved a temperature of about 300-350 °C (Brace & Kohlstedt, 1980; Wallis et al., 2015). Firstly, the maximum depth of the background microseismicity, which defines the base of the seismogenic regime (e.g., Sibson, 1989; Scholz, 2019) or the canonical BDT, is located at 14-15 km in this portion of the Apennines (Chiaraluce et al., 2017). Secondly, a new heat flow map built on the temperature data from 174 boreholes poses the modelled BDT at depths between 15-20 km (Pauselli et al., 2019). Thirdly, frictional sliding of muscovite-rich phyllosilicates is favoured up to temperatures as high as 600 °C (Den Hartog et al., 2013). These temperatures are significantly higher than the 200 °C expected at 10 km depth in the active portion of the Apennines (Pauselli et al., 2019), indicating that brittle frictional sliding is the main deformation mechanism for basement rocks at these depths. Finally, the seismicity cut-off is not planar (Fig. 9a-b), as it should be for a temperature-controlled cut-off, but it rather mimics the basal geometry of the major thrusts of the area that are imbricated and root into the basement (Fig. 9a and Barchi et al., 2021). Following the Norcia 30$^{th}$ October mainshock, an increment of diffuse microseismicity is observed within the basement (Fig. 9a-b). A possible explanation for that is found in the structural and frictional heterogeneous nature of the basement. Within the basement we have documented the presence of quartz-rich lenses, with size ranging from centimetres to hundreds of meters (e.g., Fig. 9c, 3 and 4), showing brittle structures such as faults with small displacement and veins (Fig. 3). These rocks are characterized by relatively high friction, high healing rates, and a velocity strengthening/neutral behaviour. The quartz-rich lenses are therefore strong and competent objects interspersed within the weak foliated phyllosilicate-rich matrix (Fig. 9c). Lithological heterogeneity promotes differences in strain rate and finite strain magnitude (e.g., Goodwin and Tikoff, 2002) with local strain rate gradients that induce amplified shear stresses in the competent lenses (Beal and Fagereng 2019). During tectonic loading, shear strain-rate increase can result in amplified shear stresses along the competent lenses and trigger a dynamic instability also in a slightly velocity strengthening/neutral material (e.g., Boatwright and Cocco, 1996) like those represented by quartz-rich lenses hosted within the basement. Therefore, we interpret that the deep microseismicity following the Norcia mainshock (Fig. 9b) originates from these competent

lenses, which deform in response to the post-seismic increase of shear strain rate. The seismicity located within the basement is mainly characterized by M < 2.0 earthquakes (Fig. 9a) with a few events in the range 2.0 < M < 4.0. The 0 < M < 2.0 events represent ruptures with dimensions ranging from 10 to about 300 m (Sibson, 1989) that is the same scale of the competent lenses observed in the field (Fig. 9c-d). The few larger ruptures can be explained via the interaction of several competent lenses forming force chains that are activated simultaneously (e.g., Beal and Fagereng 2019) or by basement portions with rheology not entirely dominated by phyllosilicates.

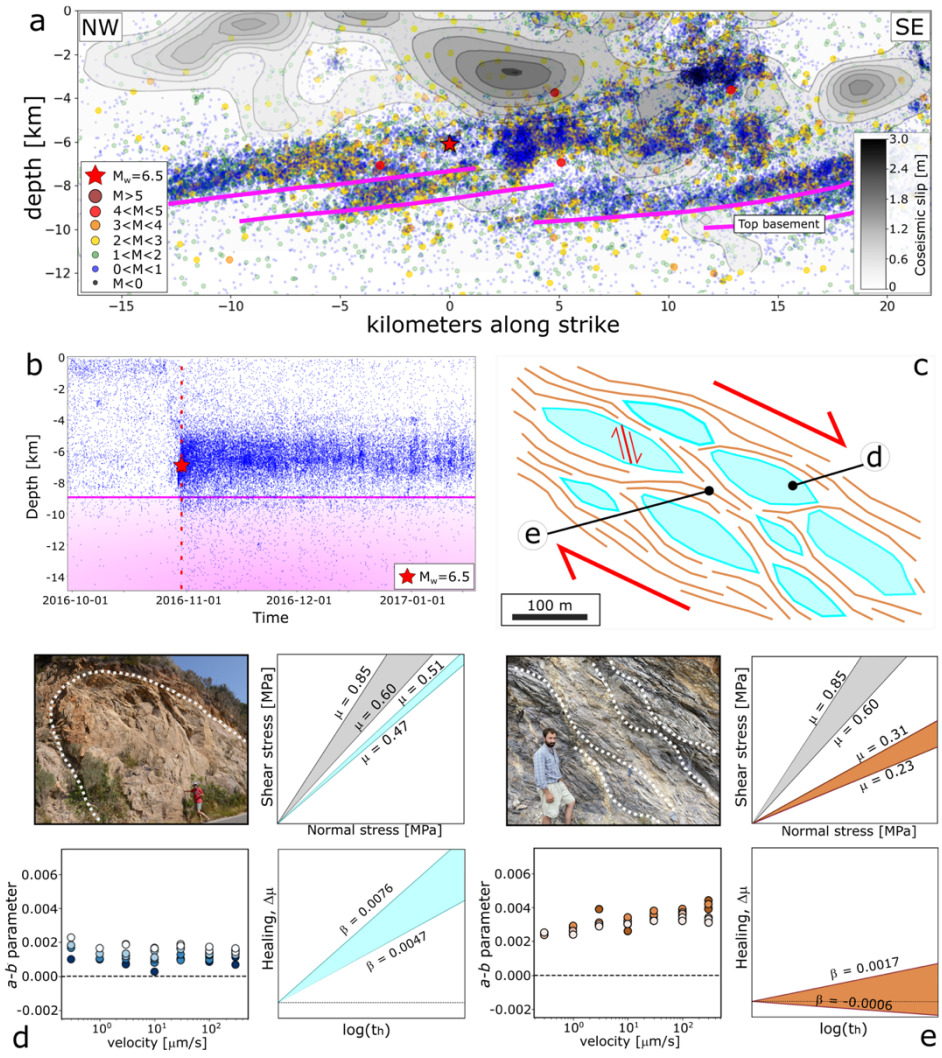


Fig. 9: The road to integration for the role of basement in the seismicity cut-off of the Apennines. a) vertical cross section (see trace in Fig.1a) parallel to the strike of Norcia, Mw = 6.5 mainshock, integrating seismicity recorded in the 20 days following the mainshock (Tan et al., 2021): all events within 2 km from the cross-section vertical plane are shown. In-depth geometry of the basement (purple lines) is reconstructed on the grounds of seismic profiles and borehole data (Barchi et al., 2021). Co-seismic slip is in grey scale (Scognamiglio et al., 2018 and Chiaraluce et al., 2017). b) Depth-time seismicity distribution in proximity of the Norcia mainshock (red star and dotted line) along the same longitudinal section presented in panel a. The purple line indicates the average depth of the

basement. c) Schematic representation for a basement shear zone: this reconstruction is based on the geological interpretation of figure 3a, and details reported in panel d and e. Quartz-rich lenses in light blue and structural and mechanical details in panel d. Interconnected phyllosilicate-rich horizons in brown and structural and mechanical details in panel e.

## 6 Conclusions

In the active region of the Apennines, the integration of seismic reflection profiles with high resolution seismological data show that the strongest seismic sequences are confined within the sedimentary cover. For the Amatrice-Norcia 2016 seismic sequence the integration of geophysical data highlights a seismicity cut-off at 9-10 km of depth in correspondence of the top of the basement that shows several steps produced during the Pliocene compressional tectonic phase. Outcrops of exhumed basement rocks schematically consists of structural and mechanical heterogeneous zones of distributed deformation along interconnected phyllosilicate-rich horizons surrounding quartz-rich lenses up to hundred meters thick. Due to their interconnectivity, the rheology of the basement is controlled by the phyllosilicate-rich horizons. These rocks show low friction, $0.23 < \mu < 0.31$, very low or null healing rates, $-0.0006 < \beta < 0.0017$, and marked rate strengthening behaviour. The integration of field and laboratory data depicts the basement as a several kilometre thick, weak layer, which accommodates deformation predominantly by aseismic creep, hence representing a good horizon for a frictionally controlled seismicity cut-off. Following the mainshock, the increase of seismic activity at higher depths (i.e., within the basement) is interpreted as the brittle reactivation of quartz-rich competent lenses following post-mainshock shear strain rate increase. The integration of subsurface geology and seismological data with structural observations and friction experiments on rocks that represent exhumed analogues of those present at seismogenic depths depict a model in which the depth of the seismogenic zone is dictated by the frictional, rate-strengthening properties of basement rocks.

## 7 Acknowledgement

We thank T. Tesei for discussions regarding this work and N. Bigaroni for assistance during experimental procedures. We also thank dr. P. Scarlato for support at the INGV HP-HT laboratory, dr. D. Mannetta for his help with sample preparation. This research was supported by ERC grant Nr. 259256 GLASS and Ateneo 2018 to C. Collettini and ERC grant TECTONIC Nr. 835012 to C. Marone.

# Rheological heterogeneities at the roots of the seismogenic zone

**G. Volpe**[a], G. Pozzi[b], M.E. Locchi[a], E. Tinti[a,b], M.M. Scuderi[a], C. Marone[a,c], C. Collettini[a,b]

a: Dipartimento di Scienze della Terra, La Sapienza Università di Roma, Rome, Italy.

b: Istituto Nazionale di Geofisica e Vulcanologia, Rome, Italy.

c: Department of Geoscience, The Pennsylvania State University, USA.

*Published in Geology*

https://doi.org/10.1130/G51432.1

## Abstract

Although rheological heterogeneities are invoked to explain differences in fault slip behavior, case studies where an interdisciplinary approach is adopted to capture their specific role are still rare. In this work we integrate geophysical, geological, and laboratory data to explain how rheological heterogeneities influence the earthquake activity at the roots of the seismogenic zone. During the 2016–2017 Central Italy sequence, following the major earthquakes, we observe a deepening of seismicity within the basement associated to a transient stress change. Part of this seismicity is organized in clusters of events, with similar size and waveforms. The structural study of exhumed basement rocks highlights a heterogeneous fabric made of strong, quartz-rich lenses (up to 200 meters) surrounded by a weak, interconnected phyllosilicate-rich matrix. Laboratory experiments simulating the mainshock-induced increase of loading-rate show that the matrix lithology experiences an accelerating and self-decelerating aseismic creep, whereas the lens lithology show dynamic instabilities. Our results suggest that the post-mainshock loading-rate increase favors accelerated creep within the matrix, which promotes, as consequence, seismic instabilities within the lenses in the form of clustered seismicity. Our findings emphasize the strong connection between seismicity and the structural and frictional properties of the seismogenic zone.

## 1 Introduction

Geological investigations on exhumed faults and shear zones define heterogenous fault structures (e.g., Fagereng and Sibson, 2010) ranging from localized deformation on one or more discrete planes to distributed deformation within thick shear zones. A common view is that shear localization results from cataclastic processes affecting granular fault rocks, whereas phyllosilicate-rich rocks, promotes the development of thick and distributed shear zones (e.g., Faulkner

*et al.*, 2010; Collettini *et al.*, 2019). The structural heterogeneities described along exhumed faults are strongly connected to frictional heterogeneities. Localized deformation commonly correlates with high friction, $\mu \sim 0.6$, high healing rates, and a rate-weakening behavior (Ikari *et al.*, 2011; Collettini *et al.*, 2019). For these reasons fault patches with localized deformation are considered strong (high friction), locked (high healing rates) and potentially unstable (rate weakening). On the other hand, distributed frictional sliding along thick phyllosilicate-rich shear zones results in low friction, $0.1 < \mu < 0.3$, low healing rates, and rate-strengthening behavior and thus these fault patches are typically weak, favoring stable creep (Ikari *et al.*, 2011; Lockner *et al.,* 2011; Collettini *et al.*, 2019). 30 years of high-resolution earthquake detection and location have highlighted distinctive features of seismicity that seem to be connected to geological and frictional heterogeneities. Along plate boundary faults or subduction zones, small earthquakes with identical waveforms have been interpreted as repeated ruptures originating from the same fault patch (Nadeau *et al.*, 1994; Igarashi *et al.*, 2003; Uchida and Burgmann, 2019). The recurrence time of repeaters as function of loading-rate suggests that repeaters nucleate from discrete structures representing small and locked fault patches (i.e., asperities) loaded by the surrounding fault creep (Uchida and Burgmann, 2019; Waldhauser *et al.*, 2021). Along intracontinental faults, low loading-rates do not allow for long-term (decades) characterization of repeaters. Here, it appears that the activity of repeaters is isolated to shorter intervals, less than 1 month and can be related to special conditions such as changes in the loading-rate preceding and following large mainshocks or transients of high fluid pressure (Chiaraluce *et al.,* 2007; Vuan *et al.*, 2017; Uchida and Burgmann, 2019; Essing and Poli, 2022). Loading by large mainshocks can also promote a transient deepening of the base of the seismogenic zone (Ellis and Stockhert, 2004; Cheng and Ben-Zion, 2019). This provides useful insights on the stress state of the overlying seismogenic zone. Although field, laboratory and seismological observations can provide a coherent picture of how fault heterogeneities may influence slip behavior (Fagereng and Sibson, 2010; Uchida and Burgmann, 2019; Fagereng and Beall, 2021; Bedford *et al.,* 2022), this picture remains fuzzy because case studies where complementary observations are integrated are still rare. Here, we address this gap by studying the 2016-2017 Central Italy seismic sequence. We show that clustered aftershock activity at the base of the seismogenic zone is promoted by the increased loading-rates induced by mainshocks within otherwise creeping rock volumes.

## 2 Results

### 2.1 Seismicity within the basement

The 2016-2017, Central Italy seismic sequence started on 24 August 2016 with the Amatrice $M_w$=6.0 earthquake (Fig. 1A). This first mainshock was followed by other two large earthquakes: the $M_w$=5.9 Visso and $M_w$=6.5 Norcia earthquakes on 26 and 30 October, respectively. On 18 January 2017 the $M_w$=5.5 Campotosto earthquake (the largest of four events with $M_w$>5.0) occurred on the SE portion of the sequence (Fig. 1A). The seismic sequence activated a NW-SE trending, 80-km long normal fault system. The base of the seismogenic zone (defined as the depth above which the 95% of seismicity occurs e.g., Sibson, 1989; Magistrale, 2002) is located at ~9km of depth, where seismic reflection profiles mark the top of the acoustic basement (Barchi *et al.*, 2021; Volpe et al., 2022a). Within the seismogenic zone, seismicity is localized on SW-dipping normal faults hosting the mainshocks (e.g., Chiaraluce *et al.*, 2017) and distributed on imbricated bands located between 5-9 km of depth (SM2). These bands have been variously interpreted: as extensional detachment (Waldhauser *et al.,* 2021), reactivated ancient thrusts (Improta *et al.,* 2019), or distributed deformation favored by a ductile-brittle rheology (Collettini *et al.*, 2022). Below the seismogenic zone, the rheology of the basement is controlled by the rate-strengthening nature of phyllosilicate-rich rocks, promoting a frictionally controlled seismicity cutoff (Volpe *et al.*, 2022a, SM2) and providing key information to understand the deformation processes at play at the roots of the seismogenic zone. To gain insight into the deformation processes of the basement, we analyze the evolution in space and time of the basement seismicity building on a high-resolution seismic catalogue spanning a 1-year period (Tan *et al.* 2021). We observe in the basement an abrupt increase of seismicity rate (Fig. 1B) immediately after the mainshocks ($M_w$ > 5.5). Then, the seismicity rate decreases to a sequence background level. Part of the basement seismicity (15 %) is organized in 625 small clusters (Fig. 1C) that we highlighted via a spatial-temporal clustering algorithm (SM3) and analyzed in space and time. While most clusters are sparse, some are instead organized along east-dipping sub-parallel structures (SM2). All clusters are characterized by earthquakes of small magnitude (0 < $M_w$ < 3.5), with mode of $M_w$=1.1 (Fig. 2A), corresponding to an average rupture radius < 400 m (Fig. 2B), with a mode ~35 m. The clusters show a short-term activity (< 13 days) with variation of the seismicity rate through time (Fig. 2C). The largest events are homogeneously distributed in time without any correlation with the mainshocks (Fig. 2D) consistently with a swarm-like evolution (Vidale and Shearer, 2006). To further explore cluster seismicity, we studied the waveform similarity of earthquakes within each of 125 randomly selected clusters. This was performed by cross-correlation coefficient (ccc) analysis over long windows, capturing the entire wave train: from the P-wave arrival to 2 seconds after the S-wave arrival (SM4 and SM5). The mode of the cumulative distribution of all components ranges between 0.8 and 0.9 (Fig. 2E) and ~72% of the clusters are characterized by more than 2 events with ccc > 0.9. Most of the analyzed clusters consist of more than 4 spatially separated events, occurring in a short time window, and with

partially overlapping source regions (Fig. 2F). These data suggest that the Apenninic basement is structurally complex and composed of small asperities that host swarm-like (i.e., burst-type) earthquakes when subject to mainshock-induced stress increases (Fig. 1B, C).

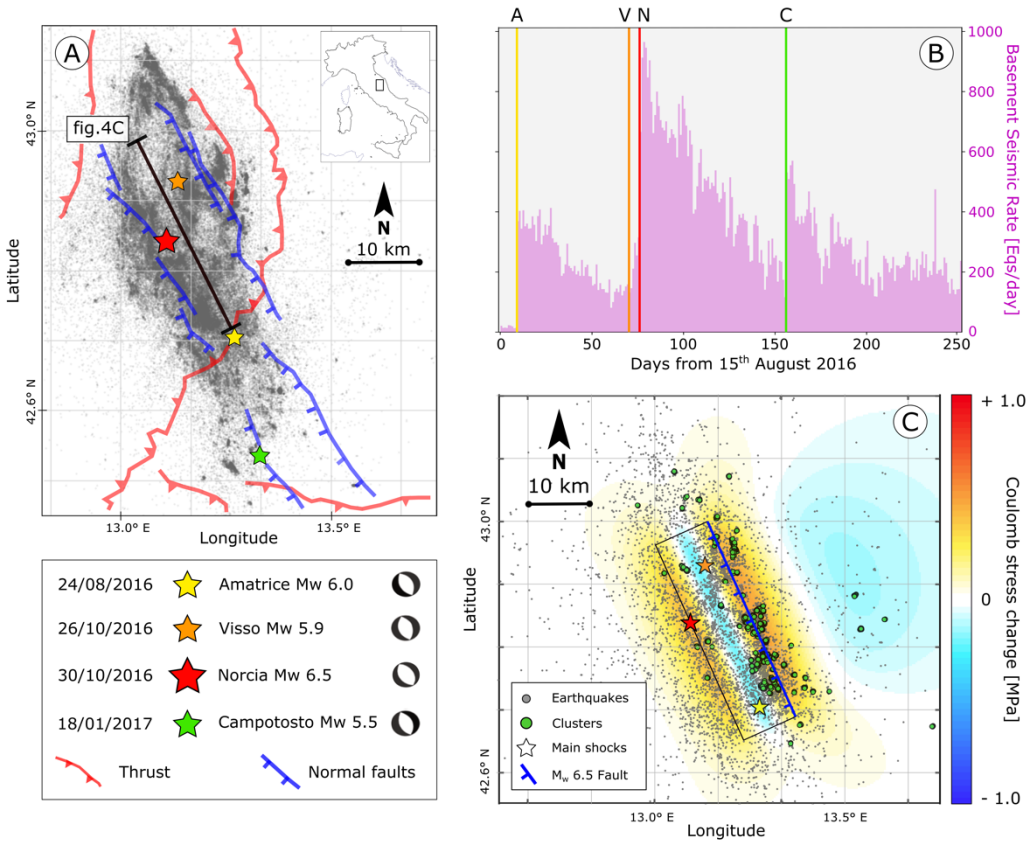


Figure 1: A) map distribution of earthquakes during the Central-Italy 2016-2017 seismic sequence (Tan *et al.*, 2021). Stars highlight mainshocks epicenters. Lines show traces of the major regional faults. B) Evolution of the basement seismic rate (depth > 9 km) during the sequence. Vertical lines mark the occurrence of the mainshocks: A, Amatrice; V, Visso; N, Norcia; C, Campotosto. C) Plan view at a depth of 10 km showing Coulomb stress change (Supplemental material, SM1) and aftershocks (from 10 to 11 km) of the Norcia mainshock within 30 days. The black rectangle is the Norcia mainshock fault-box.

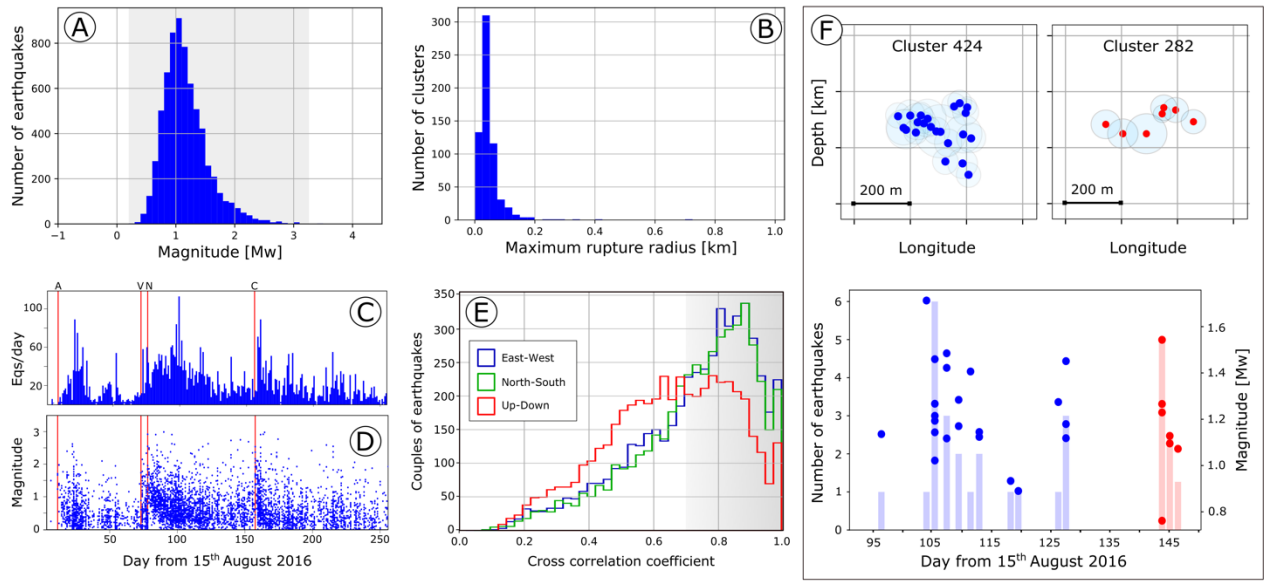


Figure 2: A) Magnitude distribution of clustered events; B) distribution of the maximum rupture radius for each cluster considering a stress drop of 3 MPa (e.g., Kanamori and Anderson, 1975); C) daily evolution of the clusters seismic rate; D) daily evolution of the magnitude of the clustered events, E) cross-correlation coefficient distributions for each seismogram component; F) cross-sections of two clusters (upper panel) with associated rupture radius, number of earthquakes, and magnitude distribution in time (lower panel).

## 2.2 Basement structures and frictional properties

Details on the geology of the basement are provided from both deep boreholes within the seismically active area of the Apennines (Pialli *et al.*, 1998) and geological outcrops (Volpe *et al.*, 2022a; Giuntoli and Viola, 2022). Basement fabric can be described as an interconnected matrix (Fig. 3A, B) of highly deformed and foliated phyllosilicate-rich rocks (Fig. 3A) that envelopes hundred-meter-wide lenses made of quartz-rich rocks (Fig. 3A, B) and populated by veins and faults.

The phyllosilicate-rich rocks have low friction coefficient ($\mu = 0.28$), low healing rate ($\beta = 0.0002$), and rate strengthening behavior (a-b = 0.0034, and Volpe *et al.*, 2022a). These rocks are thus weak horizons that can easily creep at the low loading-rates of the central Apennines (3 mm/y, Anderlini *et al.,* 2016). The quartz-rich lenses have higher friction ($\mu = 0.50$), high healing rates ($\beta = 0.0069$), and nearly rate-neutral behavior (a-b = 0.001, and Volpe *et al.*, 2022a); therefore, they represent asperities within the basement. We posit that, following the mainshocks, the transient stress increase within the basement (Fig. 1C) produces complex slip behavior controlled by the basement geometry and its frictional properties. To assess this behavior, we performed a suite of laboratory experiments simulating the post-mainshock stressing rate increase (details in SM6). We tested both phyllosilicate-rich matrix and quartz-rich lenses using 3 shear-

stressing rate protocols (Fig. 3E, F). We started from a stress level at 80% of the steady state frictional strength ($\tau_{ss}$, the stress required to reactivate the fault) and we increased stepwise the stress while monitoring the fault slip behavior (Fig. 3C, D). When the shear stress is below $\tau_{ss}$ (Fig. 3) the experimental fault is stable and deforms at creeping velocities of tens of nm/s (Fig. 3C, D). When the shear stress reaches $\tau_{ss}$ we observe different styles of fault reactivation depending on the rock-type. The phyllosilicate-rich matrix gently accelerates to v ~ 1 µm/s and then self-decelerates (Fig. 3C). Conversely, the quartz-rich lenses abruptly accelerate to slip velocities higher than mm/s (Fig. 3D). Our results suggest that a transient stress increase can result in creep acceleration for both materials, but only the quartz-rich lenses evolve into an earthquake-like instability.

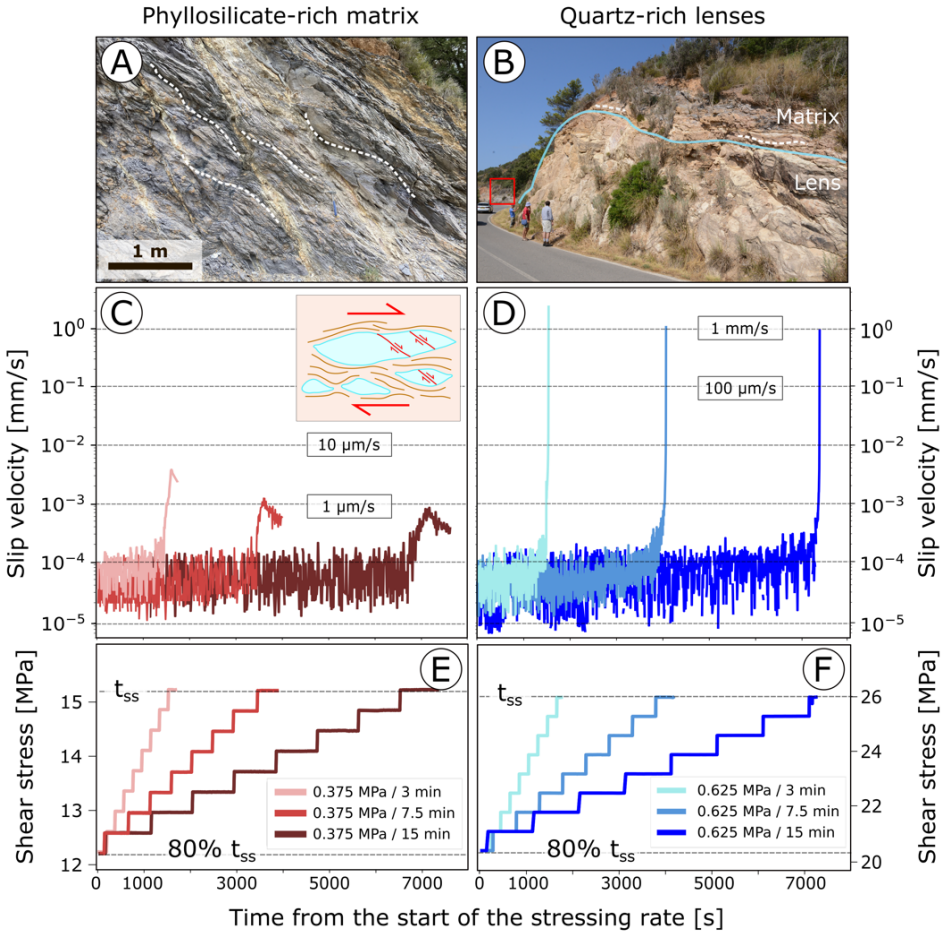


Figure 3: the upper row shows photos of exhumed basement rocks in the mt. Argentario (Tuscany, Italy); A) highly deformed matrix characterized by pervasive foliation marked by dashed white lines (location in red box in panel B). B) contact between strong lens and foliated matrix (cyan line); C) and D) evolution of slip velocity versus time for phyllosilicate-rich matrix (C) and quartz-rich lenses (D) for three loading-rate protocols, represented in (E) and (F), respectively. The mineralogy is given in SM7.

## 3 Discussion and Conclusion

Our data provide an integrated view (Fig. 4) on the style of deformation at the roots of the seismogenic zone during the Central Italy 2016-2017 seismic sequence. Following the mainshocks, the seismicity significantly increases within the basement (Fig. 1). About 15% of the basement seismicity is organized in small clusters that occur in crustal volumes loaded by the mainshocks (Fig. 1C). The remaining seismicity is homogeneously distributed and can be due to several factors including small lenses, earthquakes occurring within the matrix or within small inherited faults. Clusters are generally characterized by short-term activity (< 13 days), low average magnitudes ($M_w$ ~ 1.1), and they consist of events with partial overlapping source regions (Fig. 2). Outcrops of basement lithologies (Fig. 3), representing exhumed analogues of rocks where clustering activity occurs, show pervasive and distributed deformation along interconnected and phyllosilicate-rich networks (matrix) that surround quartz-rich lenses (hundreds of meters wide) with fractures and localized faults. Laboratory friction experiments with variable loading-rates show that the phyllosilicate-rich rocks deform by an accelerating and self-decelerating aseismic creep, whereas the quartz-rich rocks reactivate via dynamic instabilities. Our findings provide insights on the mechanisms that control the deepening of the seismogenic zone (e.g., Sibson, 1989; Cheng and Ben-Zion, 2019). The base of the seismogenic zone is generally linked to the brittle-ductile transition (BDT, Brace and Kohlstedt, 1980; Sibson, 1989), and in this view, the BDT divides an upper crust characterized by brittle and seismogenic faults, from a lower crust where deformation is accommodated aseismically by viscous shearing in thick quartz-rich mylonites at temperature > 300°C (Brace and Kohlstedt, 1980). In central Apennines, rheological models building on heat flow data locate the BDT at about 15 km of depth for quartz-rich lithologies (Pauselli *et al.*, 2019). However, during the 2016-2017 Central Italy seismic sequence, a marked seismicity cut-off occurs at ~9km of depth, in correspondence of the phyllitic basement (Fig. 4C, SM2 and Volpe *et al.*, 2022a). Following the mainshocks we observe a deepening of the base of the seismogenic regime, with an increase of the seismicity rate within the basement (Fig. 1A, Fig. 4C and SM8). We posit that this transient deepening is related to the polyphasic frictional rheology of the basement rocks. Following the mainshocks ($M_w$>5.5) an increase of loading-rate (Fig. 1B) causes accelerating and self-decelerating aseismic creep in the weak phyllosilicate-rich matrix (Fig. 4A, B; Ellis and Stockhert, 2004). The accelerated creep of the matrix transiently increases the stress at the edges and within the quartz-rich lenses. Small faults contained within single or neighboring lenses can thus reactivate, producing small cluster activity (Fig. 4A, D). In this interpretation, the post-mainshocks transient deepening of seismicity within the basement (Fig. 1B and Fig. 4C) results from a frictional aseismic-to-seismic transition within a rheological heterogeneous deformation zone (e.g.,

Fagereng and Beall, 2021) rather than strain-rate induced ductile-to-brittle switch (Sibson, 1989; Cheng and Ben-Zion, 2019). On a larger scale the mainshock-induced stress change causes in the whole basement an aftershock sequence that decays inversely with time (Fig. 1B, C). The following stressing rate change causes a long-term response in the matrix (e.g., Toda *et al.*, 2002; Ellis and Stockhert, 2004), which induces the observed burst-type activity of the clusters (Fig. 2C). The long-term accelerated creep within the phyllosilicate-rich basement is supported by InSAR data and geodetic models highlighting tens of cm of afterslip in the months following the Norcia mainshock at 10 km of depth (Pousse-Beltran *et al.*, 2020; Mandler *et al.*, 2021). These observations, together with the occurrence of basement seismicity in a large volume and in a relatively short time (Fig. 1C), suggest that this seismicity is consistent with stress transfer processes modulated by the phyllosilicates-rich matrix. Our analysis highlights the fundamental role of structural and frictional heterogeneities in modulating the seismicity at the roots of the seismogenic zone. These results provide complementary and supporting evidence to the seismological observation of clusters of repeating earthquakes, which are interpreted as the result of rupture of discrete structures loaded by surrounding fault creep (Nadeau *et al.*, 1994; Igarashi *et al.*, 2003; Waldhauser and Ellsworth, 2004; Avouac, 2015; Uchida and Burgmann, 2019).

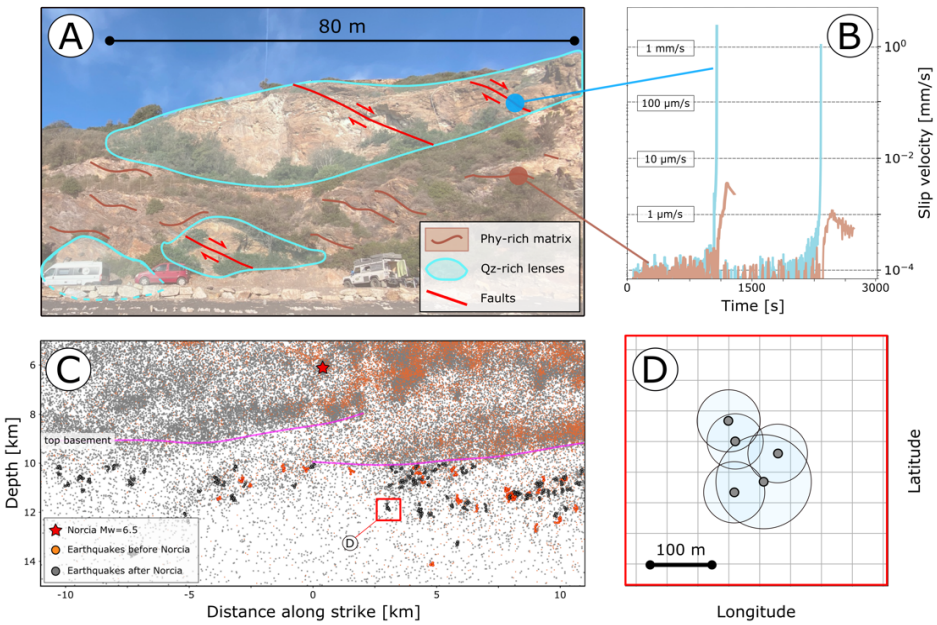


Figure 4: the road to integration. A) geological interpretation of a selected outcrop of exhumed basement rocks (Elba Island). B) experimental results showing different styles of reactivation between matrix (aseismic) and lenses (seismic). C) geological cross section (trace of the section in Fig. 1A) showing seismicity recorded 50 days before (orange dots) and after (grey dots) the Norcia $M_w$=6.5 mainshock. Represented earthquakes are within 5 km from the cross-section. Clusters are highlighted in darker colors. D) plan-view of a selected cluster highlighting earthquakes with partial overlapping rupture area.

## 4 Acknowledgement

We thank M.R. Barchi and E. Carminati for fruitful discussions regarding the basement structures. This research was supported by European Research Council (ERC) grant 259256 GLASS and DPC to C. Collettini and ERC grant TECTONIC 835012 to C. Marone. Funding for G. Pozzi is provided by ERC grant FEAR 856559.

# Chapter III

# *The role of clay-rich sediments in the seismicity of shallow subduction zones*

---

## Frictional instabilities in clay illuminate the origin of slow earthquakes

**G. Volpe**[a], C. Collettini[a,b], J. Taddeucci[b], C. Marone[a,c], G. Pozzi[b]

a: Dipartimento di Scienze della Terra, La Sapienza Università di Roma, Rome, Italy.

b: Istituto Nazionale di Geofisica e Vulcanologia, Rome, Italy.

c: Department of Geoscience, The Pennsylvania State University, USA.

*Submitted*

### Abstract

The shallowest regions of subduction megathrusts mainly deform aseismically, but they can sporadically host slow-slip events and tsunami earthquakes, thus representing a severe seismic hazard. However, the mechanisms behind these phenomena remain enigmatic because the frictional properties of shallow subduction zones, usually rich in clay, do not allow for earthquake slip according to standard friction theory. Here, we present new experimental data showing that clay-rich faults with bulk rate-strengthening behavior and null healing-rate, typically associated only with aseismic creep, can contemporaneously creep and nucleate slow-slip events. Our experiments document slow ruptures occurring within thin shear zones, driven by structural and stress heterogeneities developed on the experimental faults. We propose that bulk rate-strengthening frictional behavior promotes long-term aseismic creep whereas localized frictional shear allows slow rupture nucleation and quasi-dynamic propagation typical of rate-weakening behavior. Our results provide a new understanding of fault friction and illustrate the complex behavior of clay-rich faults, providing a new paradigm for interpretation of the spectrum of fault slip modes including slow-slip events and tsunami earthquakes.

### 1 Introduction

Subduction zones accommodate deformation in a wide spectrum of fault slip motion: from aseismic creep to the quasi-dynamic transients of tremor and slow earthquakes, to the full-dynamic ruptures of regular earthquakes (Ide et al., 2007; Peng and Gomberg, 2010; Lay et al., 2012; Burgmann, 2018). In contrast to regular earthquakes, which represent dynamic failure of locked faults, slow earthquakes represent quasi-dynamic fault slip along weakly coupled subduction interfaces (Ide et al., 2007; Peng and Gomberg, 2010; Lay et al., 2012; Scholz, 2019). Slow earthquakes are characterized by low stress drops, long rupture duration, and low rupture velocity resulting in depleted high-frequency seismic radiation (Polet and Kanamori, 2000; Ide et al., 2007; Peng and Gomberg, 2010; Lay, 2015; Scholz, 2019). Although slow earthquakes have been extensively studied on the deeper portion of subduction zones (depth < 50 km, Rogers and Dragert, 2003; Lay et al., 2012; Burgmann, 2018), recent investigations reveal their occurrence along the shallowest portion of subduction zones (depth < 15 km) and thus above the seismogenic zone (Peng and Gomberg, 2010; Lay et al., 2012; Saffer and Wallace 2015). Within the family of shallow slow earthquakes, tsunami earthquakes (Kanamori, 1972) represent a severe seismic hazard because they nucleate up-dip of the seismogenic zone and propagate up to the trench generating unusually large tsunami for their magnitudes, i.e., $M_w$<8 (Kanamori and Kikuchi, 1993; Bilke and Lay, 2002; Lay et al., 2012; Lay, 2015; Scholz, 2019). Significant tsunami earthquakes include the 1947 Hikurangi event (Bell et al., 2014), the 1992 Nicaragua earthquake (Kanamori and Kikuchi, 1993), the 1994 and 2006 Java earthquakes (Bilek and Engdahl, 2007), and the 2010 Mentawai earthquake (Lay, 2015), many of which occurred in seismic gaps or in regions of low earthquake potential (Bilek and Engdahl, 2007; Lay et al., 2012; Lay, 2015). The shallow regions of subduction megathrusts are characterized by weak seismic coupling (Saffer and Wallace, 2016; Scholz, 2019; Wallace, 2020; Shreedharan et al., 2023) where unconsolidated clay-rich sediments are the most abundant mineral phase (Vrolijk, 1990; von Huene and Scholl, 1991). The low rigidity of the clay-rich sediments has been invoked to explain the anomalously slow rupture process of slow earthquakes (Kanamori and Kikuchi, 1993; Bilek and Lay, 2002; Ito and Obara, 2006; Lay et al., 2012; Wallace, 2020). The low frictional strength together with low healing rate of clay-rich fault rocks, assessed by laboratory experiments (Saffer and Marone, 2003; Ikari et al., 2011; Ikari and Saffer, 2011; DenHartog et al., 2013; Okamoto et al., 2018; Shreedharan et al., 2023), support the inferred frictional weakness and limited seismic coupling of these subduction interfaces (Saffer and Wallace, 2016; Scholz, 2019). However, the dominant rate-strengthening behavior of clay-rich fault rocks cannot explain slow earthquake nucleation (Marone and Saffer, 2003; Ikari et al., 2011; DenHartog et al., 2013; Okamoto et al., 2018). In some laboratory experiments conducted on clay-rich fault rocks a transitional from rate-strengthening to rate-weakening frictional behavior with decreasing loading velocities was observed (Ikari and Kopf, 2017) and invoked as a potential mechanism to explain slow earthquakes

nucleation (Saffer and Wallace, 2015). Recent works show that ultralow healing rates on weak faults can influence nucleation and recurrence-time of slow slip events (e.g., Shreedharan et al., 2023). While these observations suggest the possibility for earthquake nucleation within clay-rich faults, they do not provide a comprehensive characterization of the coexistence of slow slips on continuously creeping faults. Therefore, the underlying processes are still elusive. Here, by integrating together friction experiments, microstructural analysis, and an innovative video documentation of laboratory slow earthquakes, we provide an explanation for this peculiar behavior pointing to differences between bulk and local properties of the fault zone.

## 2 Results

To assess the seismogenic potential of materials relevant for the shallowest regions of subduction zones we tested pure montmorillonite (SM1), a clay mineral abundant in the sediments of several foredeep settings: e.g., Java, Costa Rica, Hikurangi, Nankai (Vrolijk, 1990; von Huene and Scholl, 1991). We performed experiments at room temperature, 100% relative humidity, and normal stresses ($\sigma_N$) ranging from 5 to 100 MPa using the double direct shear (DDS) geometry (Fig. 1, Methods and SM2). We measured shear strength (Fig. 1a), the velocity dependence of friction (Fig. 1b), the healing rate (Fig. SM3), and the fault slip behavior at low sliding velocity (<0.1 µm/s, Fig. 1c, d and Methods). The velocity dependence of friction, expressed with the *(a-b)* parameter (rate and state friction, RSF), defines the potential for unstable slip while the healing rate is a measure of frictional strength recovery during times when faults are locks or sliding slowly (Dieterich, 1979; Ruina, 1983; Marone, 1998). In agreement with previous work (Saffer and Marone, 2003), we found that montmorillonite obeys the Coulomb shear failure law at low normal stress, with a linear frictional envelope up to $\sigma_N$ = 25 MPa and friction coefficient µ = 0.26 whereas for $\sigma_N$ >25 MPa, the shear resistance of montmorillonite is independent of normal stress, indicating a transition from frictional to ductile deformation (Fig. 1a), with a shear resistance ~6 MPa. We measured *(a-b)* during velocity steps tests from 0.1 µm/s up to 300 µm/s and found rate-strengthening behavior with positive values of *(a-b)* (Fig. 1b and SM4). At loading velocities of 0.1 µm/s we observed slow slip events in the form of stick-slip motion with shear stress drops of tens of kPa (Fig. 1c). The emergence of slip instabilities is controlled by both applied normal stress and loading velocity: the montmorillonite is unstable only at normal stresses between 5 and 50 MPa (Fig. 1c) and loading velocities lower than 0.3 µm/s. The largest stress drops are found at $\sigma_N$ = 12.5 MPa whereas at higher and lower $\sigma_N$, the stress drops are smaller (Fig. 1c). The healing rates we measured in slide-hold-slide test are zero for all normal stress tested (Fig. SM3). Overall, we document a transition from frictional to ductile rheology (Fig. 1a) with frictional properties pointing to permanent fault weakness and continuous

aseismic creep (Fig. 1b), punctuated by small instabilities (Fig. 1c, d). The occurrence of frictional instabilities in a rate-strengthening material is of considerable interest and requires an extensive analysis. Therefore, in the following we firstly document fault fabric characterizing frictional and ductile rheology and then we explore the dynamics of such frictional instabilities. Microstructural analysis of experimentally deformed samples shows that the inner geometry of the experimental fault changes as a function of normal stress (Fig. 1e, f). At low normal stress (Fig. 1e), deformation is restricted to a thin zone (< 100 µm thick) that develops parallel to the shear direction and localized along one side of the fault zone (Fig. 1e, g). The material in the shear zone is foliated (S-C fabric), with montmorillonite lamellae oriented favorably to the shear direction (Fig. 1g). Outside, the material appears undeformed and preserves the original vermicular shape of montmorillonite aggregates (Fig. 1h). At higher normal stresses deformation is less localized and involves a thicker shear zone (Fig. SM5). At $\sigma_N$ = 100 MPa deformation is indeed distributed through the whole sample layer, which shows a pervasive and regular foliation (Fig. 1f, I and, l).

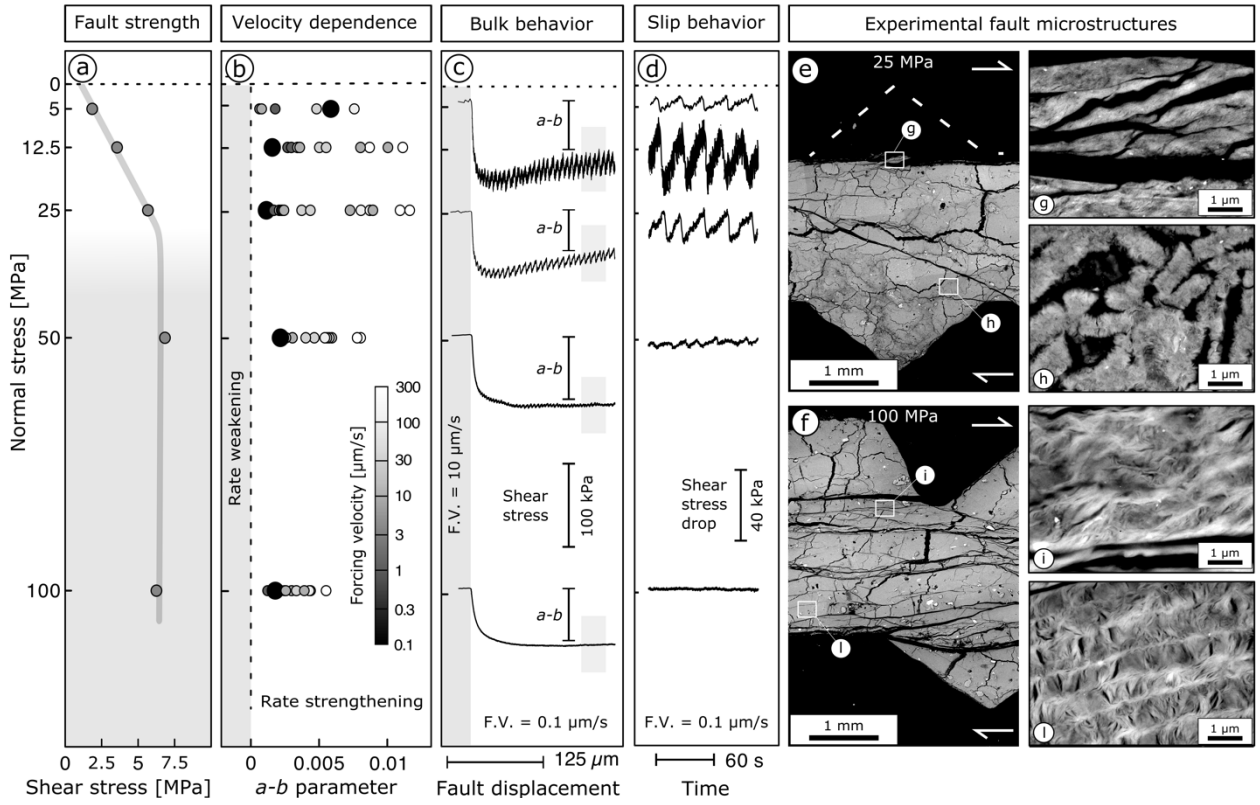


Figure 1: evolution of mechanical data and fault microstructures with normal stress. a) envelope of the steady-state shear stress showing a transition from frictional to ductile above $\sigma_N$ = 50 MPa. b) velocity dependence of friction (*a-b* parameter) in function of load point velocity (color bar in the lower-right corner). c) evolution of the shear stress during a velocity step from 10 µm/s to 0.1 µm/s where velocity strengthening trend is observed. d) evolution of the fault slip behavior (stick-slip motion) during shearing at

loading velocity of 0.1 μm/s. e) and f) microstructures of the experimental fault at 25 MPa and 100 MPa, respectively. Images are obtained using a Scanning Electron Microscope in Back-Scattered Electron mode (Methods). At low normal stress the microstructure shows a highly localized deformation zone (< 100 μm thick, g and h) whereas at higher normal stress the entire volume of the gouge is pervasively deformed resulting in a well-developed foliation (i, l).

To explore the dynamics of frictional instabilities we designed an experimental setup to directly observe the deformation of the sample, similarly to experiments performed in analogue materials (Nielsen et al., 2010; Kaneko et al., 2016; Shlomai and Fineberg, 2016; Gounon et al., 2022; Rubino et al., 2023; Cebry et al., 2022; Steinhardt et al., 2023). These tests were performed using the same experimental protocol and boundary conditions but using a transparent (Acrylic) central slider block of the DDS setup (Fig. 2a). This allowed high-resolution video analysis of the fault surface during deformation and slip. Videos were recorded using a high-speed (500 Hz), high-resolution (> 300 ppi) digital camera, capturing the reflection of a light source on the fault-block interface (Fig. 2a). Changes in the intensity of reflected light (quantified with a grey scale) correspond to changes in the state of stress, which can be detected at every point of the fault surface (Fig. 2b, e.g., Dieterich and Kilgore, 1994; Viswanathan and Sundaram, 2017; Gounon et al., 2022). Each slip event corresponds to a systematic variation of the overall surface reflectivity (Fig. 2b) and the local variation of the surface reflectivity reveals the spatio-temporal evolution of the frictional instability (Fig. 2c). We use a representative event to illustrate the rupture process (SM6). Note that the substitution of the DDS central block alters neither the bulk mechanical behavior nor the stick-slip instabilities (SM7); results for the acrylic and steel blocks are the same.

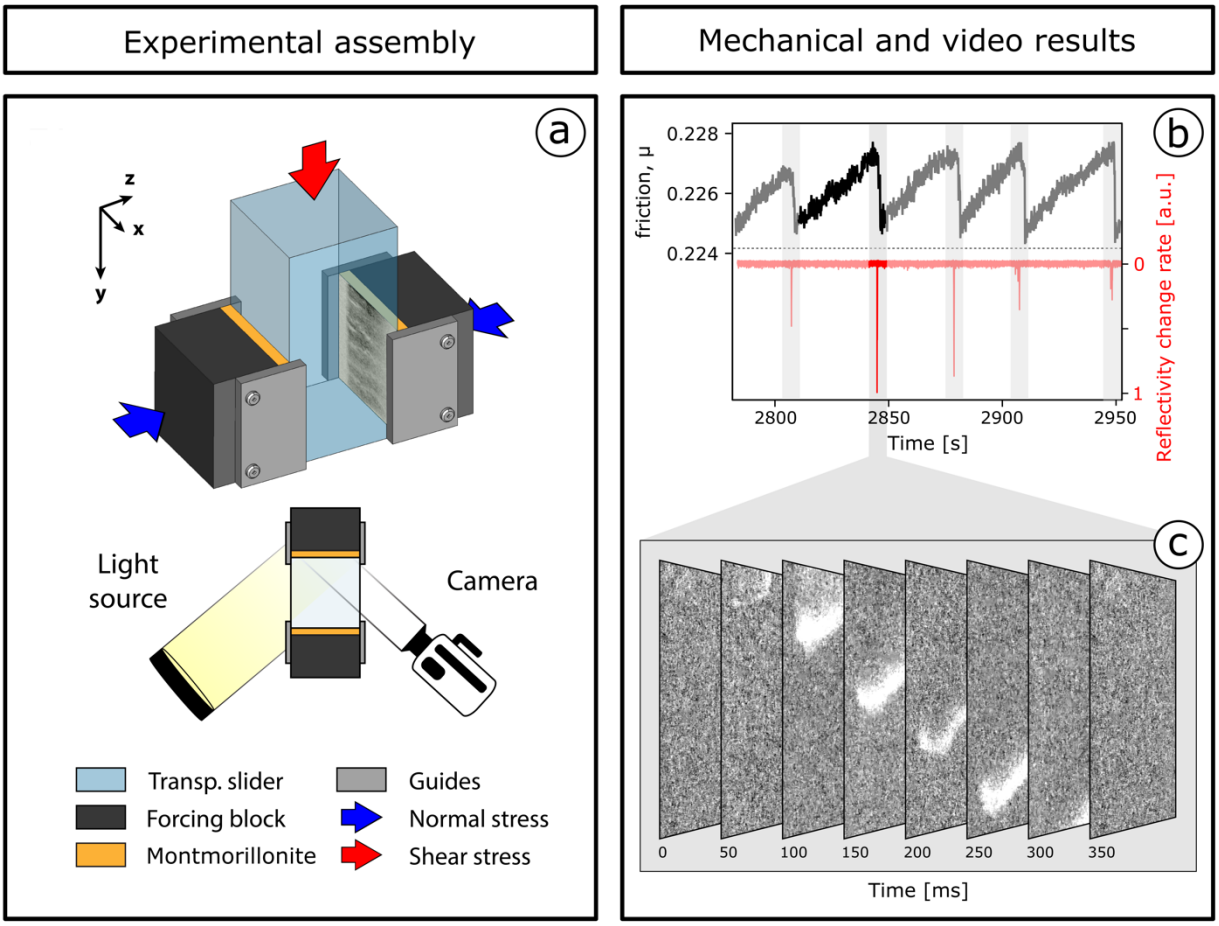


Figure 2: a) experimental design and assembly used for the experiment performed with the high-resolution video analysis. b) comparison between mechanical behavior and bulk reflectivity change rate. c) frames of the video showing the spatio-temporal evolution of the rupture process of the selected event (Methods).

The rupture front can be tracked with the position of the first change in local reflectivity, corresponding to the local stress change (white patches in Fig. 2c and colored lines in Fig. 3a). The rupture starts as a small patch that slowly (< 3 mm/s) grows until it reaches a critical size of ~ 1cm (Fig. 3a warm colors). During this nucleation phase, as the patch widens (Fig. 3b) the local stress decreases (Fig. 3c). After this nucleation phase, the rupture front accelerates and propagates across the fault at an average velocity of ~15 cm/s (Fig. 3b). Behind the rupture front, the local stress first decreases to a minimum value and then gradually increases with time, i.e., stress recovery (Fig. 3c). For a specific time-window, the stress drop is restricted to the region between the rupture front and the onset of stress recovery (Fig. 3d and inset). The region with negative stress change represents the breakdown zone of the propagating rupture (Cocco et al., 2023). Our observations document rupture propagation along the fault in the form of self-healing wrinkle-like rupture (e.g., Andrews and Ben-Zion 1997; Lykotrafitis et al., 2006; Lambert et al., 2021). In our experiments, the

location of the nucleation site is not related to pre-imposed asperities (i.e., Cebry et al., 2022; Steinhardt et al., 2023), but it is connected to stress inhomogeneities on the fault caused by fault architecture (Fig. 1e) and previous ruptures (i.e., Fig. 3c and d). These stress heterogeneities also modulate rupture front velocity (Fig. 3b), the local stress drop (Fig. 3c), and the nucleation sites of the next ruptures (SM6).

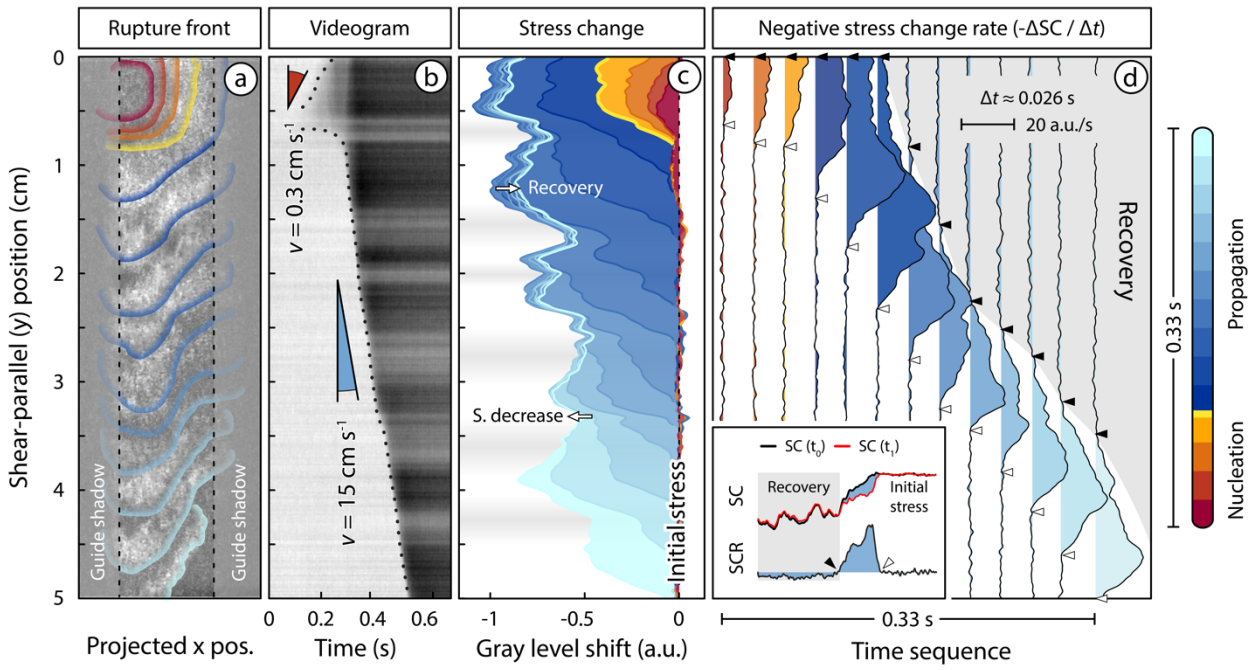


Figure 3: Evolution in space and time of the rupture front properties of a single stick-slip event imaged from video analysis: a) temporal evolution of the rupture front on the fault surface; b) space-time position of the rupture front within the vertical dashed line in panel a; c) stress change and d) stress change rate along the fault during time highlighted by changes in reflectivity (grey level in arbitrary scale) that is proportional to the stress on fault. Inset of panel d) describe the evolution of stress change (SC) and stress change rate (SCR) along the fault for a single time-window from $t_0$ to $t_1$ (details in SM8). The breakdown zone is the restricted between the initial stress region and the recovery region. Horizontal shades in panels c) represent zones of stress heterogeneities caused by fault architecture (panel b).

## 3 Slow-slip instabilities

Our laboratory experiments on clay-rich faults document a range of behaviors including low frictional strength, bulk rate-strengthening behavior and null healing rates. We observe a transition from frictional to ductile rheology at normal stress > 25 MPa that is associated with a change from localized to distributed deformation (Fig. 1). These results are consistent with previous experimental works (Saffer and Marone, 2003) that use the rate-strengthening behaviour of montmorillonite as justification for the observed aseismic creep of the shallowest regions of subduction zones (Saffer

and Marone, 2003; Saffer and Wallace, 2015; Lay, 2015; Scholz, 2019). However, superimposed on the bulk rate-strengthening frictional rheology, we observe small slow slip instabilities that occur at low loading velocities (Fig. 1c and d). We interpret these instabilities as the result of local, second-order alternative frictional mechanisms such as adhesion (Schallamach, 1971; Dieterich and Kilgore, 1994; Viswanathan and Sundaram, 2017) and bi-material effect (Andrews and Ben-Zion 1997; Scholz, 2019). These mechanisms can act in concert with structural and frictional heterogeneities (Wang and Bilek, 2014; Saffer and Wallace, 2015), and with a local transition to rate-weaking behaviour at low stress (Saffer et al., 2001) and low loading velocity (Ikari and Kopf, 2017). For the observed slow-slip instabilities our data and images of the rupture process (Fig. 3) point to a self-healing wrinkle-like rupture (Andrews and Ben-Zion 1997; Lykotrafitis et al., 2006; Lambert et al., 2021). Similar rupture dynamics have been investigated on other friction experiments on bare rock surfaces (Passelegue et al., 2013; McLaskey and Yamashita, 2017), plastic materials (e.g., Nielsen et al., 2010; Kaneko et al., 2016; Shlomai and Fineberg, 2016; Gounon et al., 2022), or thin layers of quartz powder (Cebry et al., 2022; Rubino et al., 2023; Steinhardt et al., 2023). These experiments, performed on rate-weakening materials, documented dynamic stress drop of up to a few MPa, and rupture velocity up to km/s. In our experiments, the stress drops, slip, and rupture velocity are significantly smaller. We connect these differences to the low rigidity, bulk rate-strengthening behavior, and null healing-rate of montmorillonite which limits the magnitude of the stress drop and the rupture velocity (e.g., Scholz, 2019; Shreedharan et al., 2023).

## 4 Implication for shallow slow earthquakes and tsunami earthquakes

Although fault dimensions and rupture velocities of natural and laboratory fault differ significantly, and a more comprehensive discussion is required, the striking similarities between natural observations and our laboratory results support the applicability of our findings to shallowest regions of subduction zones. Along the shallowest portion of subduction zones (i.e., above the up-dip limit of the seismogenic zone, Fig. 4a) the absence of regular seismicity is generally related to the abundant presence of clay-rich rocks (Vrolijk, 1990; von Huene and Scholl, 1991). These rocks are characterized by low frictional strength, low healing rates, and rate-strengthening behavior (Saffer and Marone, 2003; Ikari and Saffer, 2011; Shreedharan et al., 2023), which hinder earthquake nucleation therefore promoting aseismic deformation and low seismic coupling (Saffer and Wallace, 2015; Scholz, 2019). However, shallow subduction zones are also the regions hosting shallow slow slip (Saffer and Wallace, 2015; Wallace, 2020) and tsunami earthquakes (Kanamori, 1972; Kanamori and Kikuchi, 1993; Polet and Kanamori, 2000; Bilek and Lay, 2002; Lay et al., 2012; Lay, 2015; Fig. 4a). To explain the nucleation of these peculiar seismic phenomena within rate-strengthening and weakly coupled

faults, structural and frictional heterogeneities have been suggested to favor the development of local, unstable and coupled fault patches (Lay et al., 2012; Wang and Bilek, 2014; Saffer and Wallace, 2015), whereas the transitional frictional behavior at low stresses and low velocity has been proposed as a potential mechanism for their nucleation (Saffer and Wallace, 2015; Ikari and Kopf, 2017; Im et al., 2020). Our results indicate that a relatively unexplored yet fundamental control on shallow slow slip events is exerted by fault fabric, stress heterogeneities, and alternative frictional mechanisms. Our experimental clay-rich faults (Fig. 4b) have a bulk frictional rheology with low frictional strength, null healing rate, and rate strengthening behavior, therefore explaining the low coupling and aseismic creep observed along shallow subduction zones (Fig. 4c), however slip localization enhances the development of frictional instabilities resulting in slow slip events with slow rupture velocities (Fig. 4b, d). Our results support the recent findings suggesting a key-role of frictionally weak clay-rich rocks in the nucleation of shallow slow slip events (Ikari and Kopf, 2017; Shreedharan et al., 2023), and suggest a novel interpretation for the origin of shallow slow earthquake. Furthermore, our findings offer a new perspective on the seismogenic potential of the shallowest and weakly coupled subduction interfaces with significant implication for seismic hazard as the one represented by tsunami earthquakes.

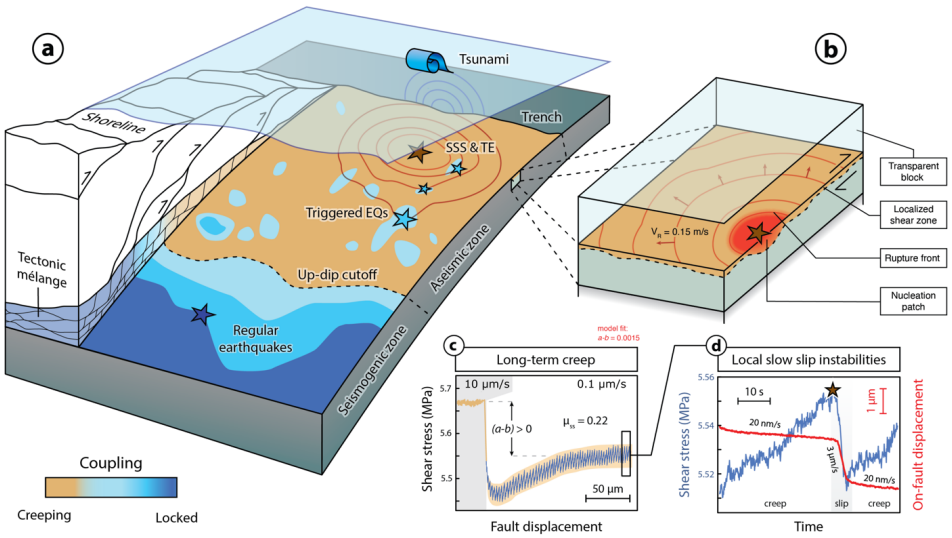


Figure 4: a) block-diagram showing structural and frictional properties of shallowest regions of subduction zones where shallow slow slip (SSS) and tsunami earthquakes (TE) occur. The color-bar shows the degree of coupling along the subduction interface. b) model of the experimental fault at sliding velocity of 0.1 μm/s where slow-slip instabilities occur. c) shear strength evolution during a velocity step displaying a rate-strengthening behavior (brown) with small instabilities (blue). d) details of a slow-slip instability: note that during the interseismic phase the fault is not completely locked, but it is continuously creeping at very low velocities, thus displaying a creep-slip rather than a canonical stick-slip behavior. These features support the coexistence of long-term aseismic creep with local slow slips.

## 5 Acknowledgement

We thank D. Mannetta for his help with thin sections preparation and M. Nazzari for the support at the SEM-INGV laboratory. We also thank prof. M.M. Scuderi, E. Tinti and M. Cocco for fruitful discussion. This research was supported by ERC grant Nr. 259256 GLASS to C. Collettini and ERC grant TECTONIC Nr. 835012 to C. Marone.

# Chapter IV

# *Study of fluid-induced reactivation of granite-hosted fault in the Central Alps*

---

## Laboratory simulation of fault reactivation by fluid injection and implications for induced seismicity at the BedrettoLab, Swiss Alps.

**G. Volpe**[a], G. Pozzi[b], C. Collettini[a,b], E. Spagnuolo[b], P. Achtziger-Zupančič[c], A. Zappone[d], L. Aldega[a], M.A. Meier[d], D. Giardini[d], M. Cocco[b]

a: Department of Earth Sciences, La Sapienza University of Rome, Italy

b: Istituto Nazionale di Geofisica e Vulcanologia, Italy

c: Department of Engineering Geology and Hydrogeology, RWTH Aachen University, Germany

d: Department of Earth Sciences, ETH Zürich, Switzerland

*Published in Tectonophysics*

https://doi.org/10.1016/j.tecto.2023.229987

### Abstract

Fluid induced fault reactivation experiments will take place as part of the "Fault Activation and Earthquake Rupture" project (FEAR) at the BedrettoLab, an underground laboratory for geosciences and geo-energy excavated within the Rotondo massif (Swiss Alps). The aim of this publication is to characterize frictional properties and permeability of the main segment of the fault zone selected for limited fluid-induced fault reactivation experiments. Firstly, we characterized fault zone microstructures in the field and in thin sections. Secondly, we assessed fault gouge mineralogy by X-ray powder diffraction analysis, yielding a composition in agreement with similar fault gouges in the same area. Finally, we performed a detailed frictional and permeability characterization in laboratory, using BRAVA (Brittle Rock deformAtion Versatile Apparatus). We performed five frictional experiments, run at the actual in-situ conditions: four

experiments for frictional properties characterization; and one further experiment where we stimulated the experimental fault by fluid pressurization applying a similar injection protocol designed for the in-situ hydraulic stimulation experiment. Additionally, we performed microstructural analysis on experimental samples to link frictional and permeability properties with fault fabric evolution. The integration of experimental results with field investigations suggests that the selected fault is potentially seismogenic and can be dynamically reactivated and controlled with hydraulic stimulation. This study highlights the importance of bridging the gap between laboratory and in-situ fault characterization, where experimental results become instrumental for the correct design of injection protocols such as those of FEAR project.

## 1 Introduction

### 1.1 The BedrettoLab and the FEAR project

The Bedretto Tunnel is a 5218 m long tunnel located in the Swiss Central Alps (Fig. 1). It links the Bedretto Valley with the Furka Base Tunnel, passing through the Rotondo massif (Keller and Schneider, 1982). The orientation of the tunnel is approximately N 317°. The rock overburden has a maximum height of 1632 m below the Pizzo Rotondo peak (3124 m a.s.l., Fig. 1b). Access to the tunnel was granted in 2018 to the ETH Zürich by the owner, the Matterhorn Gotthard Bahn, for long-term research programs, leading to the establishment of the world unique Bedretto Underground Laboratory for Geosciences and Geoenergy (BULGG or the BedrettoLab, Fig. 1b). Since its completion, the tunnel remained largely unpaved and unlined, thus offering the unique opportunity to characterize in-situ the geological properties (structural and hydrological among others) of the host rock. Detailed investigations were previously carried out along the tunnel, including studies on the groundwater systems (Lützenkirchen, 2002; Ofterdinger, 2001), the brittle fault zones structures (Lützenkirchen, 2002; Lützenkirchen and Loew, 2011), and the ductile shear zones and associated geochronology (Rast, 2020; Rast et al., 2022; Ceccato et al., 2023). This tunnel, extensively instrumented thanks to the BedrettoLab, provides an exceptional facility and a fully monitored area that can be exploited for observing earthquake processes at closer distance. In the Bedretto underground experimental site it is possible to perform experiments of induced seismicity by fluid-induced stimulation of natural faults with an unprecedented level of in-situ instrumentation compared to previous similar project (e.g., the JAGUARS project, Nakatani et al. 2008, or the NELSAM project, Reches, 2006). For this purpose, the European Research Council (ERC) funded the “Fault Activation and Earthquake Rupture” (FEAR) Synergy project that grouped scientists from the Eidgenössiche Technische Hochschule Zürich (ETH Zurich) in Switzerland, the Rheinisch-Westfälische Hochschule (RWTH Aachen University) in Germany, and the Instituto Nazionale

di Geofisica e Vulcanologia (INGV) in Italy. The main goal of the FEAR project is to perform limited and controlled fault stimulation experiments at 50-100 meters scale and over 1 km of depth with real-time control of experimental conditions and monitoring. Thanks to the wide range of expertise of scientists involved in the project, FEAR is aiming to provide a full in-situ characterization of all seismological, geological, and engineering features, concerning fault instability due to hydraulic stimulation. The careful selection of candidate fault for injection and reactivation has been thus one of the fundamental aspects of the first part of the project. The selected fault is set at 2378 meters from the tunnel entrance, corresponding in the tunnel structures database to the fault n. 48.5 (yellow star in Fig.1 and Fig. SI.1 in Supporting Information). The name "MC fault", assigned by the FEAR team, will be used throughout the text to refer to the selected fault. The aim of this study is to characterize: the frictional and hydraulic properties of the MC fault as well as its natural and experimental microstructures in the laboratory. We hereby report: the description of the main segment (the portion where most deformation has been accommodated) of the MC fault zone from the outcrop scale to the thin section; the X-ray diffraction analysis of the fault gouge; the mechanical, frictional, and permeability properties of the same material measured with laboratory experiments. We also show the results of fluid injection tests performed in the laboratory, using in-situ boundary condition and a similar injection protocol envisioned for the main FEAR experiments.

## 2 Fault characterization

### 2.1 Geological setting

The Bedretto Tunnel is entirely hosted within the Helvetic domain of the western Alps (Fig. 1). The tunnel crosses different rocks series which are, in order from the entrance, the Tremola series, the Prato series, and the Rotondo granite (Lützenkirchen, 2002; Lützenkirchen and Loew, 2011; Ma et al., 2022; Rast et al., 2022). The BedrettoLab is mainly located within the Rotondo granite (Fig. 1b), with a local overburden of ~1000 m. The Rotondo intrusion is one of various plutons within the Gotthard massif (Gamsboden, Rotondo, Medelser, Cristallina, and Fibbia) emplaced at 294 ± 1.1 Ma (Sergeev et al., 1995) during the Variscan orogeny. Successively the Rotondo granite experienced various metamorphic and tectonic phases related to the late Variscan and Alpine orogeny, recorded by several sets of ductile and brittle shear zones. Ductile deformation within the Rotondo granite is localized in a few, foliated mylonitic shear zones (Schneider, 1985; Lützenkirchen and Loew, 2011; Rast et al., 2022; Ceccato et al., 2023). Brittle structures (e.g., fractures and brittle faults) are less common and often exploit pre-existing discontinuities such as ductile shear zones

(Lützenkirchen, 2002 and Lützenkirchen and Loew, 2011; Ceccato et al., 2023). In the Aar Massif area, brittle deformation is responsible for moderate seismicity (M<2) that occurs on faults trending ~ 110° N with both extensional and strike-slip kinematics (Kastrup et al., 2004; Diehl et al., 2018; Heidbach et al., 2018; Ma et al., 2022). Stress analysis suggests that transition from normal to strike slip faulting is expected with increasing depth (Ma et al., 2022).

Several medium-to-large scale ductile and minor brittle shear zones are visible along the tunnel walls. These structures are concordant (in terms of orientation) with those observed by scanline mapping and remote sensing of the surface above the tunnel (Jordan, 2019; Ceccato et al., 2023). A complete mapping and in-detail studies of these structures are reported in literature (Lützenkirchen, 2002; Lützenkirchen and Loew, 2011; Jordan, 2019 and Rast et al., 2022; Ceccato et al., 2023). The most frequent shear zones belong to an E-W striking, steeply dipping set, which are roughly oriented perpendicularly to the tunnel. Tunnel-parallel shear zones are significantly under-sampled (Rast et al., 2022). Generally, all the shear zones dip at high angle (>50°) toward south or north. The host rock is a metagranite from greenschist to amphibolite facies, containing quartz, plagioclase, K-feldspar, and muscovite. Biotite, chlorite, and garnet occur as minor phases (~30% quartz, ~55% feldspars, ~10% phyllosilicates, ~5% accessory, Hafner, 1958; Labhart, 2005; Rast, 2022).

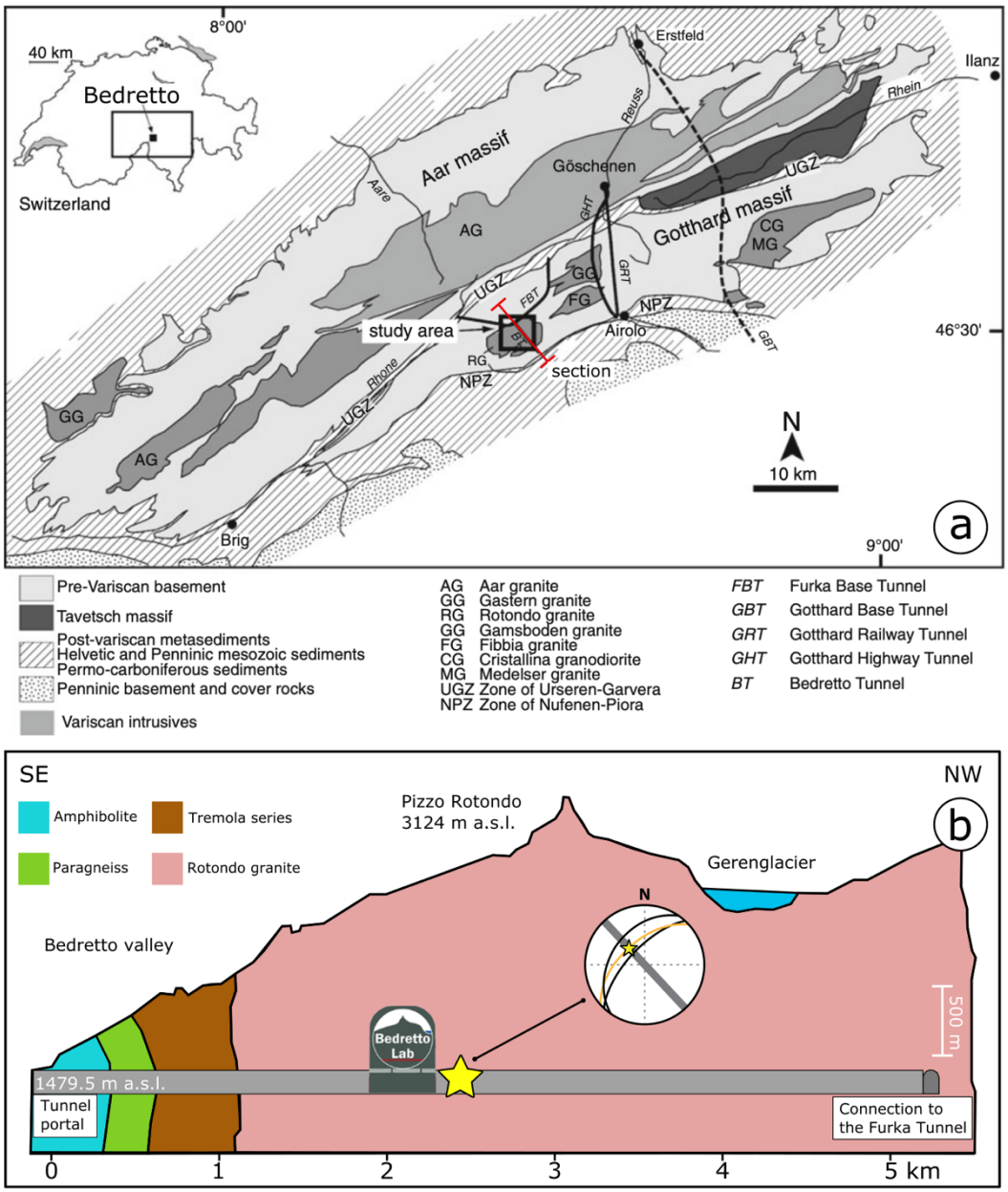


Fig.1: Geographical and geological setting of the study area. a) Geological map of the Gotthard and Aar Massif (Central Swiss Alps) with study area and trace (red line) of the geological cross section in panel b (modified after Lützenkirchen and Loew, 2011). b) Cross section of the Bedretto tunnel, indicating all the geological units intersected by the tunnel. Yellow star indicates the intersection of the MC fault (dip and dip direction: 58°/318°) with the tunnel (direction: 317° N). Image modified after Ma et al., 2022. The stereoplot includes the three main segments of the MC fault with highlighted in yellow the selected segment and in grey the tunnel direction.

Ductile shear zones occur along lithological contacts, such as the boundaries of mafic enclaves (Rast et al., 2022) or lamprophyre dykes, and are characterized by a reverse to strike-slip kinematics (Lützenkirchen, 2002; Rast et al., 2022). Shear zones are foliated with biotite and elongated quartz ribbons (Rast et al., 2022). The age of the ductile deformation is still a matter of debate. According to some authors ductile deformation is related to the late Variscan orogenic phase

(Lützenkirchen, 2002 and Lützenkirchen and Loew, 2011), for others is driven by the Alpine orogeny (Labarth, 2005). Brittle faults are preferentially localized along the pre-existing ductile shear zones, in particular the ones that are perpendicular to the tunnel and dip towards north (Lützenkirchen, 2002 and Lützenkirchen and Loew, 2011). Brittle faults generally have normal or strike-slip kinematics (Lützenkirchen and Loew, 2011; Jordan, 2019; Rast et al., 2022) and often have fault cores containing a whitish gouge. According to some authors, these faults can be potentially active with extensional kinematics in the framework of the actual stress field, which favors normal faulting in the high-altitude parts of the Alps (Heidbach et al., 2018; Kastrup et al., 2004; Diehl et al., 2018). The water inflow (up to 0.6 l/s) in the tunnel is primarily associated to diffused fracturing and localized faults (Lützenkirchen, 2002; Ofterdinger, 2001; Arnet, 2021). The tunnel-perpendicular faults with gouges are the most conductive structures and have high water inflows (Ma et al., 2022; Rast et al., 2022).

## 2.2 MC fault structure and mineralogy

A detailed characterization of the entire MC fault zone has been presented by Ceccato (Ceccato et al., 2023) and Achtziger-Zupančič in the FEAR Geology Working-Group report (written communication). In this work we focus on one of the main segments of the MC fault. The MC fault belongs to the category of the brittle faults that contain a core of fine-grained cataclasites (e.g., Lützenkirchen and Loew, 2011). The dip direction is between 315° and 335° N with a plunge of 50° to 70° and exploits a narrow mylonitic shear zone characterized by biotite decorated quartz veins parallel to the foliation. Macroscopically, the brittle deformation is localized at the splitting between the quartz vein and the mylonitic wall rock. The MC fault appears as a very localized shear zone composed of a principal narrow fault core (average thickness < 5 mm) filled by a whitish fault gouge (Fig. 2a, b) and by coarser cataclasites, which are only observed locally at dilational jogs. The fault itself does not show a well-developed damage zone, but rather the damage is a characteristic of the host rock showing a network of neat fractures. The deformation that produced the gouge at the core of the MC fault seems to overprint all the previous phases of ductile and cataclastic deformation occurred at higher temperatures than the last (strike-slip) occurred in zeolite facies, Lützenkirchen and Loew, 2011; Ceccato et al., 2023), suggesting repeated fault reactivations even in the current regional stress field (Kastrup et al., 2004; Lützenkirchen and Loew, 2011; Heidbach et al., 2018). The absence of clear kinematic indicators in the gouge does not allow to retrieve the shear-sense of faulting. However, it is possible to observe a relative displacement of ~10 cm at a dilational jog (yellow triangles in Fig. 2a), which suggest an extensional kinematics component. The fault core was carefully sampled for microstructural investigation together with the host rock (Fig. 2b) and mounted to produce a petrographic thin section

(30 μm thick, Fig. 2c). Four distinct zones can be separated by microstructural analysis (see Fig. SI.2). The first is the host rock, a protomylonitic granite composed by coarse (~1 cm) grains of K-feldspar, quartz and albite, and a finer fraction of the same minerals organized in anastomosing, discontinuous seams. Coarse grains of quartz and feldspars show undulose extinction and polygonization (subgrains). Evidence of bulging is found locally along the grain boundaries. The second zone is composed of more continuous, anastomosing ultramylonitic shear zones, which present homogenous grain size (< 100 μm, Fig. 2c), quadruple junctions, and a shear-parallel C-foliation, defined by oriented grains of biotite (Fig. 2c and Fig. SI.2 in Supporting Information). The brittle fault core (third zone) is formed by a thin layer of sub-rounded quartz and feldspar clasts (< 50 μm) embedded in a matrix of white mica and finer granular materials, defining a weak C-foliation. The last zone is a zeolite-rich vein localized at one side of the fault core, characterized by a crosshatch pattern of crystals (up to few mm in length) that suggests static growth. Some isolated zeolites lumps are also found in the cataclastic layer (e.g., Lützenkirchen and Loew, 2011). Like the MC fault, they are described as localized cataclastic shear zones that overprint previous mylonitic foliation (Lützenkirchen and Loew, 2011; Ceccato et al., 2023).

The fault gouge is incohesive (Fig. 2a). The gouge sample was oven dried at 45 °C for 48 hours. Agglomerates were then gently dismembered by hand to avoid contamination of the original grain size and coarse clasts were removed by hand. Most of the gouge in the thin principal slip zone is fine-grained (< 125 μm) as revealed by thin section analysis (Fig. 2d). We therefore sieved the material below 125 μm to minimize the contamination of the coarser, outer cataclasite, which is unavoidably collected with the sampling procedure in situ. Mineral assemblage of the sieved gouge has been assessed by X-Ray powder Diffraction (XRpD) analysis. We used a Bruker D8 Advance X-ray system provided with Lynxeye XE-T silicon-strip detector. The analysis was performed using CuKα radiation (λ = 1.5406 Å) at 30 mA and 40 kV. Powders were analyzed between 2–70° 2θ with steps of 0.02° 2θ while spinning (e.g., Volpe et al., 2022a). The semiquantitative assessment of mineral assemblage was obtained by the calculation of the peak areas and by using as calibration constants the mineral intensity factors (Moore and Reynolds, 1997). The XRpD analysis of the gouge (Fig. 2e) yields a mineral assemblage dominated by granular silicates (quartz, albite, and K-feldspar) that constitute the 77% of the whole rock composition and by phyllosilicates, mostly muscovite and minor chlorite and biotite (22% in total). Zeolite minerals such as stilbite and laumontite occur as minor phases with content of 1% (Fig. 2f). The observed bulk mineralogical composition is consistent with analyses performed on other brittle faults, dissecting the Rotondo granite (see Lützenkirchen and Loew, 2011).

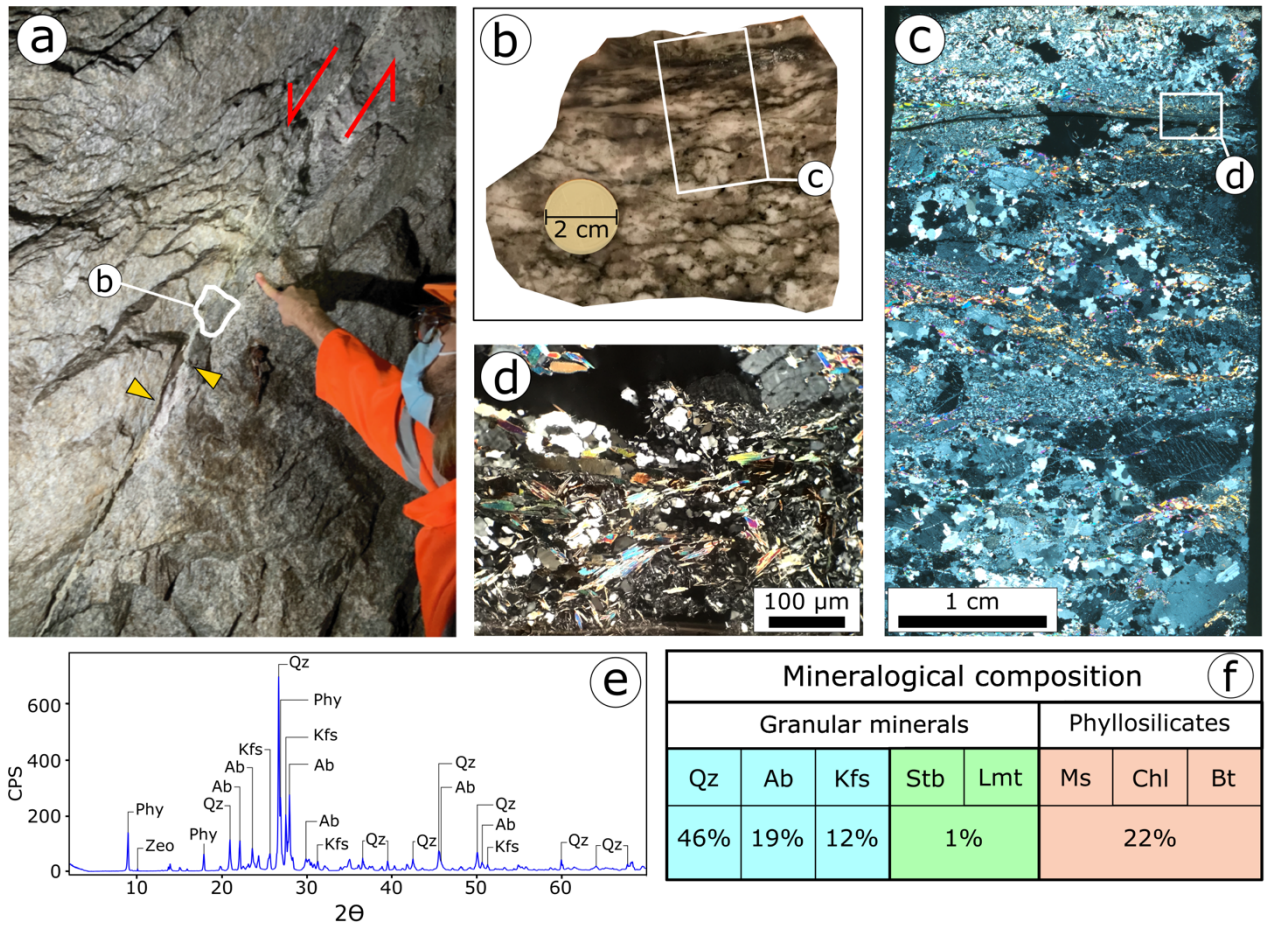


Fig.2: Structural and mineralogical characterization of the MC fault. a) Outcrop view of the selected fault in the tunnel, yellow triangles indicate conjugate point across an extensional jog; b) hand specimen of the fault zone recovered from the fault (white inset in panel a); c) crossed polars view of the fault zone in thin section (white box in panel b). d) closeup of the principal shear zone from the white box in panel c; e) XRpD pattern of the gouge from the principal shear zone (panel d); f) mineralogical assemblage of the gouge from the selected fault. Phy: phyllosilicates; Zeo: zeolites; Qz: quartz; Ab: albite; Kfs: K-feldspars; Stb: stilbite; Lmt: laumontite; Ms: muscovite; Chl: chlorite; Bt: biotite.

## 3 Frictional experiments

We performed frictional experiments to explore the frictional properties of the material composing the MC fault core. The sieved powders were tested with BRAVA, a biaxial apparatus (Collettini et al., 2014) at the INGV in Rome. We employed double direct shear configuration (DDS) consisting of three grooved steel forcing blocks squeezing two equal gouge layers (Fig. 3c, and details in paragraphs 3.1.1 and 3.1.2). Normal stress ($\sigma_n$) is exerted perpendicular to the sample layers by a horizontal fast-acting servo-controlled hydraulic piston. A second piston (vertical) exerts shear stress ($\tau$) on the central block and promotes shear deformation within the two gouge layers. The load exerted by the pistons is measured via strain-gauged load-cells installed at the piston end, with an accuracy of ±0.03 kN in a range between 0.2

kN and 1.5 MN (Collettini et al., 2014). The load is converted to stress by dividing it by the area of contact of the forcing blocks (50 by 50 mm). Displacement is measured by linear variable displacement transformers (LVDTs) with an accuracy of ±0.01 µm. Load point displacement of horizontal and vertical pistons was corrected for the elastic deformation of the experimental apparatus, knowing that the apparatus stiffnesses are 928.5 kN/mm on the vertical axis and 1283 kN/mm on the horizontal axis (Collettini et al., 2014; Giorgetti et al., 2015). The elastic response of the entire apparatus is linear at the selected experimental conditions. One experiment is carried out within the machine vessel using a jacketed DDS and applying pressure with vaseline-based oil as confining medium. This assembly is instrumented to allow control of fluid circulation perpendicular to the gouge layers across the entire area of the lateral blocks. The confining pressure ($P_c$), the upstream ($P_u$) and downstream ($P_d$) fluid pressures are exerted by three hydraulic servo-controlled intensifiers. Intensifier displacements are measured by LVDTs, accurate to ±0.1 µm, and fluid pressures by transducers, with an accuracy of ±7 kPa (Collettini et al., 2014). We used $CaCO_3$-equilibrated water, similar to those circulating in the massif, to saturate the samples.

## 3.1 Experimental methods and procedures

### 3.1.1 Frictional tests

The MC fault gouge was tested with two types of experiments. The first has been conducted for the standard characterization (Fig. 3a) of the frictional strength and the rate and state (RSF) frictional parameters (healing rate and velocity dependence of friction, e.g., Dieterich, 1979; Ruina, 1983; Marone 1998). The first type of experiments was carried to characterize the frictional properties of the fault at four different normal stresses (5, 15, 25, 35 MPa), which include the in-situ effective normal stress of 15 MPa. (e.g., Ma et al., 2022; Bröker & Ma, 2022). The sample is sheared at room temperature and at water-saturated conditions. These experiments consist of several stages listed here. Firstly, the samples are installed and saturated at low normal load of 0.5 MPa for 30 minutes. Then the normal stress is increased at steps of 0.5 MPa to the targeted normal stress, which is maintained constant throughout the experiment. After the attainment of a constant thinning rate, the sample is sheared for a total displacement of 7.5 mm at a slip rate of 10 □m/s (Fig. 3a). This stage is known as “run-in” and lets the fault to accommodate enough shear displacement to achieve a steady-state friction (Fig. 3a stage 1). The following stage, the slide-hold-slide series (SHS), consists of periods of hold, gradually increasing from 1 to 1000 s and separated by shearing phase of 500 µm at 10 µm/s (Fig. 3a, stage 2). The last stage consists of velocity steps in which the sample is sheared at increasing velocity, 0.3 to 300 □m/s, for 0.5 mm of shear displacement for each velocity step (Fig. 3a, stage 3).

Our characterization of frictional properties includes the steady-state frictional strength, the healing behavior in SHS tests, and velocity dependence of friction. We used the RSF friction theory (Dieterich, 1979; Ruina, 1983; Marone 1998) as framework for our analysis. The friction coefficient, $\mu$, is retrieved as the linear constant of proportionality between steady-state shear stress and normal stress, using Eq. 1:

$$\tau = \mu\sigma_n + c \quad (1)$$

where c is the cohesion term. During SHS test, the frictional healing ($\Delta\mu$) was obtained as the difference between the friction peak measured during re-shear following each hold and the steady state friction before the hold (Marone, 1998; Fig. 3a, stage 2). Frictional healing rate ( ) was retrieved as the linear variation of $\Delta\mu$ with logarithm of the hold time ($t_h$).

$$\beta = \Delta\mu/\log10(Dt_h) \quad (2)$$

In the velocity step tests, a quasi-instantaneous step in shear velocity from $V_0$ to V corresponds to a quasi-instantaneous variation of frictional strength which scales with $a$ $\log_e(V/V_0)$, where $a$ is an empirical parameter known as *direct effect* (Dieterich, 1979; Ruina, 1983). The subsequent evolution of friction to a new steady-state, scales with $b$ $\log_e(V/V_0)$, where $b$ is an empirical parameter known as *evolution effect* (Dieterich, 1979; Ruina, 1983; Fig. 3a stage 3). The $a$-$b$ parameter, which defines the velocity dependence of friction, is described by:

$$(a-b) = \Delta\mu_{ss} / \log_e(V/V_0) \quad (3)$$

where $\Delta\mu_{ss}$ is the difference between the dynamic steady-state frictional strength after and before the step in shearing velocity from $V_0$ to V (Dieterich, 1979, Ruina, 1983). Negative value of ($a$-$b$) defines a velocity-weakening behavior, which is a required condition for the developing of frictional instability (Dieterich and Kilgore, 1994; Marone 1998). Positive value of ($a$-$b$) defines a velocity-strengthening behavior, suggesting aseismic creep as the likely fault slip behavior. Each velocity step was modelled by using RSF equations (Eq., 4) coupled with the Dieterich law (Eq. 5), an evolution law that defines the state variable $\vartheta$ (Dieterich, 1979):

$$\mu = \mu_0 + a \log_e(V/V_0) + b \log_e(V_0\theta /D_c) \quad (4)$$

$$d\vartheta/dt = 1 - \vartheta V/D_c \quad (5)$$

where $\mu_0$ is frictional strength at the steady state for slip velocity $V_0$, V is the frictional slip rate and $D_c$ is the distance necessary to renew the population of asperities, the so-called *critical slip distance* (Dieterich, 1979, Ruina, 1983). The state variable, $\vartheta$, is interpreted to represent the average lifetime of the asperities (Ruina, 1983). To model velocity steps,

the previous two equations are coupled with another equation (Eq. 6) which defines the elastic coupling between the sliding surface and the loading medium:

$$d\mu/dt = K(V_{lp}-V) \quad (6)$$

where $V_{lp}$ is the loading point velocity and K is the stiffness normalized by normal stress (1/mm) of both the assembly and the loading apparatus (Saffer and Marone, 2003). These equations are solved simultaneously using a fifth order Runge-Kutta integration. *a*, *b*, and $D_c$ were retrieved, for each velocity step, as best fit values using a, least squares iterative method to solve the inverse non-linear problem (Blanpied et al., 1998; Saffer and Marone, 2003).

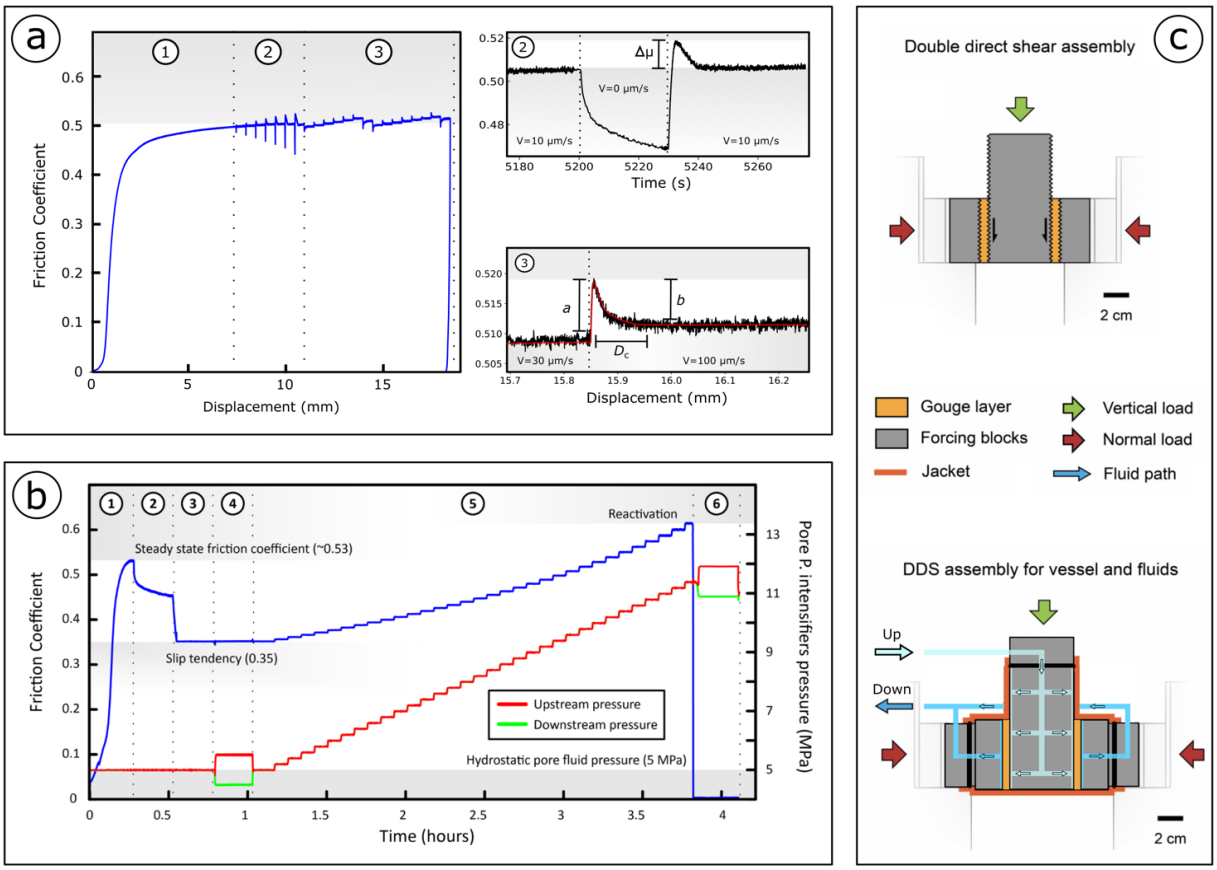


Fig.3: Experimental procedures, frictional analysis, and experimental assemblage. a) experimental design and procedures for the standard characterization of the RSF parameters. Stage 1: run-in where frictional strength is measured. Stage 2: slide-hold-slide test where frictional restrengthening is measured. Stage 3: velocity step tests where the velocity dependence of friction is evaluated b) experimental design of the injection experiment. Stage 1: run-in. Stage 2: hold phase and decelerating creep. Stage 3: the fault shear stress is set at the slip tendency. Stage 4: pre-injection permeability measurement. Stage 5: injection test and fault reactivation. Stage 6: post-reactivation permeability measurement. c) Double Direct Shear, DDS, experimental assemblages used during the experiments: standard characterization, top panel; injection test, bottom panel.

### 3.1.2 Injection test

With the second type of experiments, we evaluated the fault slip behavior during hydraulic stimulation by fluid injection (Fig. 3). This experiment was performed in the pressure vessel at confining pressure $P_c$ = 15 MPa, pore fluid pressure $P_f$ = 5 MPa and initial effective normal stress of $\sigma'_n$ = 15 MPa ($\sigma'_n = P_c + \Delta\sigma_n - P_f$, with $\Delta\sigma_n$ = 5 MPa, details in Scuderi and Collettini, 2016). These values represent the in-situ stress conditions of the MC fault, where the measured pore-fluid pressure is about 5 MPa and the effective normal stress is about 15 MPa (Ma et al., 2022; Bröker & Ma, 2022). For this type of experiment, we used a different DDS assembly, consisting of three forcing blocks provided with channels to allow fluid to flow perpendicularly to the layers of gouge. The blocks are connected to the external fluid pressure intensifiers (Fig. 3c Lower panel) and equipped with grooved porous frits (permeability = $10^{-14}$ $m^2$). This assemblage ensures a homogenous fluid distribution on the entire surface of the sample, while forcing shear to be localized within the layers of gouge. For this configuration, the nominal frictional contact area is 55.4 by 55.5 mm, and the initial layer thickness is 5 mm (Fig. 3c lower panel). The whole sample assembly (i.e., the gouge layers and the forcing blocks) was separated from the confining oil by a rubber jacket (e.g., Scuderi and Collettini, 2016, 2018). For this second type of experiments, we followed the procedures described by Scuderi and Collettini (2018). We began by applying the confining pressure, $P_c$, at steps of 1 MPa until reaching 5 MPa. Subsequently, we increased the normal stress by $\Delta\sigma_n$ = 5 MPa (steps of 0.30 MPa), compacting the sample for 30 minutes. We then started applying the pore fluid pressure by increasing the upstream pressure ($P_u$) to 1 MPa and leaving the downstream lines open to the atmosphere until constant flow was attained through the assembly. After the full saturation of the gouge layers, we connected the downstream lines to the intensifier and waited for equilibration of the downstream pressure ($P_d$). Pore fluid pressure was then increased stepwise (1 MPa for each step) until the targeted pore fluid pressure was reached. The sample was left compacting to achieve a steady-state layer thickness. After this preliminary stage, the sample was sheared at 10 µm/s of velocity for a total shear displacement of 10 mm (''run-in'') letting the fault achieve a steady state shear stress, $\tau_{ss}$, (Fig. 3b stage 1). We then stop the vertical piston to let the sample relax for 15 minutes and achieve a residual shear strength (Fig. 3b stage 2). This last stage is necessary to let the fault achieve an equilibrium porosity and an optimal fabric arrangement (e.g., Scuderi and Collettini, 2018). Thirdly, we set the fault to a constant shear stress of 5.25 MPa to match the in-situ state of stress inferred from slip tendency analysis (Ma et al., 2022), which is $\tau/\sigma'_n$ = 0.35. Again, the sample was left to equilibrate for 45 minutes (Fig. 3b stage 3). Before starting the fluid injection, we performed a fault-perpendicular permeability test, using the constant head method (e.g., Ikari et al., 2009) (Fig. 3b stage 4), meaning 1 MPa of differential pressure ($\Delta P_f$) was applied between $P_u$ and $P_d$ and the flow rate (Q) was monitored. Permeability (*k*) is obtained, using Darcy's law (Eq. 7):

$$k = (Q\,\eta\,\Delta h)/(A\,\Delta P_f). \quad (7)$$

where Q is the average flow rate ($m^3/s$) across the gouge layer, calculated from the intensifier displacements over time multiplied by the intensifier cross section (0.0016 $m^2$), η is water viscosity ($1.002\times10^{-9}$ MPa s); Δh is the gouge layer thickness measured by LVDTs, A is the nominal area of the gouge layer (0.0030 $m^2$). Constant pressure difference was maintained until steady-state flow rate was achieved; this was assumed when the upstream and downstream flow rates were within 5% of each other and had reached a constant value (e.g., Ikari et al., 2009; Scuderi and Collettini, 2016; 2018). The injection test consisted of a stepwise increase of the fluid pressure, in agreement with the injection protocols designed for the MC fault stimulation: 0.2 MPa every 5 minutes (Fig. 3b stage 5). During the injection test, we monitored fault slip and fault layer thickness evolution. The test was stopped upon achievement of dynamic slip conditions (slip velocities > 1 mm/s). After fault relaxation to a residual shear strength, we performed another permeability test to observe possible changes in permeability induced by the fault fabric evolution during reactivation (Fig. 3b stage 6).

#### 3.1.3 Microstructural analysis.

After each experiment, the deformed gouge layers were carefully extracted from the experimental assembly and prepared for the microstructural analysis following the procedures described by Volpe (Volpe et al., 2022b). The microstructural analysis of recovered microstructures was conducted on the kinematic section (e.g., Passchier, 1990; Volpe et al., 2022b). The microstructural imagery was obtained by a Field-Emission Scanning-Electron-Microscope (SEM) in back-scattered imaging mode (BSE).

## 4 Mechanical results

### 4.1 Frictional properties characterization

For all the considered normal stress conditions, the experimental fault displays a first stage of shear strengthening followed by a steady-state shear stress (Fig. 4a) which scale linearly with normal stress, indicating brittle behavior (Fig. 4b). These values are fitted by the Coulomb criterion, giving a friction coefficient, $\mu$ = 0.49 ± 0.006 (Fig. 4b), which is slightly below the Byerlee's range of friction ($0.6 < \mu_{ss} < 0.85$, Byerlee, 1978) and negligible cohesion (< 0.2 MPa). The frictional restrengthening scales linearly with the hold time, yielding healing rates, *b*, between 0.0039 and 0.0072 (Fig. 4c). Both □$\mu$ and □ values do not show any clear correlation with normal stress (Fig. 4c). The fault gouge shows a slight velocity strengthening to neutral behavior for all the experiments with values ranging between ~0 and ~0.004 (Fig. 4d).

The *a-b* parameter does not show any clear trend with shear velocity or normal stress (Fig. 4d). We do not observe any systematic variation of the *a-b* parameter for the two series of velocity steps, suggesting no evolution with strain.

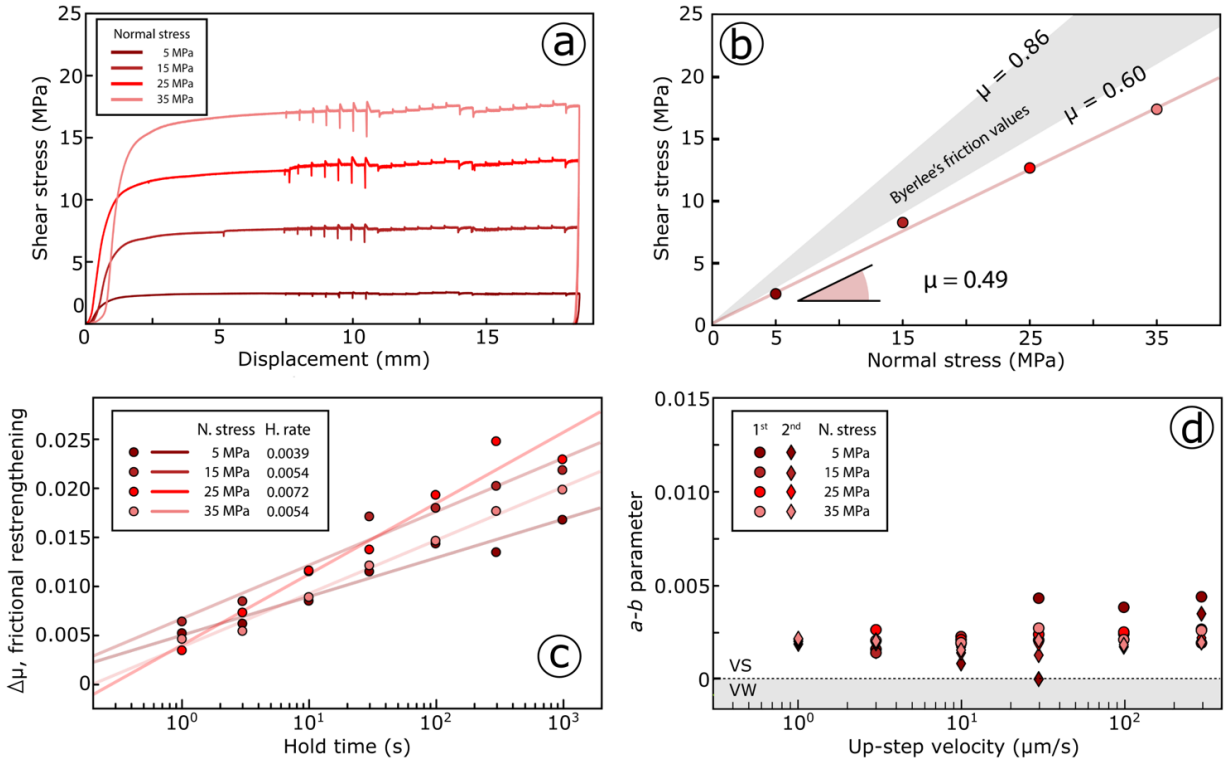


Fig.4: experimental results from the standard frictional properties characterization of the gouge from the selected fault. a) raw data frictional curves in a shear stress – displacement plot; b) Mohr-Coulomb envelop of the gouge; c) frictional restrengthening in function of hold time, slopes represent the healing rate; d) velocity dependence of friction, VS: velocity strengthening behavior, VW: velocity weakening behavior (detailed summary of the experimental results can be found in the supporting information SI.3).

## 4.2 Injection test (fault reactivation)

During the stage 1 of the experiment (Fig. 3b stage 1), we sheared the gouge for 10 mm at 15 MPa of effective normal stress until it attained a stable frictional strength of $\mu$ = 0.53, consistent with the friction coefficient obtained from the Coulomb envelope at room pressure and water saturated conditions (Fig. 5a). During the injection phase (Fig. 3b stage 5), we evaluate the fault slip behavior. Fault slip evolved in a way similar to a trimodal creep behavior (e.g., Scuderi et al., 2017 and references therein; Fig. 5b and d). During the first ten steps of fluid pressure increase (up to $P_f$ = 15 MPa, Fig. 3b), the fault displayed a decelerating creep, marked by the convex trend of the slip evolution curve (Fig. 5b). Successively, the fault showed a steady state creep with an average velocity of 3.5 nm/s (Fig. 5b and d). Accelerating creep was observed once the on-fault stress conditions crossed and overcame the Coulomb failure envelope (Fig. 5a, red arrow). At this point, the fault started sliding at increasing sliding velocity with an exponential evolution, mimicking

a dynamic instability with velocities higher than 1 mm/s (Fig. 5d). At this velocity we stopped the experiment due to achievement of the maximum displacement of the piston. It is worth to emphasize that dynamic fault reactivation was not achieved when the state of stress reached the failure envelope (between yellow and red triangles in figure 5a) but only when the fluid pressure was further raised by 1.2 MPa (six fluid injection steps), leading to fast slip acceleration.

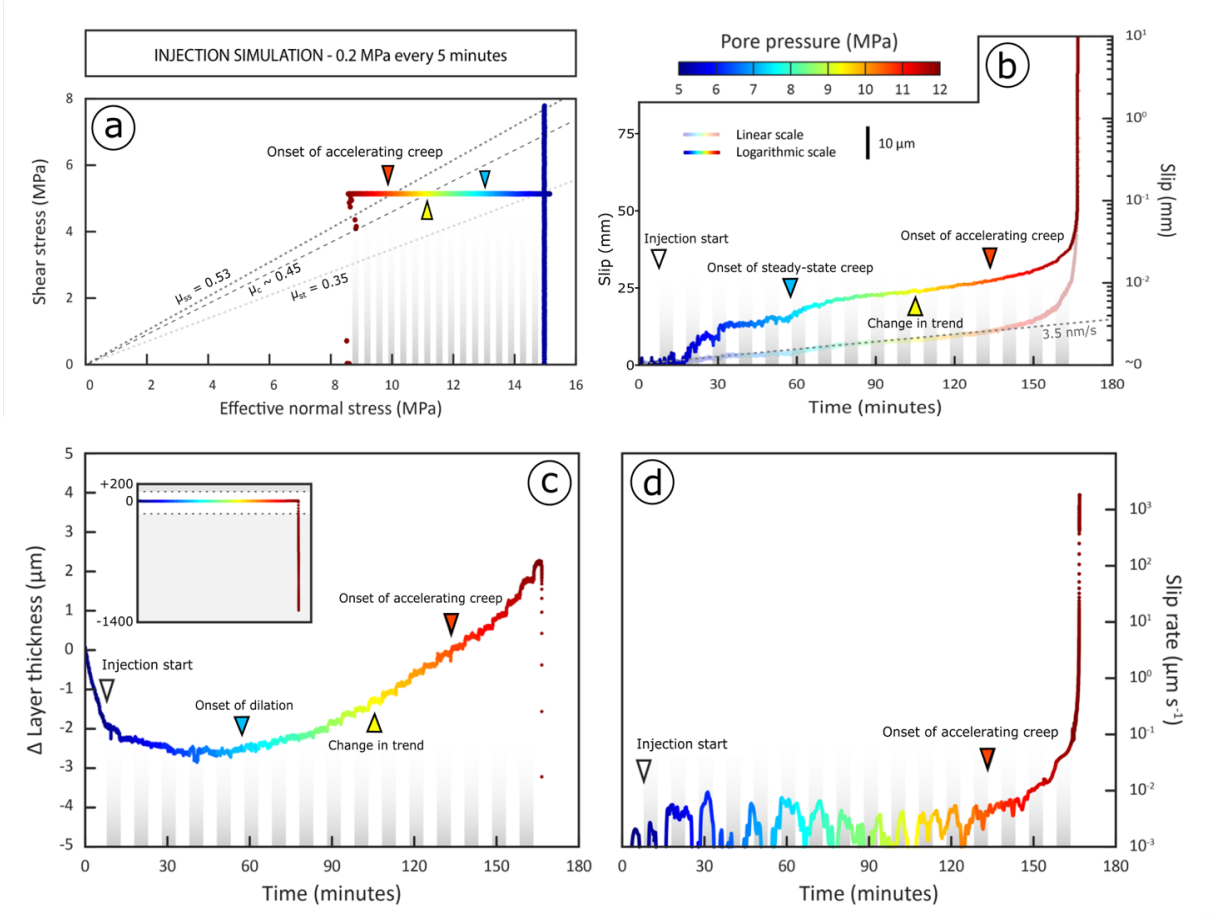


Fig.5: experimental results from the injection experiment. a) evolution of effective normal stress and shear stress during the experiment. Frictional strength, $\mu_{ss}$; slip tendency, $\mu_{st}$; creep relaxation strength, $\mu_c$ (for further information see SI.4). b) Slip as function of time during the injection phase of the experiment (linear scale on left y-axis, logarithmic scale on right y-axis); c) variations of the gouge layer thickness during the injection phase (inset indicates the whole evolution of the gouge layer thickness during stage 5); d) slip rate as function of time during the injection phase. The triangles indicate major changes during the experiments. Note that triangles with same color refer to the same intervals for all the panels. Gray and white vertical bands represent steps of fluid pressure.

During the fluid injection (stage 5 in Fig. 3b), we carefully monitored the evolution of the gouge layer thickness as a proxy for porosity and poroelastic response of the gouge (e.g., Samuelson et al., 2009; Fig. 5c). During the early phases of stage 5 (Fig. 3b), we documented an initial phase where the fault gouge undergone decelerating compaction (Fig. 5c) in correspondence of decelerating creep (Fig. 5b). During this phase, the fault compacted by ~2.5 µm (Fig. 5c). Dilation

starts at the beginning of the steady-state creep (Fig. 5c). Through this stage the experimental fault dilated by ~2.5 μm (Fig. 5c). During the first part of the steady-state creep, the layer thickness evolution is characterized by a slight and gradual dilation (Fig. 5c). Successively, the evolution of the layer thickness is marked by a trend of dilation and compaction modulated by the steps of fluid injection (Fig. 5c and Agliardi et al., 2020). At each step, the gouge first dilates then gradually compacts (Fig. SI.5 in Supporting Information). This dilation-compaction behavior is observed below the fault's relaxation creep envelope ($\mu_c \sim 0.45$, Fig. 5a). Above the relaxation creep envelope, the initial dilation is followed by a secondary dilation at each step. This trend continues with incrementally faster dilation as the failure envelope is approached (Fig. 5c and Fig. SI.5 and SI.6 in Supporting Information). Once the on-fault stress conditions crossed the reactivation envelope, the fault started slipping into accelerating creep, during which dilation strongly accelerated and culminated with a total increment of 2.5 μm (from onset of accelerating creep, Fig. 5c). During the dynamic slip the fault rapidly compacted by ~1 mm (inset of Fig. 5c and Fig. SI.5 and SI.6 in Supporting Information).

### 4.3 Fault perpendicular permeability

Fault perpendicular permeability was measured before the injection phase and after the reactivation (Fig. 3b stage 4 and 6). The pre-injection permeability was $9.3\times10^{-17}$ $m^2$. The post injection permeability measured just after fault reactivation (Fig. 3b stage 6) was about $2.9\times10^{-17}$ $m^2$.

## 5 Experimental microstructures

The microstructural analysis was carried on the samples from the standard characterization experiments. Here we report those of the experiment performed at $\sigma_n$ = 15 MPa, which represents the in-situ stress conditions (Fig. 6). The other microstructures are included in the Supporting Information (SI.7).

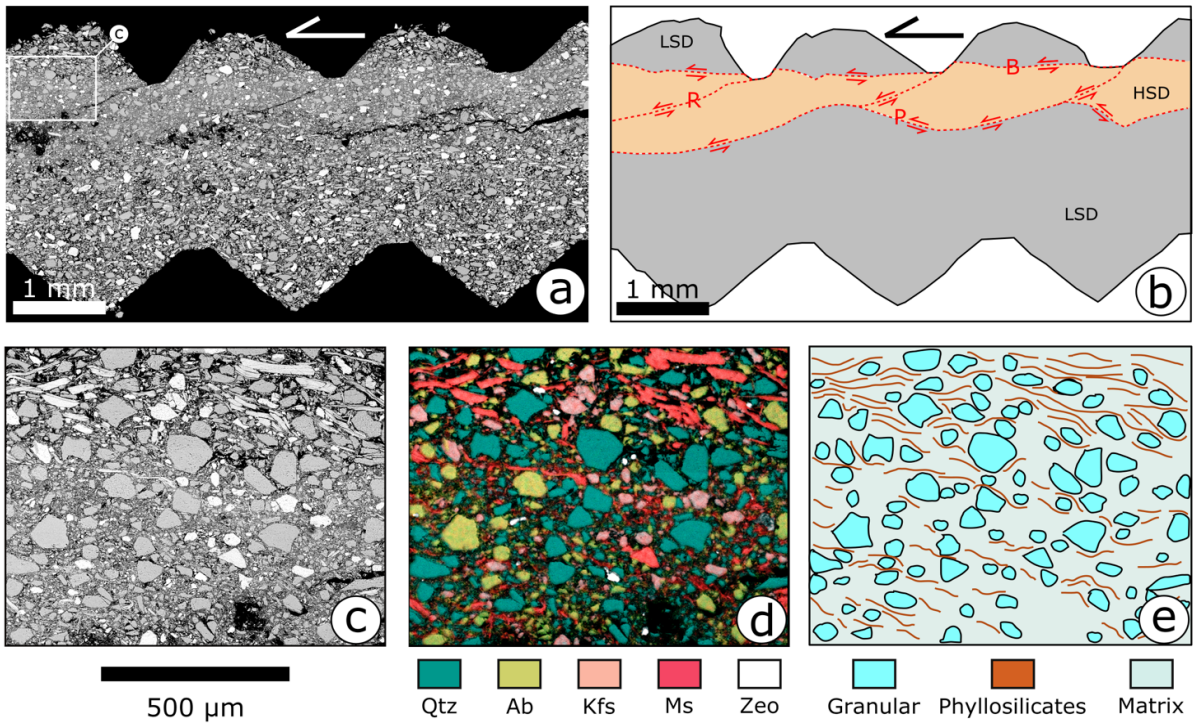


Fig.6: Microstructural characterization of experimental post-mortem gouge. a) panoramic view of the deformed gouge at 15 MPa (arrows mark the direction of shear); b) microstructural interpretation of panel a: low strain domains in grey and high strain domains in orange are shown. In the high strain domains, the structural features are labeled according to the Logan (1979) nomenclature (Y-P-B-R). c) close-up of the principal shear zone (white box in panel a); d) Energy Dispersive X-ray Spectroscopy (EDS) map of the principal shear zone in panel c showing granular and sheet silicates minerals; e) schematic microstructural line drawing of the principal shear zone.

The deformed gouge at water saturated conditions shows the development of Y-B-P-R fabric (Logan, 1979; Volpe et al., 2022b) with severe grain-size reduction along localized shear zones (Fig. 6 a, b, c). The low strain domains (LSD) are almost undeformed and display a grain size close to the original (~125 µm), observable within the indentations (Fig. 6a, b, c). The deformation is mainly localized along a single comminuted zone, the principal slipping zone, localized at the slider block boundary (e.g., Fig. 6a, b). R (Riedel) and P (compressive) shear zones are evidenced by opened fractures induced by decompression (Fig. 6a, b; Volpe et al., 2022b) and are localized within the principal slip zone. At higher magnification, the principal slipping zone contains fractured grains characterized by a heterogeneous shape and size, often mantled by phyllosilicates. Oriented platelets of biotite produce a weak s-foliation (proto-foliation, e.g., Giorgetti et al., 2015; Volpe et al., 2022b) oriented favorably with the direction of shear (Fig. 6c, d, e). The microstructure suggests deformation dominated by cataclastic processes (fracturing, grain-size reduction, and frictional sliding along grain boundaries, e.g., Sibson, 1977) supported by the grain load-bearing framework made by the granular fraction (e.g.,

quartz, feldspars in Fig. 6c, d). Minor frictional sliding along foliation may occur along the phyllosilicates proto-foliation (Fig. 6d, e).

## 6 Discussions

### 6.1 Mineralogy, fabric, and frictional properties

Mineralogy, fabric, and frictional properties have been analyzed to define key aspects of the mechanical behavior of the MC fault to understand fault suitability for the activities of the FEAR project. Our analysis focused on the fine gouge fraction collected in-situ from the MC fault core. We followed this approach since gouge bearing faults seem to be the most common character for brittle faults within the Bedretto tunnel and therefore those that should experience fluid induced reactivation during the FEAR activities. Microstructural analysis of the in-situ samples shows a discrete layer (< 5 mm) of extremely comminuted minerals, which have been segregated from the coarser and angular cataclasite by sieving (< 125 μm). The mechanical behavior of this material has been characterized with laboratory friction experiments. The gouge deformed at 10 μm/s deforms with a steady state friction coefficient of $\mu \approx 0.49$. The stress values plotted in a normal stress vs. shear stress diagram, are distributed in a straight line concordant with the Coulomb criterion (Fig. 4b) and indicative of a deformation mainly controlled by the frictional properties of fault rock. With slide-hold-slide tests we observed moderate to high healing rates ($0.0032 < \beta < 0.0072$) and velocity neutral or slightly velocity strengthening behavior is documented with velocity stepping tests (Fig. 4). These results are consistent with data from studies on gouge with similar mineral assemblages (Tembe et al., 2010; Ikari et al., 2011; Volpe et al., 2022b), which consisted of a mixture of abundant granular minerals (quartz and feldspars, 78%) and phyllosilicates (muscovite with minor chlorite and biotite; 22%). The high quartz and feldspar content allows for the development of a load-bearing granular framework which supports most of the deformation (Fig. 6c). Indeed, moderately high friction and healing rates suggest that the main deformation mechanism is cataclasis (e.g., Sibson, 1977; Marone and Scholz, 1988; Scholz, 2019). Positive healing corresponds to growth of contact area at asperities (grain contact junction) with hold time (Dieterich and Kilgore, 1994; Marone, 1998). However, the slightly lower values of friction and healing rates compared to those measured on granite powders with similar composition (e.g., Carpenter et al., 2016) can be interpret as the result of the influence of sheet silicates in the fine fraction of the MC fault gouge. Furthermore, the MC fault gouge presents slightly positive *a-b* values, different from the rate-weakening behavior expected for granite bare surfaces and gouges (e.g., Marone et al., 1990; Ikari et al., 2011). This interpretation is supported by microstructures that depicts a fabric within the principal shear zone, where the granular fraction is weakly affected by grain-size reduction and is

discontinuously embedded and mantled by the more comminuted phyllosilicate-rich matrix (Fig. 5d, e). This suggests that cataclasis is the main deformation mechanism, but also that part of the deformation is accommodated by frictional sliding along the phyllosilicates foliae, thus reducing hard interaction within granular fraction (e.g., Saffer and Marone, 2003; Collettini et al., 2009; Niemeijer et al., 2010; Giorgetti et al., 2015; Volpe et al., 2022b). These microstructures shed light on the interpretation of the experimentally measured fault permeability. The gouge, in the injection experiment, displayed a fault perpendicular permeability in the order of $10^{-17}$ to $10^{-16}$ $m^2$. These values are in agreement with the permeability of gouges of similar mineralogical composition tested at similar boundary conditions (e.g., Crawford et al., 2008; Ikari et al., 2009). Purely granular gouges display values of permeability generally higher than $10^{-16}$ $m^2$ (e.g., Crawford et al., 2008). It is in fact known that fault gouge permeability decreases with increasing phyllosilicate content (e.g., Saffer and Marone, 2003; Crawford et al., 2008; Ikari et al., 2009). In our case, the phyllosilicate content (22%) is sufficiently high to promote such a permeability reduction. We also measured permeability before and after the injection phase (Fig. 3b stage 4 and 6), yielding a permeability of $9.32*10^{-17}$ $m^2$ (10 mm of slip) and $2.91\times10^{-17}$ $m^2$ (20 mm of slip), respectively. We interpret this as the effect of grain size reduction and porosity decrease of the PSZ with increasing strain (e.g., Faulkner and Rutter, 2003; Ikari et al., 2009; Scuderi et al., 2017), accumulated especially during the dynamic reactivation phase (10 mm). Incremental deformation may also favor interconnection of the phyllosilicate matrix, resulting in similar observations (e.g., Fig. 6c, d, e, e.g., Ikari et al., 2009). Notably, the yielded permeability values agree with the in-situ permeability measurements made on faults within similar crystalline rocks (Shapiro et al., 1997; Achtziger-Zupančič et al., 2017; Schoenball et al., 2018).

## 6.2 Fault slip behavior during pressurization

During stage 1 of the injection test (Fig. 3b), the gouge attained a frictional strength concordant with the frictional strength obtained from the Coulomb envelope at room pressure and water saturated conditions (Fig. 4b and Fig. 5a). During stage 5 of the experiment (Fig. 3b), the fault exhibited the typical trimodal creep behavior which has been previously described (e.g., Scuderi et al., 2017 and references therein). The first phase is associated with decelerating creep and lasted nine steps of fluid injection (corresponding to a pore fluid pressure increase of 1.8 MPa). Throughout decelerating creep, the fault is characterized by gradual compaction due to fabric rearrangement favored by closure of small cracks and changes in grain arrangement (e.g., Samuelson et al., 2009; Ikari et al., 2009; Scuderi et al., 2017). Here, the gouge reached a stationary layer thickness that corresponds to a steady state porosity and fabric (e.g., Marone et al., 1998; Ikari et al., 2009; 2011; Scuderi et al., 2017). This stationary layer thickness resulted also from the balance

between fluid injection induced dilatancy and the overall gouge compaction (e.g., Scuderi and Collettini, 2018 and Fig. SI.5 in Supporting Information). The second phase is associated to steady-state creep, during which the fault slides at a nearly constant velocity of ~3.5 nm/s (Fig. 5d). This creeping velocity is in the range of the steady-state creep velocity observed for granular-rich gouges (carbonates) in similar creep experiments (Scuderi et al., 2017). The onset of steady-state creep occurred in correspondence of the onset of dilation (Fig. 5c and Fig. SI.5 and SI.6 in Supporting Information). During the steady-state creep the fault crossed its creep relaxation envelope ($\mu$ = 0.45, Fig. 5a). In correspondence to the crossing point, we observed a gentle increase in sliding velocity as well as a change in layer thickness evolution: from dilation-compaction modulated by fluid injection to continuous dilation (higher upon pressurization; lower following the pressurization step e.g., Fig. 5c and Fig. SI.5 in Supporting Information). Similar correspondence between layer thickness evolution and fault slip behavior was already observed in other works (e.g., French et al., 2016; Scuderi et al., 2017 and Scuderi and Collettini, 2018 and Fig. SI.6 in Supporting Information). As the stress state of the experimental fault crossed the failure envelope (Fig. 5a), the fault entered into accelerating creep phase, throughout which the gouge started sliding at increasing velocity, still strongly dilating (Fig. 5c). Further fluid injections promoted an exponential increase in fault slip velocity that resulted in dynamic frictional instability; during the dynamic reactivation the gouge dramatically compacted (Fig. 5c). The dynamic reactivation occurred at an effective normal stress of 8.4 MPa, that corresponds to a frictional strength of $\mu$ = 0.61 for the imposed constant shear stress of 5.25 MPa (Fig. 5a). This frictional strength value is 0.12 above the laboratory measured Coulomb envelope ($\mu$ = 0.49 ±0.006, Fig. 5a) corresponding to 0.9 MPa of shear stress above the reactivation criterion at the same normal stress. Several processes can act together to promote reactivation at higher frictional strength. These include, but are not limited to, the healing properties of the material (Fig. 4c), the slightly velocity strengthening behavior of the fault rock (Fig. 4d), the short time between fluid pressure steps not allowing the accelerating creep to evolve into a dynamic instability, and non-uniform pore fluid pressure distribution within the experimental fault (e.g., Passelegue et al., 2020).

### 6.3 Implications for fault reactivation and induced seismicity in the BedrettoLab

Rock deformation experiments, aimed at reproducing the injection protocol designed for the reactivation of the MC fault within the Bedretto laboratory, show that the MC fault can produce an earthquake instability upon pressurization. This instability occurs (Fig. 5b and d) even though the fault rock is characterized by a slightly velocity strengthening/velocity neutral behavior (Fig. 4d), and therefore within the rate and state frictional framework should experience stable sliding and fault creep (e.g., Marone and Scholz, 1988; Marone, 1998). Our interpretation for this

behavior is that during fluid pressure stimulation, the weakening induced by the increase of fluid pressure is higher than the velocity strengthening behavior of the material, and therefore a dynamic frictional instability is promoted. Similar results have been observed in other laboratory experiments, suggesting that changes in pore fluid pressure may overcome the frictional changes forecasted by classical RSF friction laws, hence exerting a strong influence on nucleation of earthquakes (Sawai et al., 2016; French et al., 2016; Scuderi et al., 2017; Proctor et al., 2020). Can we expect the same slip behavior for the natural MC fault within the Bedretto tunnel? To address this question, it is important to emphasize that our experiments reproduced ideal conditions, where the fault has a finite lateral extension and is characterized by homogeneous gouge distribution. These conditions allow a strong and direct control on the stress state (e.g., shear stress, normal stress, and fluid pressure), fault evolution (dilation/compaction, slip) within each phase of the experiment. In addition, we can supply a constant distribution of fluid pressure along the entire fault and induced fluid pressure steps that were distributed homogeneously throughout the entire fault structure. Within the natural MC fault, it is unrealistic to expect boundary conditions similar to those well-constrained in laboratory experiments. For example, lithological heterogeneities and multiple fault surfaces may affect stress distribution, and/or the widespread fracture system associated to the MC fault might limit the fluid pressure pulse to a restricted area. In other words, it will be difficult if not impossible to pressurize the entire MC fault in the same way of the 5x5cm wide experimental fault pressurized in our laboratory tests. Despite these important differences we think that the laboratory experiments can provide important insights into the hydromechanical coupling of the fault during fluid pressure stimulation and increase interpretability of the results once the MC fault will be stimulated in the BedrettoLab. From our rock deformation experiments we depicted two end-members scenarios for fluid pressure induced MC fault reactivation. In the first case, the pressurization rate is high enough to bring the stress state of the fault beyond the failure envelope (Fig. 7, red curve). This case can be also achieved for high injection rates, largely exceeding the hydraulic diffusivity of the fault zone, especially in the case of low fault permeability values (i.e., Rutter and Hackston, 2017; Passelegue et al., 2018; 2020; Wang et al., 2020; Ji et al., 2022a). Here, the weakening induced by fluid pressurization is sufficient to exceed the moderate velocity strengthening behavior of the gouge, and therefore promotes earthquake slip (e.g., Sawai et al., 2016; Scuderi et al., 2017; Proctor et al., 2020). This scenario is assimilable with what we observed in our rock deformation experiments (Fig. 5a) with the exception that, in laboratory experiments the shear stress is maintained constant until the onset of dynamic instability (Fig. 7, blue curve), whereas in the natural case, slip accommodated along the fault relieves progressively the shear stress. The load control of injection tests i.e., constant shear stress, prevents the reproduction of this behavior in rock deformation experiments in its entity, (Fig. 7, blue curve). In the second case,

the fracture system associated to the MC fault (as well as newly developed fractures) results in an overall high permeability that prevents significant fluid pressure to induce fault weakening, i.e., a reduction of the effective normal stress significantly beyond the failure envelope (Fig. 7, green curve). This case is also valid when a lower injection rate is applied to relatively lower permeabilities (i.e., French et al., 2016; Rutter and Hackston, 2017; Passelegue et al., 2018; 2020; Wang et al., 2020; Ji et al., 2022b). For these boundary conditions, our laboratory results predict that weakening induced by fluid pressure build-up is counteracted by the slight velocity strengthening behavior of the fault gouge and therefore fault creep or accelerated fault creep is the most likely slip behavior (Fig. 7, green curve). However, even in the second case, continued and accelerated creep may increase shear stress at the edges of the creeping zone and trigger instabilities (e.g., Guglielmi et al., 2015; Cappa et al., 2019) even on faults with a moderate velocity strengthening behavior (e.g., Boatwright and Cocco, 1996). This second case was recently recorded during hydraulic fracturing activities in Alberta, Canada (Eyre et al., 2019), where the accelerated creep, produced by the hydraulic stimulations of strongly velocity strengthening clay-rich lithologies (Scuderi and Collettini, 2018), promoted an increase of stress along neighboring faults contained within carbonatic rocks where earthquakes nucleated (Eyre et al., 2019).

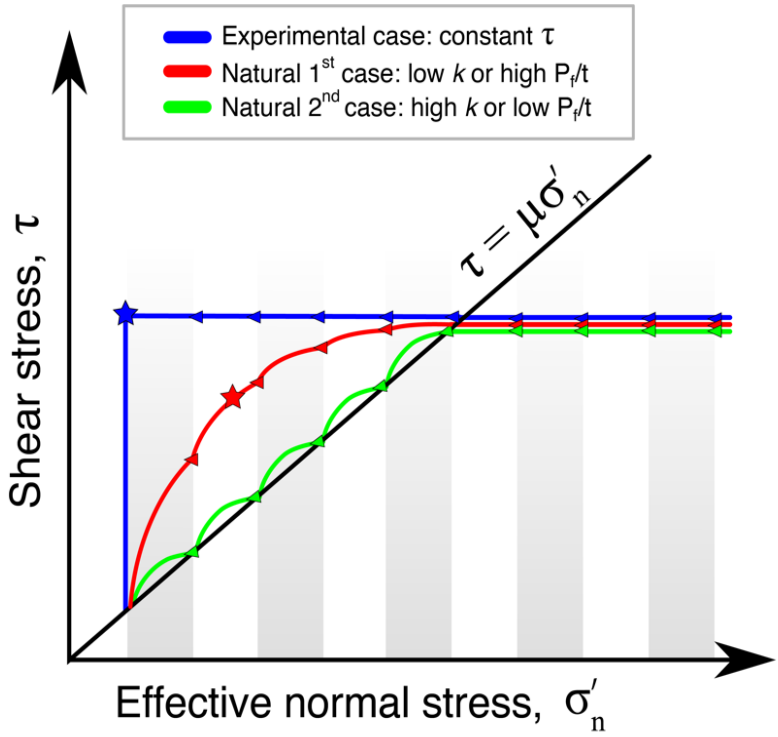


Fig. 7: Schematic evolution of the stress state during reactivation. Blu curve shows the experimental case where the shear stress is maintained constant until abrupt fault dynamic reactivation (blue star). Red curve represents the first scenario, where either the natural fault has low permeability (low *k*) or the injection rates (high $P_f/t$) are high enough to allow fluid pressure build-up beyond

the failure envelope and promote earthquake slip (red stars). Green curve represents the second scenario where the high permeability of the natural fault (high *k*) or low injection rates (low $P_f/t$) prevents fluid pressure build-up significantly beyond the failure envelope favoring fault creep or accelerated fault creep as the most likely slip behavior. Gray and white vertical bands represent steps of fluid pressure. Note that the figure is not in scale and stress paths have been exaggerated for representation purposes.

## 7 Conclusions

In this work, we have used structural geology and rock deformation experiments to characterize the main branch of the MC fault which has been selected to be reactivated via fluid pressure stimulations within the BedrettoLab (Switzerland). The MC fault is an old structure that accommodated deformation in the ductile field and was successively reactivated within the brittle field. The latter is testified by a narrow fault core with the presence of an unconsolidated, cataclastic fault gouge made of 78% of granular silicates (quartz, feldspars, and zeolites) and 22% of phyllosilicates (micas). Standard rock deformation frictional experiments conducted on the MC fault gouge depict a fault characterized by relatively high friction ($\mu$ = 0.49 ± 0.006), moderate/high healing rate and a moderate velocity strengthening/neutral behavior. Experiment designed to evaluate the slip behavior of the fault during fluid pressure stimulations shows that once the stress state approaches the failure envelope the fault starts to creep. For further weakening induced by fluid pressure builds-up, the fault experiences a dynamic instability irrespective of the rate-strengthening behavior of the gouge. We interpret that the fluid pressurization induced weakening overcomes the slightly rate strengthening behavior of the gouge promoting a laboratory earthquake during fluid pressure stimulation. Despite the important differences in boundary conditions between fluid-induced fault reactivation in rock deformation experiments and the natural MC fault in the Bedretto underground laboratory, rock deformation tests provide important insights to predict the slip behavior of the natural MC fault. We envision two possible end-member scenarios for the slip behavior of the MC fault during pressurization: In a first case, similar to rock deformation experiments, fluid injection remains localized and therefore fluid overpressure increments, in particular if they occur in short time, promote the weakening required to develop an earthquake instability. In the second case, the fracture system associated to the MC fault favors high permeability that prevent significant fluid pressure induced fault weakening. In this second case the weakening induced by fluid pressure build-up is counteracted by the slightly velocity strengthening behavior of the gouge and therefore fault creep is the most likely slip behavior. In this case, earthquakes are triggered by a possible increase of shear stress at the edges of the creeping zone. The reactivation of the MC fault in the Bedretto tunnel will be a unique opportunity to test these hypotheses, revisit the interpretations of fault slip behaviors and better address further research activities on induced

seismicity and in general on earthquake physics. The results of the current study contribute to fill the gap between laboratory measurements on experimental faults and observations at the BedrettoLab-scale on a natural fault.

## 8 Acknowledgement

We thank the BedrettoLab team to give us the opportunity to work in the tunnel. We also thank D. Mannetta for his help with thin sections preparation and M. Nazzari for the support at the SEM-INGV laboratory. This study has received funding from the European Research Council (ERC) under the European Union's Horizon 2020 research and innovation program. M. Cocco and D. Giardini participated in this work as Principal Investigators of the Horizon 2020 ERC project FEAR (grant 856559). G. Pozzi, E. Spagnuolo, P. Achtziger-Zupancic, A. Zappone and M.A. Meier participated in this work in the framework of the ERC project FEAR. We thank A. Ceccato and the FEAR Geology Working Group for providing information and helpful discussion. This research was also supported by ERC grant Nr. 259256 GLASS and Ateneo 2018 to C. Collettini. We also thank J. Mecklenburgh, Yinlin Ji, and an anonymous Reviewer for their constructive reviews that increase the quality of the manuscript.

# 5 Conclusions

In this PhD thesis, I investigated the seismogenic potential of phyllosilicate-rich fault in four cases study that encompass a large gamut of geological settings: from laboratory to nature, from natural to induced seismicity, from the top to the base of the seismogenic zone, and from extensional to compressive tectonic. The use of an interdisciplinary approach that integrated together rock deformation experiments, structural geology, microstructural, and seismological analysis provided the opportunity to understand the role and the seismogenic potential of phyllosilicate-rich faults in each of the case studies.

In the first chapter I investigated the role of fault fabric in influencing the frictional properties of phyllosilicate-granular mixtures. In this work I integrated an extensive literature review of brittle fault fabric with the results of new frictional and microstructural analysis. In this work I highlight that Y-B-P-R and S-C-C' fabrics represent two endmembers associated respectively to frictionally strong and weak faults. I argue that the transition from one fabric to the other is controlled by the amount of phyllosilicates together with processes that favor their mobility, with the main effect to develop a weak interconnected network of well-oriented planes. These observations suggest that the fault fabric is a crucial controlling factor of the bulk mechanical properties of faults. Furthermore, I presented a systematic and in detail analysis of secondary fabric features such as the shape of grains, the foliation regularity, the mantling of grains, and foliation flattening. These secondary features can promote with strain sensible changes in the frictional properties of the fault, such as the transition from velocity strengthening to velocity weakening behavior. The potential of these observations need confirmation from further studies with increased microstructural documentation.

In the second chapter, I investigated the role of the phyllitic basement in the seismo-tectonic context of the Central Apennines. In this work I show that this heterogeneous domain is characterized by the presence of a weak phyllosilicate-rich matrix that envelope strong quartz-rich lenses, which result in complex mechanical behavior. The integration of experimental results with field structural analysis suggests that the seismogenic activity results from the mechanical interplay between each component of the fault zone. Most of the tectonic motion is accommodated by the phyllosilicate-rich matrix that, due to its frictional properties (low friction, low healing rate, and velocity strengthening), deforms by aseismic creep while lenses act as low-strain domains. However, during transient high loading rates, the matrix and the lenses show different deformation styles: the phyllosilicate-rich matrix deforms by accelerated aseismic

creep whereas the quartz-rich lenses reactivate by dynamic failure into seismic slip. The integration of the structural, frictional, and seismological analysis suggests that an increase in tectonic loading-rates favors an accelerated creep within the matrix, which transfer stress to the lenses and consequently promotes seismic swarms of repeating earthquakes organized in small clusters. These results provide complementary and supporting evidence to the seismological observation of clusters of repeating earthquakes, which are interpreted as the result of repeated ruptures of discrete structures loaded by surrounding fault creep (Nadeau et al., 1994; Igarashi et al., 2003; Avouac, 2015; Uchida and Bürgmann, 2019). Moreover, the results also highlight how transient changes in the tectonic loading-rate can results in a switch from stable to unstable slip along complex faults (e.g., Fagereng and Beall, 2019; Im et al., 2022; Passelegue et al., 2022), providing an interpretation of the triggering of seismic swarms (e.g., Vidale and Shearer, 2006; Toda et al., 2002). Overall, these findings emphasize how structural, frictional, and stress-strain heterogeneities are fundamental aspects for understanding fault slip behavior of heterogeneous fault zones.

In Chapter III, I investigated the occurrence of seismicity along the shallow portions of subduction megathrusts. New frictional experiments performed on clay-rich fault gouge at the boundary conditions typical of shallow subduction zones show that, despite having a bulk rate-strengthening behavior and null healing rate, the clay-rich fault material can contemporaneously creep and nucleate spontaneously slow slip events. These instabilities, imaged by a new analytical technique, are slow slip events nucleating and propagating within a thin shear zone, driven by structural and stress heterogeneities. The integration of the results of mechanical, microstructural, and image analysis, suggest that seismicity in phyllosilicate-rich weak faults is controlled by fault fabric, stress heterogeneities, and alternative frictional mechanisms. These results offer a new and unexplored perspective on the seismogenic potential frictionally weak faults with significant implications for seismic hazard.

Finally, in chapter IV I investigated the seismogenic potential of phyllosilicate-rich faults in the context of induced seismicity linked to the new techniques of geo-energy exploitation such as the Enhanced Geothermal System (EGS). For this objective, I assessed the seismogenic potential of the selected fault for fluid-induced reactivation experiments within the framework of the “Fault Activation and Earthquake Rupture” project (FEAR) at the BedrettoLab (Rotondo Massif, Swiss Alps). In this work I show that a fault, even if characterized by rate-strengthening behavior, can be dynamically reactivated by fluid injection activities. This counterintuitive behavior is the result of the interplay between frictional, permeability, and microstructural properties of the fault: if the weakening induced by the fluid pressure build-up is stronger than the velocity strengthening behavior of the material, dynamic frictional instabilities are promoted.

This scenario can be achieved only if the injection rate is high enough to bring the stress state of the fault beyond the failure envelope or if the injection rates largely exceed the hydraulic diffusivity of the fault zone, especially in the case of low fault permeability (Rutter and Hackston, 2017; Passelegue et al., 2018, 2020; Wang et al., 2020; Ji et al., 2022a). This condition can be achieved if the fault gouge has an amount of phyllosilicates sufficient to produce an interconnected network which sensibly reduces fault permeability, as observed in the experimental microstructures. The results of this last study emphasize how structural, microstructural, permeability, and frictional properties can favor seismic reactivation of faults that should slip aseismically.

# 6 Open questions

This PhD thesis provides new observations and data about the seismogenic potential of phyllosilicate-rich faults in different contexts from experimental to natural and induced seismicity. Frictional, structural, microstructural, and permeability properties of phyllosilicate-rich faults have been carefully investigated to understand their role in fault slip behavior. Major findings are:

I) The evolution of fault fabric can promote significative changes in the frictional properties of phyllosilicate-rich rocks.

II) The interplay between structural and frictional heterogeneities controls the seismogenic behavior of rheologically heterogenous phyllosilicate-rich fault zones.

III) Phyllosilicate-rich faults can exhibit complex slip behavior where slow frictional instabilities coexist with stable sliding.

IV) Fabric and permeability can have a primary control on the fault slip behavior of phyllosilicate-rich faults subjected to fluid injection activities.

These findings offer a new perspective on the seismogenic potential of phyllosilicate-rich faults with significant implications for earthquake mechanisms and seismic hazard. However, there are still some unresolved aspects that deserve to be addressed in future research. These include, but are not limited to:

a) Systematic analysis of the effects of secondary microstructural features on the mechanical properties of phyllosilicate-rich faults.

b) A better understanding of the deformation mechanisms of rheologically heterogeneous faults.

c) The effect of alternative mechanical processes such as cohesion, adhesion, and plowing on the frictional fault slip behavior.

d) A better understanding of the effect of fluid pressure on the rate and state frictional properties.

These unresolved aspects might be investigated in the future thanks to a multidisciplinary approach that also involves new experimental apparatuses and techniques together with numerical modeling and machine-learning.

For point a), future developments concern the integration of the canonical analytical framework represented by microstructural and frictional analysis, with new approaches such as the one represented by Acoustic Emissions, AEs analysis. During fault deformation, AEs analysis allows to track continuously the emissions of acoustic waves produced by micro-mechanical processes such as grain fracturing, breaking of force chains, and micro-slip events. Since this method allows continuous recording, it can provide unique insights about the evolution with deformation of the microstructures and relative mechanisms, in a complementary way, microstructural analysis which gives mainly static information. Another possible output of this integration can also be represented by a new and all-around interpretative model of the deformation processes at play during frictional experiments, in which AEs attributes can be related to specific microstructural and frictional features.

Future horizons about our understanding of the deformation mechanisms of rheologically heterogeneous faults are provided by new techniques and investigation methods. New-generation 3D printers are capable of using geological instead of plastic materials. This provides the possibility to build experimental samples with specific geometries and made of specific geo-materials (with well constrained mechanical properties). This possibility allows down-scale to the lab-scale structures and geometries that can be found in the field. If geometrical properties such as the distribution of strong lenses or patches in a rheologically heterogenous fault influences the distribution of seismicity, reproducing in the lab that geometry should produce a similar seismicity distribution of AEs as in the natural case. Furthermore, the application of the novel experimental technique of direct fault imaging, illustrated in Chapter III, will be of great support for understanding in the lab the interplay between fault heterogeneities and rupture dynamics. Moreover, new numerical models can reproduce the mechanical and seismic behavior of rheologically heterogeneous faults in realistic boundary conditions over multiple seismic cycles removing the stumbling block represented by time in laboratory experiments (e.g., Fagereng and Beall, 2021; Beall et al., 2022; Casas et al., 2023). The integration of the results of these analytical techniques together with machine-learning will provide realistic, unique, and high-resolution details regarding the deformation mechanisms of rheologically heterogenous faults with a direct correlation to nature.

In Chapter III, emerged the importance of alternative frictional mechanisms such as adhesion in influencing the frictional properties and therefore the experimental fault slip behavior. Adhesion, together with other mechanisms such as cohesion and plowing coexist with the canonical frictional mechanisms (e.g., Scholz and Engelder, 1976; Scholz, 2019) and are capable to strongly influence the style of reactivation of both natural and experimental faults (Ikari and Hupers, 2021; Pozzi et al., 2022). Phyllosilicates are minerals with high surface energy which is a property generally related to

their adhesive behavior (Miller, 2010). Minerals such as calcite and anhydrites, are strongly reactive to aqueous fluids with specific chemistry. Their reactivity can enhance cementation, increasing the cohesion of a fault, therefore its strength. This can lead to a change of style of reactivation, from aseismic to seismic (Ikari and Hupers, 2021; Pozzi et al., 2022). Large displacement crustal faults, such as plate boundary faults and subduction megathrusts juxtapose rocks with different mechanical and frictional properties producing rheological heterogeneities (e.g., Fagereng and Sibson, 2010; Zoback et al., 2011; Collettini et al., 2011; Tesei et al., 2014; Fagereng and Beall, 2021). In some cases, strong and stiff rocks are put directly in contact with weak and soft rocks, these last accommodating most of the deformation (e.g., Fagereng and Sibson, 2010; Tesei et al., 2013). The interface between these two rock-types can be rough at different length-scales (Wang and Bilek, 2014; Candela and Brodsky, 2016) and shearing along such interfaces can results in a frictional behavior strongly influenced by plowing and wearing (e.g., Scholz and Engelder, 1976; Dieterich and Smith, 2010; Scholz, 2019; Gounon et al., 2022). Knowing how geometrical heterogeneities control the frictional response of a fault, thus the fault slip behavior, is of crucial importance, since most of the largest and seismically active faults worldwide are characterized by complex geometries (e.g., Sibson, 1985; Okubo and Aki, 1987; Wang and Bilek, 2014; Schmittbuhl et al., 2016).

The last point (point d) represents one of the long-lasting questions of fault mechanics: which is the role of fluid pressure on fault slip behavior? Several theoretical and experimental works showed and proposed different and sometimes contrasting effects of fluid pressure on fault slip behavior (Segall and Rice, 1995; Scuderi and Collettini, 2016; Faulkner et al., 2018). A fundamental improvement in this topic would be to understand the micro-mechanisms behind changes in the rate and state frictional properties caused by changes in fluid pressure. This goal can be achieved by the development of new experimental techniques and assemblies that allow probing with high-resolution and directly on-fault fluid pressure changes (e.g., Passelegue et al., 2018; Proctor et al., 2020; Brantut, 2020) together with changes in fault-parallel and perpendicular permeability. The integration of these observations with mechanical and microstructural observations, will provide an integrated fault model, where all these features are strongly coupled. Also in this case, numerical and machine learning techniques will offer fundamental support for the building and validation of this integrated fault model.

# 7 References


Achtziger-Zupančič, P., Loew, S., & Mariethoz, G. 2017. A new global database to improve predictions of permeability distribution in crystalline rocks at site scale. Journal of Geophysical Research: Solid Earth, 122(5), 3513-3539.

Agliardi, F., Scuderi, M. M., Fusi, N., & Collettini, C. 2020. Slow-to-fast transition of giant creeping rockslides modulated by undrained loading in basal shear zones. Nature communications, 11(1), 1-11.

Aldinucci, M., Gandin, A., & Sandrelli, F. 2008. The Mesozoic continental rifting in the Mediterranean area: insights from the Verrucano tectofacies of southern Tuscany (Northern Apennines, Italy). International Journal of Earth Sciences, 97(6), 1247-1269.

Anderlini, L., Serpelloni, E., & Belardinelli, M. E. 2016. Creep and locking of a low-angle normal fault: Insights from the Altotiberina fault in the northern Apennines (Italy). Geophysical Research Letters, 43(9), 4321-4329.

Andrews, D. J., & Ben-Zion, Y. 1997. Wrinkle-like slip pulse on a fault between different materials. Journal of Geophysical Research: Solid Earth, 102(B1), 553-571.

Anelli L., Gorza M., Pieri M. & Riva M. 1994. Subsurface well data in the Northern Apennines (Italy). Mem. Soc. Geol. It., 48, 461-471.

Anthony, J. L., & Marone, C. 2005. Influence of particle characteristics on granular friction. Journal of Geophysical Research: Solid Earth, 110(B8).

Aretusini, S., Mittempergher, S., Plümper, O., Spagnuolo, E., Gualtieri, A. F., & Di Toro, G. 2017. Production of nanoparticles during experimental deformation of smectite and implications for seismic slip. Earth and Planetary Science Letters, 463, 221-231.

Arnet, M. 2021. Deep Alpine Fluids: Origin, Pathways and dynamic remobilisation in response to hydraulic stimulations at the Bedretto Underground Laboratory for Geoenergies (BULGG) - (Master's thesis).

Avouac, J. P. 2015. From geodetic imaging of seismic and aseismic fault slip to dynamic modelling of the seismic cycle. Annual Review of Earth and Planetary Sciences, 43, 233-271.

Baccheschi, P., De Gori, P., Villani, F., Trippetta, F., & Chiarabba, C. 2020. The preparatory phase of the Mw 6.1 2009 L'Aquila (Italy) normal faulting earthquake traced by foreshock time-lapse tomography. Geology, 48(1), 49-55.

Bally, A. W., Burbi, L., Cooper, C., and Ghelardoni, R. 1986. Balanced cross-sections and seismic reflection profiles

across the central Apennines. Memorie della Società Geologica Italiana, 35, 257–310.

Barbot, S. 2022. A Rate-, State-, and Temperature-Dependent Friction Law With Competing Healing Mechanisms. Journal of Geophysical Research: Solid Earth, 127(11), e2022JB025106.

Barchi, M. R., De Feyter, A., Magnani, M. B., Minelli, G., Pialli, G., & Sotera, M. 1998. The structural style of the Umbria-Marche fold and thrust belt. Memorie della Società Geologica Italiana, 52, 557–578.

Barchi, M. R., & Collettini, C. 2019. Seismicity of central Italy in the context of the geological history of the Umbria-Marche Apennines. In C. Koeberl, and D. M. Bice (Eds.), 250 Million Years of Earth History in Central Italy: Celebrating 25 Years of the Geological Observatory of Coldigioco. (Vol. 542, p.p. 175–190). Geological Society of America Special Paper.

Barchi, M. R., Carboni, F., Michele, M., Ercoli, M., Giorgetti, C., Porreca, M., S. Azzaro & Chiaraluce, L. 2021. The influence of subsurface geology on the distribution of earthquakes during the 2016-–2017 Central Italy seismic sequence. Tectonophysics, 807, 228797.

Barth, N. C., Boulton, C., Carpenter, B. M., Batt, G. E., & Toy, V. G. 2013. Slip localization on the southern Alpine fault, New Zealand. Tectonics, 32(3), 620-640.

Bartlett, W. L., Friedman, M., & Logan, J. M. 1981. Experimental folding and faulting of rocks under confining pressure Part IX. Wrench faults in limestone layers. Tectonophysics, 79(3-4), 255-277.

Baumberger, T., Heslot, F., & Perrin, B. 1994. Crossover from creep to inertial motion in friction dynamics. Nature, 367(6463), 544-546.

Beall, A., Fagereng, Å., & Ellis, S. 2019. Strength of strained two-phase mixtures: Application to rapid creep and stress amplification in subduction zone mélange. Geophysical Research Letters, 46(1), 169-178.

Bedford, J. D., & Faulkner, D. R. 2021. The role of grain size and effective normal stress on localization and the frictional stability of simulated quartz gouge. Geophysical Research Letters, 48(7), e2020GL092023.

Bedford, J. D., Faulkner, D. R., & Lapusta, N. 2022. Fault rock heterogeneity can produce fault weakness and reduce fault stability. Nature communications, 13(1), 1-7.

Beeler, N. M., Tullis, T. E., Blanpied, M. L., & Weeks, J. D. 1996. Frictional behavior of large displacement experimental faults. Journal of Geophysical Research: Solid Earth, 101(B4), 8697-8715.

Bell, R., Holden, C., Power, W., Wang, X., & Downes, G. 2014. Hikurangi margin tsunami earthquake generated by slow seismic rupture over a subducted seamount. Earth and Planetary Science Letters, 397, 1-9.

Behnsen, J., & Faulkner, D. R. 2012. The effect of mineralogy and effective normal stress on frictional strength of sheet

silicates. Journal of Structural Geology, 42, 49-61.

Ben-Zion, Y., & Sammis, C. G. 2013. Shear heating during distributed fracturing and pulverization of rocks. Geology, 41(2), 139-142.

Berthé, D., Choukroune, P., & Jégouzo, P. 1979. Orthogneiss, mylonite and non coaxial deformation of granites: the example of the South Armorican Shear Zone. Journal of Structural Geology, 1(1), 31-42.

Beynon, J., and Faulkner, D. 2020. Dry, damp, or drenched? The effect of water saturation on the frictional properties of clay fault gouges. Journal of Structural Geology, 140, 104094.

Biegel, R. L., Sammis, C. G., & Dieterich, J. H. 1989. The frictional properties of a simulated gouge having a fractal particle distribution. Journal of Structural Geology, 11(7), 827-846.

Bigi, S., Casero, P., Chiarabba, C., & Di Bucci, D. 2013. Contrasting surface active faults and deep seismogenic sources unveiled by the 2009 L'Aquila earthquake sequence (Italy). Terra Nova, 25(1), 21-29.

Bilek, S. L., & Lay, T. 2002. Tsunami earthquakes possibly widespread manifestations of frictional conditional stability. Geophysical Research Letters, 29(14), 18-1.

Bilek, S. L., & Engdahl, E. R. 2007. Rupture characterization and aftershock relocations for the 1994 and 2006 tsunami earthquakes in the Java subduction zone. Geophysical Research Letters, 34(20).

Blanpied, M. L., Marone, C. J., Lockner, D. A., Byerlee, J. D., & King, D. P. 1998. Quantitative measure of the variation in fault rheology due to fluid-rock interactions. Journal of Geophysical Research: Solid Earth, 103(B5), 9691-9712.

Boatwright, J., & Cocco, M. 1996. Frictional constraints on crustal faulting. Journal of Geophysical Research: Solid Earth, 101(B6), 13895-13909.

Bortolotti, V., Fazzuoli, M., Pandeli, E., Principi, G., Babbini, A., & Corti, S. 2001. Geology of central and eastern Elba Island, Italy. Ofioliti, 26(2a), 97-150.

Bos, B., Peach, C. J., & Spiers, C. J. 2000. Frictional-viscous flow of simulated fault gouge caused by the combined effects of phyllosilicates and pressure solution. Tectonophysics, 327(3-4), 173-194.

Bos, B., & Spiers, C. J. 2001. Experimental investigation into the microstructural and mechanical evolution of phyllosilicate-bearing fault rock under conditions favouring pressure solution. Journal of Structural Geology, 23(8), 1187-1202.

Bowden, F. P., and Tabor, D. 1950. The Friction and Lubrication of Solids: Part 1. Oxford: Clarendon Press.

Byerlee, J. 1978. Friction of rocks. Pure Appl. Geophys. 116, 615–626.

Brace, W. F., & Kohlstedt, D. L. 1980. Limits on lithospheric stress imposed by laboratory experiments. Journal of Geophysical Research: Solid Earth, 85(B11), 6248-6252.

Brantut, N. 2020. Dilatancy-induced fluid pressure drop during dynamic rupture: Direct experimental evidence and consequences for earthquake dynamics. Earth and Planetary Science Letters, 538, 116179.

Bröker, K., & Ma, X. 2022. Estimating the least principal stress in a granitic rock mass: systematic mini-frac tests and elaborated pressure transient analysis. Rock Mechanics and Rock Engineering, 55(4), 1931-1954.

Bürgmann, R. 2018. The geophysics, geology and mechanics of slow fault slip. Earth and Planetary Science Letters, 495, 112-134.

Buttinelli, M., Petracchini, L., Maesano, F. E., D'Ambrogi, C., Scrocca, D., Marino, M., Capotorti, F., Bigi, S., Cavinato, G.P., Mariucci, M.T., Montone, P. & Di Bucci, D. 2021. The impact of structural complexity, fault segmentation, and reactivation on seismotectonics: Constraints from the upper crust of the 2016–2017 Central Italy seismic sequence area. Tectonophysics, 810, 228861.

Caine, J. S., Evans, J. P., & Forster, C. B. 1996. Fault zone architecture and permeability structure. Geology, 24(11), 1025-1028.

Cappa, F., Scuderi, M. M., Collettini, C., Guglielmi, Y., & Avouac, J. P. 2019. Stabilization of fault slip by fluid injection in the laboratory and in situ. Science advances, 5(3), eaau4065.

Carminati, E., & Doglioni, C. 2012. Alps vs. Apennines: the paradigm of a tectonically asymmetric Earth. Earth-Science Reviews, 112(1-2), 67-96.

Carminati, E., Lustrino, M., & Doglioni, C. 2012. Geodynamic evolution of the central and western Mediterranean: Tectonics vs. igneous petrology constraints. Tectonophysics, 579, 173-192.

Carpenter, B. M., Marone, C., & Saffer, D. M. 2011. Weakness of the San Andreas Fault revealed by samples from the active fault zone. Nature Geoscience, 4(4), 251-254.

Carpenter, B. M., Scuderi, M. M., Collettini, C., & Marone, C. 2014. Frictional heterogeneities on carbonate-bearing normal faults: Insights from the Monte Maggio Fault, Italy. Journal of Geophysical Research: Solid Earth, 119(12), 9062-9076.

Carpenter, B. M., Saffer, D. M., & Marone, C. 2015. Frictional properties of the active San Andreas Fault at SAFOD: Implications for fault strength and slip behaviour. Journal of Geophysical Research: Solid Earth, 120(7), 5273-5289.

Carpenter, B. M., Ikari, M. J., & Marone, C. 2016. Laboratory observations of time-dependent frictional strengthening

and stress relaxation in natural and synthetic fault gouges. Journal of Geophysical Research: Solid Earth, 121(2), 1183-1201.

Carpenter, B. M., Collettini, C., Viti, C., & Cavallo, A. 2016. The influence of normal stress and sliding velocity on the frictional behaviour of calcite at room temperature: insights from laboratory experiments and microstructural observations. Geophysical Journal International, 205(1), 548-561.

Casas, N., Mollon, G., & Daouadji, A. 2023. Influence of Grain-Scale Properties on Localization Patterns and Slip Weakening Within Dense Granular Fault Gouges. Journal of Geophysical Research: Solid Earth, 128(3), e2022JB025666.

Cassinis, G., Perotti, C., & Santi, G. 2018. Post-Variscan Verrucano-like deposits in Italy, and the onset of the alpine tectono-sedimentary cycle. Earth-Science Reviews, 185, 476-497.

Cebry, S. B. L., Ke, C. Y., Shreedharan, S., Marone, C., Kammer, D. S., & McLaskey, G. C. 2022. Creep fronts and complexity in laboratory earthquake sequences illuminate delayed earthquake triggering. Nature communications, 13(1), 6839.

Ceccato, A., Behr, W. M., & Zappone, A. S. 2023. The mechanical evolution of the European continental crust through the Alpine orogenic cycle: insights from the Rotondo granite (Gotthard massif, Central Swiss Alps) (No. EGU23-8225). Copernicus Meetings.

Centamore, E., Deiana, G., Micarelli, A., & Potetti, M. 1986. Il Trias-Paleogene delle Marche.

Chen, W. P., & Molnar, P. 1983. Focal depths of intracontinental and intraplate earthquakes and their implications for the thermal and mechanical properties of the lithosphere. Journal of Geophysical Research: Solid Earth, 88(B5), 4183-4214.

Cheng, Y., & Ben-Zion, Y. 2019. Transient brittle-ductile transition depth induced by moderate-large earthquakes in southern and Baja California. Geophysical Research Letters, 46(20), 11109-11117.

Chester, F. M., Friedman, M., & Logan, J. M. 1985. Foliated cataclasites. Tectonophysics, 111(1-2), 139-146.

Chester, F. M., & Logan, J. M. 1987. Composite planar fabric of gouge from the Punchbowl Fault, California. Journal of Structural Geology, 9(5-6), 621-IN6.

Chester, F. M., & Higgs, N. G. 1992. Multimechanism friction constitutive model for ultrafine quartz gouge at hypocentral conditions. Journal of Geophysical Research: Solid Earth, 97(B2), 1859-1870.

Chester, F. M., Evans, J. P., & Biegel, R. L. 1993. Internal structure and weakening mechanisms of the San Andreas fault. Journal of Geophysical Research: Solid Earth, 98(B1), 771-786.

Chiarabba, C., Amato, A., Anselmi, M., Baccheschi, P., Bianchi, I., Cattaneo, M., Cerere, G., Chiaraluce, L., Ciaccio, M. G., De Gori, P., De Luca, G., Di Bona, M., Di Stefano, R., Faenza, L., Govoni, A., Improta, L., Lucente, F. P., Marchetti, A., Margheriti, L., Mele, F., Michelini, A., Monachesi, G., Moretti, M., Pastori, M., Piana Agostinetti, N., Piccinini, D., Roselli, P., Seccia, D., & Valoroso, L. 2009. The 2009 L'Aquila (central Italy) MW6.3 earthquake: Main shock and aftershocks. Geophysical Research Letters, 36(18).

Chiarabba, C., De Gori, P., Improta, L., Lucente, F. P., Moretti, M., Govoni, A., Di Bona, M., Margheriti, L., Marchetti, A. & Nardi, A. 2014. Frontal compression along the Apennines thrust system: The Emilia 2012 example from seismicity to crustal structure. Journal of Geodynamics, 82, 98-109.

Chiaraluce, L., Ellsworth W. L., Chiarabba, C., & Cocco, M. 2003. Imaging the complexity of an active normal fault system: the 1997 Colfiorito (central Italy) case study. Journal of Geophysical Research, 108(B6), doi:10.1029/2002jb002166.

Chiaraluce, L., Chiarabba, C., Collettini, C., Piccinini, D., & Cocco, M. 2007. Architecture and mechanics of an active low-angle normal fault: Alto Tiberina fault, northern Apennines, Italy. Journal of Geophysical Research: Solid Earth, 112(B10).

Chiaraluce, L., Barchi, M. R., Carannante, S., Collettini, C., Mirabella, F., Pauselli, C., & Valoroso, L. 2017. The role of rheology, crustal structures and lithology in the seismicity distribution of the northern Apennines. Tectonophysics, 694, 280-291.

Chiaraluce, L., Di Stefano, R., Tinti, E., Scognamiglio, L., Michele, M., Casarotti, E., Cattaneo, M., De Gori, P., Chiarabba, C., Monachesi, G., Lombardi, A., Valoroso, L., Latorre, D., & Marzorati, S. 2017. The 2016 central Italy seismic sequence: A first look at the mainshocks, aftershocks, and source models. Seismological Research Letters, 88(3), 757-771.

Cladouhos, T. T. 1999. Shape preferred orientations of survivor grains in fault gouge. Journal of Structural Geology, 21(4), 419-436.

Cocco, M., Aretusini, S., Cornelio, C., Nielsen, S. B., Spagnuolo, E., Tinti, E., & Di Toro, G. 2023. Fracture energy and breakdown work during earthquakes. Annual Review of Earth and Planetary Sciences, 51.

Collettini, C., & Barchi, M. R. 2002. A low-angle normal fault in the Umbria region (Central Italy): a mechanical model for the related microseismicity. Tectonophysics, 359(1-2), 97-115.

Collettini, C., & Holdsworth, R. E. 2004. Fault zone weakening and character of slip along low-angle normal faults: insights from the Zuccale fault, Elba, Italy. Journal of the Geological Society, 161(6), 1039-1051.

Collettini, C., Niemeijer, A., Viti, C., Marone, C.J., 2009b. Fault zone fabric and fault weakness. Nature 462, 907–910.

Collettini, C., Niemeijer, A., Viti, C., Smith, S.A., Marone, C. 2011b. Fault structure, frictional properties and mixed-mode fault slip behaviour. Earth Planet Sci. Lett. 311 (3–4), 316–327.

Collettini, C., Di Stefano, G., Carpenter, B., Scarlato, P., Tesei, T., Mollo, S., Trippetta, F., Marone, C., Romeo, G. & Chiaraluce, L. 2014. A novel and versatile apparatus for brittle rock deformation. International journal of rock mechanics and mining sciences, 66, 114-123.

Collettini, C., Tesei, T., Scuderi, M.M., Carpenter, B.M., Viti, C. 2019. Beyond Byerlee friction, weak faults, and implications for slip behaviour. Earth Planet Sci. Lett. 519, 245–263.

Crawford, B. R., Faulkner, D. R., & Rutter, E. H. 2008. Strength, porosity, and permeability development during hydrostatic and shear loading of synthetic quartz-clay fault gouge. Journal of Geophysical Research: Solid Earth, 113(B3).

Cresta, S., Monechi, S., & Parisi, G. 1989. Stratigrafia del mesozoico e cenozoico nell'area umbro-marchigiana. Memorie descrittive della Carta Geologica d'italia, 34, 185.

De Paola, N., Collettini, C., Faulkner, D.R., Trippetta, F. 2008. Fault zone architecture and deformation processes within evaporitic rocks in the upper crust. Tectonics 27.

Den Hartog, S. A. M., Niemeijer, A. R., & Spiers, C. J. 2013. Friction on subduction megathrust faults: Beyond the illite–muscovite transition. Earth and Planetary Science Letters, 373, 8-19.

Diehl, T., Clinton, J., Deichmann, N., Cauzzi, C., Kästli, P., Kraft, T., Molinari, I., Bose, M., Michel, C., Hobiger, M., Haslinger, F., Fah, D., & Wiemer, S. 2018. Earthquakes in Switzerland and surrounding regions during 2015 and 2016. Swiss Journal of Geosciences, 111(1), 221-244.

Dieterich, J.H. 1979. Modeling of rock friction 1. Experimental results and constitutive equations. J. Geophys. Res., Solid Earth 84, 2161–2168. https://doi.org/10. 1029/JB084iB05p02161.

Dieterich, J.H., Kilgore, B.D. 1994. Direct observation of frictional contacts: new insights for state-dependent properties. Pure Appl. Geophys. 143, 283–302. https://doi.org/10.1007/BF00874332.

Dieterich, J. H., & Smith, D. E. 2010. Nonplanar faults: Mechanics of slip and off-fault damage. Mechanics, structure and evolution of fault zones, 1799-1815.

Ellis, S., & Stöckhert, B. 2004. Elevated stresses and creep rates beneath the brittle-ductile transition caused by seismic faulting in the upper crust. Journal of Geophysical Research: Solid Earth, 109(B5).

Essing, D., & Poli, P. 2022. Spatiotemporal Evolution of the Seismicity in the Alto Tiberina Fault System Revealed by a

High-Resolution Template Matching Catalog. Journal of Geophysical Research: Solid Earth, 127(10), e2022JB024845.

Eyre, T. S., Eaton, D. W., Garagash, D. I., Zecevic, M., Venieri, M., Weir, R., & Lawton, D. C. 2019. The role of aseismic slip in hydraulic fracturing–induced seismicity. Science advances, 5(8), eaav7172.

Fagereng, A., Sibson, R.H. 2010. Melange rheology and seismic style. Geology 38, 751–754.

Fagereng, Å., & Beall, A. 2021. Is complex fault zone behaviour a reflection of rheological heterogeneity?. Philosophical Transactions of the Royal Society A, 379(2193), 20190421.

Faulkner, D. R., & Rutter, E. H. 2003. The effect of temperature, the nature of the pore fluid, and subyield differential stress on the permeability of phyllosilicate-rich fault gouge. Journal of Geophysical Research: Solid Earth, 108(B5).

Faulkner, D. R., Lewis, A. C., & Rutter, E. H. 2003. On the internal structure and mechanics of large strike-slip fault zones: field observations of the Carboneras fault in southeastern Spain. Tectonophysics, 367(3-4), 235-251.

Faulkner, D. R., Jackson, C. A. L., Lunn, R. J., Schlische, R. W., Shipton, Z. K., Wibberley, C. A. J., & Withjack, M. O. 2010. A review of recent developments concerning the structure, mechanics, and fluid flow properties of fault zones. Journal of Structural Geology, 32(11), 1557-1575.

Faulkner, D. R., Sanchez-Roa, C., Boulton, C., & Den Hartog, S. A. M. 2018. Pore fluid pressure development in compacting fault gouge in theory, experiments, and nature. Journal of Geophysical Research: Solid Earth, 123(1), 226-241.

French, M. E., Zhu, W., & Banker, J. 2016. Fault slip controlled by stress path and fluid pressurization rate. Geophysical Research Letters, 43(9), 4330-4339.

Frye, K. M., & Marone, C. 2002. Effect of humidity on granular friction at room temperature. Journal of Geophysical Research: Solid Earth, 107(B11), ETG-11.

Giorgetti, C., Carpenter, B.M., Collettini, C. 2015. Frictional behaviour of talc-calcite mixtures. J. Geophys. Res., Solid Earth 120. https://doi.org/10.1002/ 2015JB011970.

Giuntoli, F., & Viola, G. 2022. A likely geological record of deep tremor and slow slip events from a subducted continental broken formation. Scientific Reports, 12(1), 4506.

Goodwin, L. B., & Tikoff, B. 2002. Competency contrast, kinematics, and the development of foliations and lineations in the crust. Journal of structural Geology, 24(6-7), 1065-1085.

Gounon, A., Latour, S., Letort, J., & El Arem, S. 2022. Rupture nucleation on a periodically heterogeneous

interface. Geophysical Research Letters, 49(20), e2021GL096816.

Govoni, A., Marchetti, A., De Gori, P., Di Bona, M., Lucente, F. P., Improta, L., Chiarabba, C., Nardi, A., Margheriti, L., Piana Agostinetti, N., Di Giovambattista, R., Latorre, D., Anselmi, M., Ciaccio, M. G., Moretti, M., Castellano, C., & Piccinini, D. 2014. The 2012 Emilia seismic sequence (Northern Italy): Imaging the thrust fault system by accurate aftershock location. Tectonophysics, 622, 44-55.

Gu, J. C., Rice, J. R., Ruina, A. L., & Simon, T. T. 1984. Slip motion and stability of a single degree of freedom elastic system with rate and state dependent friction. Journal of the Mechanics and Physics of Solids, 32(3), 167-196.

Gu, Y., & Wong, T. F. 1994. Nonlinear dynamics of the transition from stable sliding to cyclic-stick-slip in rock. GEOPHYSICAL MONOGRAPH-AMERICAN GEOPHYSICAL UNION, 83, 15-15.

Guglielmi, Y., Cappa, F., Avouac, J. P., Henry, P., & Elsworth, D. 2015. Seismicity triggered by fluid injection–induced aseismic slip. Science, 348(6240), 1224-1226.

Hafner, S. 1958. Petrographie des südwestlichen Gotthardmassivs zwischen St. Gotthardpass und Nufenenpass (Doctoral dissertation, ETH Zurich).

Haines, S. H., Van Der Pluijm, B. A., Ikari, M. J., Saffer, D. M., & Marone, C. 2009. Clay fabric intensity in natural and artificial fault gouges: Implications for brittle fault zone processes and sedimentary basin clay fabric evolution. Journal of Geophysical Research: Solid Earth, 114(B5).

Haines, S. H., Kaproth, B., Marone, C., Saffer, D., & Van der Pluijm, B. 2013. Shear zones in clay-rich fault gouge: A laboratory study of fabric development and evolution. Journal of Structural Geology, 51, 206-225.

Heidbach, O., Rajabi, M., Cui, X., Fuchs, K., Müller, B., Reinecker, J., Reiter, K., Tingay, M., Wenzel, F., Xie, F., Ziegler, M. O., Zoback, M.-L., and Zoback, M. 2018. The World Stress Map database release 2016: Crustal stress pattern across scales, Tectonophysics, 744, 484–498, https://doi.org/10.1016/j.tecto.2018.07.007.

Holdsworth, R. E. 2004. Weak faults--rotten cores. Science, 303(5655), 181-182.

Holdsworth, R. E., Van Diggelen, E. W. E., Spiers, C. J., De Bresser, J. H. P., Walker, R. J., & Bowen, L. 2011. Fault rocks from the SAFOD core samples: implications for weakening at shallow depths along the San Andreas Fault, California. Journal of Structural Geology, 33(2), 132-144.

Ide, S., Beroza, G. C., Shelly, D. R., & Uchide, T. 2007. A scaling law for slow earthquakes. Nature, 447(7140), 76-79.

Ide, S., & Beroza, G. C. 2023. Slow earthquake scaling reconsidered as a boundary between distinct modes of rupture propagation. Proceedings of the National Academy of Sciences, 120(32), e2222102120.

Igarashi, T., Matsuzawa, T., & Hasegawa, A. 2003. Repeating earthquakes and interplate aseismic slip in the northeastern Japan subduction zone. Journal of Geophysical Research: Solid Earth, 108(B5).

Ikari, M. J., Saffer, D. M., & Marone, C. 2007. Effect of hydration state on the frictional properties of montmorillonite-based fault gouge. Journal of Geophysical Research: Solid Earth, 112(B6).

Ikari, M. J., Saffer, D. M., & Marone, C. 2009. Frictional and hydrologic properties of clay-rich fault gouge. Journal of Geophysical Research: Solid Earth, 114(B5).

Ikari, M. J., Marone, C., & Saffer, D. M. 2011. On the relation between fault strength and frictional stability. Geology, 39(1), 83-86.

Ikari, M. J., & Saffer, D. M. 2011. Comparison of frictional strength and velocity dependence between fault zones in the Nankai accretionary complex. Geochemistry, Geophysics, Geosystems, 12(4).

Ikari, M. J., & Kopf, A. J. 2017. Seismic potential of weak, near-surface faults revealed at plate tectonic slip rates. Science Advances, 3(11), e1701269.

Ikari, M. J., & Hüpers, A. 2021. Velocity-weakening friction induced by laboratory-controlled lithification. Earth and Planetary Science Letters, 554, 116682.

Im, K., Saffer, D., Marone, C., & Avouac, J. P. 2020. Slip-rate-dependent friction as a universal mechanism for slow slip events. Nature Geoscience, 13(10), 705-710.

Imber, J., Holdsworth, R. E., Butler, C. A., & Strachan, R. A. 2001. A reappraisal of the Sibson-Scholz fault zone model: The nature of the frictional to viscous ("brittle-ductile") transition along a long-lived, crustal-scale fault, Outer Hebrides, Scotland. Tectonics, 20(5), 601-624.

Improta, L., Latorre, D., Margheriti, L., Nardi, A., Marchetti, A., Lombardi, A. M., Castello, B., Villani, F., Ciaccio, M.G., Mele, F.M. & Moretti, M. 2019. Multi-segment rupture of the 2016 Amatrice-Visso-Norcia seismic sequence (central Italy) constrained by the first high-quality catalog of Early Aftershocks. Scientific reports, 9(1), 1-13.

Ito, Y., & Obara, K. 2006. Very low frequency earthquakes within accretionary prisms are very low stress-drop earthquakes. Geophysical Research Letters, 33(9).

Ji, Y., Hofmann, H., Rutter, E. H., & Zang, A. 2022a. Transition From Slow to Fast Injection-Induced Slip of an Experimental Fault in Granite Promoted by Elevated Temperature. Geophysical Research Letters, 49(23), e2022GL101212.

Ji, Y., Wang, L., Hofmann, H., Kwiatek, G., & Dresen, G. 2022b. High-rate fluid injection reduces the nucleation length of laboratory earthquakes on critically stressed faults in granite. Geophysical Research Letters,

e2022GL100418.

Jolivet, R., & Frank, W. B. 2020. The transient and intermittent nature of slow slip. AGU Advances, 1(1), e2019AV000126.

Jordan, D. 2019. Geological characterization of the Bedretto underground laboratory for geoenergies (Master's thesis, ETH Zurich, Geological Institute).

Janecke, S. U., & Evans, J. P. 1988. Feldspar-influenced rock rheologies. Geology, 16(12), 1064-1067.

Kanamori, H. 1972. Mechanism of tsunami earthquakes. Physics of the earth and planetary interiors, 6(5), 346-359.

Kanamori, H., & Anderson, D. L. 1975. Theoretical basis of some empirical relations in seismology. Bulletin of the seismological society of America, 65(5), 1073-1095.

Kanamori, H., & Kikuchi, M. 1993. The 1992 Nicaragua earthquake: a slow tsunami earthquake associated with subducted sediments. Nature, 361(6414), 714-716.

Kaneko, Y., Nielsen, S. B., & Carpenter, B. M. 2016. The onset of laboratory earthquakes explained by nucleating rupture on a rate-and-state fault. Journal of Geophysical Research: Solid Earth, 121(8), 6071-6091.

Kastrup, U., Zoback, M. L., Deichmann, N., Evans, K. F., Giardini, D., & Michael, A. J. 2004. Stress field variations in the Swiss Alps and the northern Alpine foreland derived from inversion of fault plane solutions. Journal of Geophysical Research: Solid Earth, 109(B1).

Kato, A., Obara, K., Igarashi, T., Tsuruoka, H., Nakagawa, S., & Hirata, N. 2012. Propagation of slow slip leading up to the 2011 M w 9.0 Tohoku-Oki earthquake. Science, 335(6069), 705-708.

Kato, A., & Nakagawa, S. 2014. Multiple slow-slip events during a foreshock sequence of the 2014 Iquique, Chile Mw 8.1 earthquake. Geophysical Research Letters, 41(15), 5420-5427.

Kato, A., & Ben-Zion, Y. 2021. The generation of large earthquakes. Nature Reviews Earth & Environment, 2(1), 26-39.

Keller, F., & Schneider, T. R. 1982. Geologie und Geotechnik. Schweizer Ingenieur und Architekt, 100(24), 512-520.

King, D. S. H., & Marone, C. 2012. Frictional properties of olivine at high temperature with applications to the strength and dynamics of the oceanic lithosphere. Journal of Geophysical Research: Solid Earth, 117(B12).

Kirkpatrick, J. D., Fagereng, Å., & Shelly, D. R. 2021. Geological constraints on the mechanisms of slow earthquakes. Nature Reviews Earth & Environment, 2(4), 285-301.

Labhart, T. 2005. Erläuterungen Zum Geologischen Atlas Des Schweiz 1: 25 000. Val Bedretto, Atlasblatt, 68.

Lambert, V., Lapusta, N., & Perry, S. 2021. Propagation of large earthquakes as self-healing pulses or mild

cracks. Nature, 591(7849), 252-258.

Latorre, D., Mirabella, F., Chiaraluce, L., Trippetta, F., & Lomax, A. 2016. Assessment of earthquake locations in 3-D deterministic velocity models: A case study from the Altotiberina Near Fault Observatory (Italy). Journal of Geophysical Research: Solid Earth, 121, 8113–8135.

Lay, T., Kanamori, H., Ammon, C. J., Koper, K. D., Hutko, A. R., Ye, L., Yue, H. & Rushing, T. M. 2012. Depth-varying rupture properties of subduction zone megathrust faults. Journal of Geophysical Research: Solid Earth, 117(B4).

Lay, T. 2015. The surge of great earthquakes from 2004 to 2014. Earth and Planetary Science Letters, 409, 133-146.

Lazzarotto A, Aldinucci M, Cirilli S, Costantini A, Decandia FA, Pandeli E, Sandrelli F, Spina A. 2003. Stratigraphic correlation of the Upper Palaeozoic-Triassic successions in southern Tuscany, Italy. Bollettino della Societa` Geologica Italiana, 2: 25–35, Roma.

Leeman, J. R., Saffer, D. M., Scuderi, M. M., & Marone, C. 2016. Laboratory observations of slow earthquakes and the spectrum of tectonic fault slip modes. Nature communications, 7(1), 1-6.

Lin, A. 1999. S–C cataclasite in granitic rock. Tectonophysics, 304(3), 257-273.

Lin, A. 2001. S–C fabrics developed in cataclastic rocks from the Nojima fault zone, Japan, and their implications for tectonic history. Journal of Structural Geology, 23(6-7), 1167-1178.

Lister, G. S., & Snoke, A. W. 1984. SC mylonites. Journal of Structural Geology, 6(6), 617-638.

Lockner, D. A., Morrow, C., Moore, D., & Hickman, S. 2011. Low strength of deep San Andreas fault gouge from SAFOD core. Nature, 472(7341), 82-85.

Logan, J. M. 1979. Experimental studies of simulated gouge and their application to studies of natural fault zones. In Proceedings of conference VIII-analysis of actual fault zones in bedrock (pp. 305-343).

Logan, J. M., Dengo, C. A., Higgs, N. G., & Wang, Z. Z. 1992. Fabrics of experimental fault zones: Their development and relationship to mechanical behaviour. In International geophysics (Vol. 51, pp. 33-67). Academic Press.

Lützenkirchen, V. H. 2002. Structural geology and hydrogeology of brittle fault zones in the central and eastern Gotthard massif, Switzerland (Doctoral dissertation, ETH Zurich).

Lützenkirchen, V., & Loew, S. 2011. Late Alpine brittle faulting in the Rotondo granite (Switzerland): deformation mechanisms and fault evolution. Swiss Journal of Geosciences, 104(1), 31-54.

Lykotrafitis, G., Rosakis, A. J., & Ravichandran, G. 2006. Self-healing pulse-like shear ruptures in the laboratory. Science, 313(5794), 1765-1768.

Lyu, Z., Rivière, J., Yang, Q., & Marone, C. 2019. On the mechanics of granular shear: the effect of normal stress and layer thickness on stick-slip properties. Tectonophysics, 763, 86-99.

Ma, X., Hertrich, M., Amann, F., Bröker, K., Gholizadeh Doonechaly, N., Gischig, V., Hochreutener, R., Kastli, P., Krietsch, H., Marti, M., Nageli, B., Nejati, M., Obermann, A., Plenkers, K., Rinaldi, A. P., Shakas, A., Villiger, L., Wenning, Q., Zappone, A., Bethmann, F., Castilla, R., Seberto, F., Meier, P., Driesner, T., Loew, S., Maurer, H., Saar, M. O., Wiemer, S. & Giardini, D. 2022. Multi-disciplinary characterizations of the BedrettoLab–a new underground geoscience research facility. Solid Earth, 13(2), 301-322.

Magistrale, H. 2002. Relative contributions of crustal temperature and composition to controlling the depth of earthquakes in southern California. Geophysical Research Letters, 29(10), 87-1.

Mair, K., & Marone, C. 1999. Friction of simulated fault gouge for a wide range of velocities and normal stresses. Journal of Geophysical Research: Solid Earth, 104(B12), 28899-28914.

Mair, K., Frye, K. M., & Marone, C. 2002. Influence of grain characteristics on the friction of granular shear zones. Journal of Geophysical Research: Solid Earth, 107(B10), ECV-4.

Mair, K., & Abe, S. 2008. 3D numerical simulations of fault gouge evolution during shear: Grain size reduction and strain localization. Earth and Planetary Science Letters, 274(1-2), 72-81.

Mandl, G., De Jong, L. N. J., & Maltha, A. 1977. Shear zones in granular material. Rock mechanics, 9(2), 95-144.

Mandler, E., Pintori, F., Gualandi, A., Anderlini, L., Serpelloni, E., & Belardinelli, M. E. 2021. Post-Seismic Deformation Related to the 2016 Central Italy Seismic Sequence From GPS Displacement Time-Series. Journal of Geophysical Research: Solid Earth, 126(9), e2021JB022200.

Mariani, E., Brodie, K. H., & Rutter, E. H. 2006. Experimental deformation of muscovite shear zones at high temperatures under hydrothermal conditions and the strength of phyllosilicate-bearing faults in nature. Journal of Structural Geology, 28(9), 1569-1587.

Marone, C., & Scholz, C. H. 1988. The depth of seismic faulting and the upper transition from stable to unstable slip regimes. Geophysical Research Letters, 15(6), 621-624.

Marone, C., & Scholz, C. H. 1989. Particle-size distribution and microstructures within simulated fault gouge. Journal of Structural Geology, 11(7), 799-814.

Marone, C., Raleigh, C. B., & Scholz, C. H. 1990. Frictional behavior and constitutive modeling of simulated fault gouge. Journal of Geophysical Research: Solid Earth, 95(B5), 7007-7025.

Marone, C. 1998a. Laboratory-derived friction laws and their application to seismic faulting. Annu. Rev. Earth Planet.

Sci. 26, 643–696. https://doi.org/10.1146/ annurev.earth.26.1.643.

Marone, C., & Saffer, D. M. 2015. The mechanics of frictional healing and slip instability during the seismic cycle. In Earthquake Seismology (pp. 111-138). Elsevier Inc..

Marone, C. 2019. The spectrum of fault slip modes from elastodynamic rupture to slow earthquakes, Proc. Internat. School of Physics "Enrico Fermi" on Mechanics of Earthquake Faulting, pp 81-94, Eds. Bizzarri, A., Das, S. & A. Petri, IOS Press: Amsterdam, The Netherlands, 2019.

Mclaskey, G. C., & Yamashita, F. 2017. Slow and fast ruptures on a laboratory fault controlled by loading characteristics. Journal of Geophysical Research: Solid Earth, 122(5), 3719-3738.

Menegon, L., & Fagereng, Å. 2021. Tectonic pressure gradients during viscous creep drive fluid flow and brittle failure at the base of the seismogenic zone. Geology, 49(10), 1255-1259.

Michele, M., Chiaraluce, L., Di Stefano, R., & Waldhauser, F. 2020. Fine-scale structure of the 2016–2017 Central Italy seismic sequence from data recorded at the Italian National Network. Journal of Geophysical Research, Solid Earth, 125, e2019JB018440.

Miller, C. M. 2011. Adhesion and the surface energy components of natural minerals and aggregates (Doctoral dissertation, Texas A & M University).

Mirabella, F., Barchi, M. R., & Lupattelli, A. 2008. Seismic reflection data in the Umbria Marche region: Limits and capabilities to unravel the subsurface structure in a seismically active area. Annals of Geophysics, 51(2–3), 383–396,

Mitchell, T. M., & Faulkner, D. R. 2009. The nature and origin of off-fault damage surrounding strike-slip fault zones with a wide range of displacements: A field study from the Atacama fault system, northern Chile. Journal of Structural Geology, 31(8), 802-816.

Mitchell, E. K., Fialko, Y., and Brown, K. M. 2015. Frictional properties of gabbro at conditions corresponding to slow slip events in subduction zones. Geochem. Geophys. Geosystems 16 (11): 4006–4020, doi: 10.1002/2015gc006093.

Montone, P., & Mariucci, M. T. 2016. The new release of the Italian contemporary stress map. Geophysical Journal International, 205(3), 1525-1531.

Montone, P. & Mariucci, M. T. 2020. Constraints on the Structure of the Shallow Crust in Central Italy from Geophysical Log Data. Sci Rep., 10, 3834, https://doi.org/10.1038/s41598-020-60855-0.

Moore, D. E., & Lockner, D. A., Summers, R., Shengli, M. A., & Byerlee, J. D. 1996. Strength of chrysotile-serpentinite

gouge under hydrothermal conditions: Can it explain a weak San Andreas fault?. Geology, 24(11), 1041-1044.

Moore, D. E., & Lockner, D. A. 2004. Crystallographic controls on the frictional behaviour of dry and water-saturated sheet structure minerals. Journal of Geophysical Research: Solid Earth, 109(B3).

Moore, D. E., & Lockner, D. A. 2007. Comparative deformation behavior of minerals in serpentinized ultramafic rock: Application to the slab-mantle interface in subduction zones. International Geology Review, 49(5), 401-415.

Moore, D. E., & Lockner, D. A. 2008. Talc friction in the temperature range 25–400 C: Relevance for fault-zone weakening. Tectonophysics, 449(1-4), 120-132.

Moore, D. E., & Lockner, D. A. 2011. Frictional strengths of talc-serpentine and talc-quartz mixtures. Journal of Geophysical Research: Solid Earth, 116(B1).

Moore, D.M., Reynolds, R.C. Jr., 1997. X-Ray Diffraction and the identification and analysis of clay minerals. Oxford University Press, Oxford, UK, 378 pp.

Moretti, A., Meletti, C., & Ottria, G. 1990. Studio stratigrafico e strutturale dei Monti Romani (GR-VT)-1: Dal Paleozoico all'orogenesi alpidica. Bollettino della Società geologica italiana, 109(3), 557-581.

Nadeau, R., Antolik, M., Johnson, P. A., Foxall, W., & McEvilly, T. V. 1994. Seismological studies at Parkfield III: Microearthquake clusters in the study of fault-zone dynamics. Bulletin of the Seismological Society of America, 84(2), 247-263.

Nakatani, M., & Scholz, C. H. 2004. Frictional healing of quartz gouge under hydrothermal conditions: 1. Experimental evidence for solution transfer healing mechanism. Journal of Geophysical Research: Solid Earth, 109(B7).

Nakatani, M., Yabe, Y., Philipp, J., Morema, G., Stanchits, S., & Dresen, G. 2008. Acoustic emission measurements in a deep gold mine in South Africa: Project overview and some typical waveforms. In SSA Annual Meeting 2008 (Santa Fe, New Mexico 2008).

Nielsen, S., Taddeucci, J., & Vinciguerra, S. 2010. Experimental observation of stick-slip instability fronts. Geophysical Journal International, 180(2), 697-702.

Niemeijer, A. R., & Spiers, C. J. 2005. Influence of phyllosilicates on fault strength in the brittle-ductile transition: Insights from rock analogue experiments. Geological Society, London, Special Publications, 245(1), 303-327.

Niemeijer, A. R., & Spiers, C. J. 2006. Velocity dependence of strength and healing behaviour in simulated phyllosilicate-bearing fault gouge. Tectonophysics, 427(1-4), 231-253.

Niemeijer, A. R., & Spiers, C. J. 2007. A microphysical model for strong velocity weakening in phyllosilicate-bearing

fault gouges. Journal of Geophysical Research: Solid Earth, 112(B10).

Niemeijer, A., Marone, C., & Elsworth, D. 2010. Fabric induced weakness of tectonic faults. Geophysical Research Letters, 37(3).

Niemeijer, A. R. 2018. Velocity-dependent slip weakening by the combined operation of pressure solution and foliation development. Scientific reports, 8(1), 1-10.

Ofterdinger, U. S. 2001. Ground water flow systems in the Rotondo granite, Central Alps (Switzerland) (Doctoral dissertation, ETH Zurich).

Okamoto, A. S., Verberne, B. A., Niemeijer, A. R., Takahashi, M., Shimizu, I., Ueda, T., & Spiers, C. J. 2019. Frictional properties of simulated chlorite gouge at hydrothermal conditions: Implications for subduction megathrusts. Journal of Geophysical Research: Solid Earth, 124(5), 4545-4565.

Okubo, P. G., & Aki, K. 1987. Fractal geometry in the San Andreas fault system. Journal of Geophysical Research: Solid Earth, 92(B1), 345-355.

Orellana, L. F., Scuderi, M. M., Collettini, C., & Violay, M. 2018. Frictional properties of Opalinus Clay: Implications for nuclear waste storage. Journal of Geophysical Research: Solid Earth, 123(1), 157-175.

Pandeli E, Gianelli G, Puxeddu M, Elter FM. 1994. The paleozoic basement of the Northern Apennines: stratigraphy, tectonometamorphic evolution and Alpine hydrothermal processes. Memorie della Societa` Geologica Italiana 48: 627–654, Roma.

Passchier, C. W. 1990. A Mohr circle construction to plot the stretch history of material lines. Journal of Structural Geology, 12(4), 513-515.

Passelègue, F. X., Schubnel, A., Nielsen, S., Bhat, H. S., & Madariaga, R. 2013. From sub-Rayleigh to supershear ruptures during stick-slip experiments on crustal rocks. Science, 340(6137), 1208-1211.

Passelègue, F. X., Brantut, N., & Mitchell, T. M. 2018. Fault reactivation by fluid injection: controls from stress state and injection rate. Geophysical Research Letters, 45(23), 12-837.

Passelègue, F. X., Aubry, J., Nicolas, A., Fondriest, M., Deldicque, D., Schubnel, A., & Di Toro, G. 2019. From fault creep to slow and fast earthquakes in carbonates. Geology, 47(8), 744-748.

Passelègue, F. X., Almakari, M., Dublanchet, P., Barras, F., Fortin, J., & Violay, M. 2020. Initial effective stress controls the nature of earthquakes. Nature communications, 11(1), 5132.

Patacca, E., Scandone, P., Di Luzio, E., Cavinato, G. P., & Parotto, M. 2008. Structural architecture of the central Apennines: Interpretation of the CROP 11 seismic profile from the Adriatic coast to the orographic

divide. Tectonics, 27(3).

Pauselli, C., Gola, G., Mancinelli, P., Trumpy, E., Saccone, M., Manzella, A., & Ranalli, G. 2019. A new surface heat flow map of the Northern Apennines between latitudes 42.5 and 44.5 N. Geothermics, 81, 39-52.

Peng, Z., & Gomberg, J. 2010. An integrated perspective of the continuum between earthquakes and slow-slip phenomena. Nature geoscience, 3(9), 599-607.

Perfettini, H., Avouac, J. P., Tavera, H., Kositsky, A., Nocquet, J. M., Bondoux, F., Chlieh, M., Sladen, A., Audin, L., Farber, D.L. & Soler, P. 2010. Seismic and aseismic slip on the Central Peru megathrust. Nature, 465(7294), 78-81.

Perrin, C., Manighetti, I., Ampuero, J. P., Cappa, F., & Gaudemer, Y. 2016. Location of largest earthquake slip and fast rupture controlled by along-strike change in fault structural maturity due to fault growth. Journal of Geophysical Research: Solid Earth, 121(5), 3666-3685

Pialli, G. 1998. Results of the CROP03 deep seismic reflection profile. Mem. Soc. Geol. It., 52, 657.

Platt, J. P., & Vissers, R. L. M. 1980. Extensional structures in anisotropic rocks. Journal of Structural Geology, 2(4), 397-410.

Polet, J., & Kanamori, H. 2000. Shallow subduction zone earthquakes and their tsunamigenic potential. Geophysical Journal International, 142(3), 684-702.

Ponziani, F., De Franco, R., Minelli, G., Biella, G., Federico, C., & Pialli, G. 1995. Crustal shortening and duplication of the Moho in the Northern Apennines: a view from seismic refraction data. Tectonophysics, 252(1-4), 391-418.

Porreca, M., Minelli, G., Ercoli, M., Brobia, A., Mancinelli, P., Cruciani, F., Giorgetti, C., Carboni, C., Mirabella, F., Cavinato, G., Cannata, A., Pauselli, C., & Barchi, M. R. 2018. Seismic reflection profiles and subsurface geology of the area interested by the 2016–2017 earthquake sequence (Central Italy). Tectonics, 37, 1–22, https://doi.org/10.1002/2017TC004915, 2018.

Pousse-Beltran, L., Socquet, A., Benedetti, L., Doin, M. P., Rizza, M., & d'Agostino, N. 2020. Localized afterslip at geometrical complexities revealed by InSAR after the 2016 Central Italy seismic sequence. Journal of Geophysical Research: Solid Earth, 125(11), e2019JB019065.

Pozzi, G., De Paola, N., Nielsen, S. B., Holdsworth, R. E., & Bowen, L. 2018. A new interpretation for the nature and significance of mirror-like surfaces in experimental carbonate-hosted seismic faults. Geology, 46(7), 583-586.

Pozzi, G., Scuderi, M. M., Tinti, E., Nazzari, M., & Collettini, C. 2022. The role of fault rock fabric in the dynamics of

laboratory faults. Journal of Geophysical Research: Solid Earth, 127(6), e2021JB023779.

Proctor, B., Lockner, D. A., Kilgore, B. D., Mitchell, T. M., & Beeler, N. M. 2020. Direct evidence for fluid pressure, dilatancy, and compaction affecting slip in isolated faults. Geophysical Research Letters, 47(16), e2019GL086767.

Rast, M. 2020. Geology, geochronology, and rock magnetics along bedretto tunnel (gotthard massif, central alps) and numerical modelling of quartz-biotite aggregates-appendix a.

Rast, M., Galli, A., Ruh, J. B., Guillong, M., & Madonna, C. 2022. Geology along the Bedretto tunnel: kinematic and geochronological constraints on the evolution of the Gotthard Massif (Central Alps). Swiss Journal of Geosciences, 115(1), 1-31.

Reches, Z. E. 2006. Building a natural earthquake laboratory at focal depth (DAFSAM-NELSAM Project, South Africa). Scientific Drilling, 3, 30-33.

Riedel, W. 1929. Zur Mechanik geologischer Brucherscheinungen ein Beitrag zum Problem der Fiederspatten. Zentbl. Miner. Geol. Palaont. Abt., 354-368.

Rogers, G., & Dragert, H. 2003. Episodic tremor and slip on the Cascadia subduction zone: The chatter of silent slip. Science, 300(5627), 1942-1943.

Rubino, V., Lapusta, N., & Rosakis, A. J. 2022. Intermittent lab earthquakes in dynamically weakening fault gouge. Nature, 606(7916), 922-929.

Ruggieri, R., Scuderi, M. M., Trippetta, F., Tinti, E., Brignoli, M., Mantica, S., Petroselli, S., Osculati, L., Volontè, G. & Collettini, C. 2021. The role of shale content and pore-water saturation on frictional properties of simulated carbonate faults. Tectonophysics, 807, 228811.

Ruina, A. 1983. Slip instability and state variable friction laws. J. Geophys. Res. 88, 10359–10370. https://doi.org/10.1029/JB088iB12p10359.

Rutter, E. H., Maddock, R. H., Hall, S. H., & White, S. H. 1986. Comparative microstructures of natural and experimentally produced clay-bearing fault gouges. Pure and applied geophysics, 124(1), 3-30.

Rutter, E. & Hackston, 2017. A. On the effective stress law for rock-on-rock frictional sliding, and fault slip triggered by means of fluid injection. Philos Trans A Math Phys Eng Sci 375, 20160001, doi:10.1098/rsta.2016.0001.

Saffer, D. M., Frye, K. M., Marone, C., & Mair, K. 2001. Laboratory results indicating complex and potentially unstable frictional behavior of smectite clay. Geophysical Research Letters, 28(12), 2297-2300.

Saffer, D. M., & Marone, C. 2003. Comparison of smectite-and illite-rich gouge frictional properties: application to the

updip limit of the seismogenic zone along subduction megathrusts. Earth and Planetary Science Letters, 215(1-2), 219-235.

Saffer, D. M., & Wallace, L. M. 2015. The frictional, hydrologic, metamorphic and thermal habitat of shallow slow earthquakes. Nature Geoscience, 8(8), 594-600.

Samuelson, J., Elsworth, D., & Marone, C. 2009. Shear-induced dilatancy of fluid-saturated faults: Experiment and theory. Journal of Geophysical Research: Solid Earth, 114(B12).

Sawai, M., Niemeijer, A. R., Plümper, O., Hirose, T., & Spiers, C. J. 2016. Nucleation of frictional instability caused by fluid pressurization in subducted blueschist. Geophysical Research Letters, 43(6), 2543-2551.

Schallamach, A. 1971. How does rubber slide?. Wear, 17(4), 301-312.

Schmittbuhl, J., Karabulut, H., Lengliné, O., & Bouchon, M. 2016. Seismicity distribution and locking depth along the M ain M armara F ault, T urkey. Geochemistry, Geophysics, Geosystems, 17(3), 954-965.

Schneider, T. R. 1985. Basistunnel Furka—Geologische Aufnahme des Fensters Bedretto. Brig, Furka-Oberalp-Bahn AG.

Schoenball, M., Walsh, F. R., Weingarten, M., & Ellsworth, W. L. 2018. How faults wake up: the Guthrie-Langston, Oklahoma earthquakes. The Leading Edge, 37(2), 100-106.

Scholz, C. H., & Engelder, J. T. 1976. The role of asperity indentation and ploughing in rock friction—I: Asperity creep and stick-slip. In International Journal of Rock Mechanics and Mining Sciences & Geomechanics Abstracts (Vol. 13, No. 5, pp. 149-154). Pergamon.

Scholz, C. H. 1998. Earthquakes and friction laws. Nature, 391(6662), 37-42.

Scholz, C. H. 2019. The mechanics of earthquakes and faulting. Cambridge university press.

Scognamiglio, L., Tinti, E., Casarotti, E., Pucci, S., Villani, F., Cocco, M., A. Michelini & Dreger, D. 2018. Complex fault geometry and rupture dynamics of the MW 6.5, 30 October 2016, Central Italy earthquake. Journal of Geophysical Research: Solid Earth, 123(4), 2943-2964.

Scrocca, D., Carminati, E., & Doglioni, C. 2005. Deep structure of the southern Apennines, Italy: Thin-skinned or thick-skinned?. Tectonics, 24(3).

Scuderi, M. M., Niemeijer, A. R., Collettini, C., & Marone, C. 2013. Frictional properties and slip stability of active faults within carbonate–evaporite sequences: The role of dolomite and anhydrite. Earth and Planetary Science Letters, 369, 220-232.

Scuderi, M. M., Carpenter, B. M., & Marone, C. 2014. Physicochemical processes of frictional healing: Effects of water on stick-slip stress drop and friction of granular fault gouge. Journal of Geophysical Research: Solid

Earth, 119(5), 4090-4105.

Scuderi, M. M., & Collettini, C. 2016. The role of fluid pressure in induced vs. triggered seismicity: Insights from rock deformation experiments on carbonates. Scientific reports, 6(1), 1-9.

Scuderi, M. M., Collettini, C., Viti, C., Tinti, E., & Marone, C. 2017. Evolution of shear fabric in granular fault gouge from stable sliding to stick slip and implications for fault slip mode. Geology, 45(8), 731-734.

Scuderi, M. M., & Collettini, C. 2018. Fluid injection and the mechanics of frictional stability of shale-bearing faults. Journal of Geophysical Research: Solid Earth, 123(10), 8364-8384.

Scuderi, M. M., Tinti, E., Cocco, M., & Collettini, C. 2020. The role of shear fabric in controlling breakdown processes during laboratory slow-slip events. Journal of Geophysical Research: Solid Earth, 125(11), e2020JB020405.

Segall, P., & Rice, J. R. 1995. Dilatancy, compaction, and slip instability of a fluid-infiltrated fault. Journal of Geophysical Research: Solid Earth, 100(B11), 22155-22171.

Sergeev, S. A., Meier, M., & Steiger, R. H. 1995. Improving the resolution of single-grain U/Pb dating by use of zircon extracted from feldspar: Application to the Variscan magmatic cycle in the central Alps. Earth and Planetary Science Letters, 134(1-2), 37-51.

Shapiro, S. A., Huenges, E., & Borm, G. 1997. Estimating the crust permeability from fluid-injection-induced seismic emission at the KTB site. Geophysical Journal International, 131(2), F15-F18.

Shelly, D. R., Ellsworth, W. L., & Hill, D. P. 2016. Fluid-faulting evolution in high definition: Connecting fault structure and frequency-magnitude variations during the 2014 Long Valley Caldera, California, earthquake swarm. Journal of Geophysical Research: Solid Earth, 121(3), 1776-1795.

Shreedharan, S., Saffer, D., Wallace, L. M., & Williams, C. 2023. Ultralow frictional healing explains recurring slow slip events. Science, 379(6633), 712-717.

Shlomai, H., & Fineberg, J. 2016. The structure of slip-pulses and supershear ruptures driving slip in bimaterial friction. Nature communications, 7(1), 11787.

Smith, S. A. F., Tesei, T., Scott, J. M., & Collettini, C. 2017. Reactivation of normal faults as high-angle reverse faults due to low frictional strength: Experimental data from the Moonlight Fault Zone, New Zealand. Journal of Structural Geology, 105, 34-43.

Sibson, R. 1977. Fault rocks and fault mechanisms. J. Geol. Soc. (Lond.) 133, 191–213. https://doi.org/10.1144/gsjgs.133.3.0191.

Sibson, R. H. 1989. Earthquake faulting as a structural process. Journal of structural geology, 11(1-2), 1-14.

Sibson, R. H. 1994. Crustal stress, faulting and fluid flow. Geological Society, London, Special Publications, 78(1), 69-84.

Smith, S. A. F., Holdsworth, R. E., & Collettini, C. 2011. Interactions between low-angle normal faults and plutonism in the upper crust: Insights from the Island of Elba, Italy. Bulletin, 123(1-2), 329-346.

Steinhardt, W., Dillavou, S., Agajanian, M., Rubinstein, S. M., & Brodsky, E. E. 2023. Seismological stress drops for confined ruptures are invariant to normal stress. Geophysical Research Letters, 50(9), e2022GL101366.

Tan, Y. J., Waldhauser, F., Ellsworth, W. L., Zhang, M., Zhu, W., Michele, M., Chiaraluce, C., Beroza, C. G. & Segou, M. 2021. Machine-Learning-Based High-Resolution Earthquake Catalog Reveals How Complex Fault Structures Were Activated during the 2016–2017 Central Italy Sequence. The Seismic Record, 1(1), 11-19.

Tarling, M. S., Smith, S. A., Scott, J. M., Rooney, J. S., Viti, C., & Gordon, K. C. 2019. The internal structure and composition of a plate-boundary-scale serpentinite shear zone: the Livingstone Fault, New Zealand. Solid Earth, 10(4), 1025-1047.

Tchalenko, J. S. 1968. The evolution of kink-bands and the development of compression textures in sheared clays. Tectonophysics, 6(2), 159-174.

Tembe, S., Lockner, D. A., & Wong, T. F. 2010. Effect of clay content and mineralogy on frictional sliding behaviour of simulated gouges: Binary and ternary mixtures of quartz, illite, and montmorillonite. Journal of Geophysical Research: Solid Earth, 115(B3).

Tesei, T., Collettini, C., Carpenter, B. M., Viti, C., & Marone, C. 2012. Frictional strength and healing behaviour of phyllosilicate-rich faults. Journal of Geophysical Research: Solid Earth, 117(B9).

Tesei, T., Collettini, C., Barchi, M.R., Carpenter, B.M., Di Stefano, G. 2014. Heterogeneous strength and fault zone complexity of carbonate-bearing thrusts with possible implications for seismicity. Earth Planet. Sci. Lett. 408, 307–318. https://doi.org/10.1016/j.epsl.2014.10.021.

Tesei, T., Harbord, C. W. A., De Paola, N., Collettini, C., & Viti, C. 2018. Friction of mineralogically controlled serpentinites and implications for fault weakness. Journal of Geophysical Research: Solid Earth, 123(8), 6976-6991.

Toda, S., Stein, R. S., & Sagiya, T. 2002. Evidence from the AD 2000 Izu islands earthquake swarm that stressing rate governs seismicity. Nature, 419(6902), 58-61.

Tongiorgi, M., Rau, A., & Martini, I. P. 1977. Sedimentology of early-alpine, fluvio-marine, clastic deposits (Verrucano, Triassic) in the Monti Pisani (Italy). Sedimentary Geology, 17(3-4), 311-332.

Trippetta, F., Collettini, C., Meredith, P. G., & Vinciguerra, S. 2013. Evolution of the elastic moduli of seismogenic

Triassic Evaporites subjected to cyclic stressing. Tectonophysics, 592, 67-79.

Trippetta, F., Collettini, C., Barchi, M.R., Lupattelli, A., & Mirabella, F. 2013b. A multidisciplinary study of a natural example of CO2 geological storage in central Italy: International Journal of Greenhouse Gas Control, v. 12, p. 72–83, https://doi.org/10.1016/j.ijggc.2012.11.010.

Tullis, J., Snoke, A. W., & Todd, V. R. 1982. Significance and petrogenesis of mylonitic rocks. Geology, 10(5), 227-230.

Uchida, N., & Bürgmann, R. 2019. Repeating earthquakes. Annual Review of Earth and Planetary Sciences, 47, 305-332.

Verberne, B. A., Niemeijer, A. R., De Bresser, J. H., & Spiers, C. J. 2015. Mechanical behavior and microstructure of simulated calcite fault gouge sheared at 20–600 C: Implications for natural faults in limestones. Journal of Geophysical Research: Solid Earth, 120(12), 8169-8196.

Verrucchi, C., Pandeli, E., Minissale, A., Andreotti, P., & Paolieri, M. 1994. New data for the geochemical characterization of the Tuscan Paleozoic sequences (Northern Apennines, Italy). Mem. Soc. Geol. It., 48, 655-666.

Vidale, J. E., & Shearer, P. M. 2006. A survey of 71 earthquake bursts across southern California: Exploring the role of pore fluid pressure fluctuations and aseismic slip as drivers. Journal of Geophysical Research: Solid Earth, 111(B5).

Viswanathan, K., & Sundaram, N. K. 2017. Distinct stick-slip modes in adhesive polymer interfaces. Wear, 376, 1271-1278.

Viti, C., & Collettini, C. 2009. Growth and deformation mechanisms of talc along a natural fault: a micro/nanostructural investigation. Contributions to Mineralogy and Petrology, 158, 529-542.

Von Huene, R., & Scholl, D. W. 1991. Observations at convergent margins concerning sediment subduction, subduction erosion, and the growth of continental crust. Reviews of Geophysics, 29(3), 279-316.

Volpe, G., Pozzi, G., Carminati, E., Barchi, M. R., Scuderi, M. M., Tinti, E., Aldega, L., Marone, C. & Collettini, C. 2022a. Frictional controls on the seismogenic zone: Insights from the Apenninic basement, Central Italy. Earth and Planetary Science Letters, 583, 117444.

Volpe, G., Pozzi, G., & Collettini, C. 2022b. YBPR or SCC'? Suggestion for the nomenclature of experimental brittle fault fabric in phyllosilicate-granular mixtures. Journal of Structural Geology, 165, 104743.

Volpe, G., Pozzi, G., Locchi, M. E., Tinti, E., Scuderi, M. M., Marone, C., & Collettini, C. 2023. Rheological heterogeneities at the roots of the seismogenic zone. Geology, 51(10), 988-992.

Vrolijk, P. 1990. On the mechanical role of smectite in subduction zones. Geology, 18(8), 703-707.

Vuan, A., Sugan, M., Chiaraluce, L., & Di Stefano, R. 2017. Loading rate variations along a midcrustal shear zone preceding the Mw6.0 earthquake of 24 August 2016 in Central Italy. Geophysical Research Letters, 44(24), 12-170.

Yasuhara, H., Marone, C., & Elsworth, D. 2005. Fault zone restrengthening and frictional healing: The role of pressure solution. Journal of Geophysical Research: Solid Earth, 110(B6).

Waldhauser, F., Ellsworth, W. L., Schaff, D. P., & Cole, A. 2004. Streaks, multiplets, and holes: High-resolution spatio-temporal behavior of Parkfield seismicity. Geophysical Research Letters, 31(18).

Waldhauser, F., Michele, M., Chiaraluce, L., Di Stefano, R., Schaff, D.P., 2021. Fault planes, fault zone structure and detachment fragmentation resolved with high-precision aftershock locations of the 2016–2017 central Italy sequence. Geophys. Res. Lett. 48 (16), e2021GL092918.

Wallace, L. M. 2020. Slow slip events in New Zealand. Annual Review of Earth and Planetary Sciences, 48, 175-203.

Wallis, D., Lloyd, G. E., Phillips, R. J., Parsons, A. J., & Walshaw, D. 2015. Low effective fault strength due to frictional-viscous flow in phyllonites, Karakoram Fault Zone, NW India. Journal of Structural Geology, 77, 45-61.

Wang, K., & Bilek, S. L. 2011. Do subducting seamounts generate or stop large earthquakes?. Geology, 39(9), 819-822.

Wang, K., & Bilek, S. L. 2014. Invited review paper: Fault creep caused by subduction of rough seafloor relief. Tectonophysics, 610, 1-24.

Wang, L., Kwiatek, G., Rybacki, E., Bonnelye, A., Bohnhoff, M., & Dresen, G. 2020. Laboratory study on fluid-induced fault slip behavior: The role of fluid pressurization rate. Geophysical Research Letters, 47(6), e2019GL086627.

White, S. H., Burrows, S. E., Carreras, J., Shaw, N. D., & Humphreys, F. J. 1980. On mylonites in ductile shear zones. Journal of structural geology, 2(1-2), 175-187.

Wibberley, C. A. 2002. Hydraulic diffusivity of fault gouge zones and implications for thermal pressurization during seismic slip. Earth, planets and space, 54(11), 1153-1171.

Wintsch, R. P., Christoffersen, R., & Kronenberg, A. K. 1995. Fluid-rock reaction weakening of fault zones. Journal of Geophysical Research: Solid Earth, 100(B7), 13021-13032.

Wise, D. U., Dunn, D. E., Engelder, J. T., Geiser, P. A., Hatcher, R. D., Kish, S. A., Odom, A. L. & Schamel, S. 1984. Fault-related rocks: Suggestions for terminology. Geology, 12(7), 391-394.

Zoback, M., Hickman, S., Ellsworth, W., & SAFOD Science Team. 2011. Scientific drilling into the San Andreas fault zone–an overview of SAFOD's first five years. Scientific Drilling, 11, 14-28.

# 8 Appendix

## Appendix of chapter I

## *Study of the frictional mechanisms of phyllosilicate-rich fault rocks at the microscale.*

### Y-B-P-R or S-C-C'? Suggestion for the nomenclature of experimental brittle fault fabric in phyllosilicate-granular mixtures

G. Volpe[a], G. Pozzi[b], C. Collettini[a,b]

a: Università degli Studi di Roma, La Sapienza, Italy

b: Istituto Nazionale di Geofisica e Vulcanologia, Italy

*Published in Journal of Structural Geology*

## Supplementary materials

The following supplementary materials include SM.1 – XRD analysis, SM.2 – Friction analysis, SM.3 – Experiment Id-number, SM.4 – Mechanical results and raw data curves and SM.5 – Polymineralic grain disaggregation.

### SM.1 XRD analysis

The XRD analysis carried on the tested gouges showed a similar composition among the samples (Fig. SM1). Generally, the gouges are composed of quartz and phyllosilicates in different percentage with minor oxides (rutile and hematite) and carbonates (calcite and dolomite). The semi-quantitative analysis provided the following mineralogical composition:

- Phy58: 36% quartz, 58% phyllosilicates (muscovite, paragonite, chlorite), 6% rutile.

- Phy46: 37% quartz, 46% phyllosilicates (muscovite, chlorite), 16% hematite, 1% rutile.
- Phy35: 65% quartz, 33% phyllosilicates (muscovite, paragonite, chlorite), 2% rutile.
- Phy24: 66% quartz, 24% phyllosilicates (pyrophyllite 9%, muscovite, chlorite), 8% carbonates (calcite and dolomite), 2% hematite.

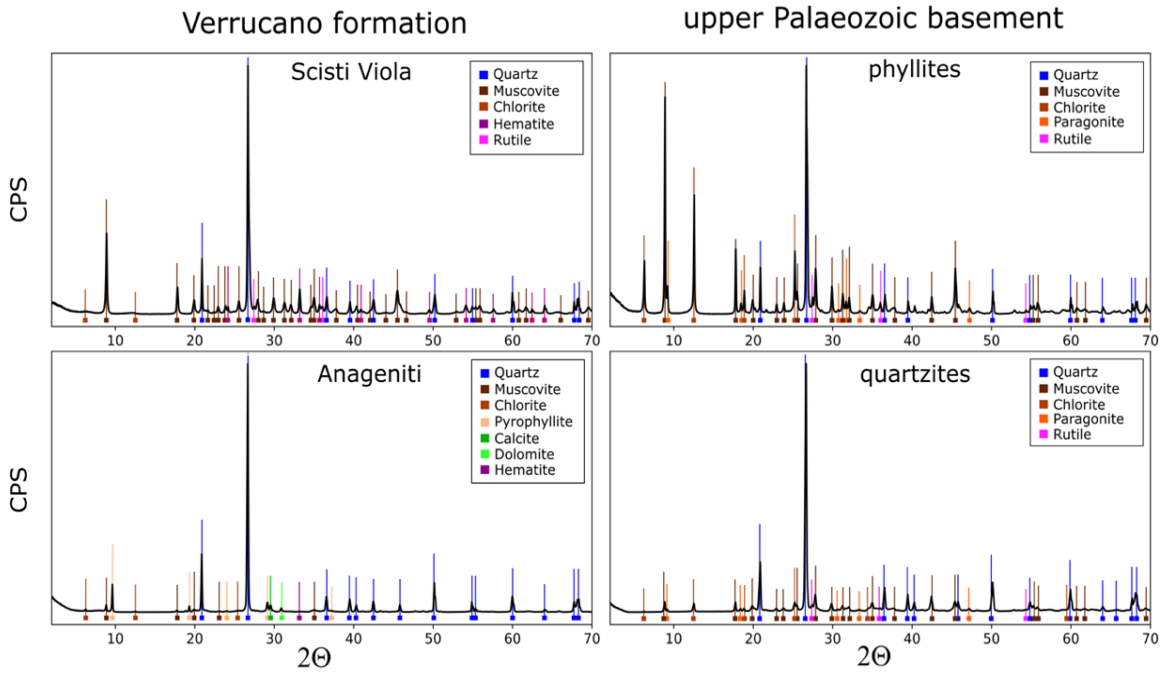


Fig. SM1: selected XRD patterns of the tested gouges. Phyllosilicate-rich gouges (upper row) and granular-rich gouges (lower row). After Volpe et al., 2022a.

## SM.2 Friction analysis

Our friction measurements include steady-state sliding friction, healing behavior during slide-hold-slide tests, and velocity/state dependence of friction. The rate and state friction theory (Dieterich, 1979; Ruina, 1983) is used as framework for this analysis. The steady state friction coefficient (μ) was calculated as the shear stress normal stress ratio, and assuming negligible cohesion.

$\mu ss = \tau ss / \sigma n$

During slide-hold-slide tests, the amount of frictional healing (Δμ) was calculated as the difference between the peak friction measured upon re-shear after each hold and the pre-hold steady state friction (Marone, 1998). Frictional healing rate ($\beta$) was calculated by diving the frictional healing (Δμ) by the logarithm of the hold time, log10(Δt).

$\beta = \Delta\mu / \log10(\Delta t)$

During velocity steps test, the near-instantaneous step in sliding velocity from $V_0$ to V corresponds to an instantaneous change in friction that scales as the friction parameter $a\ln(V/V_0)$, where *a* is an empirical constant defined as the direct effect. The subsequent evolution to a new steady-state value of friction scales as the friction parameter $b\ln(V/V_0)$, where *b* is an empirical constant defined as the evolution effect (Dieterich, 1979; Ruina, 1983). The velocity dependence of friction, described by the *a*-*b* parameter, is defined as:

$(a-b) = \Delta\mu ss / \ln(V/V0)$

where $\Delta\mu ss$ is the difference between the dynamic steady-state friction after and before a change in sliding velocity from $V_0$ to V (Dieterich, 1979, Ruina, 1983). Positive values of (*a*-*b*) define velocity-strengthening behavior, indicating that aseismic creep is expected. Negative values of (*a*-*b*) define velocity-weakening behavior, which is a condition required to develop a frictional instability (Dieterich and Kilgore, 1994; Marone 1998). The velocity steps were modelled using the Dieterich time-dependent evolution law coupled with the RSF equation (Dieterich, 1979):

$\mu = \mu_0 + a \ln(V/V_0) + b \ln(V\theta /Dc)$

$d\theta/dt = 1 - \theta V/Dc$

Where $\mu_0$ is friction for steady-state slip at velocity $V_0$, V is the frictional slip rate and Dc is the critical slip distance needed to renew the asperities. Parameter θ, also calculated as Dc/V at steady state, represents the state variable that describes the average lifetime of the asperities (Ruina, 1983). For modelling, these two equations are coupled with an equation that describes the elastic coupling between the frictional surface and the loading surrounding:

$d\mu/dt = K(Vlp-V)$

Where Vlp is the measured loading point velocity and K is the stiffness of the loading apparatus and the assembly, normalized by the normal stress, in units of coefficient of friction per displacement (Saffer and Marone, 2003). These last three equations are simultaneously solved by using a fifth order Runge-Kutta numerical integration. The constitutive parameters a, b, and Dc for each velocity step, were obtained as best fit parameter values using an iterative, least squares method to solve the nonlinear inverse problem (Blanpied et al., 1998; Saffer and Marone, 2003).

## SM.3 Experiment id-numbers

| Rock | Normal stress [MPa] | experimental numbers | |
|---|---|---|---|
| | | dry | wet |
| Phy58 | 25 | b934 | b955 |
| | 50 | b937 | b973 |
| | 75 | b940 | b974 |
| | 100 | b945 | b975 |
| Phy46 | 25 | | b996 |
| | 50 | | b997 |
| | 75 | | b998 |
| | 100 | | b999 |
| Phy35 | 25 | | b987 |
| | 50 | | b988 |
| | 75 | | b989 |
| | 100 | | b990 |
| Phy24 | 25 | b1102 | b1003 |
| | 50 | b1101 | b1006 |
| | 75 | b1100 | b1008 |
| | 100 | b1099 | b1007 |

Fig. SM2: Table of the experiment identifying number (bxxxx) for each of the experiment performed for this work.

## SM.4 Mechanical results and raw data curves

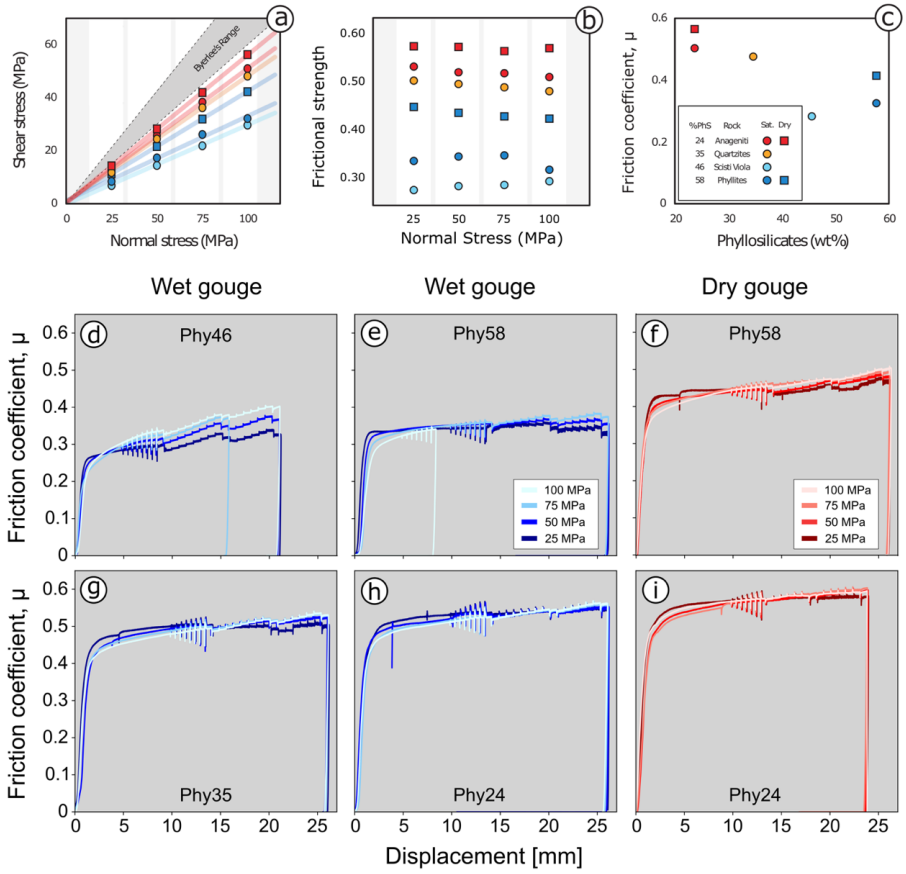

Fig. SM3: brief summary of the mechanical results: a) shear stress vs normal stress plot and coulomb envelopes of the gouges. b) Frictional strength in function of normal stress of the tested gouges. Note the small variation of the stress in Phy24, Phy35 and Phy46. c) relation between friction coefficient and phyllosilicates content. d) to i) friction vs displacement curves for each gouge. Note strain hardening in Phy46. Integrated after Volpe et al., 2022a.

## SM.5 Polymineralic grain disaggregation

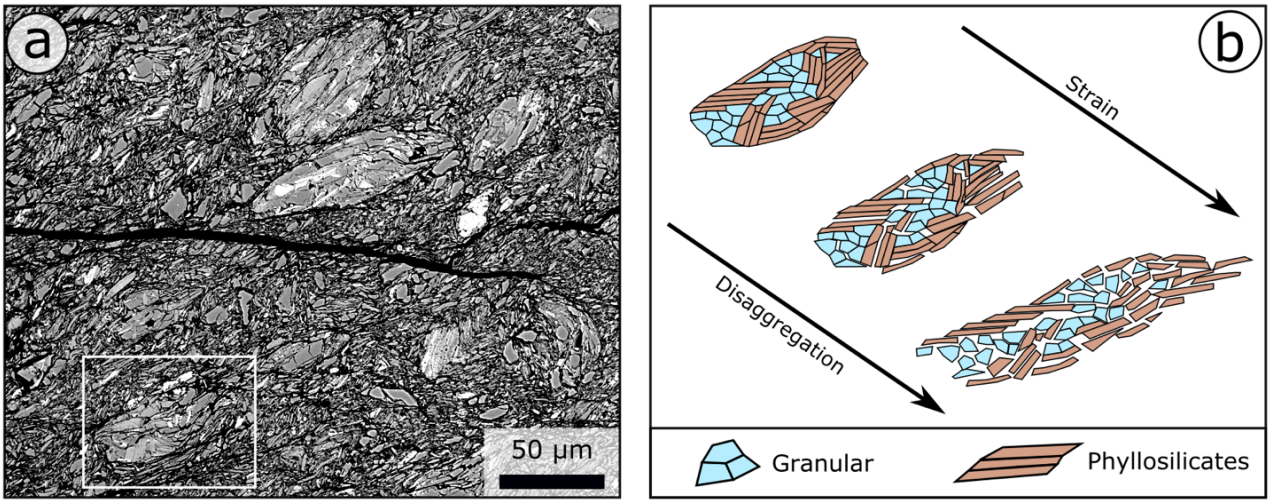


Fig. SM4: Disaggregation of a polymineralic aggregate grain along the preexisting mineral boundaries. a) example of microstructures (Phy58) showing different polymineralic aggregate grains with different degree of deformation. b) deformation history of a selected grains (white box in panel a).

# Appendix of chapter II

## *The role of Apennine basement in the seismic context of central Italy*

---

### Frictional controls on the seismogenic zone: insights from the Apenninic basement, Central Italy

G. Volpe [a], G. Pozzi [b], E. Carminati [a], M.R. Barchi [c], M.M. Scuderi [a], E. Tinti [a], L. Aldega [a], C. Marone [a,d], C. Collettini [a]

a: Università degli Studi di Roma, La Sapienza, Italy

b: Istituto Nazionale di Geofisica e Vulcanologia, Italy

c: Dipartimento di Fisica e Geologia, Università degli Studi di Perugia, Italy

d: Department of Geoscience, The Pennsylvania State University, USA

*Published in Earth and Planetary Science Letters*

## Supplementary materials

### 1 XRD analysis

The XRD analysis carried on the powders of basement rocks showed a similar composition among the samples (Fig.S1, Table 1). Generally, basement rocks are composed of quartz and phyllosilicates in different percentage with minor oxides (rutile and hematite) and carbonates (calcite and dolomite). The semi-quantitative analysis provided the following mineralogical composition:

- upper Palaeozoic phyllites: 36% quartz, 58% phyllosilicates (muscovite, paragonite, chlorite), 6% rutile.
- upper Palaeozoic quartzites: 65% quartz, 33% phyllosilicates (muscovite, paragonite, chlorite), 2% rutile.
- Anageniti: 66% quartz, 24% phyllosilicates (pyrophyllite 9%, muscovite, chlorite), 8% carbonates (calcite and dolomite), 2% hematite.
- Scisti Viola: 37% quartz, 46% phyllosilicates (muscovite, chlorite), 16% hematite, 1% rutile.

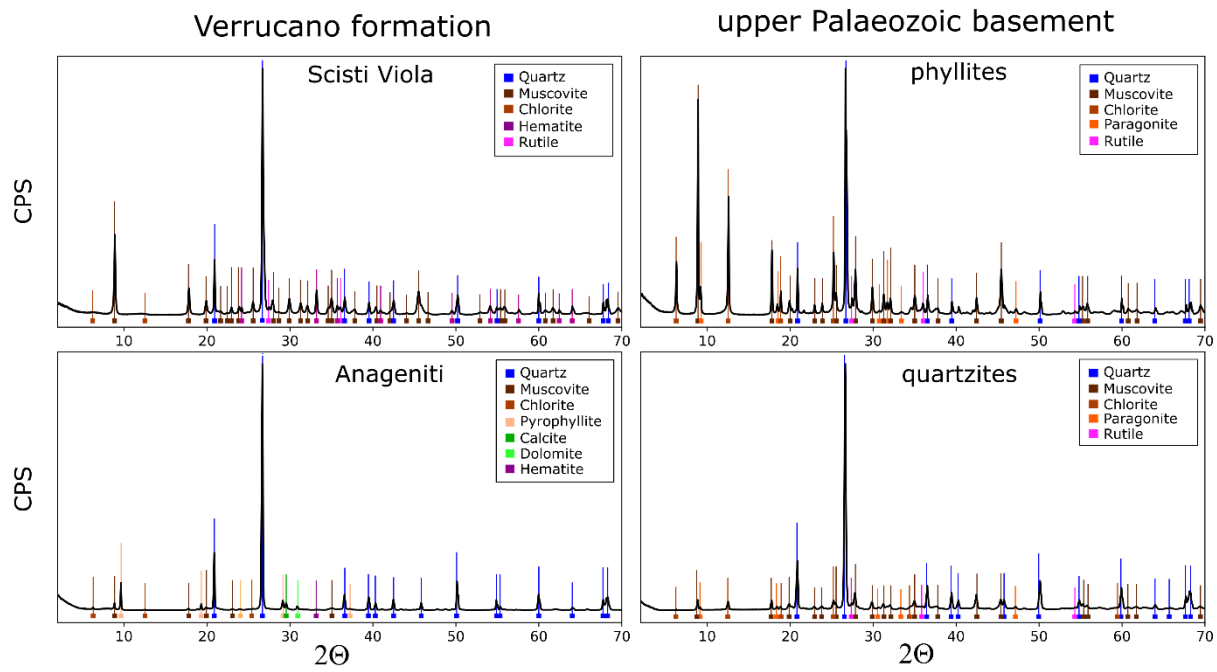


Fig. S1: selected XRD patterns of the tested basement rocks. Verrucano formation, left column, upper Palaeozoic basement, right column.

## 2 Thin sections

Thin section of basement rocks, of 30 µm of thickness, were cut perpendicularly to foliation planes and parallel to the sense of shear to have a better view of the microstructures. Images acquired using a petrographic microscope are reported in Fig. S2. The sampled basement rocks show different microstructures that span between highly anisotropic (foliated) to isotropic (massive) textures. The Scisti Viola (Fig.S2a) and upper Palaeozoic phyllites (Fig.S2c) are characterized by a highly anisotropic texture due to pervasive plane-parallel foliation made of an alignment of phyllosilicate crystals that bound minor quartz microlithons. Upper Palaeozoic quartzites show a schist-to-gneissic texture made of aligned phyllosilicate seams that envelop quartz-rich lenses (Fig.S2d). Anageniti is characterized by an isotropic, grain-supported texture made of sub-rounded quartz grains (up to several centimetres in diameter) with an interstitial non-foliated phyllosilicate matrix (Fig.S2b).

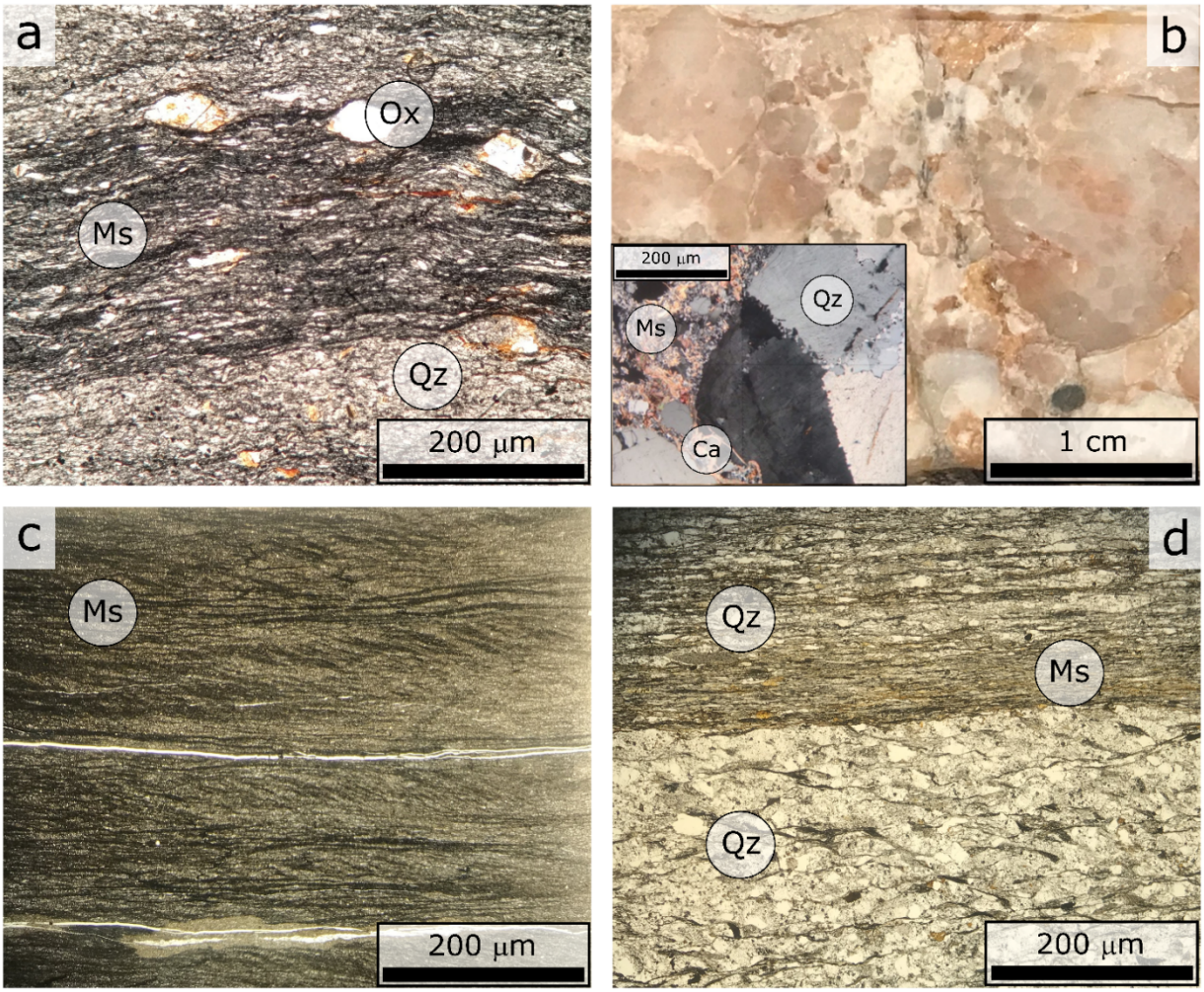


Fig. S2: microstructures from thin section observation at optical microscope, 10 X. a), Scisti Viola (crossed polarized light). b), Anageniti microstructures at centimetre scale and in thin section (crossed polarized light in the inset). c), upper Palaeozoic phyllites in plane polarized light. d), upper Palaeozoic quartzites in plane polarized light. Mineral abbreviations within circles. Qz, quartz; Ms, muscovite (and other phyllosilicates as paragonite, chlorite and pyrophyllite); Ca, carbonates (Calcite and Dolomite); Ox, pseudomorphs replaced by oxides.

# Rheological heterogeneities at the roots of the seismogenic zone

**G. Volpe**[a], G. Pozzi[b], M.E. Locchi[a], E. Tinti[a,b], M.M. Scuderi[a], C. Marone[a,c], C. Collettini[a,b]

a: Dipartimento di Scienze della Terra, La Sapienza Università di Roma, Rome, Italy.

b: Istituto Nazionale di Geofisica e Vulcanologia, Rome, Italy.

c: Department of Geoscience, The Pennsylvania State University, USA.

*Published in Geology*

## Supplemental materials

- **Supplemental material 1: Coulomb stress change**
  - Figure S1
- **Supplemental material 2: Basement geometries**
  - Figure S2
- **Supplemental material 3: Clustering methods**
  - Table S1
  - Figure S3
- **Supplemental material 4: Cross Correlation analysis**
  - Table S2
  - Figure S4
- **Supplemental material 5: Clusters**
  - Figure S5
  - Figure S6
  - Figure S7
- **Supplemental material 6: Experimental apparatus and procedures**
  - Table S3
  - Figure S8

- **Supplemental material 7: Basement gouges**
- **Supplemental material 8: Seismicity cutoff evolution**
    - Figure S9

## Supplemental material 1: Coulomb stress change

To evaluate the static Coulomb stress change caused by the Norcia $M_w$ 6.5 mainshock (fig. S1), we used the software Coulomb 3.3 (Toda et al., 2011). We considered the Norcia-mainshock fault as source fault (strike = N155°, dip = 47°, rake = -90°, length = 35km, e.g, Scognamiglio et al., 2018), and used as receiver faults the faults with orientation: strike = N155°, dip = 47° and rake = -90, thus parallel to the source fault. The model was run using 0.6 as friction coefficient and 0.4 meters as the average coseismic slip (Scognamiglio et al., 2018). Friction coefficient of 0.6 is representative of the friction coefficient of seismogenic faults hosted in the carbonate rocks (Carpenter et al., 2014). We compared the distribution of basement seismicity (Tan et al., 2021 catalogue) with the Coulomb stress change at three different depths (10, 12 and 14 km) (fig. S1 and fig. 1c main text). We plotted the earthquakes distribution for the 30 days following Norcia mainshock in a depth range of 2 km from the depth of the modeled maps of the Coulomb stress change (10-12, 12-14, 14-16 km, respectively, fig. S1). We observe a high correspondence between areas with increasing stress (hot colors in the adopted colormap) and seismicity and cluster distribution.

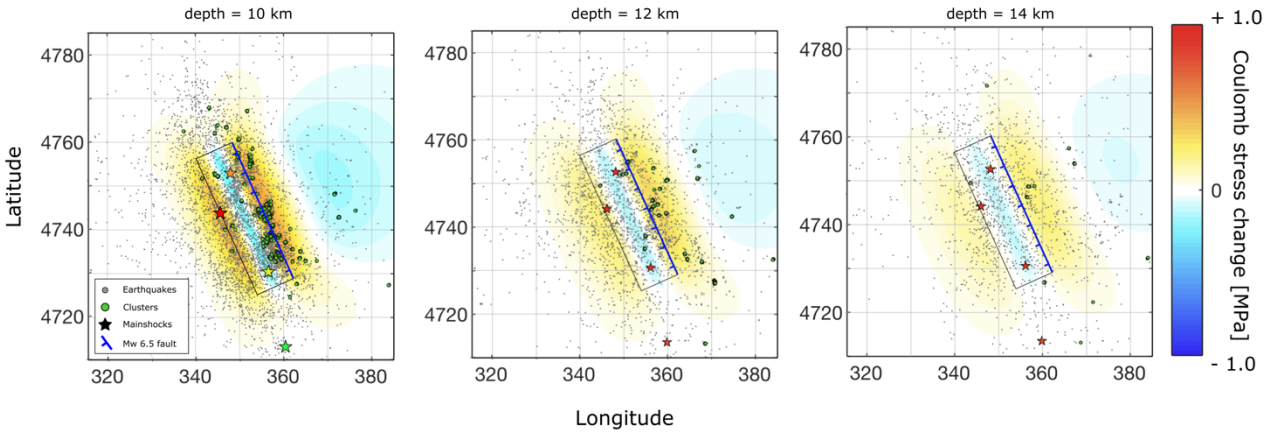


Figure S1: Plan view of the Coulomb stress changes calculated at the three depths (10, 12 and 14 km). The intersection of the fault with the surface is highlighted in blue.

### References

Carpenter, B. M., Scuderi, M. M., Collettini, C., & Marone, C. 2014. Frictional heterogeneities on carbonate-bearing normal faults: Insights from the Monte Maggio Fault, Italy. Journal of Geophysical Research: Solid Earth, 119(12), 9062-9076.

Scognamiglio, L., Tinti, E., Casarotti, E., Pucci, S., Villani, F., Cocco, M., Michelini, A., Dreger, D., 2018. Complex fault geometry and rupture dynamics of the MW 6.5, 30 October 2016, Central Italy earthquake. J. Geophys. Res., Solid Earth 123 (4), 2943–2964.

Tan, Y.J., Waldhauser, F., Ellsworth, W.L., Zhang, M., Zhu, W., Michele, M., Chiaraluce, C., Beroza, C.G., Segou, M., 2021. Machine-learning-based high-resolution earth- quake catalog reveals how complex fault structures were activated during the 2016–2017 central Italy sequence. Seismic Rec. 1 (1), 11–19.

Toda, S., Stein, R. S., Sevilgen, V., & Lin, J. 2011. Coulomb 3.3 Graphic-rich deformation and stress-change software for earthquake, tectonic, and volcano research and teaching—user guide. US Geological Survey open-file report, 1060(2011), 63.

## Supplemental material 2: Basement geometries

We analyzed the seismicity of the Central Italy 2016-2017 seismic sequence using the catalogue of Tan et al., 2021. Here we show the whole seismic sequence in map view and in 6 selected cross-sections: 3 parallel (fig. S2 b, c, d) and 3 perpendicular to the strike of the $M_w$ = 6.5 event (fig. S2 e, f, g). In the cross sections the top of the phyllitic basement is constrained from seismic reflection profiles (Barchi et al., 2021; Collettini t al.,2022). In all the 6 cross-sections, 2-4 km thick, imbricated bands with denser seismicity are present between 5 and about 9 km of depth. The base of the imbricated bands coincides with the top of the basement (dashed purple lines) that is affected by compressional steps (Barchi et al., 2021). These compressional steps result from thrusts rooted into the basement allowing the superimposition of the basement slices above the overlying rocks as also observed in some deep boreholes of the active area of the Apennines (San Donato, Perugia, and Pieve Santo Stefano boreholes Bally et al., 1986; Barchi et al., 1998; Trippetta et al., 2013). Within the basement, seismicity results generally sparse and not localized along evident geological structures. Clusters are also homogeneously distributed in the basement except for some subparallel, east-dipping structures (fig. S2e and g). These structures can represent the prosecution within the basement of active, crustal scale extensional shear zones (Chiaraluce et al., 2017; Vuan et al., 2019; Waldhauser et al., 2021) or ancient structures within the basement that are reactivated following the stress increase (Improta et al., 2019) promoted by the mainshock (e.g., fig. 1c main text)

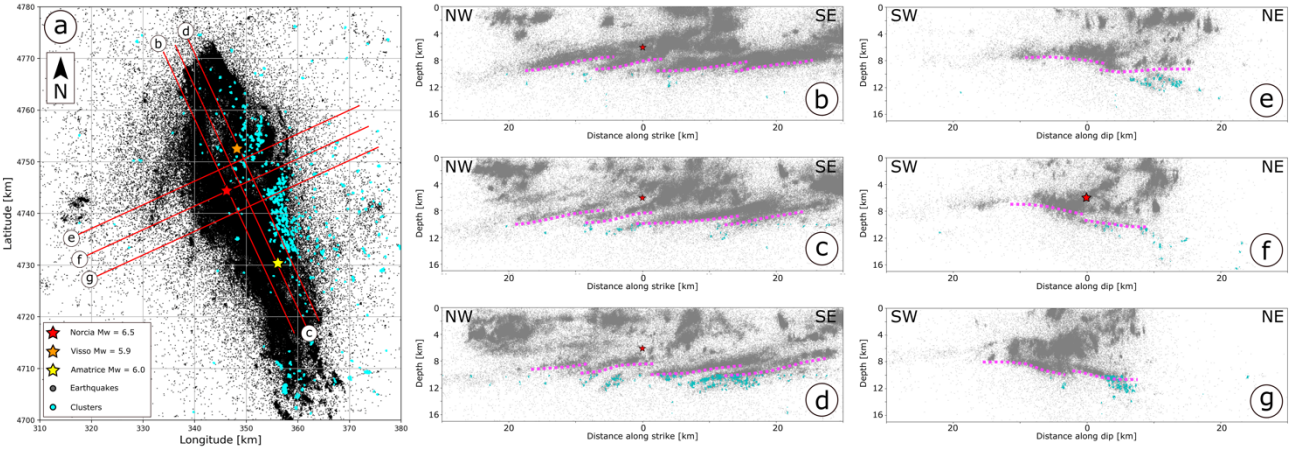


Figure S2: Seismicity distribution in map view (a) and cross sections (b to g), the location of the cross-section traces is reported in panel a. Black dots represent the earthquakes, cyan dots highlight earthquakes belonging to clusters, dashed purple lines mark the depth of the top of the acoustic basement as inferred from seismic reflection profiles (e.g., Barchi et al., 2021; Collettini et al., 2022). All events within 2 km from the cross-section are shown.

## References


Bally, A.W., Burbi, L., Cooper, C., Ghelardoni, R., 1986. Balanced cross-sections and seismic reflection profiles across the central Apennines. Mem. Soc. Geol. Ital. 35, 257–310.

Barchi, M.R., De Feyter, A., Magnani, M.B., Minelli, G., Pialli, G., Sotera, M., 1998. The structural style of the Umbria-Marche fold and thrust belt. Mem. Soc. Geol. Ital. 52, 557–578.

Barchi, M.R., Carboni, F., Michele, M., Ercoli, M., Giorgetti, C., Porreca, M., Azzaro, S., Chiaraluce, L., 2021. The influence of subsurface geology on the distribution of earthquakes during the 2016—2017 Central Italy seismic sequence. Tectono- physics 807, 228797.

Chiaraluce, L., Barchi, M.R., Carannante, S., Collettini, C., Mirabella, F., Pauselli, C., Valoroso, L., 2017. The role of rheology, crustal structures, and lithology in the seismicity distribution of the northern Apennines. Tectonophysics 694, 280–291.

Collettini, C., Barchi, M. R., De Paola, N., Trippetta, F., & Tinti, E. 2022. Rock and fault rheology explain differences between on fault and distributed seismicity. Nature Communications, 13(1), 5627.

Improta, L., Latorre, D., Margheriti, L., Nardi, A., Marchetti, A., Lombardi, A.M., Castello, B., Villani, F., Ciaccio, M.G., Mele, F.M., Moretti, M., 2019. Multi-segment rupture of the 2016 Amatrice-Visso-Norcia seismic sequence (central Italy) con- strained by the first high-quality catalog of Early Aftershocks. Sci. Rep. 9 (1), 1–13.

Trippetta, F., Collettini, C., Meredith, P.G., Vinciguerra, S., 2013. Evolution of the elastic moduli of seismogenic Triassic

Evaporites subjected to cyclic stressing. Tectonophysics 592, 67–79.

Vuan, A., Sugan, M., Chiaraluce, L., & Di Stefano, R. 2017. Loading rate variations along a midcrustal shear zone preceding the Mw6. 0 earthquake of 24 August 2016 in Central Italy. Geophysical Research Letters, 44(24), 12-170.

Waldhauser, F., Michele, M., Chiaraluce, L., Di Stefano, R., Schaff, D.P., 2021. Fault planes, fault zone structure and detachment fragmentation resolved with high-precision aftershock locations of the 2016–2017 central Italy sequence. Geophys. Res. Lett. 48 (16), e2021GL092918.

## Supplemental material 3: Clustering methods

The clustering analysis on the basement seismicity (depth > 10 km) was performed by using the spatial-temporal clustering algorithm ST-DBSCAN (Birant and Kut, 2007). We used as input data the epicentral coordinates (latitude and longitude converted into UTM coordinate system), the hypocentral depth (km), and the origin time. ST-DBSCAN identifies and builds clusters as a function of the following input constraints: maximum distance between neighboring events; maximum time interval between neighboring events; minimum number of events in each cluster. The outputs from the algorithm are represented by ''non-clustered'' seismicity and clustered seismicity.

To study how input constraints influence clustering analysis, we conducted a total of 6 clustering tests using different spatial and temporal constraints (see the six columns of Table S1). For each clustering test we calculated: the number of clusters, the percentage of clustered events relative to the total number of events, the mean temporal duration of the 90% of clusters, the dimension of the clusters expressed in maximum, mean and mode of the equivalent radius assuming spherical clusters, the maximum, mean and mode of the magnitude ($M_w$), and the maximum, mean and mode of the radius of the events considering the maximum, mean and mode magnitude of the clusters and assuming a circular rupture model with 3 MPa stress drop (Kanamori and Anderson, 1975). Results are reported in Table S1.

| | Clustering tests results | | | | | |
|---|---|---|---|---|---|---|
| | ***a*** **150 metres - 7 days** | ***b*** **150 metres - 14 days** | ***c*** **150 metres - 30 days** | ***d*** **450 metres - 7 days** | ***e*** **450 metres - 14 days** | ***f*** **450 metres - 30 days** |
| **Number of clusters** | 572 | 631 | 740 | 1053 | 1116 | 1154 |
| **clustered Eqs/total Eqs** | 12% | 15% | 16% | 22% | 28% | 42% |
| **duration 90% cluster [days]** | 8 | 13 | 50 | 12 | 26 | 74 |
| **Max magnitude [Mw]** | 4.23 | 4.23 | 4.23 | 4.23 | 4.23 | 4.43 |
| **Mean magnitude [Mw]** | 1.16 | 1.15 | 1.15 | 1.15 | 1.15 | 1.12 |
| **Mode magnitude [Mw]** | 1.03 | 1.03 | 1.03 | 1.04 | 1.04 | 1.04 |
| **Rupture radius mode [m]** | 18 | 18 | 18 | 18 | 18 | 18 |
| **Rupture radius max [m]** | 712 | 712 | 712 | 712 | 712 | 898 |
| **Rupture radius mean [m]** | 21 | 20 | 20 | 20 | 20 | 20 |
| **Equivalent radius mode [m]** | 90 | 110 | 112 | 165 | 210 | 290 |
| **Equivalent radius mean [m]** | 140 | 145 | 162 | 283 | 340 | 451 |
| **Equivalent radius max [m]** | 530 | 562 | 1863 | 1320 | 1495 | 3364 |

Table S1: summary of the results of the clustering tests. Letters from *a* to *f* refer to the applied spatial-temporal constraints. 150 meter and 450 meters are the maximum distances between neighboring events. 7, 14, and 30 days are the maximum time interval between neighboring events.

The different clustering constraints produce similar results in term of magnitude of the events and so in terms of rupture radius indicating that the clustering results are not affected by the input constraints. Differences are observed for the number of clusters, percentage of clustered earthquakes, duration, and equivalent radius (geometrical and temporal attributes of the clusters). Generally, by increasing the spatial (maximum distance between events) and temporal (maximum time interval between events) constraints (Table S1), we obtain larger values of the considered parameters.

In our analysis we have used 150 meters and 14 days as spatial-temporal constraints respectively (column *b* in table S1). This selection is justified as follows. The 99% of the basement seismicity has magnitudes between 0 and 3 (mean $M_w$~1.1) corresponding to rupture dimensions in the range between 10 and 200 meters (mean ~20 m). The maximum distance of 450 meters between neighboring events (*d*, *e*, and *f* in Table S1) is in general too large to allow earthquake ruptures overlap. The temporal constrain, from 7 to 30 days, does not influence significantly the clustering analysis and we adopted 14 days that is in the middle of the selected range.

To shed light on the differences among the clustering results we also evaluated the evolution of the number of clusters with depth (fig. S3). We found that, with the exception for clustering *f*, the clustering tests reported similar values (see Table S1) and similar distributions of clusters in depth. Most of the cluster activity occurs in the shallower part of the

basement (9 < depth < 12, e.g., fig. S3 g) which is characterized by a higher spatial and temporal density of earthquakes in respect to the deeper part of the basement (> 12 km).

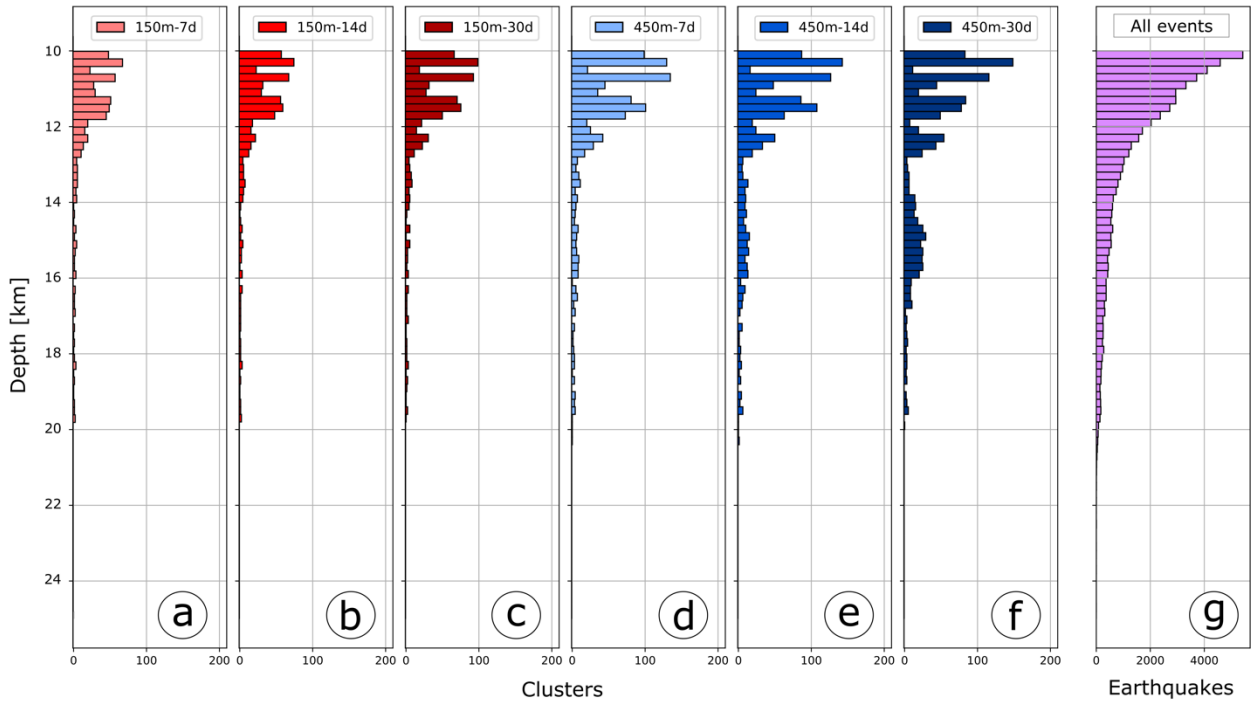


Figure S3: distribution of cluster with depth for the 6 clustering tests (a to f) compared with the distribution with depth of the earthquakes within the basement (g). Spatial and temporal constraints are reported at the top of the histograms.

### References

Birant, D., & Kut, A. 2007. ST-DBSCAN: An algorithm for clustering spatial–temporal data. Data & knowledge engineering, 60(1), 208-221.

Kanamori, H., & Anderson, D. L. 1975. Theoretical basis of some empirical relations in seismology. Bulletin of the seismological society of America, 65(5), 1073-1095.

## Supplemental material 4: Cross-Correlation analysis

To better investigate the origin of the clustered seismicity we performed a cross-correlation analysis on the waveforms resulting from the clustered earthquakes. We firstly selected for each cluster, a pool of seismic stations (broadband velocimeters) from the national seismic network of the Istituto Nazionale di Geofisica e Vulcanologia (INGV) within a radius of 20 km from the epicentral centroid of the cluster. Among them we selected the seismic station with the best signal-to-noise ratio (see Table S2). We collected the waveforms for all the three components (east-west, north-south,

and up-down), we filtered them between [1.5-15 Hz] (Schaff and Waldhauser, 2005) and normalized for their peak amplitude (e.g., Igarashi et al., 2003; Schaff and Waldhasuer, 2005). We selected a temporal window that includes the earthquake signal from the P-wave arrival to two seconds after S-wave arrival (e.g., Igarashi et al., 2003; Schaff and Waldhasuer, 2005 and figs. S6, S7 and S8). Finally, for each component, we applied an iterative cross-correlation analysis between couples of events.

| Type | Name | Location | | | Channels |
|---|---|---|---|---|---|
| | | Longitude [W] | Latitude [N] | Altitude [m asl] | |
| Continuous | MMO1 | 42.90 | 13.33 | 957 | EH |
| | CING | 43.38 | 13.20 | 626 | HH |
| | NRCA | 42.83 | 13.11 | 927 | BH |
| | SMA1 | 42.63 | 13.34 | 1150 | EH |
| | MC2 | 42.91 | 13.19 | 2 | EH |
| | TERO | 42.62 | 13.60 | 673 | BH |
| | FDMO | 43.04 | 13.09 | 550 | HH |
| | CESI | 43.00 | 12.90 | 840 | HH |
| Temporary | T1204 | 42.68 | 13.32 | 1508 | EH |
| | T1212 | 42.75 | 13.04 | 869 | EH |
| | T1214 | 42.76 | 13.21 | 1490 | EH |
| | T1215 | 42.80 | 12.87 | 695 | EH |
| | T1216 | 42.89 | 13.02 | 620 | EH |
| | T1218 | 42.67 | 13.12 | 1184 | EH |
| | T1241 | 42.86 | 13.43 | 664 | HN |

Table S2: attributes of the seismic stations used for the cross-correlation analysis.

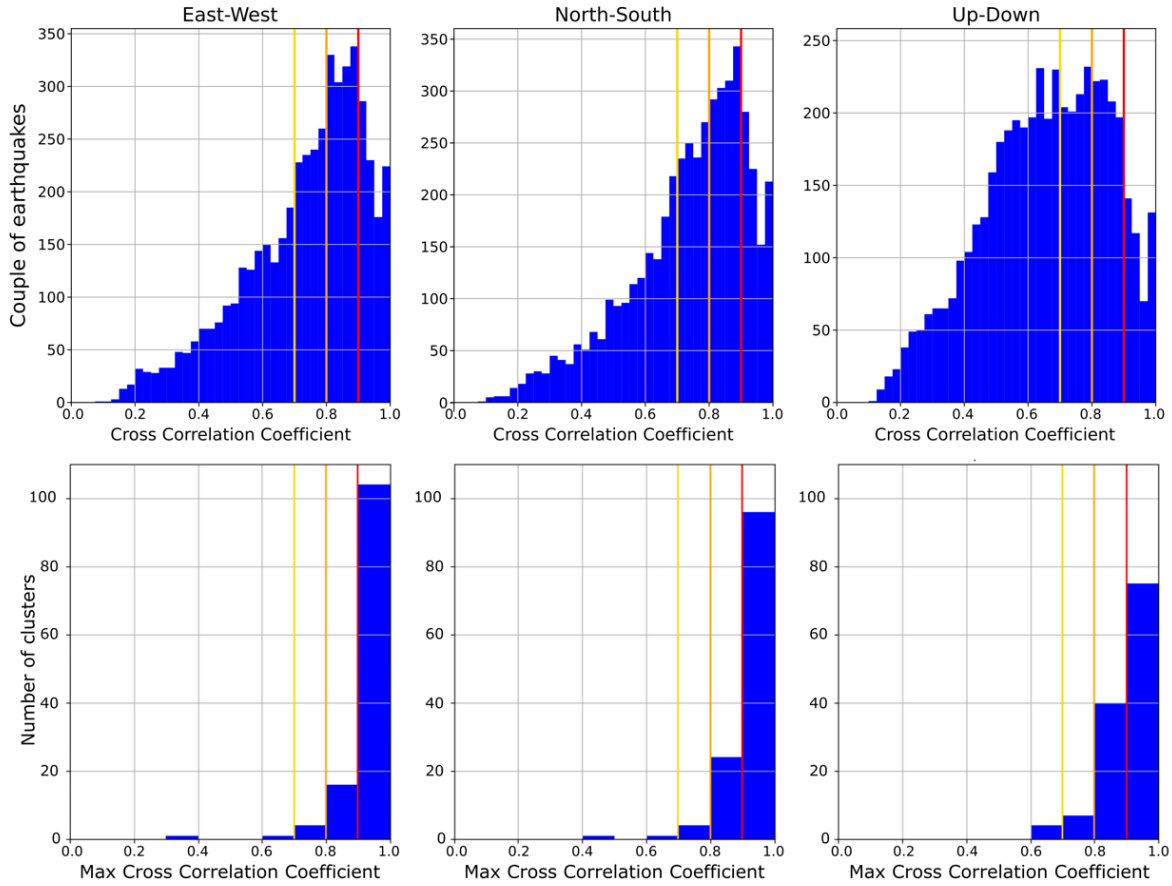


Figure S4: (upper row) distribution of the cumulative cross correlation coefficient for all the three components. The mode of the distribution is always higher than 0.7. (Lower row) maximum cross correlation coefficient of each cluster for all the three components. More than the 70% of all analyzed clusters have at least a couple of events with a cross correlation coefficient higher than 0.9, whereas more than 90% have a couple of events with cross correlation coefficient higher than 0.7.

## References

Igarashi, T., Matsuzawa, T., & Hasegawa, A. 2003. Repeating earthquakes and interplate aseismic slip in the northeastern Japan subduction zone. Journal of Geophysical Research: Solid Earth, 108(B5).

Schaff, D. P., & Waldhauser, F. 2005. Waveform cross-correlation-based differential travel-time measurements at the Northern California Seismic Network. Bulletin of the Seismological Society of America, 95(6), 2446-2461.

# Supplemental material 5: Clusters

We classified the clusters in different families stemming on their cross-correlation distribution and spatial-temporal properties. We found three different categories of clusters: a) *multi-patch multi-fault* clusters (Fig. S5); b) *multi-patch single-fault* clusters (Fig. S6); c) *single-patch single-fault* clusters (Fig. S7).

*Multi-patch multi-fault* clusters are characterized by bimodal distribution of cross-correlation coefficient with two peaks: one at low and one at high cross-correlation coefficient values. These are characterized by two different families of waveforms coming from two different patches of different faults grouped in the same cluster (Fig. S5 and fig. 2f in main text).

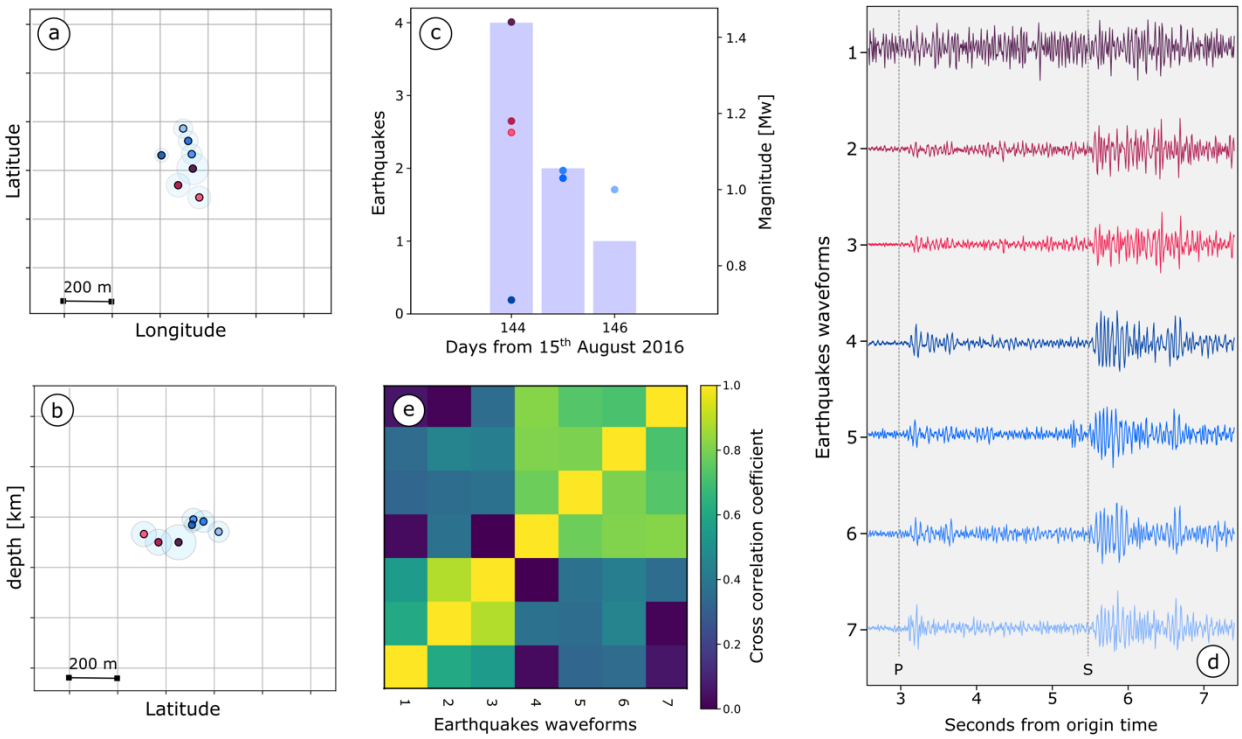


Figure S5: spatial and temporal characterization of cluster 282. Cluster representation in map view (a) and cross section (b). c) distribution of earthquakes number and magnitude for the events of the clusters in time. d) seismograms of the north-south component of the earthquakes of the cluster (from MM01 seismic stations), where P-wave arrival and S-wave arrival are highlighted. e) cross-correlation matrix of the north-south component highlighting two families of earthquakes (red and blue) characterized by two different types of seismograms, with low cross-correlation coefficient among the two families.

*Multi-patch single-fault* clusters are characterized by high cross correlation coefficient (>0.7) resulting from very similar waveforms originated from neighboring patches of the same fault or from faults with partially overlapping region (Fig. S6).

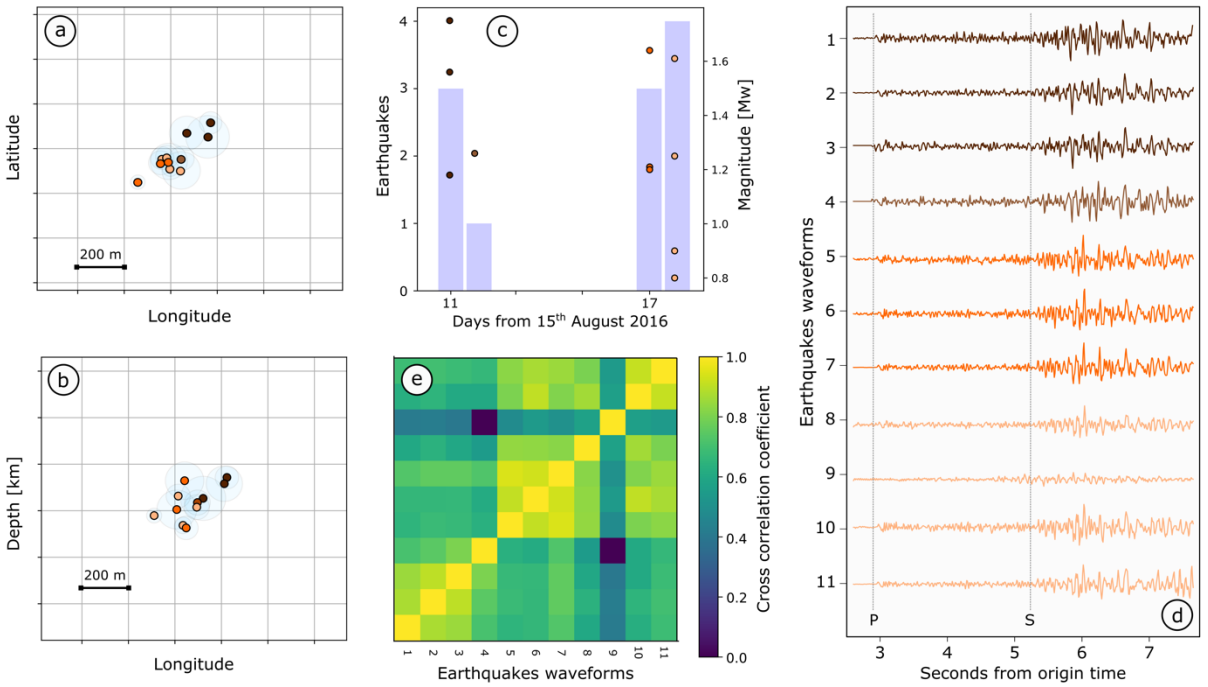


Figure S6: spatial and temporal characterization of cluster 172. Cluster representation in map view (a) and cross section (b). c) distribution of earthquakes number and magnitude for the events of the clusters in time. d) seismograms of the up-down component of the earthquakes of the cluster (from MC2 seismic stations), where P-wave arrival and S-wave arrival are highlighted. e) cross-correlation matrix of the north-south component highlighting two families of earthquakes (brown and orange) characterized by two different types of seismograms originating from two neighboring fault patches; indeed, the two families share quite high cross-correlation coefficient.

*Single-patch single-fault* clusters are characterized by very high cross correlation coefficient (> 0.8) resulting from very similar waveforms originated from the same fault patch or from partially overlapping fault patches that are reactivated several times (Fig. S7 and fig. 2f in main text).

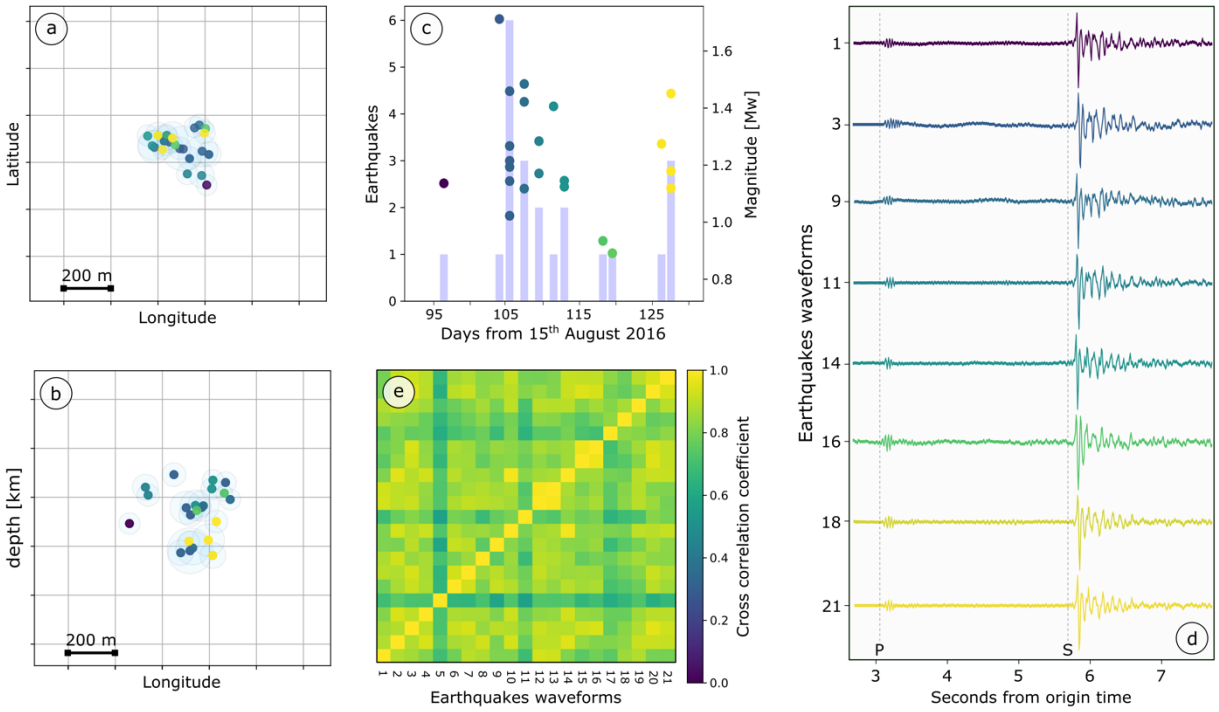


Figure S7: spatial and temporal characterization of cluster 424. Cluster representation in map view (a) and cross section (b). c) distribution of earthquakes number and magnitude for the events of the clusters in time. d) seismograms of the east-west component of the earthquakes of the cluster (from MMO1 seismic stations), where P-wave arrival and S-wave arrival are highlighted. e) cross-correlation matrix of the east-west component highlighting a single family of earthquakes characterized by very similar seismograms and originating from the same fault patches thus resulting in very high cross correlation coefficient.

## Supplemental material 6: Experimental apparatus and procedures

The gouges were tested with BRAVA, a servo-controlled biaxial testing apparatus (Collettini et al., 2014) hosted at the Istituto Nazionale di Geofisica e Vulcanologia of Rome. We used the double direct shear configuration (DDS) consisting of three steel grooved blocks squeezing two identical layers of gouge of 0.5 cm of thickness. Normal stress ($\sigma_n$) is exerted perpendicular to the gouge layers by a horizontal fast-acting servo-controlled hydraulic piston (Collettini et al., 2014). A vertical piston is used to apply shear stress ($\tau$) through the central block, inducing shear deformation within the gouge layers (Collettini et al., 2014). The load exerted by the pistons is measured via strain-gauged load-cells installed at the piston nose, with an accuracy of ±0.03 kN in a range between 0.2 kN and 1.5 MN (Collettini et al., 2014). The load is converted to stress by dividing it by the area of contact within the forcing blocks (50 by 50 mm). Displacements are measured via linear variable displacement transformers (LVDT) with an accuracy of ±0.01 µm. Load point displacement of the vertical and horizontal pistons were corrected for the elastic deformation of the experimental apparatus,

considering that the apparatus stiffness is 1283 kN/mm on the horizontal axis and 928.5 kN/mm on the vertical axis (Collettini et al., 2014). The elastic response of the pistons is linear for the stresses applied during these experiments. The experiments were all performed at 50 MPa of normal stresses, at room temperature and at water-saturated conditions. These experiments consist of five stages listed below (Fig. S8). Preliminarily, the samples are installed and saturated with water at low normal stress of 0.5 MPa for 15 minutes. Then the normal stress is increased at steps of ~0.5 MPa to the targeted normal stress, which is maintained constant throughout the experiment. Once the gouge layers attained an almost steady state thickness, the shearing experiment can begin. The sample is firstly sheared for a total displacement of 10 mm at an imposed load point velocity of 10 µm/s (stage 1). This first stage allows the fault to accommodate enough displacement to reach a steady-state frictional strength. During the second stage, the vertical piston is stopped letting the fault relax for 15 minutes and achieving a residual shear strength. During stage three we set and maintained constant, for 15 minutes, the shear stress at the 80% of the previous steady state shear stress. During stage four, we started increasing stepwise the shear stress (e.g., Fryer et al., 2022) following three different stressing-rate protocols (fig 4a, b of the main test) where the magnitude of the shear stress step is maintained constant among the three protocols (2.5% of the steady-state shear stress) whereas the time interval between stress-steps changes among the three protocols, 15 minutes, 7.5 minutes, 3 minutes, respectively (Table S3 and fig. 4e, f main text).

| Gouges | | Normal stress | Steady state | 80% τss | Stressing rate protocols | | |
|---|---|---|---|---|---|---|---|
| Name | Mineralogy | σn | shear stress τss | | 2.5% τss/15 min | 2.5% τss/7.5 min | 2.5% τss/3 min |
| **Matrix** | phyllosilicates: 46%<br>quartz: 37%<br>others: 17% | 50 MPa | 15 MPa | 12 MPa | 0.375 MPa/15 min | 0.375 Mpa/7.5 min | 0.375 MPa/3 min |
| **Lenses** | phyllosilicates: 24%<br>quartz: 66%<br>others: 10% | 50 MPa | 25 MPa | 20 MPa | 0.625 MPa/15 min | 0.625 MPa/7.5 min | 0.625 MPa/3 min |

Table S3: Summary of the materials, experimental conditions, and stressing rate protocols.

Once the fault reaches slip velocity higher than 1 µm/s, usually after 8 steps, the fault reactivates entering in stage 5 (fig. 4 main text). For comparison and calibration purposes, two further experiments, one for each gouge, were performed at the same boundary conditions of the experiments previously described. During these two experiments, the fault was maintained at stage 3 for 4 hours to observe the behavior of the fault for longer time of creep. In these experiments any spontaneous acceleration has been observed.

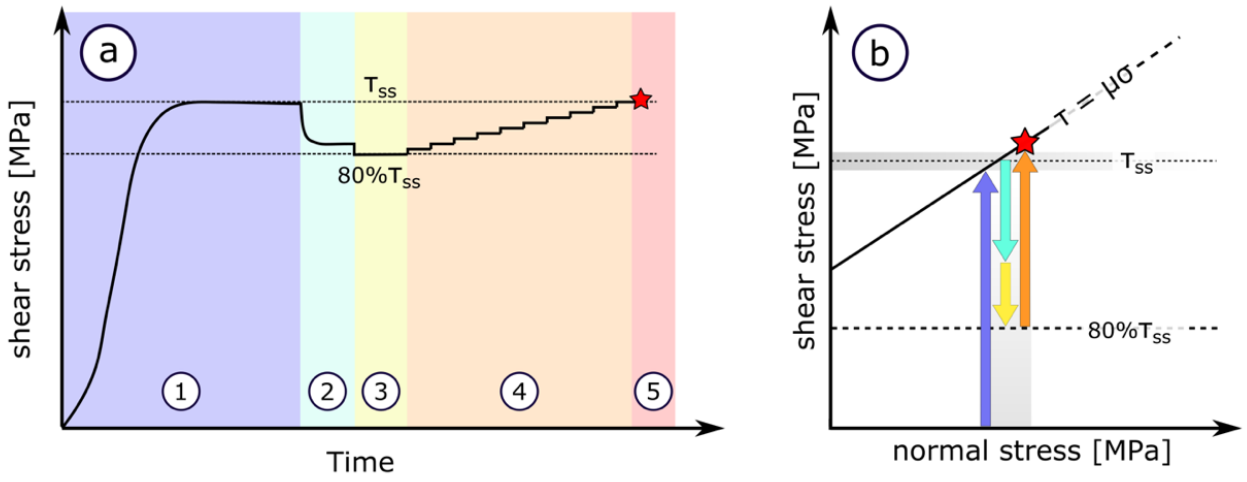


Figure S8: schematic of the experimental procedures. a) shear stress displacement curve for a typical experiment where different experimental stages are highlighted (1 to 5). b) Coulomb space where experimental stages are highlighted.

### References

Collettini, C., Di Stefano, G., Carpenter, B., Scarlato, P., Tesei, T., Mollo, S., Trippetta, F., Marone, C., Romeo, G., Chiaraluce, L., 2014. A novel and versatile apparatus for brittle rock deformation. Int. J. Rock Mech. Min. Sci. 66, 114–123.

Fryer, B., Giorgetti, C., Passelègue, F., Momeni, S., Lecampion, B., & Violay, M. 2022. The influence of roughness on experimental fault mechanical behavior and associated microseismicity. Journal of Geophysical Research: Solid Earth, 127(8), e2022JB025113.

## Supplemental material 7: Basement gouges

We focused our investigation on the Verrucano formation which represents the shallower stratigraphic layer of the acoustic basement in the central Apennines (Tongiorgi et al., 1977; Aldinucci et al., 2008). This formation is one of the most continuous of the basement in central Apennines, in fact, it crops-out in the western part of Tuscany (e.g., Aldinucci et al., 2008) and it has been drilled in some deep-boreholes in Umbria region (Bally et al., 1986; Barchi et al., 1998), close to the area struck by the Central-Italy 2016-2017 seismic sequence. The Verrucano is a slightly metamorphosed siliciclastic formation characterized by the presence of two lithological endmembers: phyllites, represented by Scisti Viola; and meta-conglomerates, represented by Anageniti (Tongiorgi et al., 1977; Aldinucci et al., 2008). Significative outcrops of the Verrucano formation are set in the Monte Argentario area (42°23’02”N – 11°12’03”E; Volpe et al., 2022a and fig. 3 main text) and in the Eastern Elba Island (42°50’11”N – 10°26’14”E and fig. 4a main text). There, the

Verrucano is characterized by the presence of an interconnected and anastomosed network of a foliated phyllosilicate-rich lithology (Scisti Viola) enveloping more competent quartz-rich conglomerate lenses (Anageniti). The Scisti Viola represents high strain domains of pervasive and distributed deformation, whereas Anageniti represents low strain domains characterized by localized brittle features as quartz veins and small faults with decimeter-to-meter displacement (Giuntoli and Viola, 2022; Volpe et al., 2022a). From the Verrucano formation we sampled both the quartz-rich lenses, (Anageniti), and the phyllosilicate-rich matrix (Scisti Viola): Anageniti are characterized by the 76% of quartz and the 24% of phyllosilicates, whereas Scisti Viola are made of 54% of quartz and 46% of phyllosilicates (Volpe et al., 2022a and Table S3).

### References


Aldinucci, M., Gandin, A., Sandrelli, F., 2008. The Mesozoic continental rifting in the Mediterranean area: insights from the Verrucano tectofacies of southern Tuscany (Northern Apennines, Italy). Int. J. Earth Sci. 97 (6), 1247–1269.

Bally, A.W., Burbi, L., Cooper, C., Ghelardoni, R., 1986. Balanced cross-sections and seismic reflection profiles across the central Apennines. Mem. Soc. Geol. Ital. 35, 257–310.

Barchi, M.R., De Feyter, A., Magnani, M.B., Minelli, G., Pialli, G., Sotera, M., 1998. The structural style of the Umbria-Marche fold and thrust belt. Mem. Soc. Geol. Ital. 52, 557–578.

Giuntoli, F., & Viola, G. 2022. A likely geological record of deep tremor and slow slip events from a subducted continental broken formation. Scientific Reports, 12(1), 4506.

Tongiorgi, M., Rau, A., Martini, I.P., 1977. Sedimentology of early-alpine, fluvio- marine, clastic deposits (Verrucano, Triassic) in the Monti Pisani (Italy). Sedi- ment. Geol. 17 (3–4), 311–332.

Volpe, G., Pozzi, G., Carminati, E., Barchi, M. R., Scuderi, M. M., Tinti, E., Aldega, L., Marone, C. & Collettini, C. 2022. Frictional controls on the seismogenic zone: Insights from the Apenninic basement, Central Italy. Earth and Planetary Science Letters, 583, 117444.


## Supplemental material 8: Seismicity cutoff evolution

In Central Apennines, the seismicity cutoff (i.e., the base of the seismogenic zone), defined as the depth above which the 95% of seismicity occurs (e.g., Sibson, 1984; Magistrale, 2002) is located at about 9 km of depth (fig. S9a). This depth corresponds to the average top of the basement as constrained by seismic reflection profiles (e.g., Porreca et al., 2018;

Barchi et al., 2021 and fig. S2). We also related the temporal evolution of the depth of the seismicity cutoff with the evolution of the seismic rate of the basement (fig. S9b and c and fig. 1b main text). The seismicity cutoff, before each mainshock, is set above 9 km, therefore within the sedimentary covers (fig. S9b and c). Following the mainshocks, the seismicity cutoff firstly drops down within the basement (fig. S9b and c) and then it rises again in the sedimentary covers in the following months. This behavior is remarkable for the Norcia mainshock (fig. S9b, c).

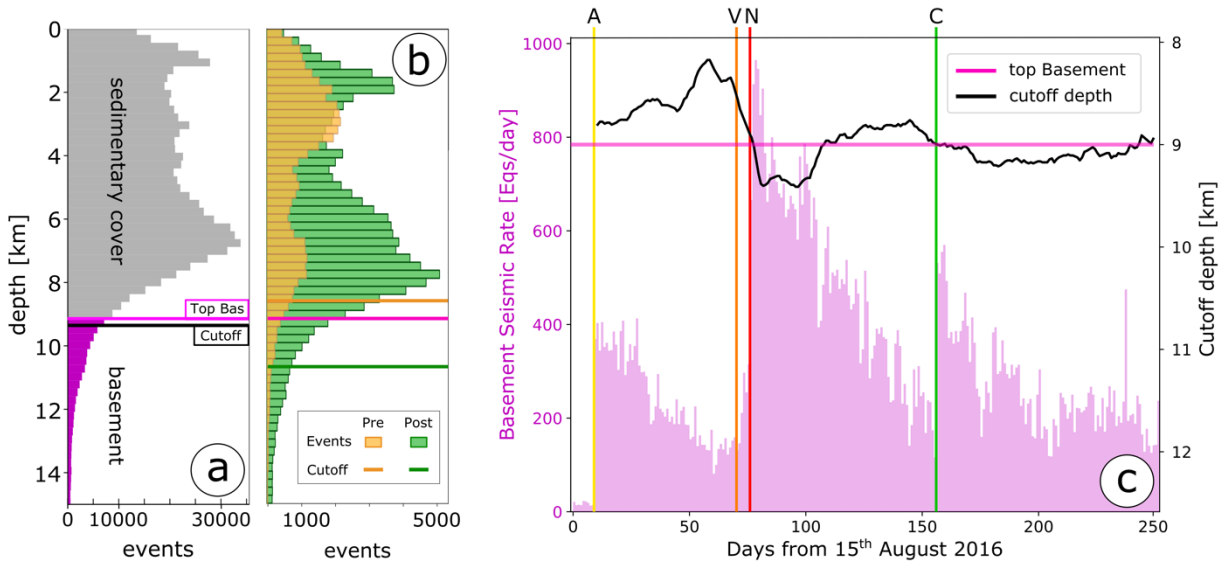


Figure S9: a) depth distribution of the seismicity during the whole sequence. Grey bars indicate the events located within the sedimentary cover, whereas purple bars indicate the events locate within the basement. Purple line marks the average top of the basement located at 9 km as inferred from seismic reflection profiles (Barchi et al., 2021). Black line marks the average cutoff depth during the sequence. b) depth distribution of seismicity during the 30 days before (orange) and after (green) the Norcia $M_w$=6.5 mainshock. Purple line highlights the top of the basement. The orange line marks the mean depth of the seismicity cutoff during 30 days before the Norcia mainshock whereas the green line marks the mean depth of the seismicity cutoff during the 20 days following the Norcia mainshock. c) evolution of the basement seismic rate (depth > 9 km) during the sequence. Vertical lines highlight the occurrence of the major earthquakes: A, Amatrice $M_w$ = 6.0; V, Visso $M_w$ = 5.9; N, Norcia $M_w$ = 6.5; C, Campotosto $M_w$ = 5.5. Purple line represents the average top of the basement. Black line represents the seismicity cutoff evolution during the sequence.

## References

Barchi, M.R., Carboni, F., Michele, M., Ercoli, M., Giorgetti, C., Porreca, M., Azzaro, S., Chiaraluce, L., 2021. The influence of subsurface geology on the distribution of earthquakes during the 2016—2017 Central Italy seismic sequence. Tectono- physics 807, 228797.

Magistrale, H. 2002. Relative contributions of crustal temperature and composition to controlling the depth of

earthquakes in southern California. Geophysical Research Letters, 29(10), 87-1.

Porreca, M., Minelli, G., Ercoli, M., Brobia, A., Mancinelli, P., Cruciani, F., Giorgetti, C., Carboni, C., Mirabella, F., Cavinato, G., Cannata, A., Pauselli, C., Barchi, M.R., 2018. Seismic reflection profiles and subsurface geology of the area interested by the 2016–2017 earthquake sequence (Central Italy). Tectonics 37, 1–22.

Sibson, R. H. 1989. Earthquake faulting as a structural process. Journal of structural geology, 11(1-2), 1-14.

# Appendix of chapter III

# *The role of clay-rich sediments in the seismicity of shallow subduction zones*

---

## Frictional instabilities in clay illuminate the origin of slow earthquakes

**G. Volpe**[a], C. Collettini[a,b], J. Taddeucci[b], C. Marone[a,c], G. Pozzi[b].

a: Dipartimento di Scienze della Terra, La Sapienza Università di Roma, Rome, Italy.

b: Istituto Nazionale di Geofisica e Vulcanologia, Rome, Italy.

c: Department of Geoscience, The Pennsylvania State University, USA.

*Submitted*

## Supplementary material

This supplementary material consists of the following contents: SM1: Montmorillonite powder; SM2: Experimental dataset; SM3: Slide-Hold-Slide test; SM4: Frictional parameters; SM5: Experimental microstructures; SM6: Video of events n 10-14; SM7: Comparison between roughness; SM8: Characterization of the rupture front propagation; M1: Experimental apparatus and procedures; M2: Frictional properties analysis; M3: Microstructural analysis; M4: Experimental design for direct video documentation; M5: Digital-image analysis.

## SM1: Montmorillonite powder

98% pure Ca-montmorillonite powder is provided by GSA resources (SM1502A). The platelets of montmorillonite have dimension around few µm. The initial material is organized in elongated vermiculite-like aggregates of montmorillonite platelets (fig. SM1 inset).

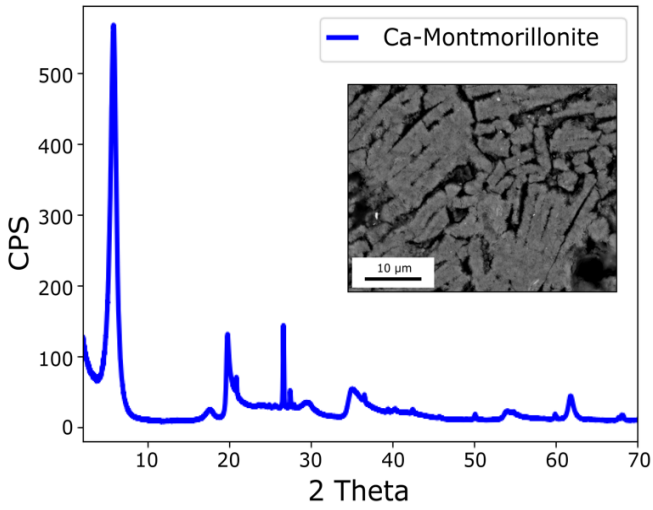


Fig. SM1: XRD diffractogram of the tested montmorillonite powder.

## SM2: Experimental dataset

| experimental number | normal stress [Mpa] | humidity | run -in | | velocity steps | | | | | | | | | | | slide-hold-slide | | | | | | Spring | Roughness |
|---|---|---|---|---|---|---|---|---|---|---|---|---|---|---|---|---|---|---|---|---|---|---|---|
| | | | Vel [µm/s] | Dx [mm] | Sliding Velocity [µm/s] | | | | | | | | | | Dx [mm] | Vel [µm/s] | Dx [mm] | Hold time [s] | | | | | |
| | | | | | 0.03 | 0.05 | 0.1 | 0.3 | 1 | 3 | 10 | 30 | 100 | 300 | | | | 30 | 100 | 300 | 1000 | | |
| b1297-b | 5 | 100% | 10 | 5 | | | X | X | X | X | X | X | X | X | 0.5 | | | | | | | plexyglass | large teeth |
| b1118 | 12.5 | 100% | 10 | 5 | | | | | X | X | X | X | X | X | 0.5 | 0.1 | 0.25 | X | X | X | X | plexyglass | large teeth |
| b1104 | 25 | 100% | 10 | 5 | | | | | X | X | X | X | X | X | 0.5 | 0.1 | 0.25 | X | X | X | X | plexyglass | large teeth |
| b1106 | 50 | 100% | 10 | 5 | | | | | X | X | X | X | X | X | 0.5 | 0.1 | 0.25 | X | X | X | X | plexyglass | large teeth |
| b1119 | 100 | 100% | 10 | 5 | | | | | X | X | X | X | X | X | 0.5 | 0.1 | 0.25 | X | X | X | X | plexyglass | large teeth |
| b1121 | 12.5 | 100% | 10 | 5 | | | | | X | X | X | X | X | X | 0.5 | 10 | 0.25 | X | X | X | X | plexyglass | large teeth |
| b1103 | 25 | 100% | 10 | 5 | | | | | X | X | X | X | X | X | 0.5 | 10 | 0.25 | X | X | X | X | plexyglass | large teeth |
| b1105 | 50 | 100% | 10 | 5 | | | | | X | X | X | X | X | X | 0.5 | 10 | 0.25 | X | X | X | X | plexyglass | large teeth |
| b1125 | 100 | 100% | 10 | 5 | | | | | X | X | X | X | X | X | 0.5 | 10 | 0.25 | X | X | X | X | plexyglass | large teeth |
| b1104 | 25 | 100% | 10 | 5 | | | | | X | X | X | X | X | X | 0.5 | 10 | 0.25 | X | X | X | X | plexyglass | large teeth |
| b1157 | 25 | 100% | 10 | 5 | | | | | X | X | X | X | X | X | 0.5 | 10 | 0.25 | X | X | X | X | plexyglass | small teeth |
| b1186 | 25 | 100% | 10 | 5 | | | | | X | X | X | X | X | X | 0.5 | 10 | 0.25 | X | X | X | X | plexyglass | nominally flat |
| b1184 | 25 | 100% | 10 | 5 | | | | | X | X | X | X | X | X | 0.5 | 10 | 0.25 | X | X | X | X | plexyglass | layered gouge |
| b1--- | 25 | 100% | 10 | 5 | X | X | X | X | X | X | X | X | X | X | 0.25 | | | | | | | plexyglass | large teeth |
| b1156 | 25 | 100% | 10 | 5 | X | X | X | X | X | X | X | X | X | X | 0.25 | | | | | | | metal | large teeth |
| b1098 | 25 | 100% | 10 | 5 | X | X | X | X | X | X | X | X | X | X | variable | | | | | | | metal | large teeth |
| b1126 | 25 | 100% | 10 | 3 | | | | | | | | | | | | | | | | | | plexyglass | large teeth |
| b1131 | 25 | 100% | 0.1 | 3 | | | | | | | | | | | | | | | | | | plexyglass | large teeth |
| b1297-a | 1 | 100% | 10 | 5 | | | X | X | X | X | X | X | X | X | 0.5 | | | | | | | | large teeth |
| b1083 | 15 | 100% | 10 | 5 | | | | | X | X | X | X | X | X | 0.5 | 0.1 | 1.5 | | | | | | large teetn |
| b1085 | 35 | 100% | 10 | 5 | | | | | X | X | X | X | X | X | 0.5 | 0.1 | 1.5 | | | | | | large teeth |
| b1296 | 21 | 100% | 10 | | | | X | | | | X | X | X | X | variable | | | | | | | plexyglass | nominally flat |

Table SM2: summary of the experimental procedures. A total of 22 experiments have been performed. The experiments for the frictional properties characterization are reported in the first 5 rows. Explicative Notes. Dx is the fault displacement. Experiments with *plexyglass spring* instead of *metal* indicate the experiments with de-stiffened apparatus to enhance instabilities. Roughness is the type of interface of the forcing blocks: *large teeth* blocks have triangular teeth spaced 2 mm; *small teeth* blocks have triangular

teeth spaced 0.8 mm; *nominally flat* blocks do not have teeth; *layered gouge* are experiments where the montmorillonite gouge is set between two thin (< 0.5 µm) layers of quartz gouge.

## SM3: Slide-Hold-Slide test

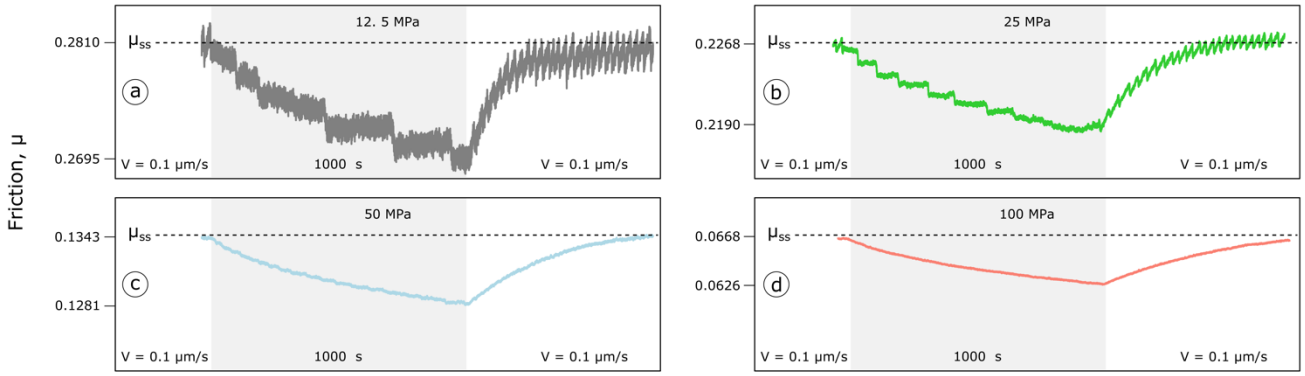


Figure SM3: Slide-hold-slide test for 1000 seconds of hold time (the longer hold time explored) for the experiments reported in the main text: a) experiments b1118, σn = 12.5 MPa; b) exp b1104, σn = 25 MPa; c) b1106, σn = 50 MPa; d) b1119, σn = 100 MPa. For all the experiments no peak in friction upon re-shear is observed implying null healing rate.

## SM4: Frictional parameters

| Experiment | Sigma | µss (10µm/s) | a | b | Dc [m] | µ0 | V0 | V1 |
|---|---|---|---|---|---|---|---|---|
| b1104 | 25 | 0.229 | 0.003179 | 0.001514 | 6.99E-05 | 0.2298 | 10 | 1 |
| | | | 0.002291 | 0.001366 | 8.02E-05 | 0.226 | 1 | 3 |
| | | | 0.003870 | 0.001812 | 1.07E-04 | 0.2272 | 3 | 10 |
| | | | 0.006008 | 0.001669 | 1.11E-04 | 0.2301 | 10 | 30 |
| | | | 0.001929 | -0.006114 | 9.55E-06 | 0.2347 | 30 | 100 |
| | | | 0.001799 | -0.009111 | 1.76E-05 | 0.2424 | 100 | 300 |
| | | | 0.009147 | 0.001902 | 3.00E-04 | 0.2533 | 300 | 10 |
| | | | 0.002487 | 0.001370 | 4.27E-05 | 0.2272 | 10 | 0.1 |
| b1106 | 50 | 0.136 | 0.003334 | 0.001176 | 9.25E-05 | 0.1367 | 10 | 1 |
| | | | 0.002726 | 0.000367 | 5.98E-05 | 0.1319 | 1 | 3 |
| | | | 0.003441 | 0.000412 | 1.16E-04 | 0.1346 | 3 | 10 |
| | | | 0.004501 | -0.000125 | 1.88E-04 | 0.1383 | 10 | 30 |
| | | | 0.004772 | -0.000897 | 1.10E-06 | 0.1423 | 30 | 100 |
| | | | 0.002722 | -0.005301 | 1.38E-05 | 0.1486 | 100 | 300 |
| | | | 0.025533 | 0.019622 | 1.65E-07 | 0.1569 | 300 | 10 |
| | | | 0.003260 | 0.001116 | 1.66E-06 | 0.138 | 10 | 0.1 |
| b1118 | 12.5 | 0.283 | 0.004262 | 0.001318 | 3.13E-05 | 0.2913 | 10 | 1 |
| | | | 0.002599 | 0.001155 | 3.31E-05 | 0.2832 | 1 | 3 |
| | | | 0.005397 | 0.001836 | 4.31E-05 | 0.2846 | 3 | 10 |
| | | | 0.007573 | 0.002574 | 1.76E-04 | 0.2884 | 10 | 30 |
| | | | 0.011087 | -2.06E-05 | 7.61E-04 | 0.2939 | 30 | 100 |
| | | | 0.002973 | -0.012782 | 2.09E-05 | 0.3056 | 100 | 300 |
| | | | 0.01069 | 0.002678 | 1.26E-04 | 0.3121 | 300 | 10 |
| | | | 0.002656 | 0.001106 | 8.74E-05 | 0.2848 | 10 | 0.1 |
| b1119 | 100 | 0.058 | 0.002259 | 0.001052 | 2.22E-06 | 0.0639 | 10 | 1 |
| | | | 0.00028 | -0.001922 | 7.02E-07 | 0.0608 | 1 | 3 |
| | | | 0.000739 | -0.001708 | 3.04E-07 | 0.0634 | 3 | 10 |
| | | | 6.85E-05 | -0.003243 | 1.69E-06 | 0.0664 | 10 | 30 |
| | | | 0.000976 | -0.003378 | 2.71E-07 | 0.07001 | 30 | 100 |
| | | | 0.000448 | -0.005043 | 5.86E-07 | 0.0753 | 100 | 300 |
| | | | 0.013506 | 0.0096095 | 3.64E-11 | 0.0813 | 300 | 10 |
| | | | 0.000475 | -0.001294 | 3.83E-08 | 0.0687 | 10 | 0.1 |
| b1297-b | 5 | 0.368 | 0.005234 | -0.001566 | 1.66E-05 | 0.3521 | 0.1 | 0.3 |
| | | | 0.001554 | -0.000525 | 3.50E-05 | 0.3593 | 0.3 | 1.0 |
| | | | 0.003390 | 0.002653 | 3.91E-05 | 0.3613 | 1.0 | 3.0 |
| | | | 0.003390 | 0.002653 | 3.92E-05 | 0.3611 | 3.0 | 10.0 |
| | | | 0.005542 | 0.007299 | 3.93E-04 | 0.3611 | 3.0 | 10.0 |
| | | | 0.006062 | 0.005141 | 1.60E-04 | 0.3611 | 3.0 | 10.0 |
| | | | 0.008140 | 0.002527 | 1.59E-04 | 0.3583 | 10.0 | 30.0 |
| | | | 0.013119 | 0.004338 | 4.90E-04 | 0.3612 | 30.0 | 100.0 |
| | | | 0.024226 | 0.007171 | 6.28E-05 | 0.3663 | 100.0 | 300.0 |

Table SM4: summary of the characterization of the frictional properties for the experiment reported in the main text.

## SM5: Experimental Microstructures

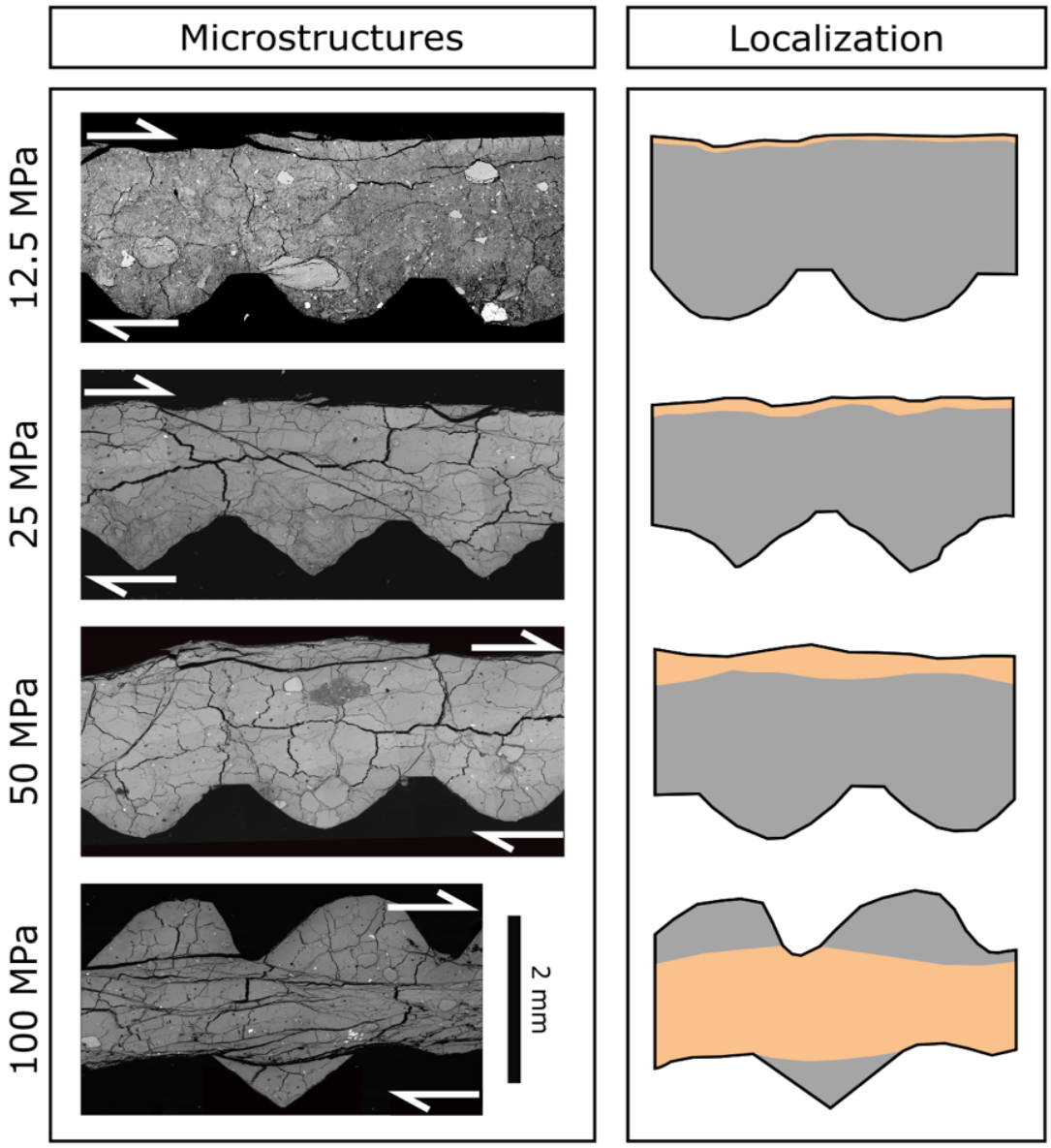


Figure SM5: Experimental microstructures of the deformed montmorillonite. In the left column are reported the collected images in SEM. In the right column are reported the interpretation of the microstructure. Gray: low strain domain, Orange: high strain domain. A decrease in localization is observed with increasing normal stress. Details of the microstructures are reported in the main text and in Fig. 1.

## SM6: Video events 10 to 14

Videos of the rupture of stick-slip event n° 10 to 14 (n° 11 in fig. 3) are available at the Google Drive link: https://drive.google.com/drive/folders/1lxi9L-n02Ywa7RGzRnnMytHPQWn_MtSd?usp=share_link.

## SM7: Comparison between roughness

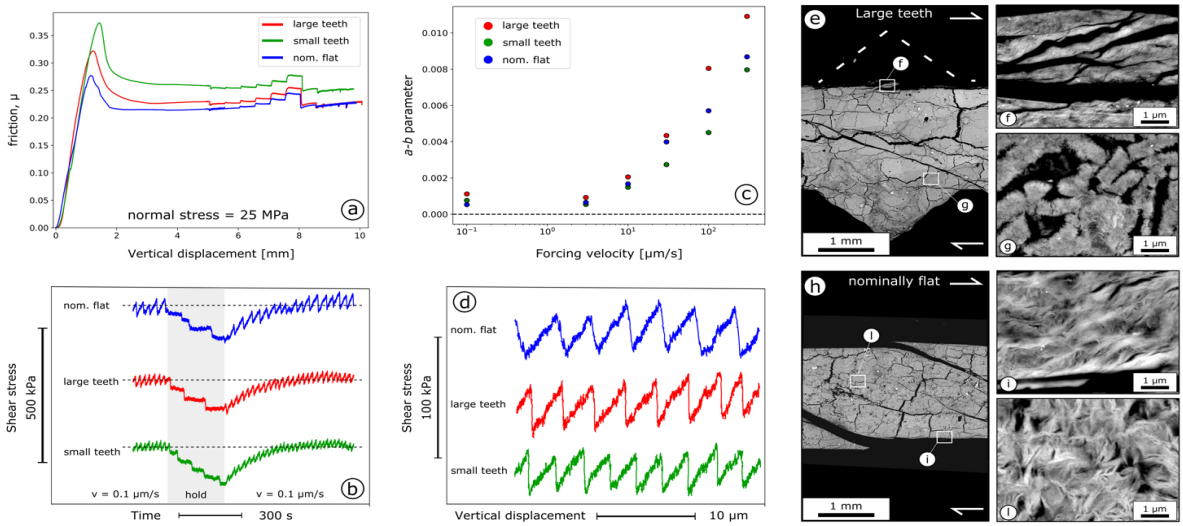


Figure SM7: comparison of the mechanical data and microstructures of experiments performed using forcing blocks with different roughness: *large teeth* – b1104; *small teeth* – b1157; *nominally flat* – b1186 (fig. SM2). The mechanical data (friction curves, healing rate, *a-b* parameter and stick-slip behavior) are similar. Microstructures show same features.

## SM8: Characterization of the rupture front propagation

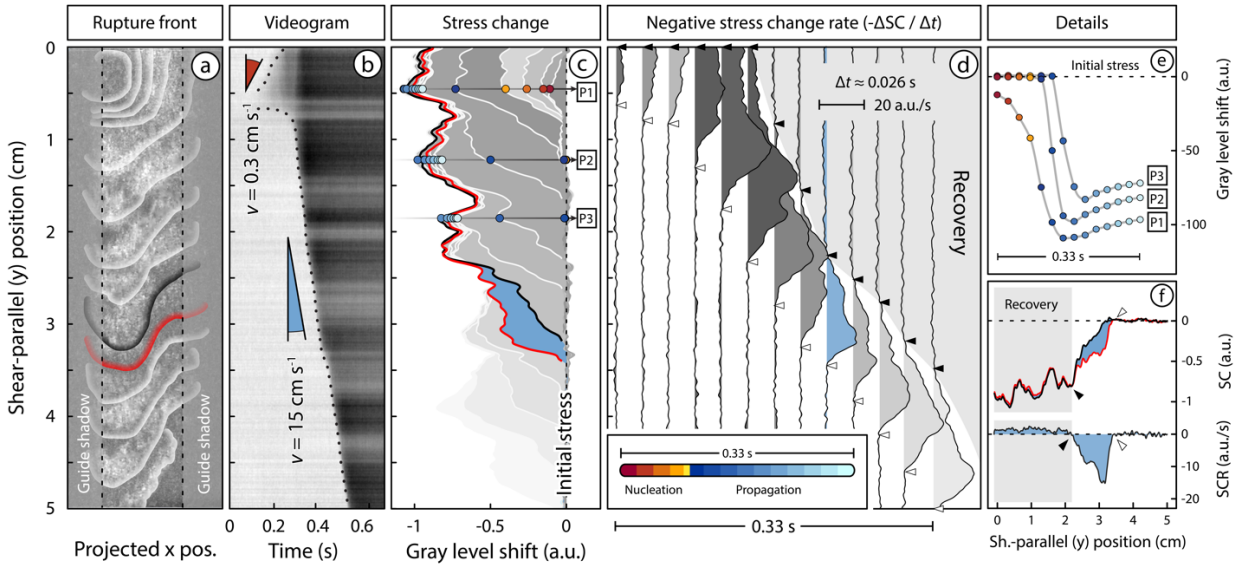


Figure SM8: characterization of the propagation of the rupture front in a time window of 0.026 seconds between $t_0$ (black) and $t_1$ (red). a) position of the rupture front at $t_0$ and $t_1$. b) videogram of the rupture nucleation and propagation showing the rupture velocity. c) stress change along the fault during the rupture where are highlighted the change in stress state on the fault surface at $t_0$ and $t_1$. d) stress change rate along the fault during time with highlighted the stress change rate in the selected time window. e) evolution of the stress change in time for selected 3 points (panel c) on the fault surface during rupture nucleation and propagation. f) stress change (upper row) and stress change rate (lower row) along the fault for the selected time-window.

# Methods

## M1: Experimental apparatus and procedures

Montmorillonite powder (details in SM1) was tested with BRAVA, a servo-controlled biaxial testing apparatus (Collettini et al., 2014) hosted at the Istituto Nazionale di Geofisica e Vulcanologia of Rome. We used the double direct shear configuration (DDS) consisting of three steel forcing blocks squeezing two identical layers of rock powder (gouge) with initial thickness of 4 mm (fig. M1a). The normal stress ($\sigma_n$) is applied perpendicular to the gouge layers with a horizontal servo-controlled hydraulic piston (Collettini et al., 2014). A vertical piston is used to apply the shear stress ($\tau$) through the central block (slider), forcing shear deformation within the gouge layers (Collettini et al., 2014). The force applied by the pistons is measured via strain-gauged load-cells with an accuracy of ±0.03 kN (Collettini et al., 2014). The load is converted to stress by dividing it by the area of contact within the forcing blocks (50 by 50 mm). Load point displacements are measured via linear variable displacement transformers (LVDT) with an accuracy of ±0.01 µm. The elastic response of the pistons is linear for the stresses applied during these experiments. To obtain dynamic instabilities in the material we reduced the stiffness of the loading system (2.96 MPa/mm) by using an acrylic block (spring) to apply the shear stress to the central slider. This procedure is widely used in literature for the study of frictional instabilities (e.g., Scuderi et al., 2016; Leeman et al., 2018).

The experimental procedure consists of five sequential stages listed below:

1. *Loading*. The normal stress is applied gradually to the sample to the target value (5, 12.5, 25, 50, 100 MPa).
2. *Relaxation*. Once the target normal stress is reached, the gouge layers are allowed to compact to attain an almost steady state thickness (~15 minutes).
3. *Run in.* After compaction, the sample is sheared for a total displacement of 5 mm at a load point velocity of 10 µm/s. This stage allows the fault to reach a steady-state frictional strength and fabric (fig. M1b).
4. *Velocity step test*. The experimental fault is sheared at increasing forcing velocity: 1, 3, 10, 30, 100, 300 µm/s, for 500 µm of displacement in each step (fig. M1c).
5. *Slide hold slide test.* This test consists of alternating sliding (displacement of 250 µm) at constant forcing velocity of 0.1 µm/s and stopping (imposing 0 velocity) at increasing hold times: 30, 100, 300, 1000 seconds (fig. M1d, e).

All experiments were performed at 100% room-humidity conditions and the samples were let humidifying overnight before the start of the experiment. We also performed several other frictional experiments with slightly different experimental procedure, aimed to characterize specific properties of the gouge (Table SM2).

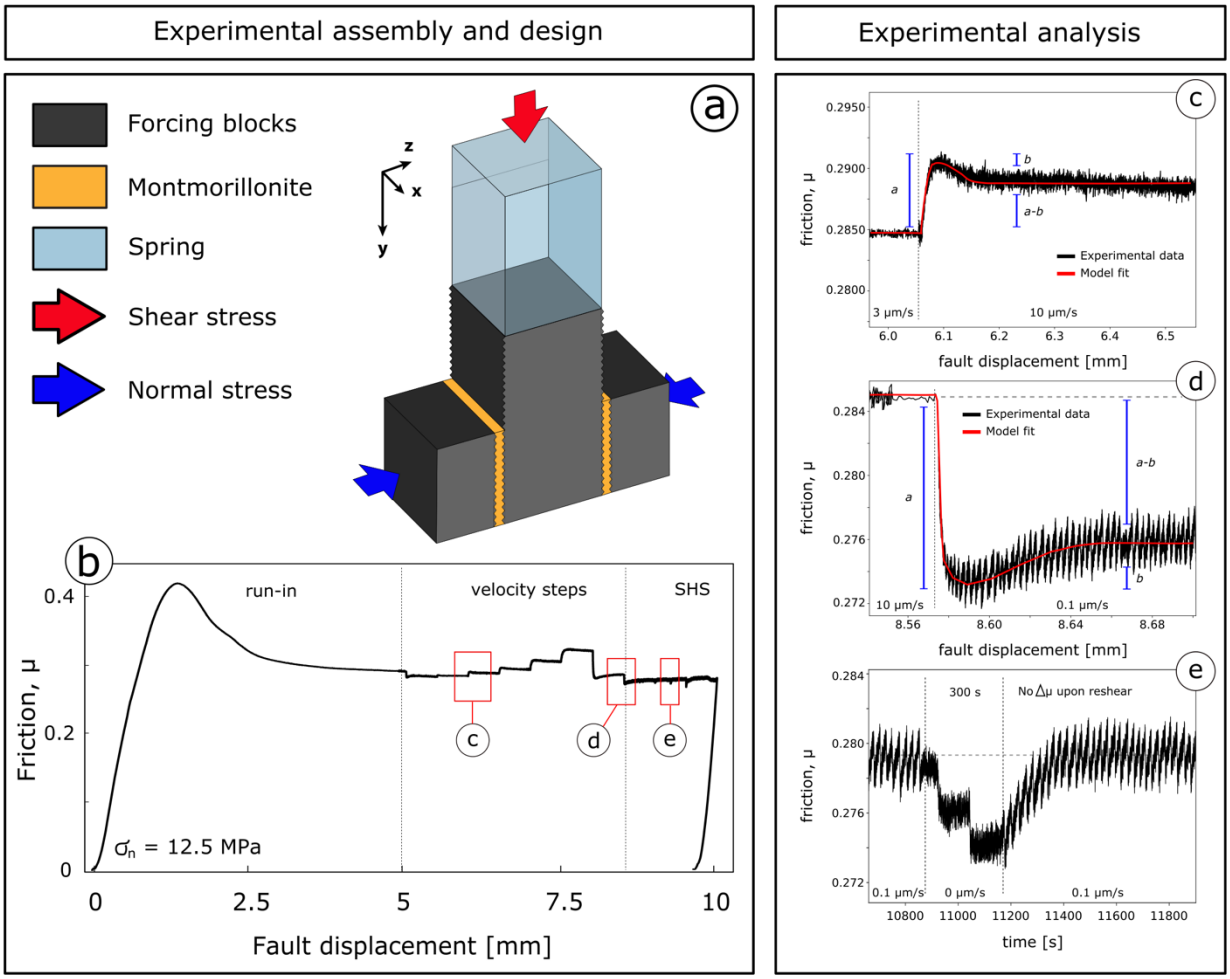


Figure M1: a) detail of the Double Direct Shear assembly. b) evolution of friction as a function of shear displacement for one experiment (b1118). Our procedure consisted of a run-in phase followed by velocity step tests and slide-hold-slide (SHS) test. c) and d) Detail of a velocity step tests from 3 to 10 μm/s and from 10 to 0.1 μm/s respectively. Black lines represent the experimental data red lines the best-fit model using RSF. e) Detail of a 300-s slide-hold-slide test showing evolution of friction with hold time and re-shear. Note that in panel d and e, the stick-slip behavior is superimposed on a trend that can be modelled using RSF.

## M2: Frictional properties analysis

We characterized the steady-state frictional strength ($\mu$), the velocity dependence of friction ($a$-$b$), and the healing behavior ($\beta$). We used the Rate and State friction theory (RSF; Dieterich, 1979; Ruina, 1983; Marone 1998) as framework

for our analysis. The friction coefficient, $\mu$, is retrieved as the linear constant of proportionality between steady-state shear stress and normal stress, using Eq. 1:

$$\tau = \mu\sigma_n + c \quad (1)$$

where c is the cohesion term, which can be assumed negligible. During the velocity step tests the forcing velocity is varied from $V_0$ to V, which causes a variation of frictional strength characterized by a direct and evolution effect (fig. M1c, d). The direct effect scales with $a \log_e(V/V_0)$, where $a$ is an empirical parameter (Dieterich, 1979; Ruina, 1983). The subsequent evolution of friction to a new steady-state, scales with $b \log_e(V/V_0)$, where $b$ is also an empirical parameter (Dieterich, 1979; Ruina, 1983). The $(a-b)$ parameter defines the velocity dependence of friction:

$$(a-b) = \Delta\mu_{ss} / \log_e(V/V_0) \quad (2)$$

where $\Delta\mu_{ss}$ is the difference between the dynamic steady-state frictional strength after and before the step in shearing velocity from $V_0$ to V (Dieterich, 1979, Ruina, 1983). Negative values of $(a-b)$ define a velocity-weakening behavior, which is a required condition for frictional instability (Dieterich and Kilgore, 1994; Marone 1998). Positive values of $(a-b)$ define a velocity-strengthening behavior, suggesting aseismic creep. Each velocity step was inverted using RSF equations (Eq., 3) coupled with the Dieterich law (Eq. 4), an evolution law that defines the state variable $\vartheta$ (Dieterich, 1979):

$$\mu = \mu_0 + a \log_e(V/V_0) + b \log_e(V_0\theta / D_c) \quad (3)$$

$$d\vartheta/dt = 1 - \vartheta V/D_c \quad (4)$$

where $\mu_0$ is steady-state frictional strength at slip velocity $V_0$ and $D_c$ is the critical slip distance (Dieterich, 1979, Ruina, 1983). To model velocity steps, equations 3 and 4 are coupled with equation 5, which defines the elastic coupling between the sliding surface and the loading medium:

$$d\mu/dt = k(V_f - V) \quad (5)$$

where $V_f$ is the forcing velocity (the one applied by the vertical piston) and $k$ is the loading system stiffness normalized by normal stress. These equations are solved simultaneously using a fifth order Runge-Kutta integration. $a$, $b$, and $D_c$ were retrieved, for each velocity step, as best fit values using a, least squares iterative method to solve the inverse non-linear problem (Blanpied et al., 1998; Saffer and Marone, 2003).

During slide hold slide test, the frictional healing ($\Delta\mu$) was obtained as the difference between the friction peak measured during re-shear following each hold and the steady state friction before the hold (Marone, 1998, fig. M1e). Frictional healing rate ($\beta$) was retrieved as the linear variation of $\Delta\mu$ with logarithm of the hold time ($t_h$).

$$\beta = \Delta\mu/\log10(\Delta t_h) \quad (6)$$

## M3: Microstructural analysis

At the end of each experiment, we carefully extracted the deformed samples to preserve the entire gouge thickness, comprised within the forcing blocks (Volpe et al., 2022b). After extraction we carefully embedded the samples in epoxy resin (Struers EpoFix) at room pressure. Once the resin was hardened, we cut the samples perpendicular to the shear plane and parallel to the sense of shear to expose the kinematic section of the microstructure (Passchier, 1990). The cut surfaces were polished with increasingly finer sandpaper, grit of 600–2000, and then by finer diamond paste, 6–1 µm, (Volpe et al., 2022b). All lapping steps were performed at low velocity and lubricated with oil-based fluids to avoid water-enhanced erosion of the samples. Polished surfaces were coated with graphite for the microstructural analysis, which was conducted with a Field-Emission Scanning-Electron-Microscope (SEM) hosted at the Istituto Nazionale di Geofisica e Vulcanologia of Rome. Imagery was collected in back-scattered mode.

## M4: Experimental design for direct video documentation

To allow direct optical documentation of the fault surface, we used the same experimental procedure described above but using a slightly modified sample assembly. We replaced the central slider with a transparent acrylic forcing block (applying shear stress). Differently from the metal slider, the acrylic block has a nominally flat surface in contact with the sample (compare figs. M1a and M2a). We also replaced the lateral forcing blocks with nominally flat surfaces to match the central slider. The coupling between the gouge and the forcing blocks is high enough to force deformation to occur within the gouge and not at the interface. This is confirmed by microstructural evidence (Fig. SM7), comparable frictional properties ($\mu$, $(a-b)$, $\beta$, Fig. SM7), and fault slip behavior (i.e., instabilities, stress drop, recurrence time, fig. SM7). A further test has been performed with intermediate roughness of the forcing blocks, obtaining the similar results. This validates the comparison between this experiment and the others, expressing a negligible influence of the applied roughness.

High-resolution analysis of the fault surface was performed with a NAC Memrecam HX-3 high-speed camera operating at 500 frames per second, a resolution of 192 (horizontal) by 600 (vertical) pixels, and a pixel pitch of 0.0833 mm/pixel. The experimental setup is depicted in Fig. M2. The camera is positioned with a line of sight tilted by 45° from the fault surface and perpendicular to the sliding direction. The fault surface is illuminated with a homogeneous source of white light placed at the other side of the central transparent sliding block. This experimental set allows the camera to record changes of reflectivity along the surface. Changes in reflectivity (imaged as variation in grey level) correspond to changes of the local state of stress projected on the fault surface. This is due to variation of coupling between the block interface and the deforming montmorillonite.

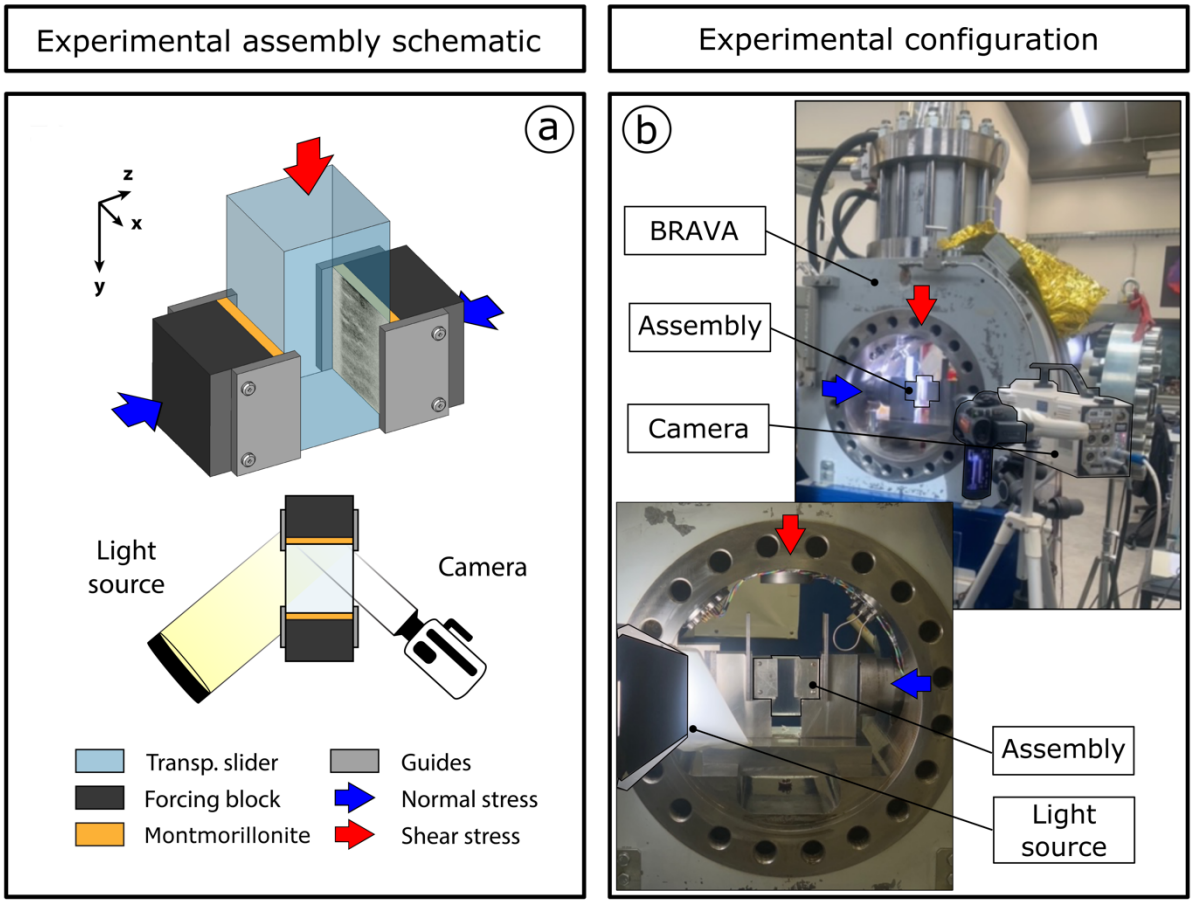


Figure M2: a) schematic of the modified DDS assembly for the video experiment. b) experimental configuration for the video experiments set on BRAVA apparatus.

## M5: Digital-image analysis

Image processing has been performed on the footage using both static and rolling background removal. In the static background removal, a background image was calculated as the pixel-wise average of the 500 frames preceding the beginning of the portion of interest of the video, which corresponds to the final part of the interseismic time and represents the initial state of stress on the fault surface. The background image was then subtracted from each of the subsequent frames. The resulting video displays changes in the grey level (quantified in arbitrary units, a.u.) relative to the background image (Fig 3a). From the static background removal video of a transient slip event (video suppl 1) we projected the average grey level along the y-axis and analyzed the variation in time, obtaining the videogram of Fig 3b. The same procedure is used at discrete times to build the variation of grey level of Fig 3c. The average grey level has been calculated has after gaussian filtering of the original images by averaging x- wise over the visible fault surface (Fig 3a). The rolling background removal consists, for each frame, of the subtraction of a previous frame with an arbitrary separation of time. The optimal separation for visualization has been selected by trial and error at 5-time frames. The resulting image has been normalized over a narrow range of grey levels to enhance contrast. The rolling background reveals the portion of the fault in which stress changes have occurred between 5-time frames, allowing to trace and visualize the position of the rupture front. Selected time frames were stacked to compose image Fig. 3a, which shows in light grey the position of the wrinkle-like pulse.

## References


Collettini, C., Di Stefano, G., Carpenter, B., Scarlato, P., Tesei, T., Mollo, S., Trippetta, F., Marone, C., Romeo, G., Chiaraluce, L., (2014). A novel and versatile apparatus for brittle rock deformation. Int. J. Rock Mech. Min. Sci. 66, 114–123.

Scuderi, M. M., Marone, C., Tinti, E., Di Stefano, G., & Collettini, C. (2016). Precursory changes in seismic velocity for the spectrum of earthquake failure modes. Nature geoscience, 9(9), 695-700.

Leeman, J. R., Marone, C., & Saffer, D. M. (2018). Frictional mechanics of slow earthquakes. Journal of Geophysical Research: Solid Earth, 123(9), 7931-7949.

Dieterich, J. H. (1979). Modeling of rock friction: 1. Experimental results and constitutive equations. Journal of Geophysical Research: Solid Earth, 84(B5), 2161-2168.

Ruina, A. (1983). Slip instability and state variable friction laws. Journal of Geophysical Research: Solid Earth, 88(B12), 10359-10370.

Marone, C. (1998). Laboratory-derived friction laws and their application to seismic faulting. Annual Review of Earth

and Planetary Sciences, 26(1), 643-696.

Blanpied, M. L., Marone, C. J., Lockner, D. A., Byerlee, J. D., & King, D. P. (1998). Quantitative measure of the variation in fault rheology due to fluid-rock interactions. Journal of Geophysical Research: Solid Earth, 103(B5), 9691-9712.

Saffer, D. M., & Marone, C. (2003). Comparison of smectite-and illite-rich gouge frictional properties: application to the updip limit of the seismogenic zone along subduction megathrusts. Earth and Planetary Science Letters, 215(1-2), 219-235.

Volpe, G., Pozzi, G., & Collettini, C. (2022). YBPR or SCC'? Suggestion for the nomenclature of experimental brittle fault fabric in phyllosilicate-granular mixtures. Journal of Structural Geology, 165, 104743.

Passchier, C.W., 1990. A Mohr circle construction to plot the stretch history of material lines. J. Struct. Geol. 12 (4), 513–515.

# Appendix of chapter IV

# *Study of fluid-induced reactivation of granite-hosted fault in the Central Alps*

---

## Laboratory simulation of fault reactivation by fluid injection and implications for induced seismicity at the BedrettoLab, Swiss Alps.

**G. Volpe**[a], G. Pozzi[b], C. Collettini[a,b], E. Spagnuolo[b], P. Achtziger-Zupančič[c], A. Zappone[d], L. Aldega[a], M.A. Meier[d], D. Giardini[d], M. Cocco[b]

a: Department of Earth Sciences, La Sapienza University of Rome, Italy

b: Istituto Nazionale di Geofisica e Vulcanologia, Italy

c: Department of Engineering Geology and Hydrogeology, RWTH Aachen University, Germany

d: Department of Earth Sciences, ETH Zürich, Switzerland

*Published in Tectonophysics*

## Supporting Information

The following Supporting Information include SI.1 – MC fault zone; SI.2 – Microstructure; SI.3 – Layer thickness evolution; SI.4 – Comparison between layer thickness evolution and vertical displacement; SI.5 – Experimental microstructures.

## SI.1 MC fault zone

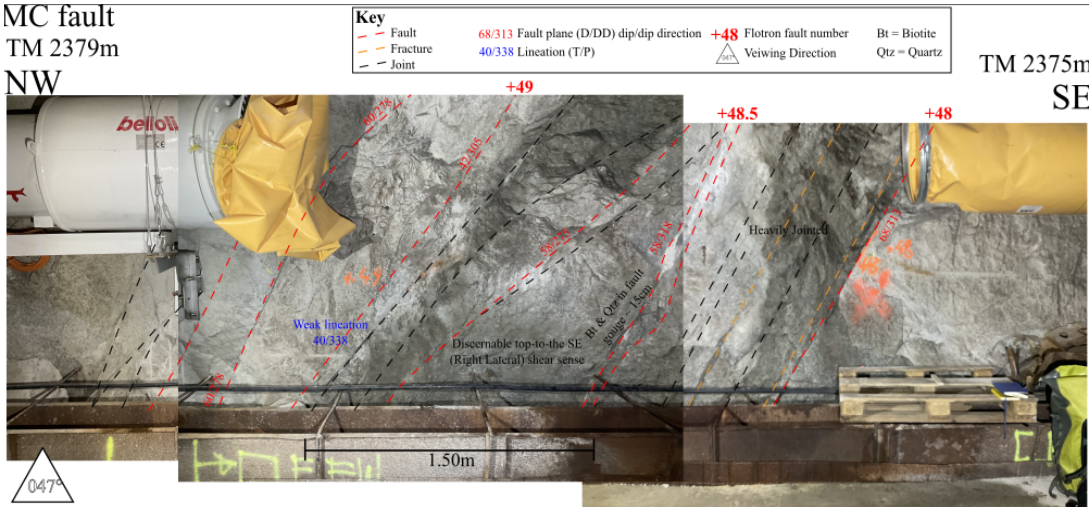


Figure SI1: photomosaic of the MC fault zone cropping out along the Bedretto tunnel (2379 tunnel meters from the entrance). Red dashed lines highlight the principal the fault surfaces. Yellow and black dashed lines represent fractures and joints respectively. The main segment of the MCF zone is the 48.5 fault, where is clearly visible the white gouge bearing fault core and the dilational jog.

## SI.2 Microstructures

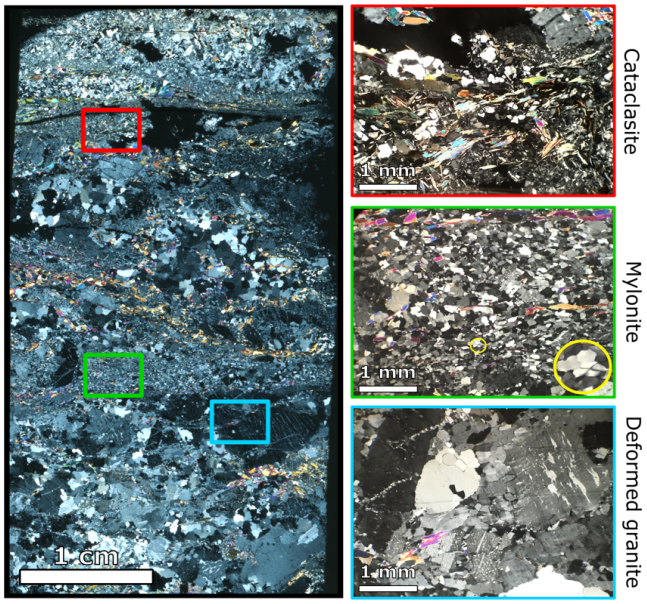


Figure SI2: Thin section of the MC fault (see Fig. 2 for details). Blue panel: deformed granite where ductile deformation is evident. Green panel: mylonite, where highly comminuted quartz grains with triple and quadruple junctions (yellow circle) and sheet silicates producing C-type foliation are visible. Red panel: cataclasite of the MC fault where subrounded grains of quartz and feldspar enveloped by a very fine-grained matrix of sheet silicates and zeolites are visible. A proto foliation marked by sheet silicates is visible.

## SI.3 Layer thickness evolution

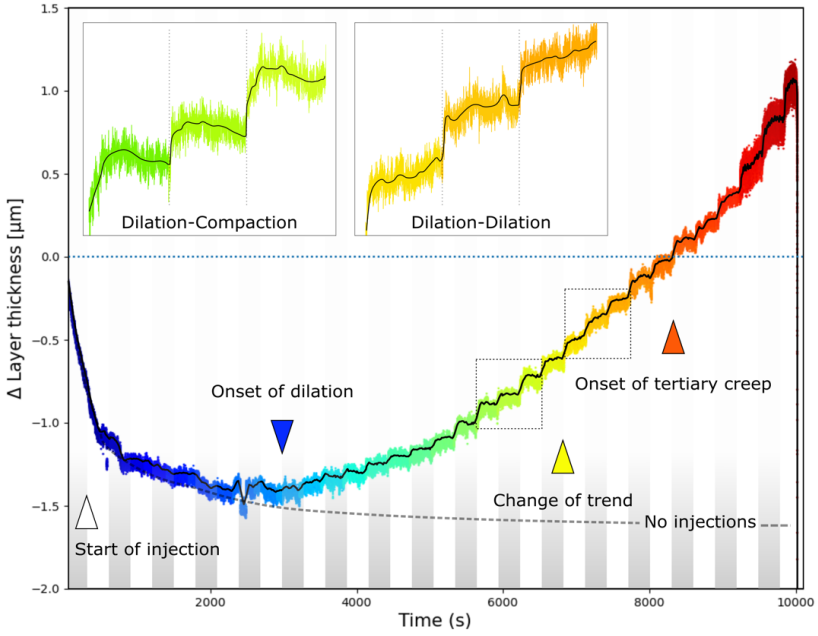


Figure SI.3: evolution of the layer thickness with time during the injection stage (stage 5). In the onsets is reported the evolution of layer thickness in selected intervals (dotted box in main panel).

## SI.4 Comparison between layer thickness evolution and vertical displacement

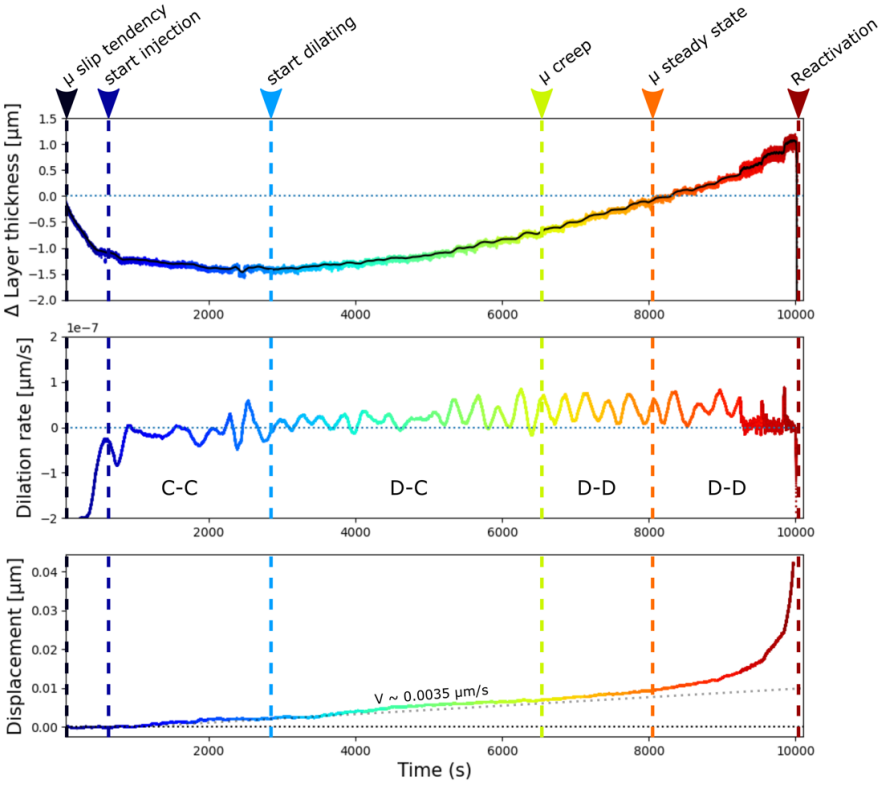


Figure SI.4: evolution of the layer thickness, dilation rate and vertical displacement with time during the injection stage (stage 5). For details refers to Fig. 5 in main text and Fig. SI.3.

## SI. 5 Experimental microstructures

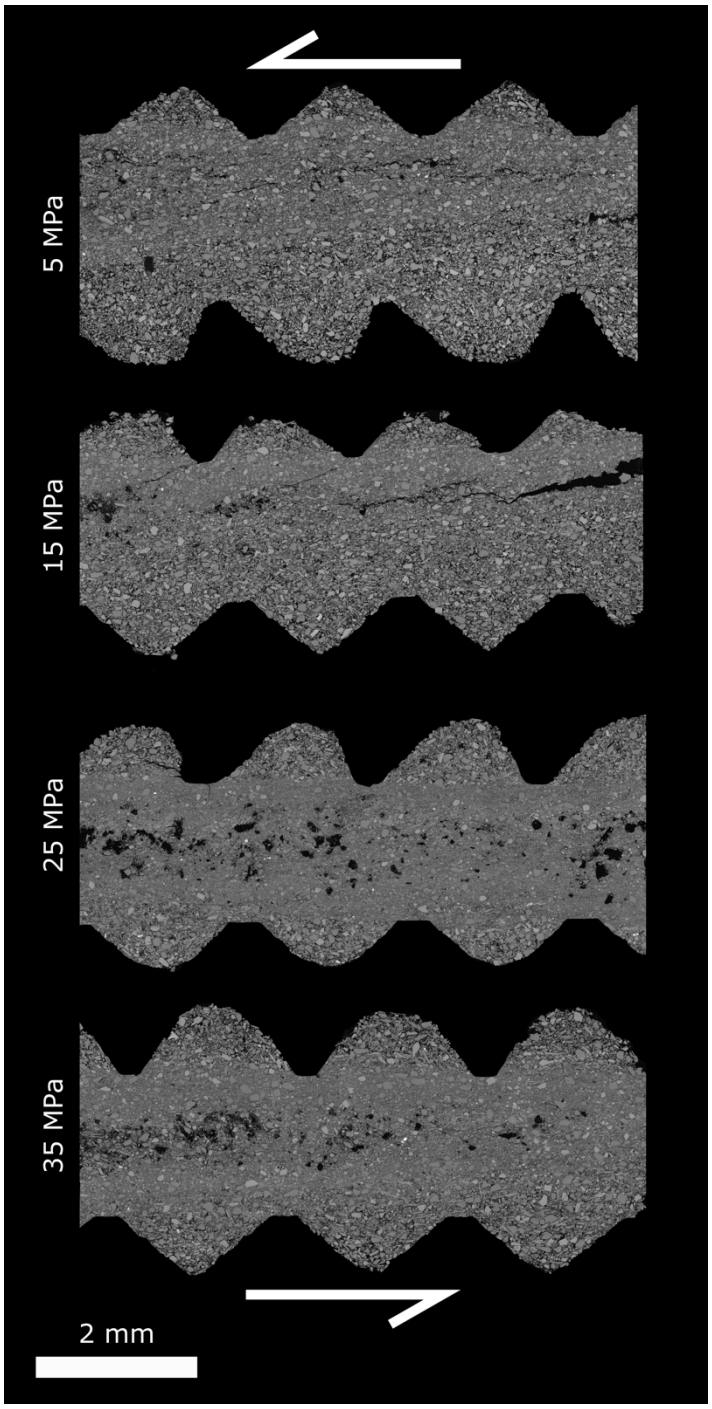


Figure SI.5: Microstructures of experimental post-mortem gouge. Images are collected in SEM-BSE mode. The normal stress for each microstructure is reported at the left of the relative microstructure.